Article

Transcranial volumetric imaging using a conformal ultrasound patch

https://doi.org/10.1038/s41586-024-07381-5

Received: 3 February 2023

Accepted: 2 April 2024

Published online: 22 May 2024

Check for updates

Sai Zhou[1,9], Xiaoxiang Gao[2,9], Geonho Park[2,9], Xinyi Yang[1,9], Baiyan Qi[1], Muyang Lin[2], Hao Huang[2], Yizhou Bian[2], Hongjie Hu[2], Xiangjun Chen[1], Ray S. Wu[2], Boyu Liu[2], Wentong Yue[2], Chengchangfeng Lu[3], Ruotao Wang[2], Pranavi Bheemreddy[3], Siyu Qin[3], Arthur Lam[4], Keith A. Wear[5], Michael Andre[6], Erik B. Kistler[6,7], David W. Newell[8] & Sheng Xu[1,2,3,6,7] ✉

Accurate and continuous monitoring of cerebral blood flow is valuable for clinical neurocritical care and fundamental neurovascular research. Transcranial Doppler (TCD) ultrasonography is a widely used non-invasive method for evaluating cerebral blood flow[1], but the conventional rigid design severely limits the measurement accuracy of the complex three-dimensional (3D) vascular networks and the practicality for prolonged recording[2]. Here we report a conformal ultrasound patch for hands-free volumetric imaging and continuous monitoring of cerebral blood flow. The 2 MHz ultrasound waves reduce the attenuation and phase aberration caused by the skull, and the copper mesh shielding layer provides conformal contact to the skin while improving the signal-to-noise ratio by 5 dB. Ultrafast ultrasound imaging based on diverging waves can accurately render the circle of Willis in 3D and minimize human errors during examinations. Focused ultrasound waves allow the recording of blood flow spectra at selected locations continuously. The high accuracy of the conformal ultrasound patch was confirmed in comparison with a conventional TCD probe on 36 participants, showing a mean difference and standard deviation of difference as -1.51 ± 4.34 cm s^{-1}, -0.84 ± 3.06 cm s^{-1} and -0.50 ± 2.55 cm s^{-1} for peak systolic velocity, mean flow velocity, and end diastolic velocity, respectively. The measurement success rate was 70.6%, compared with 75.3% for a conventional TCD probe. Furthermore, we demonstrate continuous blood flow spectra during different interventions and identify cascades of intracranial B waves during drowsiness within 4 h of recording.

Cerebral blood flow supplies oxygen and energy substrates and removes metabolic wastes to maintain proper brain functions. Continuous monitoring of cerebral haemodynamics enables screening and diagnosing brain disorders[2] as well as understanding neurovascular functions[3]. However, assessment of cerebral blood flow is challenging because cerebral vasculature is embedded deep inside the brain and protected by the skull. Various modalities to measure cerebral blood flow have been explored (Extended Data Table 1 and Supplementary Discussion 1), including positron emission tomography[4], computed tomography[5] and magnetic resonance imaging[6], which all provide adequate spatial resolution but require bulky equipment that prohibits continuous use. Emerging thermal[7], electrical[8], and optical probes[9] can be miniaturized for continuous monitoring, but these probes cannot provide sufficient spatiotemporal resolutions.

Transcranial Doppler (TCD) is widely used for cerebral haemodynamic monitoring because of its safety, low cost, portability, versatility and relatively high spatiotemporal resolutions (Supplementary Table 1). However, conventional TCD probes have several limitations. First, these probes are rigid and need to be manually held by well-trained clinicians or affixed using bulky headsets for continuous monitoring[1]. Slight misalignment between the ultrasound beam and the target vessel, often caused by hand movement, poor headset fastening or movement by the participant, can cause fluctuation, degradation or complete loss of signals[2]. Therefore, the headset is usually very tight, causing discomfort, thus limiting the typical recording time to less than 30 min (ref. 10). Second, these probes usually use a single transducer or a linear array of transducers, which can only image part of the intricate three-dimensional (3D) network of cerebral arteries. Different operators may acquire signals from different segments of the 3D network, affecting repeatability and reproducibility[1] (Extended Data Fig. 1). Furthermore, manual probe tilting is required to identify the optimal angle for the acquisition of high-quality spectra, a routine process that is both time-consuming and heavily reliant on the expertise of the operator. To address these problems, volumetric imaging can be used to guide

[1]Materials Science and Engineering Program, University of California San Diego, La Jolla, CA, USA. [2]Department of Nanoengineering, University of California San Diego, La Jolla, CA, USA. [3]Department of Electrical and Computer Engineering, University of California San Diego, La Jolla, CA, USA. [4]Department of Anesthesiology and Critical Care, University of California San Diego, La Jolla, CA, USA. [5]U.S. Food and Drug Administration, Silver Spring, MD, USA. [6]Department of Radiology, University of California San Diego, La Jolla, CA, USA. [7]Shu Chien-Gene Lay Department of Bioengineering, University of California San Diego, La Jolla, CA, USA. [8]Department of Neurosurgery, Seattle Neuroscience Institute, Seattle, WA, USA. [9]These authors contributed equally: Sai Zhou, Xiaoxiang Gao, Geonho Park, Xinyi Yang. ✉e-mail: shengxu@ucsd.edu

target selection (Supplementary Fig. 1). Although two-dimensional (2D) matrix arrays can provide volumetric imaging, currently these probes have limited spatiotemporal resolutions because of technical barriers in probe fabrication and data acquisition[11,12] (Supplementary Discussion 1).

Wearable ultrasound devices enable comfortable contact with the skin surface for sensing physiological signals in deep tissues[13–17]. However, probing inside the brain is challenging because of the strong signal attenuation (Supplementary Fig. 2 and Supplementary Discussion 2) and phase aberration (Supplementary Fig. 3 and Supplementary Discussion 3) caused by the skull. Furthermore, existing wearable ultrasound devices provide only one-dimensional (1D) signals[18], 2D images[19] or 3D images by inaccurate integration and extrapolation of multiple 2D image slices[20]. Here we report the first conformal ultrasound patch for accurate and continuous monitoring of cerebral blood flow in 3D (Supplementary Discussion 4). We use low-frequency ultrasound waves to reduce the skull-induced signal attenuation and phase aberration[21]. We add a copper mesh shielding layer to the device and adopt an ultrafast imaging technique to insonate the entire 3D region, which substantially improves the signal-to-noise ratio[22,23]. This technology represents a powerful platform for both clinical and fundamental haemodynamic studies.

Device design and characterizations

To minimize acoustic attenuation and phase aberration, four transcranial windows (temporal, orbital, submandibular and suboccipital) are commonly used for TCD[24] (Supplementary Fig. 4). These windows are relatively small (about 5 cm^2 in adults)[1], requiring a compact device design. By contrast, the cerebral arterial network has several major components, including the anterior cerebral arteries (ACA), middle cerebral arteries (MCA), posterior cerebral arteries (PCA), ophthalmic arteries, internal carotid arteries (ICA), basal artery and vertebral arteries (Supplementary Discussion 5). Most of these arteries are deep (around 40–100 mm) and widely distributed inside the brain[1] (Fig. 1a), requiring devices with a wide ultrasound field (Supplementary Fig. 5). Therefore, we used diverging waves to image the entire arterial network and focused waves to monitor local blood flow spectra at target arterial sections (Fig. 1b and Methods). Diverging waves extend the ultrasound field from a limited acoustic window (12 mm × 12 mm) to a much larger region (about 60 mm × 60 mm at 50 mm depth in this work), which allows for simultaneous insonation of multiple cerebral arteries. Focused waves minimize unnecessary ultrasound exposure to surrounding tissues for long-term monitoring of blood flow spectra.

We built a 16 × 16 matrix array with a 750-μm pitch and a 2-MHz centre frequency (Methods and Supplementary Discussion 6). The choice of such a low frequency reduces signal attenuation and phase aberration and thus enhances transcranial penetration depth[1] (Supplementary Discussions 2 and 3). The pitch is comparable to the ultrasound wavelength (that is, 770 μm in soft tissues at 2 MHz), enabling a large tilting angle of the ultrasound beam in 3D (Supplementary Fig. 6). The matrix array has an aperture of 12 mm × 12 mm, similar to that of established TCD probes[25,26], which enables insonation through the skull and focusing on deep targets[12]. Five layers of serpentine interconnections are used to address the 256 elements individually (Fig. 1a and Supplementary Fig. 7). The matrix array has excellent properties such as high electromechanical coupling coefficient, and negligible crosstalk, resulting in high sensitivity to Doppler shift (Methods and Supplementary Fig. 8). We designed a serpentine copper mesh as an electromagnetic shielding layer, which increased the signal-to-noise ratio on average by 5 dB (Methods and Supplementary Fig. 8). Encapsulation of the entire device by silicone elastomer allows for electrical insulation and conformal contact on various surfaces (Fig. 1c, Supplementary Figs. 9 and 10). The final device is 1.3 mm thick, 20 mm wide and 28 mm long, with a total weight of 0.945 g.

The ultrasound intensity of the device was measured in a water tank (Methods, Extended Data Fig. 2 and Supplementary Discussion 7). We limited the maximum derated mechanical index and derated spatial peak temporal average intensity of all ultrasound transmissions in this work to about 0.7 and 370 mW cm^{-2}, respectively. These values are well below the Food and Drug Administration Track 1 maximum recommended levels for TCD applications (that is, 1.9 and 720 mW cm^{-2}, respectively)[27]. After penetrating through a temporal bone specimen, the measured maximum derated spatial peak temporal average intensity was reduced by approximately 83% to about 63 mW cm^{-2} (Extended Data Fig. 2 and Supplementary Fig. 11). For orbital window scans, the maximum mechanical index and derated spatial peak temporal average intensity were reduced to conform to the Food and Drug Administration Track 1 recommended maximum levels for ophthalmic scans (0.23 and 17 mW cm^{-2}, respectively)[27].

To characterize its thermal effect, we attached the device to the scalp of a normal human volunteer and activated the device for 4 h. The maximum temperature rise on the skin surface was less than 1 °C (Supplementary Fig. 12). Furthermore, for estimated temperature changes of internal tissues during prolonged ultrasound exposure, we calculated the thermal index[27], the ratio between the incident acoustic power and the power required to raise the tissue temperature by 1 °C (Supplementary Discussion 7), which were 0.62 for soft tissue thermal index and 0.38 for cranium thermal index. According to an official statement of the American Institute of Ultrasound in Medicine, for a thermal index less than or equal to 1.5, there is no time limit for adult transcranial ultrasound because any thermal exposure would be below thresholds for bioeffects (https://www.aium.org/resources/official-statements/view/recommended-maximum-scanning-times-for-displayed-thermal-index-(ti)-values).

Volumetric ultrafast imaging

The temporal window is the most widely used imaging window for TCD and has become the standard for cerebral artery assessment[1] (Supplementary Fig. 13). Through the temporal window, we can achieve ultrasound insonation of the terminal ICA (TICA), which delivers blood from the neck to the major arteries in the brain, as well as the ACA, MCA and PCA, which deliver blood to most of the four brain lobes (frontal, parietal, temporal and occipital).

The cerebral arteries can be mapped by ultrafast ultrasound data acquisition followed by subsequent volumetric image reconstruction (Methods). Compared with conventional volumetric Doppler imaging, this method substantially enhances the signal-to-noise ratio (Supplementary Fig. 14). The 256 elements are activated to emit five diverging waves at different insonation angles at a 3,000-Hz pulse repetition frequency (Fig. 2a). For all insonation angles, the backscattered raw radiofrequency signals are saved. During subsequent image reconstruction, beamforming and coherent compounding (Supplementary Discussion 8) are performed on the raw signals, which allows the backscattered signals from all insonation angles to be recombined (Fig. 2a). Because signals from different insonation angles produce images of the same target object but different artefacts, signal recombination causes constructive summation of the target object but destructive summation of artefacts, boosting the object to background contrast[22]. A spatiotemporal clutter filter (for example, singular value decomposition in this work) separates tissue motion signals from blood flow signals in the compounded data based on the difference in their spatiotemporal coherences[28] (Supplementary Discussion 9). Additional filters are used to suppress the noise and enhance the vascular structures[29–31]. Finally, the filtered data are used to reconstruct a volumetric power Doppler image (Fig. 2a). The diverging waves and the multi-angle compounding method provide a wide ultrasound field, which simultaneously insonates the bilateral ACA, MCA, PCA, and TICA, mapping a large vascular

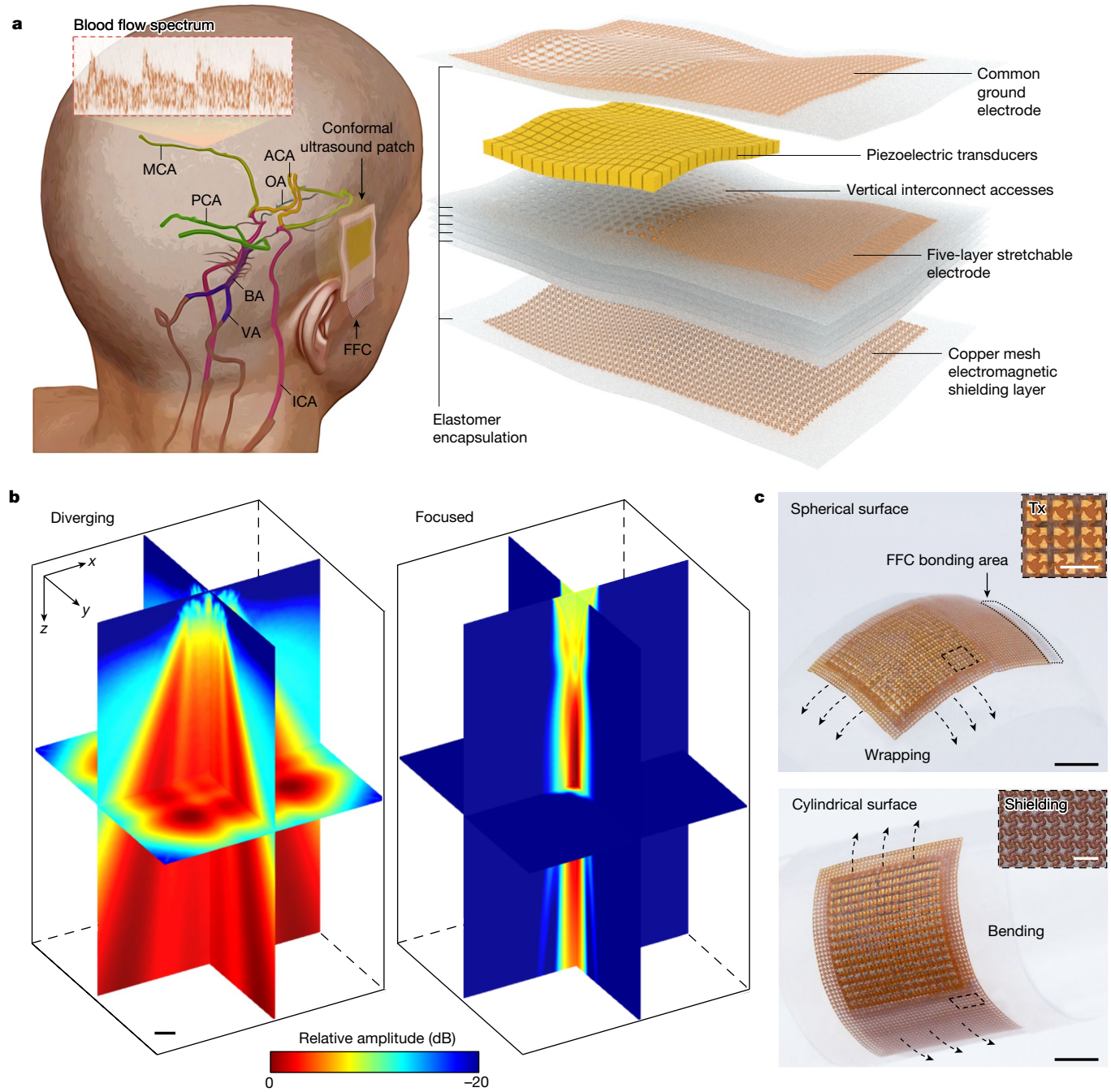

Fig. 1 | Overview of the conformal ultrasound patch for TCD. a, Schematic of the working configuration and patch structure. The patch is attached to the scalp for volumetric mapping of the major arteries in the brain[48]. Blood flow spectra of different target arteries are recorded. The patch consists of a 16 × 16 array of piezoelectric transducers connected by a five-layer stretchable electrode and a common ground electrode. A copper mesh is used as an electromagnetic shielding layer to enhance the signal-to-noise ratio. The entire device is encapsulated by a waterproof and biocompatible silicone elastomer. **b**, Simulation results of diverging and focused ultrasound fields based on 2D matrix array beamforming. The maximum derated spatial peak temporal average intensity of the focused ultrasound field is around 370 mW cm^{-2} for spectra monitoring, much below the threshold recommended by the Food and Drug Administration (720 mW cm^{-2}) (ref. 27). The simulation was performed using an open-source Matlab toolbox Field II. **c**, Optical images of the patch on a spherical surface and a cylindrical surface. The insets show the magnified transducer array (top) and the electromagnetic shielding layer (bottom). BA, basal artery; VA, vertebral arteries; OA, ophthalmic arteries; FFC, flat flexible cable; Tx, transducers. Scale bars, 5 mm (**b**,**c**); 1 mm (**c**, insets).

network (Fig. 2b for participant 1 and Supplementary Figs. 15–49 for participants 2–36).

We recorded volumetric power Doppler images during a carotid compression test and captured the flow variations in different arterial segments, which helped in identifying different cerebral arteries (Fig. 2c). Compressing the left common carotid artery mostly caused a decrease in flow in the left TICA and left MCA, a change in flow direction in the left ACA, an increase in flow in the left PCA and an increase in flow in most of the contralateral vessels (Supplementary Discussion 5). To semi-quantitatively evaluate the vascular network capacity, we evaluated the changes in the amplitude of the power Doppler signal of selected representative landmarks in each arterial segment. The results indicate that the collateral circulation could be recorded reliably (Fig. 2d and Extended Data Fig. 3).

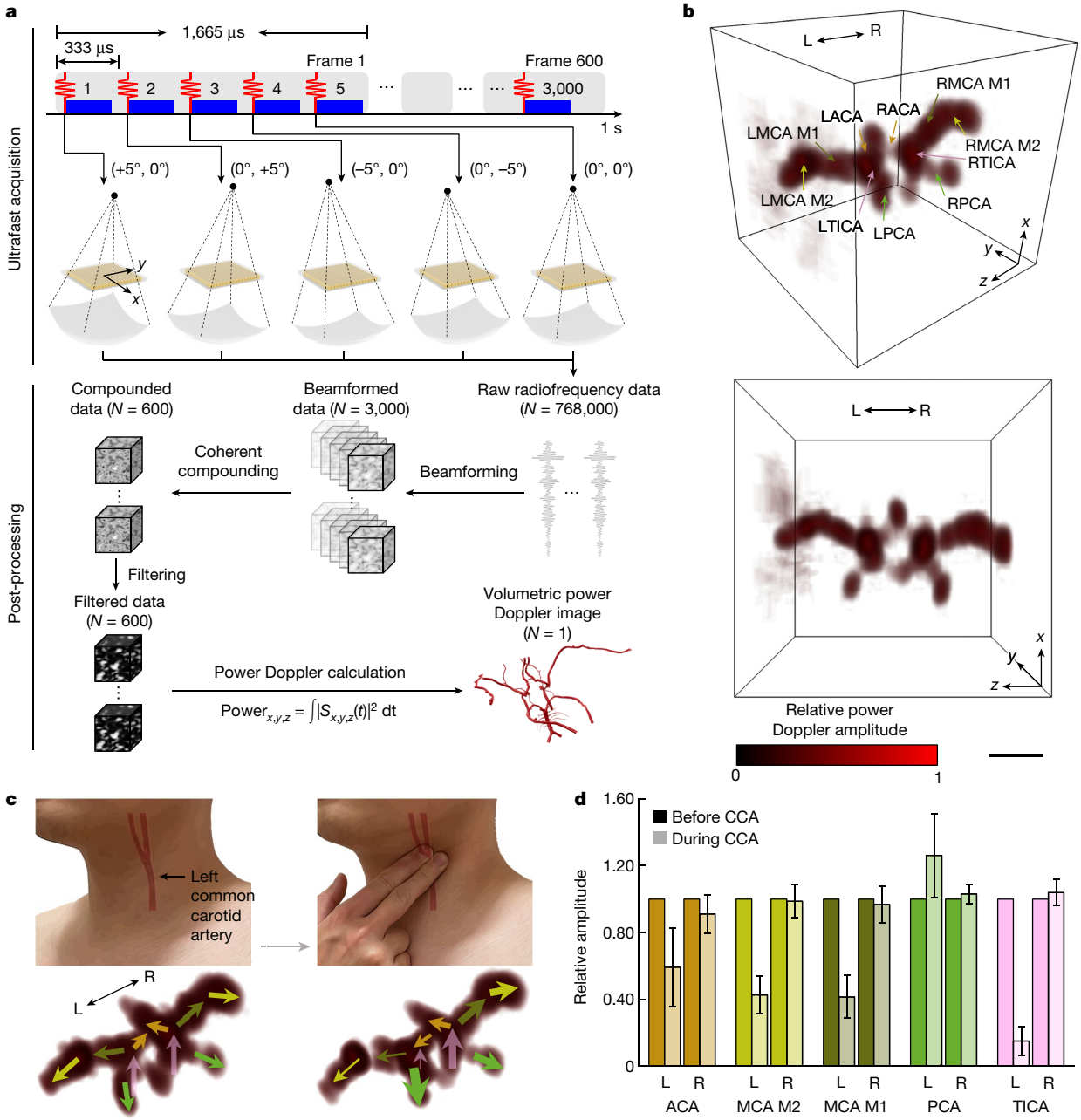

Fig. 2 | Volumetric ultrafast power Doppler imaging. a, Schematic of the imaging process. In ultrafast acquisition, five diverging waves with different insonation angles are quasi-simultaneously transmitted at a 3,000-Hz pulse repetition frequency. In post-processing, the acquired raw radiofrequency data go through beamforming, coherent compounding, singular value decomposition filtering and power Doppler calculation to reconstruct a volumetric power Doppler image. **b**, Different views of the volumetric power Doppler image of major cerebral arteries from participant 1 in a 60 × 60 × 60 mm^3 region, acquired through the temporal window. Volumetric power Doppler images from participants 2–36 can be found in Supplementary Figs. 15–49. **c**, Comparison of volumetric power Doppler images before and during the left common carotid artery being compressed. The colour and thickness-coded arrows indicate the directions and magnitudes of blood flow in different arterial segments. **d**, Bar graph of compression carotid artery test. The power Doppler amplitudes of representative landmarks of bilateral arterial segments change accordingly before and during the compression of the left common carotid artery. The measurements were repeated three times on six participants. Error bars indicate 1 s.d. of the measurements. Note that individual anatomical variations, such as hypoplasia or aplasia of certain arteries, can affect these results[49]. The hypoplasia or aplasia arteries are observed in two of the six participants in this study. Each bar is colour-coded for different arterial segments (cider for ACA, xanthic for MCA M2, juniper for MCA M1, Kelly green for PCA and carnation pink for TICA). To better evaluate the relative change before and after compression, we normalized the results before compression and only considered the relative change of the blood flow during compression. L, left; R, right; CCA, compressing carotid artery. Scale bar, 10 mm (**b**).

Data processing and validation

Blood flow measurements by the conformal ultrasound patch were validated with a conventional TCD probe. We chose the circle of Willis as the model, which is composed of several major arteries that provide blood supply to the entire brain[1]. It has widespread branches, so the circle of Willis is usually measured through all four transcranial windows[24]. Each window targets different arterial segments (Supplementary Table 2): the temporal is best for the ACA, MCA M2, MCA M1, PCA and TICA; the orbital for the ophthalmic arteries and ICA siphon;

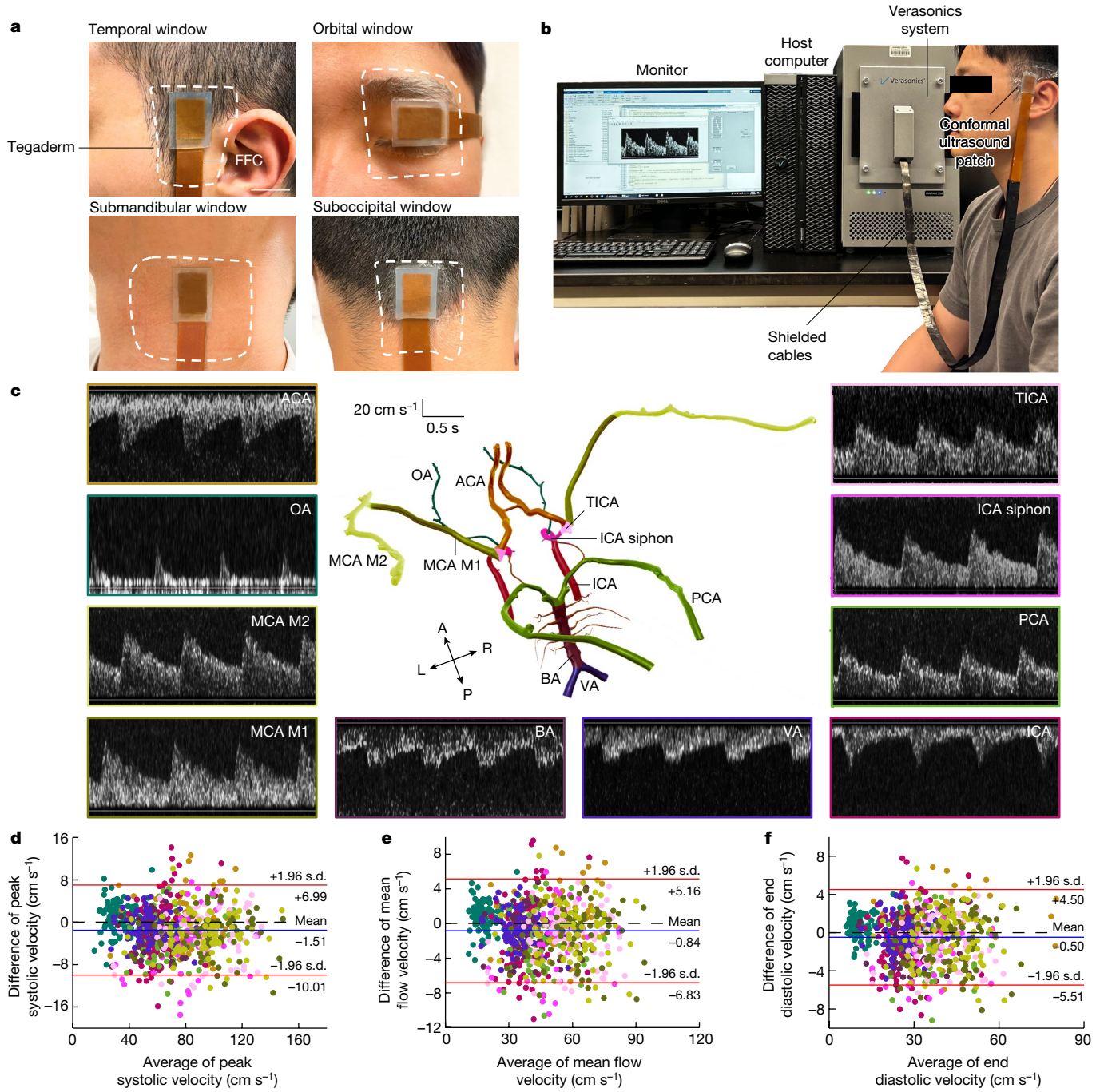

Fig. 3 | Validation of cerebral blood flow measurements. a, Optical images of the conformal ultrasound patch on four different transcranial windows, including the temporal, orbital, submandibular and suboccipital windows. **b**, Optical image of the complete setup. It includes the ultrasound patch connected to a Verasonics system by shielded (3304BC-S, 3 M) cables. The host computer controls the Verasonics system for data acquisition and processing. The blood flow spectrum is displayed on the monitor. **c**, Examples of blood flow spectra recorded from representative arterial segments from participant 1 by using the ultrasound patch. The spectra share the same scale bars. Blood flow spectra from participants 2–36 can be found in Supplementary Figs. 15–49. **d**–**f**, Bland–Altman plots of peak systolic velocity (**d**), mean flow velocity (**e**) and end diastolic velocity (**f**) measured by the ultrasound patch and a conventional TCD probe on 36 participants. Solid blue lines are the mean differences in the measurements between the two modalities. Solid red lines are 95% limits of agreement (that is, 1.96 s.d. above and below the mean differences), and black dash lines are the zero difference of the measurements between the two modalities. Each plot has 762 data points that are colour-coded for different arterial segments (that is, cider for ACA, dark cyan for ophthalmic arteries (OA), xanthic for MCA M2, juniper for MCA M1, boysenberry for basal artery (BA), blueberry for vertebral arteries (VA), hibiscus for ICA, Kelly green for PCA, magenta for ICA siphon and carnation pink for TICA). FFC, flat flexible cable; L, left; R, right; A, anterior; P, posterior. Scale bar, 2 cm (**a**).

the submandibular for the ICA; and the suboccipital for the basal artery and vertebral arteries (Fig. 3a). The setup consists of the conformal ultrasound patch linked to a commercial ultrasound machine (Vantage 256, Verasonics) with shielded cables for signal transmission, controlled by a host computer for data acquisition and processing (Fig. 3b).

We developed codes for Doppler processing to acquire high-resolution blood flow spectra (Fig. 3c for participant 1 and Supplementary Figs. 15–49 for participants 2–36) with functions such as automatic spectral envelope tracking, sample volume customization, and audio (Supplementary Discussion 10). The recorded spectra have

Table 1 | Demographics of participants

Characteristics	*n* (%) or mean ± s.d.
Sex	***n* (%)**
Male	19 (52.8)
Female	17 (47.2)
Race or ethnicity	***n* (%)**
White	15 (41.7)
Asian	13 (36.1)
Black or African	5 (13.9)
Hispanic or Latino	3 (8.3)
Underlying conditions	***n* (%)**
Diabetes	5 (13.9)
Smoking	5 (13.9)
Cardiac disease	4 (11.1)
Obesity	3 (8.3)
Kidney disease	2 (5.6)
Cerebrovascular disease	1 (2.8)
Biometrics	**Mean ± s.d.**
Age (years)	52.92±18.74
Height (cm)	167.44±9.25
Weight (kg)	68.92±11.72
Body mass index	24.46±2.80

This table presents an overview of the demographic information for all participants in this study. Details include sex, race/ethnicity, underlying conditions, age, height, weight and body mass index, providing context for the diversity of the participants, which ensures that the findings of the study are broadly applicable.

a temporal resolution around 200 Hz, a velocity resolution of less than 0.01 cm s^{-1}, and a 128-colourmap of Doppler signal intensities, which are similar to the performance of the latest conventional TCD system (https://viasonix.com/products/transcranial-doppler/). This enables us to correlate variations in blood flow velocities to the corresponding cardiac phases (Supplementary Fig. 50). Spectral envelope tracking provides peak systolic velocity and end diastolic velocity, which enables the computation of mean flow velocity, pulsatility index and resistive index (Methods and Extended Data Fig. 4). Sample volume customization can provide blood flow distribution across the entire target arterial segment, which is valuable for identifying pathologic turbulent flow (Supplementary Discussion 11) in the low-velocity zone[2] (Supplementary Fig. 51). Real-time audio provides convenience for clinical training and diagnostics (Supplementary Video 1).

For this comparison study between the conformal ultrasound patch and a conventional TCD probe, we have collected blood flow velocities of 10 arterial segments from 36 adult volunteers for three times to ensure the results are reliable and reproducible (Table 1 and Methods). Intrinsically, a complete circle of Willis is observed in only about 30% of the population[32]. Moreover, participants with specific demographics and medical history tend to have abnormal cerebral arteries and may exhibit thicker, or even inaccessible, skull windows[24]. As a result, both the conventional probes and the ultrasound patch may encounter difficulties in detecting some or all cerebral arteries (Extended Data Table 2 and Supplementary Discussion 12).

Bland–Altman plots show that the mean differences and standard deviations (s.d.) of the differences between these two devices are -1.51 ± 4.34 cm s^{-1}, -0.84 ± 3.06 cm s^{-1}, -0.50 ± 2.55 cm s^{-1}, -0.0101 ± 0.0485, and -0.0040 ± 0.0186 for peak systolic velocity, mean flow velocity, end diastolic velocity, pulsatility index and resistive index, respectively (Fig. 3d–f, Supplementary Fig. 52 and Supplementary Discussion 13). These biases are much smaller than these metrics per se, indicating good agreement between these two devices. To delve deeper into our results, we apply scatter plots for a more thorough analysis (Supplementary Figs. 52 and 53). Notably, the squared correlation coefficients for all velocity parameters and indices exceed 0.9. This strong correlation underscores the consistency in the readings between these two devices.

Monitoring under different scenarios

The brain can regulate its blood flow to meet physiological demands (Supplementary Discussion 14). Surveillance of these regulations can be used to evaluate neurological functions. The conformal ultrasound patch was used to measure (using the temporal window) MCA and PCA flows, which dominate the supply of blood to the brain. The motion tolerance of the device was determined to be within about ±20° with head roll, yaw and pitch (Supplementary Fig. 54). Rotating the head beyond this range may shift the alignment between the ultrasound beam and arteries, resulting in signal degradation or loss. We then asked the participants to conduct four different activities that modulated haemodynamics in specific cerebral arteries (Methods and Supplementary Fig. 55). Each activity was repeated 15 times to minimize interference of confounding factors.

The handgrip involves the contraction of the forearm muscles that activate the sympathetic nervous system, leading to an increase in blood supply to the brain and therefore the contralateral MCA blood flow velocity[33]. The test consists of three phases: resting baseline, right handgrip and recovery. The left MCA mean flow velocity rose rapidly at the beginning of the handgrip, then slowly plateaued at around 119% baseline velocity when the handgrip was maintained. The flow velocity decreased swiftly to 95% baseline velocity immediately after the handgrip was released and gradually reached a plateau towards the end of the recovery phase (Fig. 4a).

The Valsalva manoeuvre provides an estimate of the autoregulatory capacity[34]. It changes the intrathoracic pressure, which affects the venous return, cardiac output, blood pressure and, therefore, cerebral blood flow. We monitored the left MCA mean flow velocity during four sequential phases. In phase I, the participants inhaled deeply; the intrathoracic pressure increased, which led to a decrease in the heart rate and a slight (about 5%) increase in the cerebral blood flow. In phase IIa, the participants held their breath; the venous return decreased, which led to a decrease in the heart rate and around 12% drop in the blood flow. In phase IIb, the baroreflex was activated, which increased the heart rate and partially restored the blood flow. In phase III, the participants exhaled; blood was refilled to the pulmonary vasculature, leading to an increase in the heart rate and slight variations (an increase in most participants) in the blood flow. Finally, in phase IV, the participants resumed normal breathing; the venous return increased, resulting in a decrease in the heart rate and subsequent overshoot (about 118%) of the cerebral blood flow. Once the venous return went back to normal, the blood flow dropped back to the baseline (Fig. 4b).

Word generation is commonly used in functional TCD to understand language processing and production. In this activity, a cue tone was used for auditory signal stimulation, and then a letter was given to the participants. The participants were asked to use the letter to generate words and orally report them after a second auditory signal stimulation. The recorded left MCA mean flow velocity showed a rise (approximately 5%) from the baseline on hearing the tone and after a letter was provided. Activation of the language centre of the brain led to an increased demand for cerebral blood flow in the dominant hemisphere[35]. The velocity remained at an average of about 110% baseline during word generation and continued to increase (by about 18%) when the participant was reporting the words (Fig. 4c).

Visual stimulation can change the blood flow in the visual cortex[36]. We monitored the PCA that supplies blood to the primary vision centre in the brain (that is, the occipital lobe) when the participants

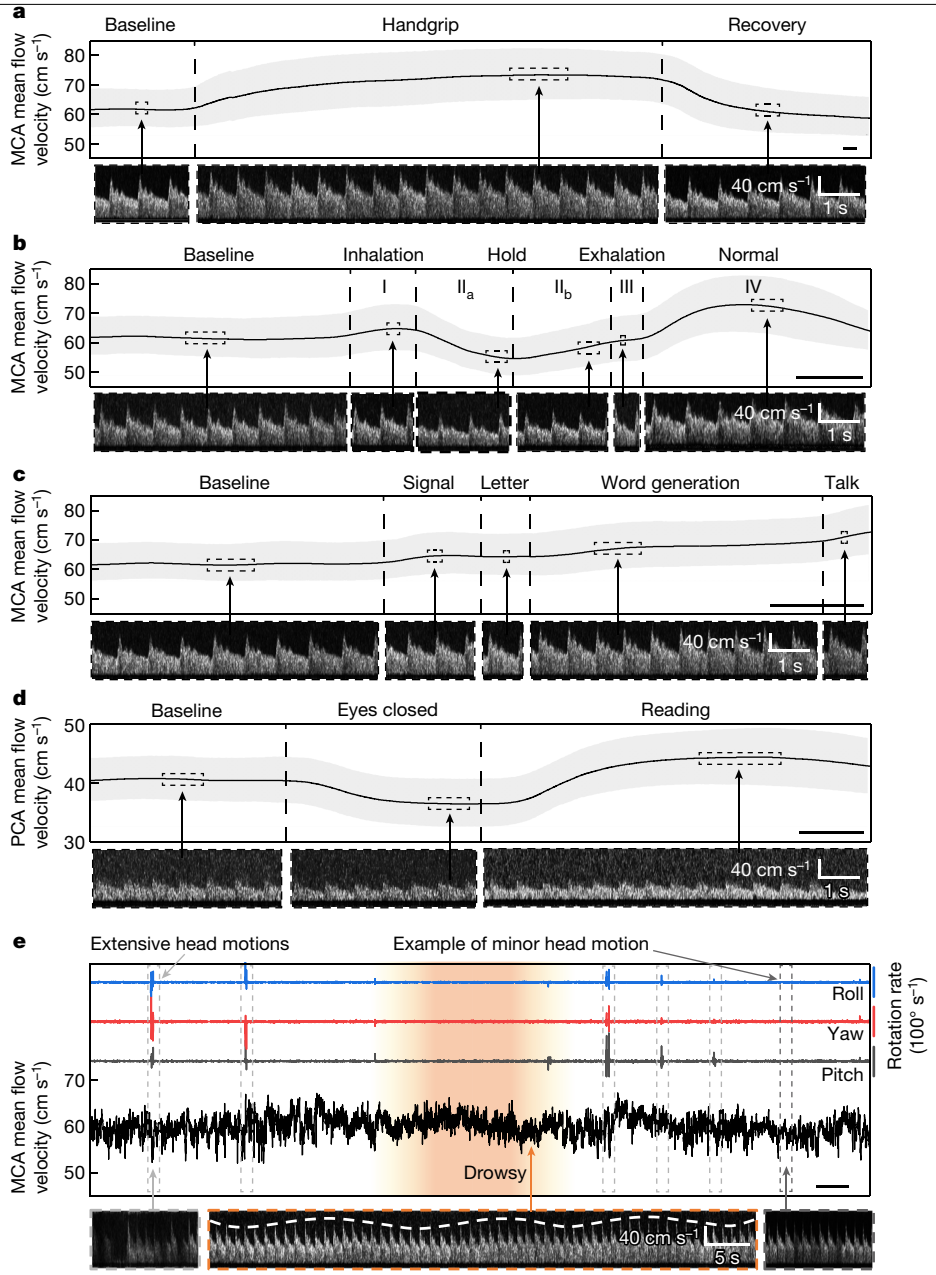

Fig. 4 | Monitoring of cerebral haemodynamics under different scenarios. **a**–**d**, Mean blood flow velocities of target arteries recorded during different activities (handgrip (**a**), Valsalva manoeuvre (**b**), word generation (**c**) and visual stimulation (**d**)). The measurements for each activity were repeated 15 times on six participants. Solid black lines are the average results and grey regions denote ±1 s.d. The corresponding spectra are snapshots showing representative flow characteristics in each phase of the activity. The blood flow spectra share the same scale bars. **e**, The mean flow velocity in the MCA and the corresponding gyroscope data during a continuous 4-h recording. Rotation rates of rolling, yawing and pitching are denoted by blue, red and black lines, respectively. Transient signal loss periods due to extensive head motions and a spectrum during this period are labelled with light-grey dashed boxes. An example of minor head motion and a spectrum during this period are labelled with dark-grey dashed boxes. The participant felt drowsy at around 2 h into the recording. The figure labelled with an orange dashed box highlights the flow characteristics during this period. Intracranial B waves with a frequency of about three cycles in 1 min are labelled by a white dashed line. The blood flow spectra share the same scale bars. Scale bars, 5 s (**a**–**d**); 10 min (**e**).

closed their eyes and then opened their eyes to read. The left PCA mean flow velocity decreased to around 90% baseline with eyes closed and gradually increased until it peaked (around 110% baseline) with reading (Fig. 4d).

These transient cerebral haemodynamic changes are the result of the activities of the participants and can be impaired or inhibited if pathological conditions exist[37]. The recorded cerebral blood flow profiles during these activities follow similar trends as those measured by conventional TCD probes[33–36], indicating a potential clinical benefit for monitoring cerebral haemodynamics using the conformal patch.

Because it allows hands-free, wearable measurements, the conformal ultrasound patch is particularly useful for prolonged surveillance (Extended Data Fig. 5). For example, intracranial B waves during sleep are closely related to the glymphatic system activities, which is important for toxic waste by-product removal in the brain and disease recovery[38,39] (Supplementary Discussion 15). These events are accompanied by slow, spontaneous oscillations in the cerebral blood flow velocity (that is, B waves) at 0.3–4 cycles per minute[40]. With the conformal ultrasound patch at the temporal window, we monitored the cerebral blood flow spectra in the MCA in a participant for 4 h continuously (Fig. 4e).

The recording has a high signal-to-noise ratio, except for transient signal fluctuations during extensive head motions (Fig. 4e and Supplementary Fig. 56). Minor head motions, which the participant naturally made, does not significantly affect the signal quality (Fig. 4e). A cascade of B waves was identified when the participant felt drowsy (Fig. 4e). Prolonged surveillance is also valuable for cerebral emboli monitoring and therefore embolic stroke prevention. Evidence suggests that extending the recording time can capture more patients positive for an embolic signal[10]. The conformal ultrasound patch could detect flowing emboli in a phantom (Supplementary Fig. 57), demonstrating the promise of prolonged recording using the conformal patch in a clinical setting.

Discussion

TCD is a powerful ultrasound modality for neurovascular diagnostics and research, but the conventional form factor limits continuous measurements of cerebral arteries and can only image 1D or 2D planes of the complex 3D network. To develop a conformal ultrasound patch for continuous TCD application, we have designed a soft 2D matrix array for volumetric imaging and electronically locating target arterial segments from the complex 3D cerebral arterial network. The conformal ultrasound patch coupled with ultrafast signal acquisition enables volumetric imaging of the cerebral arterial network and simplifies the blood flow data acquisition process from target vessels. Using the reconstructed volumetric image, we can electronically focus the low-intensity ultrasound beam to acquire cerebral blood flow measurements from various segments of the 3D arterial network. The design notably minimizes operator dependency and enhance motion tolerance in comparison to conventional TCD probes (Supplementary Discussion 16). Moreover, a comprehensive survey of feedback from all participants indicated that a majority (69.4%) prefer the conformal ultrasound patch for its comfort (Supplementary Fig. 58). With these advantages, we demonstrate not only blood flow measurements from different segments of the major cerebral arteries and transcranial monitoring of cerebral haemodynamics under different scenarios (for example, carotid compression test, handgrip, Valsalva manoeuvre, word generation and visual stimulation) but also long-term monitoring during drowsiness with minimal signal loss. These results have notable implications for both clinical diagnostic tools for brain disorders and medical research on neurovascular functions (Supplementary Discussion 16).

The synergy between the conformal ultrasound patch and ultrafast volumetric reconstruction enables haemodynamics monitoring in complex 3D vascular networks. Therefore, apart from cerebral arteries, this technology can also be used to study the complex haemodynamics in other clinically important vessels, such as the carotid bifurcation. The structural morphology of these arteries induces turbulent blood flow, prone to atherosclerosis and emboli generation[41]. The conformal ultrasound patch can detect both gas and solid emboli (Supplementary Fig. 57), potentially enabling early detection for timely intervention before severe pathological progression in major arteries.

This study primarily focuses on the development of the front-end ultrasound patch, the related ultrafast imaging algorithms and the validation of their applications in transcranial volumetric imaging and cerebral blood flow monitoring. With future development, the performance of the device and functionality could be further enhanced.

First, the conformal ultrasound patch has limited spatial resolution. Signals from major cerebral arteries can be obtained, but the patch neglects information from arterioles, venules and capillaries. Obtaining signals from all vessels can provide a more holistic insight into the cerebrovascular system. Thus, to improve the spatial resolution, contrast agents such as microbubbles[42] may be needed to generate much higher amplitude echoes compared with the surrounding tissues (Supplementary Discussion 17). Ultrafast ultrasound localization microscopy can potentially be adopted to overcome the diffraction limit, enabling super-resolution transcranial imaging and full reconstruction of deep vascular systems down to the level of capillaries[43,44]. Furthermore, by using harmonic imaging, the incident ultrasound waves can drive the microbubbles to vibrate nonlinearly, generating strong harmonic components in echoes[45] (Supplementary Discussion 18). Moreover, time reversal can be used to calculate precise time delays on each element of the transducer array and thus partially compensate for the phase aberration of the skull[46].

Second, the volumetric image reconstruction was post-processed subsequently after data acquisition. This post-processing time may hinder the workflow of the clinicians when needing to dynamically target different segments of the cerebral arterial network in real time. Improvement in volumetric reconstruction speed can be realized by a multi-threaded process with much higher computational power for image reconstruction. The calculation and image rendering processes could be highly parallelized and optimized for real-time imaging[47], which may be valuable for understanding the real-time functional connectivity of the brain.

Third, the conformal ultrasound patch was connected to the Verasonics system for all data acquisition processes. Volumetric imaging requires a relatively high-power supply to successfully transmit and receive ultrasound waves through the transcranial windows into the deep brain. Moreover, the ultrafast data acquisition process and long-term measurements of blood flow velocity can generate a large dataset (for example, 1–5 GB), which requires a powerful system for fast data transfer and processing. Back-end systems based on customized printed circuit boards or application-specific integrated circuits can significantly miniaturize the control system with reduced power consumption to provide higher freedom of movement for long-term wearability[16] (Supplementary Discussion 19).

Fourth, transient signal fluctuations were observed in the long-term recording due to ultrasound beam misalignment to the target during extensive head motions. Machine-learning algorithms can be used to identify signal loss, automatically track the targeted arterial segment, eliminate occasions of signal loss and improve reliability in clinical utility during continuous measurements.

Finally, all participants in this study were healthy without severe neurological pathologies related to cerebral haemodynamics. Further testing across large populations, including particularly those patients with neurovascular conditions, such as vasospasm, stenoses, aneurysms and embolism, can potentially enable diagnostic parameters for the early detection of major neurological pathologies.

Online content

Any methods, additional references, Nature Portfolio reporting summaries, source data, extended data, supplementary information, acknowledgements, peer review information; details of author contributions and competing interests; and statements of data and code availability are available at https://doi.org/10.1038/s41586-024-07381-5.

1. Aaslid, R. (ed.) *Transcranial Doppler Sonography* (Springer Science+Business Media, 2012).
2. Alexandrov, A. V. et al. Practice standards for transcranial Doppler (TCD) ultrasound. Part II. Clinical indications and expected outcomes. *J. Neuroimaging* **22**, 215–224 (2012).
3. Lohmann, H., Ringelstein, E. B. & Knecht, S. in *Handbook on Neurovascular Ultrasound* Vol. 21 (ed. Baumgartner, R. W.) 251–260 (Karger, 2006).
4. Gambhir, S. S. Molecular imaging of cancer with positron emission tomography. *Nat. Rev. Cancer* **2**, 683–693 (2002).
5. Withers, P. J. et al. X-ray computed tomography. *Nat. Rev. Methods Primers* **1**, 18 (2021).
6. Weiskopf, N., Edwards, L. J., Helms, G., Mohammadi, S. & Kirilina, E. Quantitative magnetic resonance imaging of brain anatomy and in vivo histology. *Nat. Rev. Phys.* **3**, 570–588 (2021).
7. Seubert, C. N., Cibula, J. E. & Mahla, M. E. in *Textbook of Neurointensive Care* (eds Layon, A. J. et al.) 109–126 (Springer, 2013).
8. Tidswell, T., Gibson, A., Bayford, R. H. & Holder, D. S. Three-dimensional electrical impedance tomography of human brain activity. *NeuroImage* **13**, 283–294 (2001).
9. Fantini, S., Sassaroli, A., Tgavalekos, K. T. & Kornbluth, J. Cerebral blood flow and autoregulation: current measurement techniques and prospects for noninvasive optical methods. *Neurophotonics* **3**, 031411 (2016).

10. Mackinnon, A. D., Aaslid, R. & Markus, H. S. Long-term ambulatory monitoring for cerebral emboli using transcranial Doppler ultrasound. *Stroke* **35**, 73–78 (2004).
11. Ivancevich, N. M. et al. Real-time 3-D contrast-enhanced transcranial ultrasound and aberration correction. *Ultrasound Med. Biol.* **34**, 1387–1395 (2008).
12. Pietrangelo, S. J., Lee, H.-S. & Sodini, C. G. A wearable transcranial Doppler ultrasound phased array system. In *Proc. Intracranial Pressure & Neuromonitoring XVI* Vol. 126 (Heldt, T.) 111–114 (Springer, 2018).
13. Lin, M., Hu, H., Zhou, S. & Xu, S. Soft wearable devices for deep-tissue sensing. *Nat. Rev. Mater.* **7**, 850–869 (2022).
14. Wang, C. et al. Bioadhesive ultrasound for long-term continuous imaging of diverse organs. *Science* **377**, 517–523 (2022).
15. Hu, H. et al. Stretchable ultrasonic arrays for the three-dimensional mapping of the modulus of deep tissue. *Nat. Biomed. Eng.* **7**, 1321–1334 (2023).
16. Lin, M. et al. A fully integrated wearable ultrasound system to monitor deep tissues in moving subjects. *Nat. Biotechnol.* **42**, 448–457 (2023).
17. Zhang, L. et al. A conformable phased-array ultrasound patch for bladder volume monitoring. *Nat. Electron.* **7**, 77–90 (2024).
18. Wang, C. et al. Monitoring of the central blood pressure waveform via a conformal ultrasonic device. *Nat. Biomed. Eng.* **2**, 687–695 (2018).
19. Hu, H. et al. A wearable cardiac ultrasound imager. *Nature* **613**, 667–675 (2023).
20. Gao, X. et al. A photoacoustic patch for three-dimensional imaging of hemoglobin and core temperature. *Nat. Commun.* **13**, 7757 (2022).
21. Kyriakou, A. et al. A review of numerical and experimental compensation techniques for skull-induced phase aberrations in transcranial focused ultrasound. *Int. J. Hyperthermia.* **30**, 36–46 (2014).
22. Montaldo, G. et al. Ultrafast compound Doppler imaging: a new approach of Doppler flow analysis. In *Proc. 2010 IEEE International Symposium on Biomedical Imaging: From Nano to Macro* 324–327 (IEEE, 2010).
23. Bercoff, J. et al. Ultrafast compound Doppler imaging: providing full blood flow characterization. *IEEE Trans. Ultrason. Ferroelectr. Freq. Control* **58**, 134–147 (2011).
24. Alexandrov, A. V. et al. Practice standards for transcranial Doppler ultrasound: part I—test performance. *J. Neuroimaging* **17**, 11–18 (2007).
25. Smith, S. W. et al. The ultrasound brain helmet: feasibility study of multiple simultaneous 3D scans of cerebral vasculature. *Ultrasound Med. Biol.* **35**, 329–338 (2009).
26. Lindsey, B. D. et al. The ultrasound brain helmet: new transducers and volume registration for in vivo simultaneous multi-transducer 3-D transcranial imaging. *IEEE Trans. Ultrason. Ferroelectr. Freq. Control* **58**, 1189–1202 (2011).
27. Food and Drug Administration. *Marketing Clearance of Diagnostic Ultrasound Systems and Transducers: Guidance for Industry and Food and Drug Administration Staff.* Report No. FDA-2017-D-5372 (Food and Drug Administration, 2023).
28. Demené, C. et al. Spatiotemporal clutter filtering of ultrafast ultrasound data highly increases Doppler and fultrasound sensitivity. *IEEE Trans. Med. Imaging* **34**, 2271–2285 (2015).
29. Jerman, T., Pernus, F., Likar, B. & Spiclin, Z. Enhancement of vascular structures in 3D and 2D angiographic images. *IEEE Trans. Med. Imaging* **35**, 2107–2118 (2016).
30. Huang, C. et al. Debiasing-based noise suppression for ultrafast ultrasound microvessel imaging. *IEEE Trans. Ultrason. Ferroelectr. Freq. Control* **66**, 1281–1291 (2019).
31. Fan, L., Zhang, F., Fan, H. & Zhang, C. Brief review of image denoising techniques. *Vis. Comput. Ind. Biomed. Art* **2**, 7 (2019).
32. Jones, J. D., Castanho, P., Bazira, P. & Sanders, K. Anatomical variations of the circle of Willis and their prevalence, with a focus on the posterior communicating artery: a literature review and meta-analysis. *Clin. Anat.* **34**, 978–990 (2021).
33. Nogueira, R. C. et al. Dynamic cerebral autoregulation changes during sub-maximal handgrip maneuver. *PLoS One* **8**, e70821 (2013).
34. Tiecks, F. P. et al. Effects of the Valsalva maneuver on cerebral circulation in healthy adults: a transcranial Doppler study. *Stroke* **26**, 1386–1392 (1995).
35. Knecht, S., Henningsen, H., Deppe, M. & Huber, T. Successive activation of both cerebral hemispheres during cued word generation. *Neuroreport* **7**, 820–824 (1996).
36. Olah, L. et al. Visually evoked cerebral vasomotor response in smoking and nonsmoking young adults, investigated by functional transcranial Doppler. *Nicotine Tob. Res.* **10**, 353–358 (2008).
37. Silverman, A. & Petersen, N. *Physiology, Cerebral Autoregulation* (StatPearls, 2022).
38. Fultz, N. E. et al. Coupled electrophysiological, hemodynamic, and cerebrospinal fluid oscillations in human sleep. *Science* **366**, 628–631 (2019).
39. Newell, D. W., Nedergaard, M. & Aaslid, R. Physiological mechanisms and significance of intracranial B waves. *Front. Neurol.* **13**, 872701 (2022).
40. Newell, D. W., Aaslid, R., Stooss, R. & Reulen, H. J. The relationship of blood flow velocity fluctuations to intracranial pressure B waves. *J. Neurosurg.* **76**, 415–421 (1992).
41. Gildenberg, P. L., O'Brien, R. P., Britt, W. J. & Frost, E. A. The efficacy of Doppler monitoring for the detection of venous air embolism. *J. Neurosurg.* **54**, 75–78 (1981).
42. Chong, W. K., Papadopoulou, V. & Dayton, P. A. Imaging with ultrasound contrast agents: current status and future. *Abdom. Radiol.* **43**, 762–772 (2018).
43. Demene, C. et al. Transcranial ultrafast ultrasound localization microscopy of brain vasculature in patients. *Nat. Biomed. Eng.* **5**, 219–228 (2021).
44. Renaudin, N. et al. Functional ultrasound localization microscopy reveals brain-wide neurovascular activity on a microscopic scale. *Nat. Methods* **19**, 1004–1012 (2022).
45. Anvari, A., Forsberg, F. & Samir, A. E. A primer on the physical principles of tissue harmonic imaging. *Radiographics* **35**, 1955–1964 (2015).
46. Fink, M. Time reversal of ultrasonic fields. I. Basic principles. *IEEE Trans. Ultrason. Ferroelectr. Freq. Control* **39**, 555–566 (1992).
47. Rabut, C. et al. 4D functional ultrasound imaging of whole-brain activity in rodents. *Nat. Methods* **16**, 994–997 (2019).
48. Human Anatomy Atlas 2024 v.2024.00.005 (Visible Body, 2024).
49. Makowicz, G., Poniatowska, R. & Lusawa, M. Variants of cerebral arteries - anterior circulation. *Pol. J. Radiol.* **78**, 42–47 (2013).

Methods

Device fabrication

Electrode design and patterning. The electrode is composed of a common ground electrode, a five-layer stretchable electrode and a copper mesh electromagnetic shielding layer. First, polyimide (poly(pyromellitic dianhydride-*co*-4,4′-oxydianiline) amic acid solution, PI2545 precursor, HD MicroSystems) was spin-coated on copper sheets (Oak-Mitsui) at 4,000 rpm for 60 s, followed by soft baking on a hotplate at 100 °C for 3 min and subsequently at 150 °C for 1 min, and then hard baking in a nitrogen oven at 300 °C for 1 h, yielding a 2-μm thick polyimide layer coated on 20 μm thick copper sheets.

Polydimethylsiloxane (Sylgard 184 silicone elastomer) was then spin-coated at 3,000 rpm for 60 s on a glass slide and cured in an 80 °C oven as a temporary substrate for electrode transfer. To improve bonding, the polyimide-coated copper sheets and the polydimethylsiloxane-coated glass slides were activated by ultraviolet light (PSD series Digital UV Ozone System, Novascan) for 3 min.

The polyimide-coated side of the copper sheet was then attached to the polydimethylsiloxane-coated glass slide. The bilayer copper/polyimide film was laser ablated (Laser Mark's, central wavelength, 1,059–1,065 nm; power, 0.228 mJ; frequency, 35 kHz; speed, 300 mm s^{-1}; and pulse width, 500 ns) following electrode patterns designed with AutoCAD (Autodesk) (Supplementary Fig. 7).

Electronic packaging. On two separate glass slides, polymethyl methacrylate (495PMMA, Kayaku Advanced Materials), serving as a sacrificial layer, was spin-coated at 2,000 rpm for 60 s and cured at 80 °C for 30 min. Then, a 12-μm thick silicone (Ecoflex-0030, Smooth-On) was spin-coated at 4,000 rpm for 60 s and cured at room temperature for 2 h.

To assemble the device, a water-soluble tape (5414 Transparent, 3 M) was used for transfer printing the ground electrode to an Ecoflex-coated glass slide and the copper mesh electromagnetic shielding layer to another Ecoflex-coated glass slide. The water-soluble tape was then removed by immersing it in 80 °C water for 30 min. Conductive epoxy (Von Roll 3022 E-Solder, EIS) was placed on the 256 bonding pads of the island-bridge layout of the common ground electrode. After that, the matrix array of 1–3 composites (Del Piezo Specialties) was bonded to the bonding pads by curing a conductive epoxy for 8 h at room temperature and then 2 h at 40 °C to avoid high-temperature-induced depolarization of the 1–3 composites.

On the glass slide with the copper mesh electromagnetic shielding layer, sequential transfer printing of the five-layer stretchable electrode was done, and it was stacked one on top of another by water-soluble tape. Each layer was bonded to a flat flexible cable (Premo-Flex FPC Jumper, Molex) using solder paste ($Sn_{42}Bi_{57.6}Ag_{0.4}$ (melting point, 138 °C)) and spin-coated with a 25-μm thick Ecoflex layer at 2,200 rpm for 60 s and cured at room temperature for 2 h. Laser ablation was used to create vertical interconnect accesses through the Ecoflex layers to expose the 256 bonding pads in the five-layer stretchable electrode[50]. Then, this glass slide was bonded to the 1–3 composite on the other glass slide using conductive epoxy followed by curing.

Finally, the gaps between the two glass slides were filled with Ecoflex followed by curing at room temperature. The glass slides were removed by dissolving the polymethyl methacrylate in acetone to release the conformal ultrasound patch.

Acoustic field simulation

We simulated the diverging and focused ultrasound beams using an open-source Matlab toolbox Field II. The medium was set as uniform with a sound speed of 1,540 m s^{-1} and a density of 1,000 kg m^{-3}. The centre frequency was set to 2 MHz, the same as that of the real probe. We applied the built-in function, 'xdc_2d_array', to create the transducer array. The transmission time delay of each transducer element could be individually set to emit a diverging beam or a focused beam.

Device performance characterizations

A network analyser (Hewlett-Packard 4195 A) was used to measure the electrical impedance and phase angle of each transducer in the device (Supplementary Fig. 8). Based on the electrical impedance graph, the resonant frequency (f_r), the frequency with the lowest electrical impedance, and anti-resonant frequency (f_a), the frequency with the highest electrical impedance, of the transducers were mapped (Supplementary Fig. 8). The effective electromechanical coupling coefficient (k_{eff}) was calculated by

$$k_{eff} = \sqrt{1 - \frac{f_r^2}{f_a^2}} \quad (1)$$

The pulse-echo response and bandwidth of the device were characterized (Supplementary Fig. 8). An aluminium block was placed 8 cm away from the device in a water tank. The back-end system (Vantage 256, Verasonics) was used to obtain raw radiofrequency signals by transmitting and receiving ultrasound pulse waves. Fast Fourier transform in Matlab R2021a was used to transfer the signals into the frequency domain.

Crosstalk between adjacent transducer elements was characterized by changing the transmitting frequencies and activation voltages (Supplementary Fig. 8). A sinusoidal peak-to-peak voltage of 15 V was applied by a functional generator (3390, Keithley) to excite one of the elements with different frequencies from 1 MHz to 3 MHz. Moreover, we used a 2-MHz transmission with activation voltages from 5 V to 25 V. The reference voltages received by adjacent elements were measured. Then, the crosstalk was calculated by

$$\text{Crosstalk} = 20 \log\left(\frac{\text{Reference voltage of the adjacent element}}{\text{Activation voltage of the excited element}}\right) \quad (2)$$

The signal-to-noise ratio with and without the copper mesh electromagnetic shielding layer was tested with a 1-mm thick thread underwater (Supplementary Fig. 8).

Safety-measurement procedures

To evaluate the safety of the device, the acoustic exposure was evaluated using a 3D ultrasound mapping system (AIMS III hydrophone scanning system, ONDA) following the provided calibration procedures. We used a calibrated hydrophone (Model HNP-0400, ONDA) to scan the ultrasound field in 3D in a water tank (Extended Data Fig. 2). The hydrophone was connected to an oscilloscope (PicoScope 5244A, ONDA), and software (Soniq v.5.3.1.0, ONDA) was used to control the scanning. We scanned a zone of 60 × 60 × 100 mm^3 below the device with a spatial resolution of 0.1 mm with and without a formalin-fixed temporal bone specimen (about 5 mm in thickness, desiccated, with skin, fascia and marrow removed, provided by the Medical Education and Anatomical Services at the University of California San Diego). The acoustic intensity was controlled by changing the activation voltage. We calculated safety indices (spatial peak pulse average intensity, spatial peak temporal average intensity, mechanical index and thermal indices) and compared them with the maximum levels recommended by the Food and Drug Administration[27].

Volumetric ultrafast power Doppler imaging

The protocol consisted of two steps: ultrafast signal acquisition and post-processing. For signal acquisition, we used different time-delay profiles to transmit the diverging waves from five virtual sources that were 22.30 mm behind the device to obtain a view angle of 40° (Fig. 2a). We used three cycles of tone burst centred at 2 MHz with a

pulse repetition frequency of 3,000 Hz to activate the transducers. A group of five diverging waves was transmitted and received repeatedly 600 times within 1 s (Fig. 2a). The digitization rate of the received analog signals was 7.8125 MHz.

For post-processing, volumetric beamforming was performed on the raw radiofrequency data from each transducer 3,000 times. The beamformed data with different diverging waves were coherently compounded to form 600 frames of images. We implemented spatiotemporal clutter filtering (for example, singular value decomposition in this work) to separate blood flow (incoherent motion within the volume) from tissue motion (coherent motion within the volume) (Supplementary Discussion 9). After filtering, the energy of the temporal signal was integrated over the whole imaging block to calculate the power Doppler intensity in 3D (Fig. 2a). The computational load is inversely proportional to the size of each reconstructing voxel in the target region. We used a $0.77 \times 0.77 \times 0.77$ mm^3 voxel, which corresponds to one wavelength of the ultrasound at 2 MHz in soft tissues, to maintain adequate spatial resolution and reasonable computational load.

To characterize the performance of this protocol, we conducted a test by using a Doppler flow phantom (ATS 523A, CIRS). We pumped Doppler fluid (769DF, CIRS) through the phantom with an internal diameter of 4 mm, positioned at an approximate depth of 60–80 mm. The volumetric flow imaging result (Supplementary Fig. 59) shows the flow profile of the phantom and is highly consistent with the ground truth collected by a conventional TCD probe (P4_2v, Verasonics).

Volumetric imaging by diverging waves is data and computation intensive. The raw radiofrequency data obtained within 1 s were approximately 800 MB. On beamforming and coherent compounding, the in-phase and quadrature data were inflated to approximately 4 GB. Subsequent processing steps, including singular value decomposition filtering, effectively reduced the final volumetric result to a more manageable size of around 5 MB. The data processing was executed within 10 min using a MacBook Pro equipped with an M1 Max chip, a 32-core graphical processing unit, and 64 GB of unified memory.

Automatic tracking of blood flow envelope

We first applied histogram equalization to enhance the contrast between the blood flow spectra and background noise, which improved the accuracy of envelope tracking (Extended Data Fig. 4). After that, we defined a step function to fit the spectra at each moment, which had a value of 1 in the frequency band lower than f_{step} (the envelope to be extracted), and 0 in the frequency band higher than f_{step} (Extended Data Fig. 4). The sum of the absolute differences at all frequencies between the spectra and the step function was defined as the error to quantify the fitting. We swept the frequency f_{step} from the lower (0 Hz) to the higher frequency (2,850 Hz) boundaries of the spectra and obtained the corresponding error values (Extended Data Fig. 4). The f_{step} value corresponding to the smallest error was the extracted envelope at this moment (Extended Data Fig. 4).

Study design for device validation

This study compared the cerebral blood flow measurements from the conformal ultrasound patch and a conventional TCD probe (P4_2v, Verasonics) to validate the agreement and correlation of their measurements at multiple arterial segments (that is, ACA, MCA M2, MCA M1, PCA, ophthalmic arteries, ICA, ICA siphon, TICA, basal artery and vertebral arteries). All studies on human participants in this work were approved by the Institutional Review Board at the University of California, San Diego (IRB #805201). The study was registered on ClinicalTrials.gov (NCT06073145). The inclusion criteria specified that the participants must be older than 18 years and in generally good health, without any severe medical conditions. The eligibility for the study was determined through a conversational screening process. Thirty-six participants in a random series were recruited and informed of the potential risks and experimental procedures. Written consent forms were obtained before the test. The results had a statistical power of 83.07% to detect a difference of 5 cm s^{-1} on blood flow velocities, assuming a s.d. of 10 cm s^{-1} using a paired t-test with a 0.05 two-sided significance level. This statistical power is larger than the general statistical power requirement (that is, 80%) for clinical trials[51,52].

S. Zhou conducted all measurements throughout the study. We have taken several steps to ensure the accuracy and reliability of the measurements. First, S. Zhou completed online courses from The Institute for Advanced Medical Education about TCD (https://www.iame.com/online-courses/vascular/transcranial-doppler-TCD-CME) before conducting the tests. Second, this student received several hands-on training sessions from A. Lam, a clinically qualified ultrasonographer with more than 30 years of experience in TCD, before performing the measurements. Third, the student strictly adhered to the guidance[24,53] to ensure the accuracy of the measurements during the testing process. Finally, D.W. Newell, another clinically qualified TCD ultrasonographer, provided guidance and supervision during the testing process and reviewed the results after the measurements, further ensuring the accuracy and reliability of the reference measurements. To illustrate the validity of the measurements made by S. Zhou, we compared the blood flow spectra obtained from A. Lam and S. Zhou by using a conventional TCD probe (Supplementary Fig. 60).

All procedures were conducted in accordance with the TCD examination guidelines[24,53]. The participants were instructed to sit comfortably in a chair. The soft ultrasound patch and conventional rigid TCD probe were performed randomly in sequence for each participant. The ultrasound patch or a conventional TCD probe was placed on the temporal, orbital, submandibular and suboccipital windows to monitor different arterial segments. The temporal window can be further divided into anterior, middle and posterior windows[1] (Supplementary Fig. 13). The temporal window that provided the best cerebral signal in the TCD examination was selected for each participant.

The procedure for adhering the patch to the skin was as follows. First, we applied a layer of ultrasound gel to the surface of the target area. Next, we positioned the patch on the designated testing spot, ensuring the even distribution of the gel without any overflow onto the device surface. Finally, we secured the patch on the testing spot using Tegaderm (1626W, 3 M). This method ensured a stable adhesion between the patch and the skin, allowing for robust data acquisition. Diverging waves were used to reconstruct the volumetric power Doppler image, which facilitated the identification of various cerebral arteries. We then used focused waves to continuously monitor the blood flow spectra at target arterial segments.

We used a fast 3 s sweep speed that allowed a detailed examination of the spectra. A higher pulse repetition frequency led to higher measurement limits of Doppler shift (that is, a wider range of blood flow velocities) and also increased the ultrasound energy exposure. To balance the measurement limits and safety concerns, we chose a pulse repetition frequency of 2,500–4,000 Hz. The zero Doppler shift line (that is, baseline) was placed near the top or bottom of the screen to avoid aliasing (Supplementary Fig. 61). In the case of weak velocity signals, we increased the gain with a slow sweeping speed to visualize the Doppler shifts in the spectra. We lowered the power output of the devices, with a derated spatial peak temporal average intensity of $I_{SPTA.3} < 17$ mW cm^{-2} (Food and Drug Administration Track 1 maximum recommended value for ophthalmic scans) to insonate through the orbital window to reduce ultrasound exposure of the eye[27].

Adhering to the ALARA (as low as reasonably achievable) principle[27] for general ultrasound diagnosis, we reduced the mechanical index and thermal index to limit the ultrasound exposure level during monitoring (Extended Data Fig. 6).

After identifying and optimizing the spectra of each arterial segment, we continued the recordings for 30 s. The time interval for switching between the patch and the TCD probe was approximately

5 min. In our study design, we anticipated generating 360 comparative sets of blood flow spectral measurements from 36 participants. However, owing to anatomical variations, some arterial segments were inaccessible, resulting in the acquisition of 254 comparative datasets. For each dataset, we conducted three repeated measurements, yielding a total of 762 individual data points for analysis. We calculated the average of peak systolic velocity, mean flow velocity, end diastolic velocity, pulsatility index and resistive index based on the recorded spectra for those 254 arterial segments. The measurements were concluded once 30 s spectral data of all arterial segments were recorded by both modalities three times. Data agreement was evaluated by Bland–Altman analysis (Fig. 3d–f and Supplementary Fig. 52). Data correlation was evaluated by scatter plots (Supplementary Figs. 52 and 53). No adverse events were reported throughout the duration of the examination.

Protocol for monitoring cerebral haemodynamics

To establish the baseline, the participants sat comfortably in a chair. The conformal ultrasound patch was attached to the temporal window. Flow spectra were monitored with focused beams on target arterial segments.

Hand grip. The protocol consisted of 40 s of resting, followed by 3 min of handgrip and subsequently 80 s of recovery (Supplementary Fig. 55). During the handgrip, the participants held a handgrip exerciser and exerted 30% of their maximum contraction force continuously. Switching of the test phases was signalled with cue tones.

Valsalva manoeuvre. The protocol started with a 20-s baseline recording. Following this, the participants inhaled deeply for 5 s (phase I), held their breath for 15 s (phases IIa and IIb), exhaled fully for 2.5 s (phase III) and finally breathed normally (phase IV) (Supplementary Fig. 55).

Word generation. After 15 s of baseline recording, the participants were first signalled by a cue tone for 3 s, given a letter visually for 2.5 s after a 2-s rest, and then asked to silently generate as many words as possible starting with this letter within 15 s and to orally report the words within 2.5 s (Supplementary Fig. 55).

Visual stimulation. A news magazine with emotionally neutral text was used. The protocol consisted of 20 s of baseline recording, 20 s of eye closing and 40 s of eye opening and reading silently (Supplementary Fig. 55). Changes between phases were signalled with cue tones.

To minimize the interference of confounding factors, each activity was performed 15 times on six participants. The interval between each test was more than 10 min or until the recorded values had returned to the baseline. The mean flow velocity was obtained from the recorded spectra and was expressed as mean ± s.d.

Long-term monitoring. The participant was instructed to lie supine on a bed and remain as still as possible throughout the monitoring session. This positioning ensured that the patch was not in direct contact with the pillow and that the head was not pressing on the patch. The ultrasound patch was securely affixed to the participant's temporal window by Tegaderm (1626W, 3 M) for volumetric imaging. The MCA position was then located and targeted by a focused ultrasound beam. We placed a wearable gyroscope in close proximity to the ultrasound patch. This enabled us to correlate head movements with any changes in signal quality. The recording was conducted without interruption for 4 h until the device was powered off.

Data availability

The data in this study are available at Figshare (https://doi.org/10.6084/m9.figshare.25448254.v1)[54].

Code availability

The code used in this study is available at GitHub (https://github.com/Yup0626/TCD).

50. Huang, Z. et al. Three-dimensional integrated stretchable electronics. *Nat. Electron.* **1**, 473–480 (2018).
51. Julious, S. A. Sample sizes for clinical trials with normal data. *Stat. Med.* **23**, 1921–1986 (2004).
52. Julious, S. A. *Sample Sizes for Clinical Trials* (CRC Press, 2023).
53. American Institute of Ultrasound in Medicine. The AIUM practice parameter for the performance of the musculoskeletal ultrasound examination. *J. Ultrasound Med.* E23–E35 (2023).
54. Zhou, S. Shared data for "Transcranial volumetric imaging using a conformal ultrasound patch". figshare https://doi.org/10.6084/m9.figshare.25448254.v1 (2024).
55. Moehring, M. A. & Spencer, M. P. Power M-mode Doppler (PMD) for observing cerebral blood flow and tracking emboli. *Ultrasound Med. Biol.* **28**, 49–57 (2002).
56. Muehllehner, G. & Karp, J. S. Positron emission tomography. *Phys. Med. Biol.* **51**, R117 (2006).
57. Høedt-Rasmussen, K., Sveinsdottir, E. & Lassen, N. A. Regional Cerebral low in Man Determined by Intra-arterial Injection of Radioactive Inert Gas. *Circ. Res.* **18**, 237–247 (1966).
58. Yandrapalli, S. & Puckett, Y. *SPECT Imaging*. (StatPearls Publishing, 2020).
59. Pindzola, R. R. & Yonas, H. The xenon-enhanced computed tomography cerebral blood flow method. *Neurosurgery* **43**, 1488–1491 (1998).
60. Hoeffner, E. G. et al. Cerebral perfusion CT: technique and clinical applications. *Radiology* **231**, 632–644 (2004).
61. Shaban, S. et al. Digital subtraction angiography in cerebrovascular disease: current practice and perspectives on diagnosis, acute treatment and prognosis. *Acta Neurol. Belg.* **122**, 763–780 (2022).
62. Boxerman, J. L. et al. Consensus recommendations for a dynamic susceptibility contrast MRI protocol for use in high-grade gliomas. *Neuro-oncology* **22**, 1262–1275 (2020).
63. Petcharunpaisan, S., Ramalho, J. & Castillo, M. Arterial spin labeling in neuroimaging. *World J. Radiol* **2**, 384–398 (2010).
64. Kety, S. S. & Schmidt, C. F. The determination of cerebral blood flow in man by the use of nitrous oxide in low concentrations. *Am. J. Physiol.* **143**, 53–66 (1945).
65. Wilson, E. M. & Halsey, J. H. Jr Bilateral jugular venous blood flow by thermal dilution. *Stroke* **1**, 348–355 (1970).
66. Carter, L. P. Thermal diffusion flowmetry. *Neurosurg. Clin. N. Am.* **7**, 749–754 (1996).
67. Bagshaw, A. P. et al. Electrical impedance tomography of human brain function using reconstruction algorithms based on the finite element method. *NeuroImage* **20**, 752–764 (2003).
68. Le Roux, P. in *Textbook of Neurointensive Care*, 127–145 (Springer, 2013).
69. Samaei, S. et al. Time-domain diffuse correlation spectroscopy (TD-DCS) for noninvasive, depth-dependent blood flow quantification in human tissue in vivo. *Sci. Rep.* **11**, 1–10 (2021).
70. Moerman, A. & Wouters, P. Near-infrared spectroscopy (NIRS) monitoring in contemporary anesthesia and critical care. *Acta Anaesthesiol. Belg.* **61**, 185–194 (2010).
71. Sanderson, M. & Yeung, H. Guidelines for the use of ultrasonic non-invasive metering techniques. *Flow Meas* **13**, 125–142 (2002).
72. Willie, C. K. et al. Utility of transcranial Doppler ultrasound for the integrative assessment of cerebrovascular function. *J. Neurosci. Methods* **196**, 221–237 (2011).
73. Bakker, S. L. et al. Cerebral haemodynamics in the elderly: the rotterdam study. *Neuroepidemiology* **23**, 178–184 (2004).
74. Brunser, A. M. et al. Transcranial Doppler in a Hispanic-Mestizo population with neurological diseases: a study of sonographic window and its determinants. *Brain Behav* **2**, 231–236 (2012).
75. Wong, K. S. et al. Use of transcranial Doppler ultrasound to predict outcome in patients with intracranial large-artery occlusive disease. *Stroke* **31**, 2641–2647 (2000).
76. Marinoni, M., Ginanneschi, A., Forleo, P. & Amaducci, L. Technical limits in transcranial Doppler recording: Inadequate acoustic windows. *Ultrasound Med. Biol.* **23**, 1275–1277 (1997).
77. Itoh, T. et al. Rate of successful recording of blood flow signals in the middle cerebral artery using transcranial Doppler sonography. *Stroke* **24**, 1192–1195 (1993).
78. Chan, M. Y. et al. Success Rate of Transcranial Doppler Scanning of Cerebral Arteries at Different Transtemporal Windows in Healthy Elderly Individuals. *Ultrasound Med. Biol.* **49**, 588–598 (2023).
79. Lee, C. H., Jeon, S. H., Wang, S. J., Shin, B. S. & Kang, H. G. Factors associated with temporal window failure in transcranial Doppler sonography. *Neurol. Sci.* **41**, 3293–3299 (2020).
80. Lin, Y.-P., Fu, M.-H. & Tan, T.-Y. Factors Associated with No or Insufficient Temporal Bone Window Using Transcranial Color-coded Sonography. *J. Med. Ultrasound* **23**, 129–132 (2015).
81. Bazan, R. et al. Evaluation of the Temporal Acoustic Window for Transcranial Doppler in a Multi-Ethnic Population in Brazil. *Ultrasound Med. Biol.* **41**, 2131–2134 (2015).
82. Yagita, Y. et al. Effect of transcranial Doppler intensity on successful recording in Japanese patients. *Ultrasound Med. Biol.* **22**, 701–705 (1996).
83. Wijnhoud, A. D., Franckena, M., van der Lugt, A., Koudstaal, P. J. & Dippel, E. D. Inadequate acoustical temporal bone window in patients with a transient ischemic attack or minor stroke: role of skull thickness and bone density. *Ultrasound Med. Biol.* **34**, 923–929 (2008).
84. Nader, J. A., Andrade, M. L., Espinosa, V., Zambrano, M. & Del Brutto, O. H. Technical difficulties due to poor acoustic insonation during transcranial Doppler recordings in Amerindians and individuals of European origin. A comparative study. *Eur. Neurol.* **73**, 230–232 (2015).

85. Kwon, J. H., Kim, J. S., Kang, D. W., Bae, K. S. & Kwon, S. U. The thickness and texture of temporal bone in brain CT predict acoustic window failure of transcranial Doppler. *J. Neuroimaging* **16**, 347–352 (2006).
86. Krejza, J. et al. Suitability of temporal bone acoustic window: conventional TCD versus transcranial color-coded duplex sonography. *J. Neuroimaging* **17**, 311–314 (2007).

Acknowledgements We thank R. Aaslid for the discussions on the experiments, S. Olson and P. Corey for the guidance on the clinical applications of the device and S. Xiang for the feedback on the Article preparation. This work was supported by the National Institutes of Health (1R21EB025521-01, 1R21EB027303-01A1, 3R21EB027303-02S1, 1R01EB033464-01 and 1R01HL171652-01). The content is solely the responsibility of the authors and does not necessarily represent the official views of the National Institutes of Health. All bio-experiments were conducted in accordance with the ethical guidelines of the National Institutes of Health and with the approval of the Institutional Review Board of the University of California San Diego. The mention of commercial products, their sources or their use in connection with material reported herein is not to be construed as either an actual or implied endorsement of these products by the Department of Health and Human Services.

Author contributions S.Z. and S.X. conceived the project. S.Z., X.G., G.P., X.Y. and B.Q. performed the experiments. S.Z. and X.G. performed the data processing and simulations. S.Z. and G.P. analysed the data. S.Z., G.P., X.G. and S.X. wrote the paper. All authors provided constructive and valuable feedback on the Article.

Competing interests The authors declare no competing interests.

Additional information

Supplementary information The online version contains supplementary material available at https://doi.org/10.1038/s41586-024-07381-5.

Correspondence and requests for materials should be addressed to Sheng Xu.

Peer review information Nature thanks Roger Zemp and the other, anonymous, reviewer(s) for their contribution to the peer review of this work.

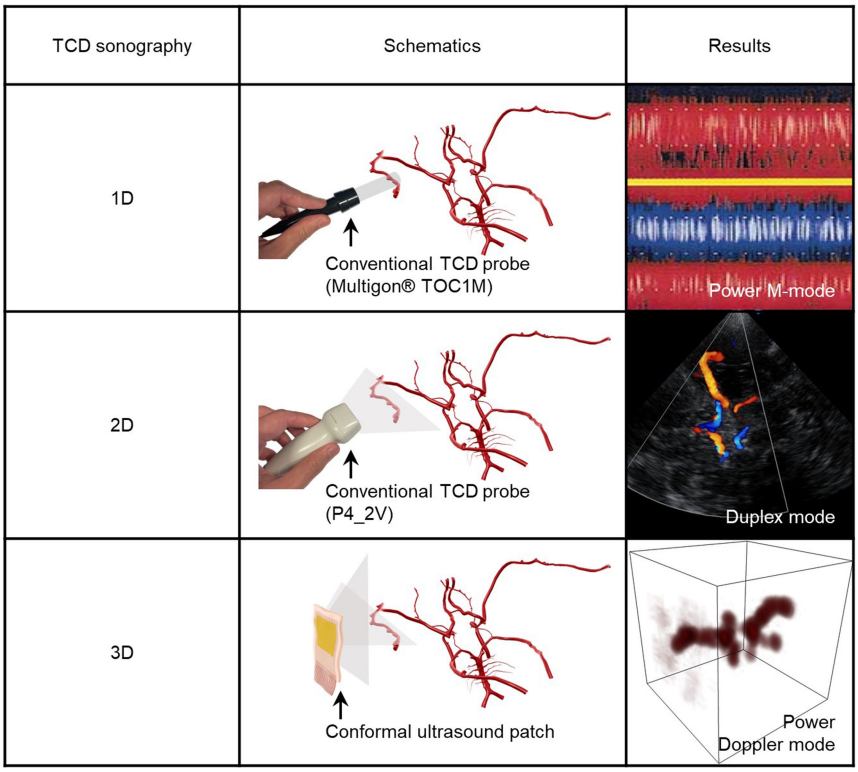

Extended Data Fig. 1 | 1D, 2D, and 3D TCD sonography. TCD sonography can be performed in different modes. The conventional TCD probe with a single transducer insonates target arteries in 1D, and the power M-mode results show collected blood flow signals[55]. The conventional phased array probe with a linear transducer array insonates target arteries in two dimensions. The acquired duplex mode (that is, combined B-mode and color Doppler mode) results show the collected tissue signals and blood flow directions in the plane (https://www.medison.ru/ultrasound/gal641.htm). The conformal ultrasound patch with a matrix array insonates the target arteries in 3D, and the power Doppler mode results show the collected volumetric blood flow signals. A much larger computation power will be needed to reconstruct volumetric duplex mode images. Because we only consider the morphology of the vasculature rather than the surrounding tissues and blood flow directions, we focus on the power Doppler mode in this study. Note that conventional probes require handholding, which is impractical for long-term monitoring and generates results that are operator-dependent. The conformal ultrasound patch is self-adherent and overcomes these two challenges.

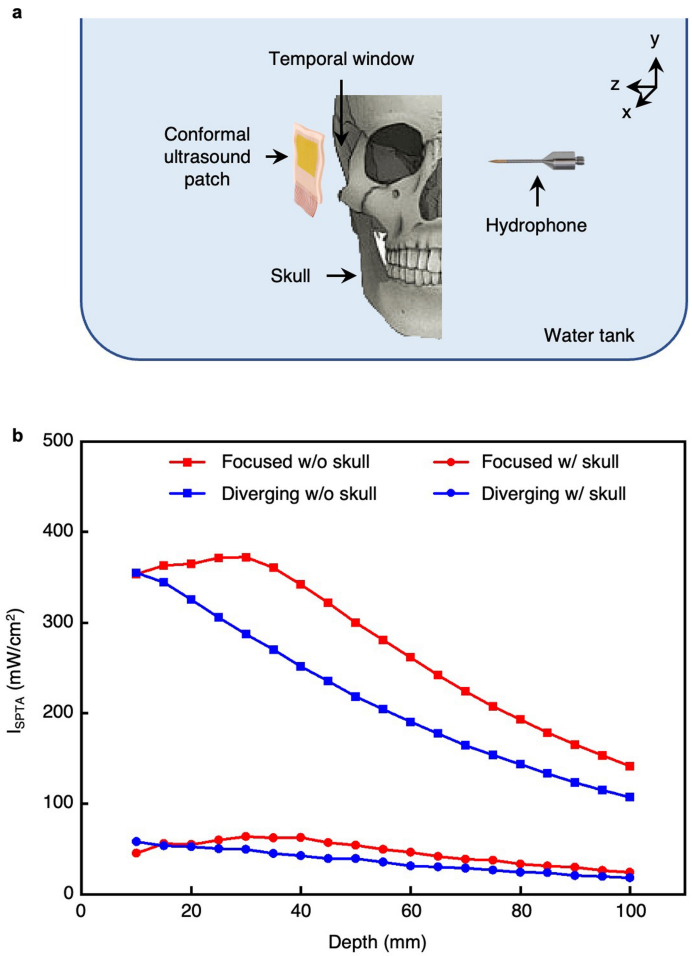

Extended Data Fig. 2 | Ultrasound exposure safety. a, System set-up for characterizing ultrasound exposure safety. The hydrophone is controlled by a 3D linear motor in a water tank. A formalin-fixed human skull sample is used to evaluate skull induced attenuation. **b**, Ultrasound intensity measured by the hydrophone. The maximum derated intensities of both diverging and focused beamforming strategies before derating are set to around 370 mW cm^{-2}. The average intensity loss of the ultrasound beams after skull penetration is around 83% for both beamforming strategies. All of the measured results are lower than the maximum level recommended by the Food and Drug Administration (that is, 720 mW cm^{-2})[27].

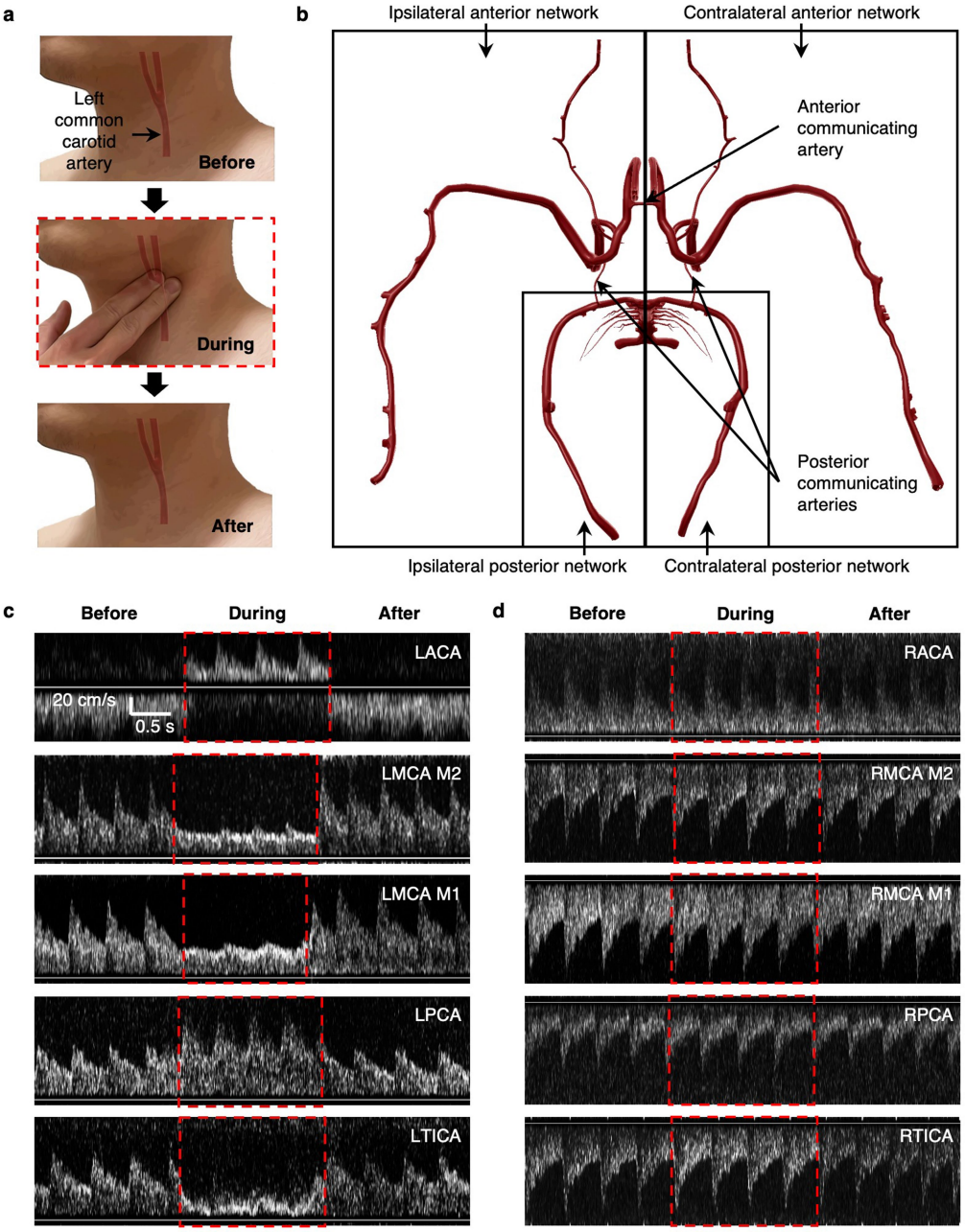

Extended Data Fig. 3 | Blood flow spectra of compressing the left common carotid artery. a, Schematics of before, during, and after the compression test. **b**, The circle of Willis can be divided into four parts, including ipsilateral anterior, contralateral anterior, ipsilateral posterior, and contralateral posterior networks. These four parts are connected by one anterior communicating artery and two posterior communicating arteries[48]. **c**, The blood flow spectra of ACA, MCA M2, MCA M1, PCA, and TICA segments on the left side before, during, and after the compression test. The red dashed boxes label the period during the compression. **d**, The blood flow spectra of ACA, MCA M2, MCA M1, PCA, and TICA segments on the right side before, during, and after the compression test. The red dashed boxes label the period during the compression. The spectra share the same scale bars.

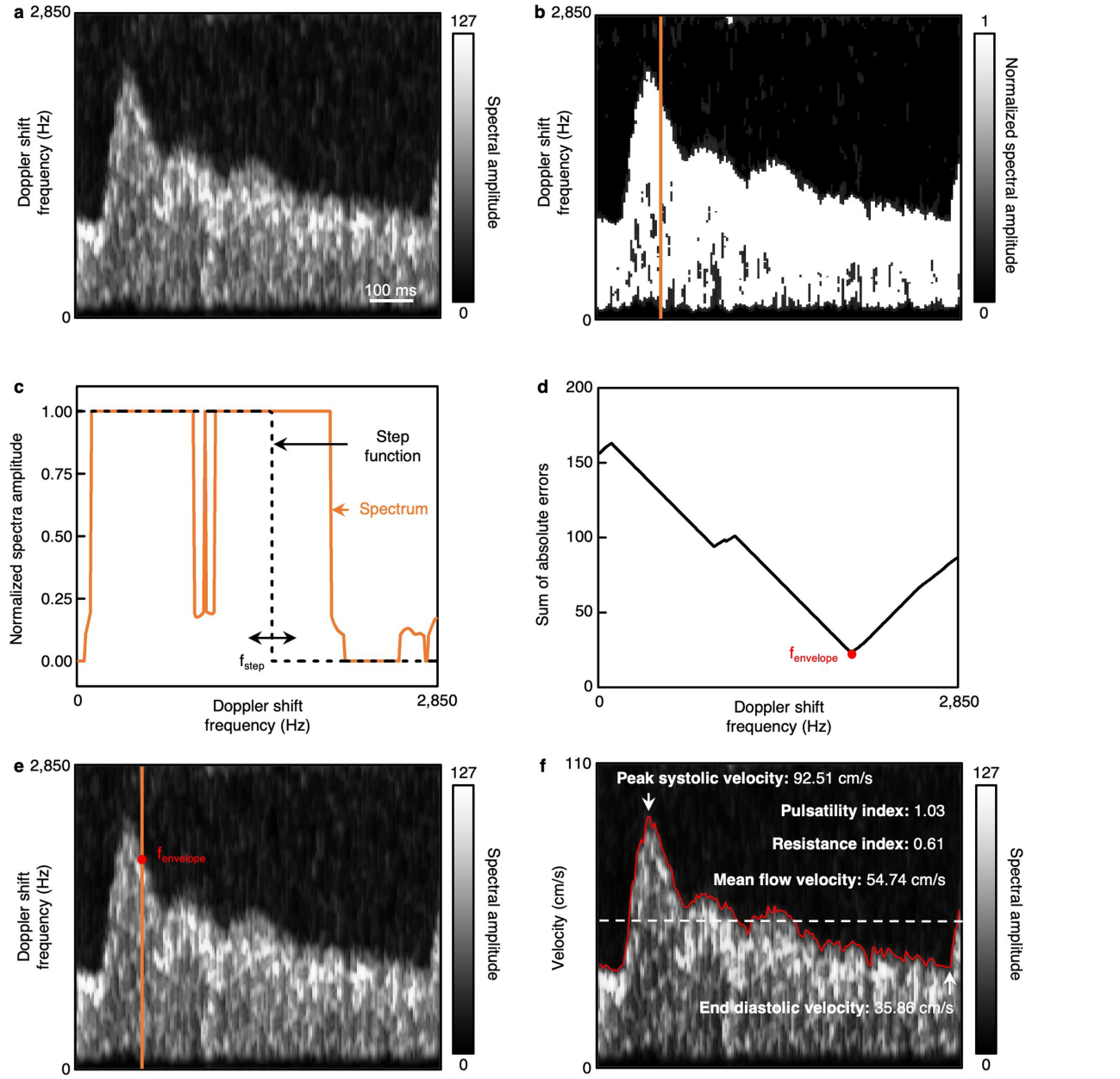

Extended Data Fig. 4 | Autonomous envelope tracking and parameter calculation. a, Spectrum Doppler of blood flow in one cardiac cycle. **b**, The spectrum Doppler is normalized first. After that, the spectrum with an amplitude higher than 0.2 is set 1, while the spectrum with an amplitude lower than 0.1 is set 0. This enhances the contrast between spectrum Doppler and noise. **c**, The orange curve is the amplitude snapshot of the enhanced spectrum in **b**, as labelled by the orange line. The enhanced spectrum has a similar shape like a step function. Therefore, we fit the spectrum using a step function to extract the envelope. The dashed black curve is one example of a step function. Changing f_{step} will form different step functions. **d**, To find the step function that fits the spectrum the best, the sum of absolute errors is defined to quantify the difference between the spectrum curve and the step function. f_{step} sweeps from 0 to 2,850 Hz. The f_{step} corresponding to the minimum sum of absolute errors is the desired $f_{envelope}$. **e**, $f_{envelope}$ is the envelope corresponding to the spectrum at one moment. **f**, The entire envelope is extracted using the above method and labelled by a red line. The peak systolic velocity, mean flow velocity, end diastolic velocity, pulsatility index, and resistance index are calculated based on the tracked envelope. The spectra share the same timescale bar.

Extended Data Fig. 5 | Optical images of using different devices for TCD sonography. a, Optical images of a participant during and after using the conventional TCD probe for 30 min. The pressing results in discomfort and redness patterns on the skin. **b**, Optical images of the participant during and after using a conventional TCD headset for 30 min. The screwing and pressing result in discomfort and redness patterns on the skin. **c**, Optical images of the participant during and after using a customized TCD headset for 30 min. This headset is designed for monitoring cerebral blood flow during brain procedures. The screwing and pressing result in discomfort and redness patterns on the skin. **d**, Optical images of the participant during and after using the conformal ultrasound patch for 30 min. This mechanical design eliminates the need for uncomfortable pressure and substantially reduces skin irritation. The images share the same scale bar. The inset images share the same scale bar.

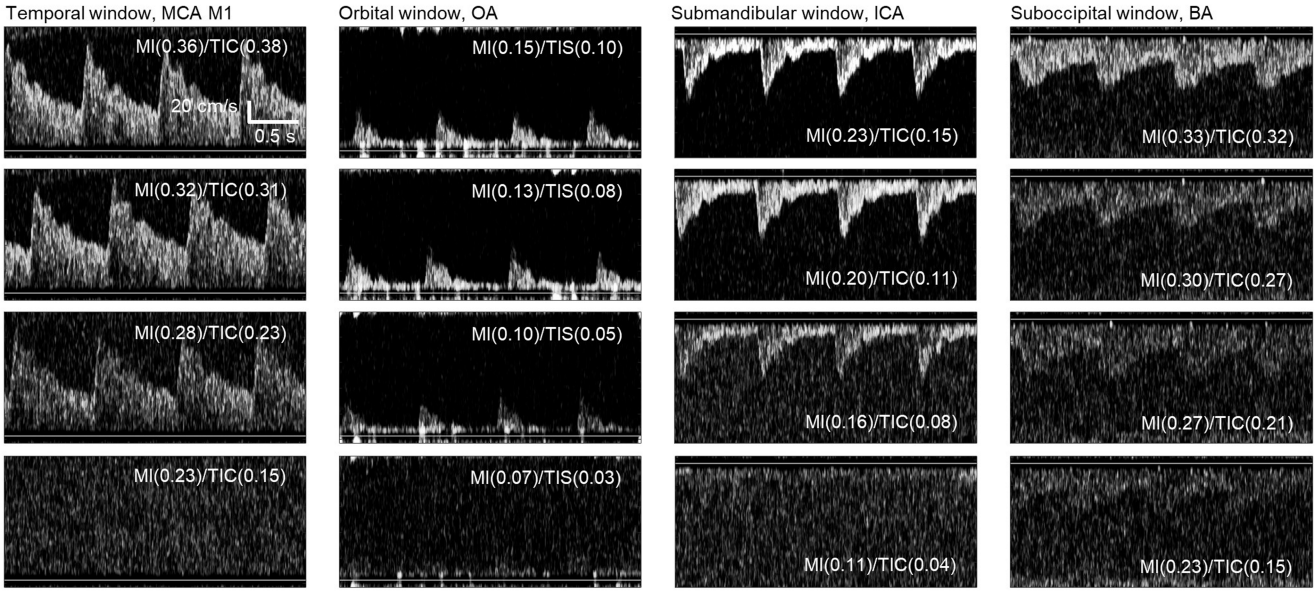

Extended Data Fig. 6 | Doppler spectra acquired from all transcranial windows by using different mechanical indices and thermal indices. As the mechanical index and thermal index decrease, the signal quality correspondingly declines. The optimal mechanical indices and thermal indices were chosen to be as low as reasonably achievable during blood flow monitoring, balancing safety and signal quality. For the temporal and suboccipital windows, the optimal mechanical index and thermal index were around 0.3; for the orbital window, we selected mechanical index around 0.13 and thermal index around 0.08; and for the submandibular window, the ideal mechanical index and thermal index were approximately 0.2 and 0.11, respectively. Importantly, these thresholds could be subject to individual variations due to physiological and anatomical differences. The spectra share the same scale bars. MI, mechanical index. TIC, cranium thermal index. TIS, soft tissue thermal index.

Extended Data Table 1 | Comparison of different techniques for cerebral blood flow monitoring

Method	Techniques	Invasiveness	Continuous	Absolute / Relative	Wearable	References
Nuclear medicine	Positron emission tomography	Yes	No	Absolute	No	[56]
	Intra-arterial injection of ^{133}Xe and ^{85}Kr	Yes	No	Absolute	No	[57]
	Single-photon emission computed tomography	Yes	No	Relative	No	[58]
X-ray	Xe-enhanced computed tomography	No	No	Absolute	No	[59]
	Perfusion computed tomography	Yes	No	Absolute	No	[60]
	Digital subtraction angiography	Yes	No	Absolute	No	[61]
Magnetic resonance imaging	Dynamic susceptibility contrast magnetic resonance imaging	Yes	No	Absolute	No	[62]
	Arterial spin labeling	No	Yes	Absolute	No	[63]
Intravascular measurements	Nitrous oxide inhalation	Yes	No	Absolute	No	[64]
Thermal probes	Jugular thermodilution	Yes	No	Absolute	No	[65]
	Thermal diffusion flowmetry	Yes	Yes	Absolute	Yes	[66]
Electrical probes	Electrical impedance tomography	No	Yes	Relative	Yes	[8,67]
	Electroencephalography	No	Yes	Relative	Yes	[7]
Optical probes	Laser Doppler flowmetry	Yes	Yes	Absolute	Yes	[68]
	Diffuse correlation spectroscopy	No	Yes	Relative	Yes	[69]
	Near-infrared spectroscopy	No	Yes	Absolute	Yes	[70]
Ultrasonography	Transit-time ultrasound flowmetry	Yes	Yes	Absolute	No	[71]
	Transcranial Doppler	No	Yes	Absolute	Yes	[72]

Invasiveness, continuous monitoring, absolute or relative quantification, and wearability of the different techniques are compared. These parameters allow for analysing the advantages and disadvantages of current techniques to guide the design of the conformal ultrasound patch. References 7,8,56–72.

Extended Data Table 2 | Exemplary large group studies on TCD success rates

Number of Participants	Sex (Female percentage)	Acoustic Intensity (mW/cm^2)	Age (mean ± standard deviation) (years)	Race / Ethnicity	Success Rate (percentage)	Reference
2,735	56.7%	N/A	71.5±6.6	N/A	75% (A; D)	[73]
749	52.2%	N/A	<60 (n = 375); 60-79 (n = 230); ≥80 (n = 144)	Hispanic–Mestizo	94.9%; 70.4%; 56.3% (O; D)	[74]
705	41.8%	N/A	67.7±11.9	Mostly Asian	75% (A; D)	[75]
624	39.7%	550	55.2±16.1	N/A	92.8% (O; N/A)	[76]
597	24.5%	100	<40 (n = 43); 40-69 (n = 384); ≥70 (n = 170)	Mostly Asian	77.1% (N/A; D)	[77]
396	64.7%	N/A	62.6±6.0	Mostly Asian	72.2% (A; D)	[78]
376	35.9%	N/A	68.4±12.1	Asian	83.5% (A; D)	[79]
355	38.6%	N/A	64.5±13.2	Mostly Asian	71.2% (O; D)	[80]
262	48.9%	N/A	66±N/A	White (n = 202); Black or African American/Asian (n = 60)	79.8% (A; D)	[81]
239	46.9%	532; 456; 380; 304; 228; 152; 76	20-49 (n = 34); 50-69 (n = 115); 70-89 (n = 90)	Asian	71.5%; 61.5%; 59.8%; 59.4%; 53.6%; 48.1%; 38.1% (N/A, D)	[82]
182	40.1%	147~200	61.2±14.2	Mostly White	82% (A; S)	[83]
140	61.0%	N/A	74.1±6.6	Amerindians (n = 70) European ancestry (n = 70)	60% (O; D)	[84]
92	38.0%	N/A	64.0±9.5	Mostly Asian	65.8% (A; D)	[85]
90	51.1%	100	57.1±11.7	White (n = 66); Black (n = 19); Hispanic (n = 5)	88.9% (A; D)	[86]
36	47.2%	100~370	52.92±18.74	White (n = 15); Asian (n = 13); Black (n = 5); Hispanic/Latino (n = 3)	75.3% for conventional rigid probe; 70.6% for our patch (A; D)	This study

A, adequate signal, including optimal and suboptimal signals (for example, only part of the arterial segments cannot be accessed); D, double sides of the temporal window; N/A, not available; O, optimal signal; S, single side of the temporal window. This table summarizes findings from various studies on the success rate of the TCD examination across different demographic groups and applied acoustic intensities. Each study is categorized by the number of participants, sex distribution, applied acoustic intensity, age distribution, race/ethnicity of the study population, and the reported success rate. The last row presents aggregated data from this study, highlighting the similar success rates of this study to the published ones. References 73–86.

nature portfolio

https://doi.org/10.1038/s41586-024-07381-5

Supplementary information

Transcranial volumetric imaging using a conformal ultrasound patch

In the format provided by the authors and unedited

Supplementary Information for

Transcranial volumetric imaging using a conformal ultrasound patch

Sai Zhou[1,9], Xiaoxiang Gao[2,9], Geonho Park[2,9], Xinyi Yang[1,9], Baiyan Qi[1], Muyang Lin[2], Hao Huang[2], Yizhou Bian[2], Hongjie Hu[2], Xiangjun Chen[1], Ray S. Wu[2], Boyu Liu[2], Wentong Yue[2], Chengchangfeng Lu[3], Ruotao Wang[2], Pranavi Bheemreddy[3], Siyu Qin[3], Arthur Lam[4], Keith A. Wear[5], Michael Andre[6], Erik B. Kistler[6,7], David W. Newell[8], Sheng Xu[1,2,3,6,7#]

[1]Materials Science and Engineering Program, University of California San Diego, La Jolla, CA 92093, USA.
[2]Department of Nanoengineering, University of California San Diego, La Jolla, CA 92093, USA.
[3]Department of Electrical and Computer Engineering, University of California San Diego, La Jolla, CA 92093, USA.
[4]Department of Anesthesiology and Critical Care, University of California San Diego, La Jolla, CA 92093, USA.
[5]U.S. Food and Drug Administration, Silver Spring, MD 20993, USA.
[6]Department of Radiology, University of California San Diego, La Jolla, CA 92093, USA.
[7]Shu Chien-Gene Lay Department of Bioengineering, University of California San Diego, La Jolla, CA 92093, USA.
[8]Department of Neurosurgery, Seattle Neuroscience Institute, Seattle, WA 98112, USA.
[9]These authors contributed equally to this work: Sai Zhou, Xiaoxiang Gao, Geonho Park, Xinyi Yang.
[#]Email: shengxu@ucsd.edu

Table of Contents

Supplementary Discussion 1: Comparison of different methods for cerebral blood flow monitoring

Various techniques have been used to measure cerebral blood flow, including nuclear medicine, X-ray, magnetic resonance imaging, intravascular measurements, thermal probes, electrical probes, optical probes, and ultrasonography (Extended Data Table 1)[1-3].

(1) Nuclear medicine: The basic principle of nuclear medicine is to inject radiotracers and detect their spatial and temporal kinetics in the cerebral vessels with radiation detectors. There are three techniques: positron emission tomography, intra-arterial injection of ^{133}Xe and ^{85}Kr, and single-photon emission computed tomography.

Positron emission tomography injects positron-emitting radiotracers (e.g., ^{15}O) and measures its concentration in the blood vessel with a positron emission tomography scanner[4]. By taking advantage of the 2 min short half-life of the radiotracer, cerebral blood flow can be calculated from the dynamics of tracer delivery through the arteries[2]. There is minimal tissue diffusion due to the short half-life of the radiotracers. Therefore, this method is accurate in quantitatively analyzing absolute cerebral blood flow, but the bulky and expensive scanner limits its widespread use, and continuous monitoring for an extended period of time is not possible due to the short half-life of the radiotracer.

The intra-arterial injection of ^{133}Xe and ^{85}Kr radiotracers is mainly performed with scintillation detectors[5]. These detectors can monitor γ-ray and β particle emissions, which are caused by the exponential decay over time of ^{133}Xe and ^{85}Kr, respectively. Quantitative cerebral blood flow can be derived from the radioisotope clearance curve. Therefore, each injection of radiotracers can only provide one cerebral blood flow measurement, and a new measurement can only be performed after ensuring the previously injected radiotracers have fully decayed[2].

Single-photon emission computed tomography administers radiotracer compounds composed of a radioactive isotope (e.g., ^{99m}Tc or ^{123}I) coupled with a biologically active ligand (e.g., hexamethylpropyleneamine oxime or ethyl cysteinate dimer)[6]. The biological carrier enables the radioactive isotope to pass through the blood-brain barrier and subsequently metabolize intracellularly in the brain tissue[2]. Compared to positron emission tomography, which measures the positron emission of the radiotracers, here the emitted lower energy γ-rays from the radiotracers are detected in single-photon emission computed tomography. The multi-headed gamma camera with collimators detects the γ decay of the radiotracers and reconstructs the spatial distribution in three dimensions (3D). By observing the γ decay over time, relative cerebral blood flow can be detected. This technique can only be performed in controlled clinical settings because of the injection of the radiotracers and the setup of bulky collimator machines.

(2) X-ray: X-ray techniques, including xenon-enhanced computed tomography, perfusion computed tomography, and digital subtraction angiography, track substances using computed tomography scanners.

Xe contrast-enhanced computed tomography takes advantage of the rapid diffusion mechanism of Xe in the brain. Xe is administrated by inhalation, and the computed tomography image can determine the cerebral blood flow based on the concentration difference of Xe diffusing through

the brain tissue and baseline measurement without Xe inhalation[2]. Any computed tomography scanner can be used for Xe contrast-enhanced applications. The concentration of Xe is critical in performing safe but reliable measurements; thus, continuous monitoring is limited by the diffusion of Xe, and the associated equipment cannot be miniaturized into wearables[7].

Perfusion computed tomography injects iodinated contrast agent into cerebral vessels and measures its relative concentration over time, which is proportional to the change in image signals in x-ray images[8]. Thus, perfusion computed tomography selects the region of interest to measure the blood volume, and high frame rate data are acquired to measure blood flow mean transit time[2]. This technique involves invasive injection and data are non-continuous. Also, the quantification of cerebral blood flow has not been validated clinically. The accuracy varies significantly among different arteries.

Digital subtraction angiography also injects iodinated contrast agent into cerebral vessels. An initial contrast-free image is taken prior to the injection. Then this image is subtracted from the images during contrast agent injection digitally[9]. This technique, therefore, has high temporal information, which can provide cerebral blood flow measurements[10].

(3) Magnetic resonance imaging: Magnetic resonance imaging produces high-quality 3D anatomical images with high magnetic fields of a large scanner, making it impractical to achieve a wearable format. This method includes dynamic susceptibility contrast magnetic resonance imaging and arterial spin labeling.

Dynamic susceptibility contrast magnetic resonance imaging administers Gd-based paramagnetic contrast agents and measures the transient decrease in brain signal intensities. This signal intensity approximates the contrast agent concentration, which can be quantitatively converted into cerebral blood volume. The technique is based on the difference in magnetic susceptibility of the contrast agent in intravascular and extravascular regions[11]. The conversion requires the injected concentration and transient signal loss during the contrast agent movement through the blood vessels, so continuous monitoring is not possible. Because this technology is a recent development, standardized protocols are not available for wide use in clinics[2].

Arterial spin labeling relies on the magnetically labeled arterial blood water protons[2]. Continuous and quantitative analysis is achieved by the radiofrequency pulses that invert the magnetization direction of the blood water protons, allowing local cerebral blood flow to be quantified by the amount of negative magnetization in one of the cerebral arteries[12].

(4) Intravascular measurements: Intravascular measurements require the injection of tracers to measure the blood flow changes after their circulation through the cerebral blood vessels. There are two methods: nitrous oxide inhalation and jugular thermodilution. Jugular thermodilution measures the temperature differences after tracer injection, and thus is discussed in thermal probes section.

Nitrous oxide is a freely diffusible tracer. The concentration of nitrous oxide is measured at the femoral arterial and the jugular venous sites to find the time it takes for the concentration to reach a steady state (i.e., the time for the concentrations of nitrous oxide at the femoral arterial site and

the jugular venous site to be the same). The time required to reach this steady state is used to calculate the cerebral blood flow[13]. Then, the diffusion dynamics of nitrous oxide can be correlated with systemic cerebral blood flow. Only one measurement of cerebral blood flow can be quantitatively obtained. The inhalation of nitrous oxide limits its use for continuous monitoring[2]. In addition, due to the catheterization of the femoral artery or the jugular vein, this technique is cumbersome and invasive, which is not suitable for long-term use.

(5) Thermal probes: Thermal probes use thermistors to measure the temperature change during thermal intervention to the cerebral blood flow. There are two techniques: jugular thermodilution and thermal diffusion flowmetry.

The jugular thermodilution method uses a catheter to inject a cold fluid that is miscible in blood into the internal jugular vein to generate a thermal perturbation[2]. Then, the temperature differences can be measured by the thermistors attached to the inner and outer walls of the catheter and further converted into a measurement of cerebral blood flow. The straightforward calculation provides a quantitative real-time continuous assessment of overall cerebral blood flow[14]. Nevertheless, this technique is invasive and patients' tolerance to the cold fluid severely limits the duration of the test.

Thermal diffusion flowmetry is based on heat transfer of biological tissues: conductive properties of the brain tissues and cerebral blood flow[2]. The reference thermistor measures the normal brain temperature while the active thermistor measures the heated site. Because thermal power is dissipated via heat transfer and the conductive properties of the brain tissues are assumed to be constant, the temperature changes are related to the convective effects of the cerebral blood flow[15]. This method can provide measurements of absolute local cerebral blood flow continuously. However, because of its invasiveness, thermal diffusion flowmetry is usually done on critically ill patients.

(6) Electrical probes: Electrical probes extract data from changes in conductivity, impedance, or potentials from tissues and cells. Electrical impedance tomography and electroencephalography methods measure these electrical signals from the brain to calculate cerebral blood flow.

Electrical impedance tomography utilizes the impedance differences between blood and the brain tissue[3]. Blood has a lower impedance than the brain tissue. Thus, as the blood flow increases in a certain region, its impedance decreases. These relative impedance changes in cerebral blood flow can be detected by applying a weak excitation current to the region of interest to create a potential field; then, an array of electrodes measures the potential changes from the known applied current[16]. Those electrodes can be engineered into a wearable format. However, because of the fringe effect of the electric field (i.e., the non-uniform electric fields around the edge of the electrodes), the signal-to-noise ratio is intrinsically low, resulting in limited spatial resolution of imaging areas of interest and blood flow measurement from individual vessels[17].

Electroencephalography detects the voltage differences stemming from the activities of neurons[18]. Oscillations of certain frequencies in the electroencephalography signals represent different brain functions, and they have a close relationship with cerebral blood flow[1]. In other words, changes in cerebral blood flow cause different oscillation frequencies. Electroencephalography is measured

noninvasively with scalp electrodes; thus, wearable continuous analysis is possible. However, due to the indirect calculation of cerebral blood flow, the data interpretation is subjective and the measurement accuracy is questionable.

(7) Optical probes: Optical methods such as laser Doppler flowmetry, diffuse correlation spectroscopy, and near-infrared spectroscopy are based on reflection, scattering, transmission, or absorption of a light source due to tissue properties, which can be used to assess cerebral blood flow.

Laser Doppler flowmetry utilizes the Doppler effect to measure the frequency shift caused by moving red blood cells. A fiber-optic probe sends a monochromatic light to the targeted vessel, and a photodetector measures the scattered light that has a Doppler-shifted frequency, which can be converted into cerebral blood flow[19]. The major merit of this technique is that it can provide highly localized detection, even down to the microcirculation. However, due to the limited penetration depth of light, the probe needs to be inserted invasively into the brain tissue[2]. In addition, the low Young's modulus of the brain causes the probe to be easily displaced. Thus, there is often signal loss, and a wearable format is not ideal.

Diffuse correlation spectroscopy detects cerebral blood flow by analyzing the scattering effect of a light source noninvasively emitted from the skin surface[2]. Near-infrared light can propagate through the skull, brain tissues, and moving red blood cells in the cerebral vessels. The scattered light from each depth in the brain is then measured from the skin surface and further analyzed to determine relative changes in blood flow. Thus, this method can only measure the relative blood flow index, the percent change relative to a baseline value. By increasing the source-detector distance on the skin surface, signals from deeper areas can be monitored but with less sensitivity due to decreased light intensity[20]. Diffuse correlation spectroscopy can be miniaturized into a wearable format.

Near-infrared spectroscopy is also a diffuse optical method but with two light sources of different wavelengths to noninvasively probe the concentration of oxyhemoglobin and deoxyhemoglobin in the cerebral cortex[21]. In the brain, the dynamic hemoglobin concentrations are the main contributors to the changes in light absorption. Thus, the absorption is used to calculate the amount of oxyhemoglobin and deoxyhemoglobin, and the absorption difference is highly correlated with cerebral blood flow[22]. However, various factors such as blood flow, blood volume, capillary density, and metabolic rate of oxygen may also affect hemoglobin concentration, limiting the calculation accuracy.

(8) Ultrasonography: When ultrasound is backscattered or reflected from the blood vessels, the received ultrasound waves contain blood flow information from inside the blood vessels. There are two ultrasound techniques for monitoring cerebral blood flow: transit-time ultrasonic flowmetry and transcranial Doppler ultrasound.

Transit-time ultrasonic flowmetry measures the time for the blood to flow from an ultrasound transducer placed upstream to another ultrasound transducer placed downstream to a blood vessel[23]. This transit time is directly proportional to the volumetric blood flow. In principle, the device can be wearable and continuous. However, because the major cerebral blood vessels are located deep

inside the brain, accurate assessments must be performed invasively by perivascularly placing the transducers on the vessel wall, which limits applications of this method to only surgical settings[2].

The transcranial Doppler (TCD) ultrasound is also based on the Doppler effect, noninvasively measuring the frequency shift between transmitted ultrasound waves and waves backscattered by moving red blood cells[24]. Thus, TCD can provide local assessment of individual vessels in the cerebral arterial network[2]. To achieve continuous monitoring, wearable TCD headsets have been developed. However, these headsets typically require tight fixation to the head, which is too uncomfortable to wear for >30 min. Also, due to the small cerebral vasculature, the signals can be easily lost because slight movements of rigid ultrasound probes may shift the ultrasound beam away from the vessels. There are some customized two-dimensional matrix arrays used to map the volumetric cerebral vascular network. For example, a "wearable phased array" used an 8 by 8 array with 1.6 mm by 1.6 mm element size[25]. The pitch size (i.e., 1.7 mm) is much larger than the ultrasound wavelength (i.e., 0.77 mm), resulting in significant grating lobes and limited spatial resolutions for volumetric reconstruction. This system was used to target the middle cerebral artery (MCA) and the signals from other cerebral arteries were ignored, which resulted in limited value for clinical decision making. Another example is a "Volumetrics Medical Imaging (VMI, Durham, NC) system" using a sparse two-dimensional array with 0.35 mm pitch size[26]. Combined with contrast agents, it could generate high spatial resolution volumetric reconstruction. However, this system used a normal line-by-line scanning mode with a much lower temporal resolution, and its bulky size is not suitable for continuous long-term monitoring.

Supplementary Discussion 2: Acoustic beam attenuation by the skull

Ultrasound is widely used to track Doppler signals of blood flow throughout the body. However, compared to other vessels in the body, the cerebral vessels are challenging to be sensed by ultrasound due to the skull-induced strong acoustic attenuation[27].

The skull is comprised of outer cortical bone and inner cancellous bone[28]. The cortical bone is mainly composed of osteon tissues with minimal porosity, and it has a much larger acoustic impedance than that of soft tissues. On the other hand, the cancellous bone is also made of osteon tissues but has anisotropic heterogeneous porous structures with 75-85% porosity[28]. The pores are filled with bone marrow, which has a similar acoustic impedance to that of soft tissues. Therefore, the overall porous cancellous bone has a different acoustic impedance from that of soft tissues and the cortical bone.

There are three major attenuation mechanisms when the ultrasound beam travels through the skull: reflection, absorption, and scattering (Supplementary Fig. 2).

First, as the acoustic waves travel through an interface of two media of different acoustic impedances, some of the wave energy gets transmitted through while some gets reflected from the interface. Therefore, there are reflections at all interfaces including scalp soft tissue-cortical bone interface, cortical bone-cancellous bone interface, and cortical bone-brain tissue interface. The larger the impedance mismatch between the two media, the larger the reflection. The acoustic impedance of soft tissues is around 1.66×10^6 $kgm^{-2}s^{-1}$, while that of osteon tissues is approximate 6.47×10^6 $kgm^{-2}s^{-1}$, creating a substantial mismatch between them[29].

Second, absorption is the process when the ultrasound energy is converted into heat. This occurs due to the mechanical nature of ultrasound waves. As the ultrasound waves pass through the tissues, the compositional elements of the tissues longitudinally vibrate and pass the pressure wave to the next tissue elements. The efficiency of ultrasound wave propagation through the tissue is related to various factors of the tissue composition (e.g., material, density, and structural orientation). Cortical bone exhibits higher attenuation coefficient (e.g., 1 to 10 $dB \cdot cm^{-1}MHz^{-1}$)[30] than that of soft tissues (e.g., 0.3 to 0.7 $dB \cdot cm^{-1}MHz^{-1}$ for most soft tissues), Higher attenuation is often associated with higher absorption and therefore higher temperature rise.

Third, as the ultrasound beam travels through a microstructure that is composed of various materials, scattering occurs, especially when the materials have large differences in acoustic impedances[29], causing the ultrasound beam to diverge in all directions. Consequently, in the skull, the porous microstructures of the cancellous bone with large differences in acoustic impedance between the osteon tissues and the bone marrow have substantial scattering effect. The scattering effect is dependent on the ultrasound wavelength and the microstructure size[31]. If the microstructures have sizes close to the ultrasound wavelength, the ultrasound waves will scatter relatively anisotropically, but if the sizes are much smaller than the wavelength, then the ultrasound waves will scatter less anisotropically. In general, longitudinal waves incident upon trabeculae can scatter into both shear and longitudinal waves. The conversion of incident longitudinal waves into scattered shear waves, followed by rapid absorption of scattered shear waves, has been shown to be a significant source of attenuation in cancellous bone[31]. In addition, the cancellous bone thickness is different in each person and the thickness is nonuniform across different regions in the skull of the same person. Therefore, different people and skull regions will cause different acoustic beam patterns[32].

In all, the skull causes all three types of attenuation that substantially decrease the signal-to-noise ratio of ultrasound probes. We have taken these factors into consideration when designing the conformal ultrasound patch. Higher ultrasound frequencies can provide better image quality but also stronger reflection, absorption, and scattering and thus smaller signal-to-noise ratio. Therefore, to balance the spatial resolution and signal-to-noise ratio, the central frequency in this work is 2 MHz. In addition, transmitting the ultrasound waves with a longer pulse duration provides a much smaller bandwidth, which leads to a higher sensitivity to Doppler shift. Temporal bone is selected as an acoustic window of the skull owing to its small thickness compared to other parts of the skull. The temporal window usually causes about 80% loss in ultrasound intensity. Therefore, a higher acoustic intensity (around 60 to 370 mW/cm^2 spatial peak temporal average intensity) is utilized to ensure sufficient acoustic energy to insonate the arteries through the skull, which gives a sufficient signal-to-noise ratio to measure Doppler shifts of blood flow in the intracranial vessels. All acoustic intensities used in this work are under the Food and Drug Administration maximum recommended level for diagnostic ultrasound[33].

While we have made substantial efforts to mitigate signal attenuation caused by the skull, we must acknowledge the persistence of certain inaccessible transcranial windows. These are typically due to factors such as increased skull thickness, density, or the presence of numerous air-filled cavities, all of which can significantly attenuate ultrasound waves. This, in turn, diminishes signal quality and obstructs reliable cerebral blood flow measurements. Such hindrances represent an inevitable limitation that is inherent to both conventional TCD probes and the conformable ultrasound patch.

Supplementary Discussion 3: Phase aberration effect

When using the conformal ultrasound patch for imaging, each transducer in the patch will emit ultrasound waves with a specific time-delay profile. These ultrasound waves are backscattered and reflected from the tissues and received by the transducer array for image reconstruction. Ideally, we assume the speed of sound in tissues is constant, and the patch has no physical deformation (i.e., all transducers are on the same flat plane). Then, to make all ultrasound waves arrive at a target in coincidence, the time-delay profile can be calculated based on the geometric path length between the target and each element in the array.

However, inhomogeneous media and irregular geometries of the transducer array will cause phase aberration, which limits spatial resolution in ultrasound imaging (Supplementary Fig. 3)[34-36]. First, the speed of sound in the body varies over a wide range. The speed of sound is very different between soft tissues and the skull, by a factor of around 2. In addition, there is variation in shape, thickness, and composition of the skull. Two locations on the same skull can experience substantial differences in ultrasound propagation speed, which makes the phase aberration even worse in transcranial studies. Second, the transducer array may have uncertain curvatures while the ultrasound patch conforms to the scalp. The geometric irregularities induce as large errors in the time-of-flight as several ultrasound wavelengths, which will lead to uncertain phase aberrations.

Low ultrasound frequencies can minimize such phase aberrations (Supplementary Fig. 3)[37]. Lower ultrasound frequencies have longer wavelengths, which lead to a smaller relative phase angle shift. As a result, ultrasound waves with lower frequencies are distorted less and thus can reconstruct better images than those with higher frequencies (Supplementary Fig. 3).

Supplementary Discussion 4: Technology advancement of the conformal ultrasound patch

Wearable ultrasound devices could sense signals in deep tissues[38]; however, their applications were drastically limited by the signal attenuation and phase aberration of the bone, which constrains their usability to soft tissues. In this study, we demonstrate the first wearable ultrasound device capable of deep tissue sensing through the bone. This capability is unprecedented and overcomes a longstanding barrier in wearable ultrasound technology.

Moreover, existing wearable ultrasound devices are limited to providing one-dimensional signals[39,40], two-dimensional images[41-44], or three-dimensional images by piecing multiple two-dimensional slices together[45,46]. The piecing approach introduces potential inaccuracies to the final result. First, it relies on extrapolation from adjacent slices to create a complete three-dimensional image, introducing errors from approximation. Second, these slices are acquired with typically about 1 s time gaps. Considering the continuous movement of the tissue, these time gaps lead to mismatch between slices. This study addresses this limitation by directly reconstructing three-dimensional images, which drastically reduces the time needed for image reconstruction and substantially enhances the image quality.

Overcoming each one of these two limitations necessitated extensive engineering innovation. This study significantly enhances the capabilities of wearable ultrasound devices, bringing their functionality in line with advanced ultrasound instruments used in clinical settings. This technology supports a wide range of medical and research applications previously thought

impossible (Supplementary Discussion 16).

Supplementary Discussion 5: Cerebral vascular network

The cerebral vessels intertwine and form a complicated network (Fig. 3e). There are four principal arteries that provide the blood supply to the brain, including the internal carotid artery (ICA) and vertebral artery on each side[47]. The ICA traverses through the base of the skull to provide the anterior supply, while the vertebral artery runs through the spinal column in the neck and provides the posterior supply (Fig. 3e)[48].

The terminal ICA (TICA), the end part of the ICA, gives off the middle cerebral artery (MCA), anterior cerebral artery (ACA), and ophthalmic artery branches. The MCA extends laterally and slightly anteriorly and carries around 80% of the blood flow to the brain (Fig. 3e)[48]. It is one of the most important cerebral arteries whose blood flow reflects the overall blood supply of the brain. The ACA reaches out medially, then turns more anteriorly until it reaches to the brain midline (Fig. 3e)[48]. The anterior communicating artery is a small segment joining each side of the ACA in the brain midline (Extended Data Fig. 3)[48]. The ophthalmic artery runs through the orbital cavity and nasally towards the eye (Fig. 3e)[48]. The combination of these arteries builds up the anterior circulation network in the brain.

The vertebral artery from each side joins at the front of the brainstem in the midline to form the basilar artery (Fig. 3e). The posterior cerebral artery (PCA) arises from the basilar artery and runs laterally and curves posteriorly (Fig. 3e)[48]. The vertebral artery, basilar artery, and PCA are the major arteries for the posterior circulation network in the brain.

At the central cranial base, the anterior and posterior circulation are connected by the posterior communicating arteries to form an anastomotic structure called the "circle of Willis" (Fig. 3e)[47]. The configuration of the cerebral arteries that form the circle of Willis is considered an engineered redundancy for collateral circulation, theoretically allowing the brain to preserve sufficient blood flow and perfusion to its contralateral aspect to avoid or limit injury in the event of focal cerebral artery blockage or stenosis[49].

Compressing the left common carotid artery can help to validate this concept. If there were no anterior communicating artery and posterior communicating arteries, compressing the left common carotid artery would block the blood flow in the left ICA and therefore induce a shortage of blood flow in ipsilateral anterior arterial segments (e.g., left TICA, left MCA, and left ACA). However, owing to the presence of the anterior communicating artery that connects the LACA and RACA, and posterior communicating arteries that connect the PCA and TICA, in healthy participants, blood would flow from the contralateral (e.g., right TICA, right MCA, and right ACA) and posterior (e.g., left and right PCA) networks into the ipsilateral anterior arteries to maintain the supply (Fig. 2c-d and Extended Data Fig. 3). Blood flow changes in all these arterial segments are important because all of them are needed to maintain appropriate blood supply in the brain during the compression test.

Note that the functional compensation can be influenced by the anatomical variations of the circle of Willis. For instance, the hypoplasia or aplasia of certain arteries, such as the anterior communicating artery or posterior communicating arteries could affect the efficiency of this

compensatory response[50,51]. Hypoplastic or aplastic arteries may have a reduced capacity to provide sufficient blood flow for compensation during the carotid compression, which could potentially put the brain at risk during instances of unilateral carotid obstruction. These anatomical variations underscore the importance of individualized assessment of cerebral perfusion and highlight the advantage of our ultrasound patch in providing a personalized and comprehensive evaluation of cerebral hemodynamics.

To visualize the circle of Willis, we used the conformal ultrasound patch to monitor the blood flow in major cerebral arteries including ICA, MCA, ACA, ophthalmic artery, vertebral artery, basilar artery, and PCA.

There are two reasons why the anterior communicating artery and posterior communicating arteries are not monitored in this work. First, the blood flow signals from the anterior communicating artery and posterior communicating arteries are typically not captured by TCD on healthy participants. Because the bilateral blood flow is balanced, the collateral circulation is closed and there is no blood flow in these arteries[48]. Second, the anterior communicating artery and posterior communicating arteries are small (about 1 mm in diameter)[52,53] and are difficult to be detected by TCD. In addition, the posterior communicating arteries are almost perpendicular to the ultrasound waves from the temporal window, which leads to extremely weak Doppler signals[48].

Other cerebral arteries are of less clinical interest and are not considered as targets for standard TCD sonography. Those arteries include the anteromedial central arteries, superior cerebellar artery, pontine arteries, anterior spinal artery, posterior spinal artery, posterior inferior cerebellar artery, etc.

The cerebral venous anatomy includes the superficial medullary veins and the deep medullary veins[54,55]. The superficial medullary veins start from subcortical veins that supply blood to the pial veins on the surface of the cortex[55]. The pial veins converge the blood and drain into the cerebral veins. Structurally, the pial veins have a circumferential smooth muscle layer to prevent them from being easily compressed at high intracranial pressures[55]. All other cerebral veins do not have muscular layers so they can expand freely[55]. Compared to the superficial medullary veins, the deep medullary veins are more extensive, which are perpendicular to the lateral ventricles and consist of venules in the white matter[56]. These two venous systems are connected via transcerebral veins that traverse through the entire cerebral parenchyma[56]. Because of the lesser interest in cerebrovenous disorders compared to arterial diseases, using TCD to diagnose cerebral venous blood flow has not yet been systematically established[57].

Supplementary Discussion 6: The rationale for choosing 16 by 16 matrix array

The primary reason for choosing a 16 by 16 array with 256 elements was due to the maximum number of elements supported by the Verasonics Vantage 256™ system. Furthermore, the complexity associated with managing a higher number of elements and their interconnections was another factor that influenced our decision to select the 16 by 16 configuration.

We acknowledge that the spatial resolution could be further improved by using a larger array, such as a 32 by 32 configuration. However, to implement this, we may need to synchronize four Vantage 256™ systems[58], which would introduce additional challenges in both hardware and software.

Four Vantage 256™ systems can support 1024 transducers, which substantially increase the computational load and lower the frame rate. Moreover, a refined design would be necessary to manage the increased complexity of the interconnections, which could present further difficulties.

Regarding fundamental limitations in the manufacturing process, a commercial 1024-channel probe (Vermon) in our group features a 32 by 32 array, including three blank columns to accommodate the interconnections. Although there are no insurmountable barriers to producing larger array sizes, our choice of the 256-element array was primarily driven by practical considerations and the need to balance performance, complexity, and resource constraints.

Supplementary Discussion 7: Safety characterization of the conformal ultrasound patch

TCD sonography follows the safety guidelines of the Food and Drug Administration for diagnostic ultrasound[33]. The conformal ultrasound patch is a medical device that may expose the operator and patient to various safety hazards. Therefore, the device must conform to relevant electrical, mechanical, and thermal safety guidelines in the intended use environment.

The Verasonics system (Vantage 256™) acts as a power source to activate the device. To maintain electrical safety, the Verasonics uses TDK/Lambda CSS500-12 OEM power supply to provide an alternating current line input that is "medical grade" in terms of leakage current and other regulatory requirements. The maximum current passing through the human body and its duration should be carefully considered to prevent any electrical hazard. The Verasonics system itself has a power output threshold of 96 V, and the maximum current from this supply is 0.5 A. The patch is activated at a maximum of around 20 V with a low pulse current (<100 μA), far below the limit. Specifically, the voltage source is in a pulsed mode, indicating that the transducers are vibrating in a transient manner. The repetitive activation of the transducers, i.e., its pulse repetition frequency, is 3000 Hz, which means that the transducers have 3000 working cycles per second. The transient working state of the device implies that the conformal ultrasound patch will experience an ultra-short (1.5 μs) stimulation period (i.e., three cycles) in each working pulse. In the pulsed excitation scheme, 99.55% of the time, no voltage is applied to the transducers, and thus no current will flow across the human body. Considering the low current amplitude and its short duration, the conformal ultrasound patch, even in case of a leakage, will not harm the operator or the patient. In fact, the device is fully encapsulated by Ecoflex silicone, which is a superb insulator. Therefore, the conformal ultrasound patch is safe for the human body.

The acoustic exposure of the device was evaluated using an ultrasound mapping system. We used a hydrophone controlled by a 3D linear motor in a water tank to measure the acoustic signal intensity (Extended Data Fig. 2). The waveforms exhibited very little nonlinear distortion and were relatively narrowband (Supplementary Fig. 3) so that pressures could be estimated without requiring deconvolution of voltage waveforms with frequency-dependent sensitivity[59]. Additionally, because the ratio of the hydrophone (HNP-0400, ONDA) sensitive element diameter d_g to the product of the wavelength λ and $F/\#$ (ratio of focal distance to aperture width) was much less than one, a hydrophone spatial averaging correction was not necessary[60].

Considering the capacitive load of the preamplifier (AH-2010-100, ONDA) when converting the voltage measurements to pressure values, the loaded sensitivity $M_L(f)$ can be estimated as:

$$M_L(f) = G(f)M_c(f)\frac{C_H}{C_H+C_A+C_c} \quad (3)$$

where $G(f)$ is the preamplifier gain (20 dB in this study), $M_c(f)$ is the hydrophone end-of-cable open circuit sensitivity (2.512 x 10^{-8} V·Pa^{-1} at 2 MHz in this study), C_H is the capacitance of hydrophone (70 pF in this study), C_A is the capacitance of preamplifier (7 pF in this study), and C_C is the capacitance of connector (zero in this study because the preamplifer is connected directly to the hydrophone)[61].

The pressure variables can be estimated as:

$$p(z) = \frac{V_{output}(z)}{M_L(f)} \quad (4)$$

where $V_{output}(z)$ is the output voltage, and z is the depth. The derated pressure variables can be estimated as:

$$p_\alpha(z) = p(z)10^{(-\alpha z f_{awf}/20dB)} \quad (5)$$

Where a is the attenuation coefficient (0.3 dB·cm^{-1}·MHz^{-1})[33], and f_{awf} is the acoustic working frequency (2 MHz in this study)[62].

The maximum derated spatial peak pulse average intensity, spatial peak temporal average intensity, and mechanical index should be measured on the worst-case pulse[63]. Therefore, we focused the matrix array at 40 mm (i.e., the shallowest focal depth for a spectral Doppler pulse used in this study) and these parameters were measured at depth of the maximum value of the attenuated pulse pressure squared integral,

$$ppsi_a(z) = \int p_\alpha^2(z,t)dt \quad (6)$$

where $ppsi$ is attenuated at a and z is varied from the break-point depth, z_{bp}, to the focal depth (40 mm in this study). The z_{bp} is defined as:

$$z_{bp} = 1.5 \times D_{eq} \quad (7)$$

where D_{eq} is the equivalent aperture diameter and is defined as:

$$D_{eq} = \sqrt{\frac{4}{\pi}A} \quad (8)$$

where A is the area of aperture. Plugging 144 mm^2 as the area of aperture in this study, z_{bp} can be estimated as 20.31 mm.

The pulse intensity integral is defined as:

$$pii_\alpha(z) = \frac{1}{\rho c}ppsi_\alpha(z) \quad (9)$$

where ρ is the density of water (997 kg·m^{-3} in this study), and c is the speed of sound in water (1480 m·s^{-1} in this study). Therefore, the derated spatial peak pulse average intensity is defined as:

$$I_{SPPA,\alpha}(z) = \frac{1}{t_d(z)}pii_\alpha(z) \quad (10)$$

where $t_d(z)$ is the pulse duration, which is 1.25 multiplied by the interval between the time when the time integral of the square of the instantaneous acoustic pressure reaches 10% and 90% of its final value[63]. And the derated spatial peak temporal average intensity can be approximated as:

$$I_{SPTA,\alpha}(z) = PRF\ pii_\alpha(z) \quad (11)$$

where PRF is the pulse repetition frequency (3000 Hz in this study).

Based on the scanning result from the ultrasound mapping system, the maximum value of the attenuated pulse pressure squared integral was located at around 30 mm depth. Plugging the output

voltage 0.3274 V, and pulse duration 5.0563 μs, the maximum derated spatial peak pulse average intensity was 24.54 W/cm^2, and the maximum derated spatial peak temporal average intensity was 372.21 mW/cm^2.

The mechanical index (MI) indicates the likelihood of producing micromechanical bio-effects, such as cavitation-related damage[33,64]. The MI is defined as:

$$MI = \frac{p_{r,\alpha}(z)}{\sqrt{f_{awf}}} \quad (12)$$

where $p_{r,\alpha}$ is the derated peak rarefactional pressure (i.e., the maximum negative instantaneous acoustic pressure in an acoustic field) in MPa, and f_{awf} is measured of acoustic working frequency in MHz. Plugging the derated peak rarefactional pressure 0.9968 MPa, the MI can be estimated as 0.70.

The relevant derated acoustic exposure maximum recommended levels are $I_{SPTA,\alpha}$≤720 mW/cm^2 and $I_{SPPA,\alpha}$≤190 W/cm^2 or MI<1.9 as defined by the Food and Drug Administration if scanning is not performed through the orbital window[33]. The maximum $I_{SPTA,\alpha}$, $I_{SPPA,\alpha}$, and MI of the ultrasound patch were measured as 372.21 mW/cm^2, 24.54 W/cm^2, and 0.70, respectively, which were all lower than the maximum recommended levels (Extended Data Fig. 2). Uncertainties in these measurements are assumed to be on the order of 15%[59]. Those values were reduced significantly when the ultrasound waves propagated through a temporal bone. If scanning is performed through the orbital window, the relevant derated acoustic exposure maximum recommended levels are $I_{SPTA,\alpha}$≤17 mW/cm^2 (Food and Drug Administration Track 1) or 50 mW/cm^2 and TI (thermal index, see below) ≤1 (Food and Drug Administration Track 3) and $I_{SPPA,\alpha}$≤28 W/cm^2 or MI<0.23 (Food and Drug Administration Track 1 and Track 3). When scanning through the orbital window, acoustic output was reduced to be below these levels.

To characterize thermal safety of the device, we measured its temperature rise when it was attached to the skin. The thermal imaging results showed minimal temperature variation (<1 °C) on the skin surface when the device was attached to the temporal window and worked for four hours continuously (Supplementary Fig. 12).

In addition, the thermal index TI was calculated to estimate tissue temperature rise[65]:

$$TI = \frac{Acoustic\ power\ output}{Acoustic\ power\ ouput\ to\ produce\ 1℃\ rise} \quad (13)$$

Specifically, the TI estimates the temperature increase in the worst-case scenario by assuming the tissue attenuation is homogeneous with an attenuation coefficient of 0.3 dB·cm^{-1}MHz^{-1} while most soft tissues have higher attenuation coefficients[33]. Therefore, in most cases, the TI overestimates the temperature increase compared to the real scenario. The Food and Drug Administration guidance recommends a maximum TI of one when scanning through the orbital window. For scanning through skull, it does not have a specific recommendation for maximum TI but requests an explanation for TI over six[33]. Using the output display standard (Track 3), the TI is required to be provided and updated in real time on the acoustic output information screen to provide ultrasonographers with an index for relative temperature change for a particular ultrasound mode[33,65]. The ultrasonographer uses this number and the ALARA (as low as reasonably achievable) principle[33] to limit the scanning time and exposure level. According to an official statement of the American Institute of Ultrasound in Medicine[66] , for adult transcranial ultrasound,

there is no dwell time limit for $TI \leq 1.5$, max dwell time <120 min for $1.5 < TI \leq 2.0$, max dwell time <60 min for $2.0 < TI \leq 2.5$, max dwell time <15 min for $2.5 < TI \leq 3.0$, max dwell time <4 min for $3.0 < TI \leq 4.0$, max dwell time <1 min for $4.0 < TI \leq 5.0$, max dwell time <15 s for $5.0 < TI \leq 6.0$, and scanning with $TI > 6.0$ is not recommended[66].

Depending on the tissues in the scanning plane, *TI* is subdivided into 3 types: soft tissue TI (TIS), bone TI (TIB), and cranium TI (TIC)[67]. TIC is relevant for scanning through skull bone, and TIS is relevant for scanning through the orbital window. Thus, for TCD applications, TIS and TIC were calculated for long-term spectral Doppler monitoring.

$$TIS_{as,ns} = \frac{P_{1\times1} \cdot f_{awf}}{210 mW MHz} \quad (14)$$

where $TIS_{as,ns}$ is the TIS at surface in non-scanning mode (i.e., Doppler mode) and $P_{1\times1}$ is the bounded-square output power over a one square centimeter area in mW.

$$TIS_{bs,ns} = \min\left[\frac{P_\alpha(z_{s,ns}) \times f_{awf}}{210 mW MHz}, \frac{I_{spta,\alpha}(z_{s,ns}) \times f_{awf}}{210 mW cm^{-2} MHz}\right] \quad (15)$$

where $TIS_{bs,ns}$ is the TIS below surface in non-scanning mode, $P_\alpha(z_{s,ns})$ is the derated output power at depth $z_{s,ns}$, and $I_{SPTA,\alpha}(z_{s,ns})$ is the derated spatial peak temporal average intensity at depth $z_{s,ns}$. Depth $z_{s,ns}$ is defined as:

$$z_{s,ns} = depth\ of\ max\{min[I_{spta,\alpha}(z) \times 1\ cm^2, P_\alpha(z)]\} \quad (16)$$

where z is varied from z_{bp} and onward.

$$TIC = \frac{P/D_{eq}}{40 mW cm^{-1}} \quad (17)$$

where *P* is output power in mW. The power values $P_{1\times1}$, P, and $P_\alpha(z_{s,ns})$ were measured from transverse hydrophone scans of the intensity distribution of the focused wave. *P* and $P_\alpha(z_{s,ns})$ were integrated over a transverse plane from the peak intensity distribution over a beam cross-sectional area in which the intensity was at least -26.2 dB of the maximum (axial) value. $TIS_{as,ns}$ can be calculated as 0.62, $TIS_{bs,ns}$ as 0.10, and $TIC\ as$ 0.38. These values were all far below the thresholds recommended by American Institute of Ultrasound in Medicine for long-term monitoring (i.e., $TI \leq 1.5$)[66].

Supplementary Discussion 8: Coherent compounding

Conventionally, an ultrasound image is obtained by a focused wave scanning line by line at different lateral positions (Supplementary Fig. 14). This method tremendously sacrifices the temporal resolution to generate an optimal image because numerous transmission and receiving events are required (Supplementary Fig. 14).

Coherent compounding is a method that combines backscattered echoes from several different angles of insonation to produce a single image with higher object conspicuity (i.e., object to background contrast)[68]. The speckle, clutter, and other acoustic artifacts may have different patterns (i.e., different phases) from different insonation angles. Combining the received echoes from a few different angles of insonation will enhance the target signals and reduce the artifacts, therefore increasing the image quality. For a given image quality, because less transmission and receiving events are required for coherent compounding based on diverging waves, it substantially increases the frame rate compared to conventional imaging using focused waves[68].

Supplementary Discussion 9: Spatiotemporal clutter filtering for ultrafast Doppler imaging

Ultrafast ultrasound imaging introduces a new paradigm for Doppler imaging[69,70]. By using diverging wave transmissions, it enables the acquisition of a large number of backscattered echoes at a very high frame rate in all fields of view, which significantly increases the sensitivity of Doppler shift[70].

In a Doppler image, clutter refers to stationary and slowly moving tissues whose signals need to be removed to highlight blood flow signals and visualize vessels precisely[71]. Conventional clutter filtering assumes that tissue motion signals and blood flow signals have completely different spectral characteristics. The tissue motion is very slow whereas red blood cells are moving fast, meaning that demodulated tissue motion signals and blood flow signals would not overlap. Therefore, theoretically, tissue motion signals could be simply removed by a high-pass filter. In reality, however, tissue motion and blood flow signals have overlap, which makes it impossible to separate them based on temporal information only[71,72].

In this work, we considered the spatiotemporal characteristics of tissue motion signals, which are different from those of blood scatterers. Tissue motion is spatially coherent, which means that tissue movement tends to drive the surrounding tissues to move in the same way/direction because of the cohesive nature of tissues[71]. These movements can be seen as a spatial shift of a group of speckles. On the other hand, the motion of red blood cells represents a reorganization of the scatterers and does not exhibit this spatial coherence[71]. Therefore, adopting such spatiotemporal information for clutter filtering can potentially improve the separation of tissue motion and blood flow.

Singular value decomposition is a mathematical operation on a matrix that can be used as a clutter filter. This method decomposes a multi-dimensional matrix (e.g., 3D for space and one dimension for time in this work) into a series of singular values and corresponding vectors. Because tissue motion signals are highly correlated, the signals from different spatial pixels exhibit a high degree of correlation and can be represented by larger singular values and corresponding vectors[71]. In contrast, blood flow signals have much less spatial coherence and lower amplitudes, which can be represented by smaller singular values and corresponding vectors[71]. Therefore, the singular value decomposition can locate the higher covariance values, which represent the tissue motion signals that can be removed[72].

Supplementary Discussion 10: Iteration of blood flow spectra processing

Compared to other blood flow spectra that contain limited information[41], we optimized the algorithms for improving the blood flow spectra resolution and integrated necessary functions for TCD sonography.

The conventional processing of blood flow signals simultaneously provides B-mode images, color Doppler images, and spectrum Doppler waveforms[41]. Each modality requires the Verasonics system to transmit and receive ultrasound waves and process the data separately. In this work, to enhance the quality of blood flow spectra, we paused the B-mode and color Doppler imaging processes and concentrated the computation power for spectra recording. The temporal resolution of the spectra was increased from around 15 Hz to >200 Hz. The velocity resolution was improved

from around 4 cm/s to <0.01 cm/s. The intensity resolution reached the threshold of conventional TCD probes (128-colormap)[73].

Supplementary Discussion 11: Turbulent blood flow

In turbulent flow, fluid varies chaotically in time and space, in contrast to laminar flow where the fluid moves in smooth paths[74]. These two types of flow can be differentiated by the Reynolds number:

$$Re = \frac{\rho V D}{\mu} \quad (18)$$

where ρ is the fluid density, V is the fluid velocity, D is the pipe diameter, and μ is the fluid viscosity. In most physiological blood flow, Reynolds numbers are moderate and far below the threshold of transitioning from laminar to turbulent flow (i.e., 2300)[75]. However, at sites of stenosis, the blood flow velocity is inversely proportional to the square of the vessel diameter, which results in a higher flow velocity, a higher Reynolds number, and thus a higher likelihood of generating turbulent flow. Downstream from the stenosis, the blood flow velocity remains high, and the vessel diameter becomes larger when entering this region, yielding an even larger Reynolds number and often turbulent flow.

These two types of flow have different patterns in the Doppler spectra[76]. For laminar flow, most of the scatters are of high velocities in the same direction. Thus, the spectra have a high intensity zone near the maximum velocity. For turbulent flow, these particles rotate and form a wide range of Doppler angles to the ultrasound beam, and therefore cover the entire range of velocities in the spectra.

Supplementary Discussion 12: Success rate of TCD sonography

TCD is a widely accepted method for monitoring cerebral blood flow. Its effectiveness, however, is intrinsically limited by the acoustic properties of the skull[77]. TCD uses specific skull areas, known as acoustic windows, which usually possess anatomical features conducive to the satisfactory transmission of ultrasound beams. Still, significant attenuation and phase aberration of the ultrasound beam by the skull may prevent adequate detection, leading to the failure of TCD examinations. The attenuation and phase aberration are largely influenced by the skull's structure, which reflects, absorbs, and scatters the ultrasound beam (Supplementary Figs. 2 and 3, and Supplementary Discussions 2 and 3).

Demographic factors such as sex, age, race/ethnicity, and the presence of specific diseases drastically impact skull structure. Women, for instance, tend to have thicker temporal bones than men[78], with a decrease in bone density, especially after menopause[79]. Aging increases the risk of examination failure due to temporal bone thickening and reduced bone density[77,80]. Additionally, racial and ethnic differences also affect temporal bone thickness and density[81,82]. Conditions like osteoporosis significantly influence the texture of the temporal bone's middle layer, further complicating the variations in skull structure[80,81].

Two primary strategies have been explored to overcome these limitations: increasing the acoustic intensity and using contrast agents. Increasing acoustic intensity will improve the success rate[83,84] but must remain within safe limits recommended by the Food and Drug Administration Track 1 (i.e., 720 mW/cm^2) to avoid tissue damage[33]. Contrast agents, while enhancing ultrasound

reflection, raise concerns about patient safety and procedural complexity and are not commonly used in TCD examinations[85].

To elucidate the impact of these on success rate of TCD examination, we have summarized relevant exemplary large group studies (Extended Data Table 2). This table reveals a marked association between these variables and the success rate, highlighting the critical role of participant characteristics in determining TCD outcomes. However, it's important to acknowledge the limitations of such data. First, while extensive, these studies are subject to potential selection bias due to their reliance on data from a single research site/institution. Secondly, the term 'success rate' lacks a standardized definition across studies, leading to inconsistencies in data interpretation. Some research defines it as the ability to acquire optimal signals through the temporal window[80,85], while others consider both optimal and suboptimal (e.g., only part of the arterial segments cannot be accessed) signal acquisitions as a measure of success[86,87]. Additionally, distinctions are made between acquiring signals from one[84] or both[88] sides of the temporal window. To enhance comparability with most of the existing studies, the definition of 'success rate' in the current study is the ability to acquire either optimal or suboptimal signals through both sides of temporal window. The definition of success rate for each study has been specified as clearly as possible (Extended Data Table 2). Thirdly, there's a notable lack of information on variables like intensity level, race/ethnicity, and medical history, leading to gaps in the dataset. These gaps lead to an incomplete understanding of how different factors affect success rates, potentially skewing comparisons. Despite these limitations, the table still offers a reliable overview of TCD examination outcomes. Notably, our findings are in line with existing research, underscoring the technical robustness and reliability of our device.

Note that in this study, we also compare the success rate of soft ultrasound devices (72.2%), which utilize two-dimensional matrix arrays, to the conventional rigid TCD probes (77.8%), which are based on phased array or single-element probes. While the soft probes promise enhanced accessibility and ease of use, they exhibit a slightly lower success rate because of the smaller element size of matrix arrays[89,90]. The smaller size results in higher impedance, leading to a larger impedance mismatch between the transducer element and the circuit. This mismatch, in turn, causes energy loss during the transmission and reception of ultrasound signals.

Supplementary Discussion 13: Pulsatility index and resistive index

The pulsatility index (PI) and the resistance index (RI) describe the spectral profile. They can be calculated as:

$$PI = \frac{(V_s - V_d)}{V_m} \quad (19)$$

$$RI = \frac{(V_s - V_d)}{V_s} \quad (20)$$

where V_s, V_d, and V_m are the peak systolic, end diastolic, and mean flow velocities, respectively. The PI and the RI are closely related to each other and are mainly affected by the differences in systolic and diastolic flow velocities. The end diastolic velocity is the residual flow velocity during diastole, reflecting the impedance of the vascular bed[91]. Under normal circumstances, the PI and the RI of intracranial vessels are smaller than those of extracranially and peripherally due to the low resistance at the distal end of the intracranial vessels. When the resistance of vascular bed increases, the spectra show low diastolic blood flow, and the PI and RI increase, and vice versa. Abnormalities in these parameters may have pathological significance clinically[92]. Spectra of low

PI and *RI* can be seen in distal arteries with arteriovenous malformations, stenosis, and occlusion[91,93]. A significantly increased *PI* and *RI* has been observed in cases of increased intracranial pressure and proximal arteries from severe aortic stenosis or occlusion sites[91,93].

Supplementary Discussion 14: Cerebral blood flow regulation mechanisms

Cerebral blood flow regulation means the cerebral vasculature can maintain blood flow equilibrium despite changes in other physiological parameters (e.g., arterial pressure, intracranial pressure, and blood viscosity). The net driving force of generating flow in cerebral arteries is cerebral perfusion pressure, defined as the difference between arterial blood pressure and venous blood pressure. The total cerebral blood flow is controlled by cerebral perfusion pressure and cerebrovascular resistance. With the ever-changing cerebral perfusion pressure, the brain adjusts cerebrovascular resistance, therefore maintaining stable blood perfusion.

Various processes, including myogenic, metabolic, endothelial, and neurogenic responses, have been considered as potential mechanisms of cerebral regulation[49,94]. The myogenic hypothesis states that the cerebrovascular resistance change is provoked by variations in vascular smooth muscle tone under different transmural pressures[95]. Specifically, transmural pressure changes initiate membrane depolarization, opens mechanically sensitive ion channels, generates an influx of calcium ions, and triggers smooth muscle cells, resulting in cerebrovascular resistance changes. The metabolic mechanism states that the regulation occurs in smaller vessels that are subject to variations in the local environment[96]. The concentration of cerebral CO_2 can accumulate and cause vasodilation when hypotension results in tissue hypoperfusion and anaerobic respiration. The opposite physiology appears in hyperperfusion with consequent decreases in CO_2 concentration and vasoconstriction. Additionally, the endothelium can be provoked by different blood flow patterns to secrete vasodilators and vasoconstrictors[97]. Finally, neurogenic mediation of cerebral vasoreactivity can alternate the vessel diameter[98]. The variation in blood flow in response to neuronal activation is reflected in blood oxygen level-dependent signals, which has been investigated in cognition, memory, visual processing, and exercise. For example, the contraction of skeletal muscle evokes the autonomic regulation. The hypothalamus that controls the autonomic nervous system activates the sympathetic nervous system and restrains the parasympathetic nervous system, leading to an increase in the blood supply to the brain. The conformal ultrasound patch with high spatiotemporal resolutions can potentially be a powerful tool for observing these acute blood flow changes and studying relevant cerebral regulation mechanisms.

Supplementary Discussion 15: Intracranial B waves

The glymphatic system plays a major role in removing waste products and metabolic debris from the central nervous system during sleep[99]. To do this, the glymphatic system controls the cerebrospinal fluid flows through the brain parenchyma for material exchange. While the cerebrospinal fluid interacts with the interstitial fluid surrounding the brain cells, it transports those waste or toxic substances from the interstitial fluid to the lymphatic vessels. This process involves the slow oscillations of the cerebrospinal fluid. Because the brain and spinal cord are surrounded by the cerebrospinal fluid, such slow oscillations can be directly reflected by the intracranial pressure change and similar fluctuant patterns in cerebral blood flow. These patterns have a typical frequency range from 0.3 to 4 cycles per min and are called intracranial B waves[100,101].

The dysfunction in cerebrospinal fluid generation or draining commonly accompanies aging, Alzheimer's disease, and sleep disturbances[102,103]. Therefore, continuous monitoring of intracranial B waves in sleep studies can be used to evaluate the functionality of the brain in neurodegeneration and other neurological pathologies, and also evaluate the effectiveness of strategies to enhance cerebral blood flow and cerebrospinal fluid oscillations to improve glymphatic flow.

Supplementary Discussion 16: Application of the conformal ultrasound patch

TCD sonography represents a safe, relatively inexpensive, and reliable method to measure cerebral hemodynamics[48]. It is the standard of care in the clinical setting and is a powerful tool for neurovascular studies[104]. Compared to conventional rigid and bulky TCD probes, the conformal ultrasound patch represents a platform technology for volumetric vascular network reconstruction and continuous long-term monitoring of blood flow spectra. This technology not only qualifies for use cases of existing TCD probes but also enables new applications that are challenging or impossible for existing counterparts.

The conformal ultrasound patches eliminate the user-dependency as typically seen in the conventional TCD probes. For placing the device, the ultrasound patch only needs to be attached to transcranial windows, and the ultrasound waves can be electrically focused on the target arterial segment based on 3D phased array control. In contrast, the conventional TCD probe requires a well-trained operator to manually tilt the probe to find the blood flow signal from the target arterial segment.

For blood flow monitoring, conventional TCD probes must be manually fixed by the operator or a rigid headset. Minor handshaking or head movement may result in misalignment between the ultrasound beam and target artery, leading to signal loss. In contrast, the ultrasound patch, designed to comfortably attach to the scalp, offers a much-increased tolerance for motion artifacts.

For the identification of target arterial segments, conventional TCD probes typically use a single transducer or a linear array of transducers, which can only image part of the intricate 3D network of cerebral arteries (Extended Data Fig. 1). Different operators may acquire signals from different segments of the 3D network, strongly affecting repeatability and reproducibility of the result. The volumetric imaging approach addresses this problem by depicting the 3D network to guide target segment identification, thus substantially reducing operator dependency.

The conformal ultrasound patches may allow earlier and continued evaluation of cerebral perfusion in emergency rescue settings[105]. The most immediate application is for long-term monitoring of patients following subarachnoid hemorrhage[106,107]. In well-resourced hospital neuro intensive care units, TCD is used routinely in these cases to serially assess for vasospasm after injury and provide information as to response to interventions[108]. However, this type of measurement is resource-intensive, operator-dependent, and although continuous during the measurement period, is essentially point-in-time as far as detecting changes in patient condition. There is thus a large unmet need for low-profile devices with capability for long-term (e.g., several days) continuous measurement of cerebral blood flow.

Other immediate applications for conformal ultrasound patches include emboli detection, particularly during the peri-operative period and in procedures involving the aortic arch as well as

those with large embolic burden (e.g., orthopedics). Emboli eminating from elsewhere in the vasculature can travel to the brain, blocking cerebral arteries and blood flow, with deleterious consequences if not properly monitored or diagnosed[109,110]. Emboli to the brain can be initially asymptomatic but may develop into transient ischemic attack or stroke. Having the ability to monitor emboli continuously in high-risk patients for long periods of time can provide insights into the mechanisms of embologenesis and propagation as well as provide timely feedback for therapeutic interventions. Specifically, the occurrence of emboli during and after mechanical thrombectomy may suggest inadequate anticoagulation and/or antiplatelet therapy, and may lead to pharmacological adjustment[111]. The presence of emboli has also been shown to predict new embolic events[112]. During and after carotid stenting or carotid endarterectomy procedures, continuous and long-term monitoring of emboli can provide timely feedback to the interventionalist/surgeon and allow anti-platelet therapy optimization and/or re-exploration[113,114]. Importantly, blood flow monitoring of the operative site may reveal the integrity of vascular perfusion in the event of temporary surgical carotid occlusion. Similarly, coiling of cerebral aneurysms can be associated with the occurrence of emboli.

Furthermore, continuous long-term post-procedure cerebral blood flow monitoring based on the conformal ultrasound patch is suggested for patients experiencing early neurological deterioration after thrombectomy or stenting. This monitoring provides important insights into conditions like hyperperfusion syndrome, intracranial steal syndrome, post-stent re-occlusion, and facilitates the comparison of collaterals over time on both sides. The prolonged monitoring helps assess the status of leptomeningeal collaterals in patients with large vessel occlusions who have undergone successful thrombectomy. Another group of patients that could significantly benefit from long-term TCD monitoring are those with recurrent transient ischemic attacks of unknown origin. In these cases, this protocol can effectively assist in ruling out transient emboli signals versus vasospasm in proximal vessels. Due to technical challenges and dependence on operator skill with the current TCD device, long-term blood flow monitoring in these mentioned conditions is not feasible. Consequently, critical information regarding brain hemodynamics during the acute phase of stroke patients is being missed.

The technology is also particularly useful for the diagnosis of transient ischemic attacks and embolic strokes from atrial fibrillation[115]. Continuous monitoring over an extended period would allow for confirmation of emboli as the cause of transient ischemic attack symptoms, distinguishing between embolic and hemodynamic causes of the symptomatology. Continuous and long-term monitoring cerebral blood flow may also reduce the impact of resulting strokes, during atrial fibrillation ablation procedures[116] and orthopedic procedures[117] where fat or cement emboli are a well-recognized complication. Finally, combining the blood flow and arterial wall pulsation measurements of the ICA can be used to estimate intracranial pressure non-invasively[118,119]. The potentially benefited areas include but are not limited to carotid and coronary artery stenosis[120], cerebral hemorrhage[121], antithrombotic treatment[122], and complications associated with surgical procedures[123,124], invasive examinations[125], sequelae of orthopedic[126], and obstetric procedures[127,128].

Beyond its conformability for continuous long-term monitoring, this technology is capable of imaging cerebral blood volume at high spatiotemporal resolutions, which is not available by existing TCD sonography.

The brain poses a significantly greater challenge for ultrasound sensing due to the skull-induced strong acoustic attenuation and aberration (Supplementary Figs. 2 and 3, and Supplementary Discussions 2 and 3). Additionally, volumetric imaging requires the simultaneous individual control of each transducer element in the two-dimensional matrix array, which significantly degrades the signal quality. Traditional beamforming focuses the ultrasound waves on a particular point in space. In volumetric imaging, this needs to be done in 3D, requiring the simultaneous control of a significantly larger number of transducer elements. Ensuring that the ultrasound waves from each element are correctly phased to maintain a tightly focused beam to scan in 3D can be technically challenging, and errors in this process can lead to degradation in image quality. In addition to software challenges, the simultaneous operation of closely packed transducers can lead to crosstalk between elements, which may degrade the clarity of the ultrasound image by introducing noise and artifacts.

To address these issues, we have applied the ultrafast ultrasound imaging technique[69,70,129] to further enhance blood flow signals acquired within the brain. Unlike traditional beamforming by using focused beams, this cutting-edge technique employs a sequence of diverging beams. This approach allows simultaneous data capture from the entire field of view with a single transmission, resulting in significantly faster image reconstruction and enhanced computational efficiency. Additionally, the high-speed nature of this technique allows imaging at extraordinarily high frame rates, often reaching over a thousand frames per second. Integrating the singular value decomposition[71] with such high-speed imaging enables the capture of rapid physiological phenomena such as blood flow dynamics in the cerebral vasculature even through the skull. Moreover, we have implemented a multilayered stretchable electrode with a well-designed copper mesh electromagnetic shielding layer. This design allows for the individual activation of each element in the two-dimensional matrix array while increasing the signal-to-noise ratio by an average of 5 dB.

The volumetric imaging allows accurate identification of the monitoring target, eliminating the user-dependency as typically seen in the one- or two-dimensional imaging of conventional TCD probes. The volumetric information can potentially help diagnose vascular diseases such as stenosis, ischemia, and subarachnoid hemorrhage, which correlate with almost imperceptible variations in vessel morphology and blood perfusion amplitude[27,105,130]. Even though they are not generated in real-time, this information could still be valuable under continuous monitoring and provides alerts of the emergencies.

Besides disease diagnosis, the conformal ultrasound patch can be used for functional TCD studies. The long-term conformability enables the device to be used for chronic awake studies on brain reactions. Taking advantages of the matrix array with the ultrafast Doppler imaging technique, the device allows monitoring cerebral functions in major arteries accurately in 3D, which is valuable for understanding how the brain works on a large scale under normal or pathological conditions[89,131]. Combining the structural and dynamic information collected from the patch will generate a profound understanding of the interaction between the circulatory system and the brain. For example, this technology can be used to study functional connectivity when different stimuli are applied[132-134]. This technology can also be combined with real-time ultrasound localization microscopy to achieve much higher spatiotemporal resolutions for capillary blood flow mapping,

which would be of great value for characterizing local neurovascular coupling[135-137].

Supplementary Discussion 17: Application feasibility and safety of microbubbles

Microbubbles, commonly known as contrast agents, have a limited duration within the human body. In our research, we demonstrated two distinct imaging modes: the 3D power Doppler imaging mode and the spectral Doppler mode. The former effectively captures the anatomical details of the circle of Willis, while the latter allows for the monitoring of blood flow in individual blood vessels. The 3D power Doppler mode was performed only once initially, specifically to localize the target blood vessels. This procedure requires less than 10 min, which is shorter than the typical duration of commonly used microbubbles[36]. Because we utilized diverging waves in this mode and the operational time is brief, microbubbles hold promise as a potential enhancer for 3D vascular network imaging in the power Doppler mode. On the other hand, the spectral Doppler mode employs a focused ultrasound beam to examine a specific region within the blood vessel, ensuring a high signal-to-noise ratio for continuous functional monitoring tests, without the need for microbubbles.

These air gas microbubbles have a typical diameter <10 μm, enclosed in lipid, protein, or polymer shells[37]. These small-sized microbubbles can easily pass through capillaries without impeding blood flow. Moreover, the microbubble shells are treated to prevent coalescence, often by incorporating Polyethylene glycol[38]. As a result, under normal conditions, microbubbles remain stable without aggregating. However, microbubble coalescence may occur under specific insonation conditions, which depend on various factors such as frequency, pressure level, duty cycle, and microbubble concentration[39,40]. Quantitative studies have been conducted to investigate these parameters in the context of imaging and therapy purposes[40]. For example, low-frequency (about 1 MHz), low-amplitude (about 100 kPa) therapeutic ultrasound requires a high duty cycle (>1%) and a high microbubble concentration level (about 2×10^8 bubbles/mL) to generate microbubble coalescences[40]. Conversely, high-frequency (around 5 MHz), wide amplitude range (100 to 1,000 kPa) imaging ultrasound does not result in coalescence even at very high duty cycles (about 10%)[40]. Most importantly, coalescence did not occur at any parameters when the microbubble concentration level is 2×10^6 bubbles/mL[40], approximating the concentration in human blood circulation[41]. In general, contrast-enhanced imaging mode, which utilizes higher frequency, lower duty cycle, and lower pressure, is less likely to generate coalescence compared to therapeutic ultrasound. In this study, although the frequency for transcranial ultrasound imaging is typically set at 2 MHz, there is room to control other parameters, such as pressure level and duty cycle within suitable ranges to decrease the possibility of coalescence. Properly using low-concentration microbubble solutions could be an effective approach to prevent coalescence.

Supplementary Discussion 18: Generation of harmonic components by microbubbles

The incident ultrasound waves can drive nonlinear vibrations of microbubbles[138,139]. Microbubbles consist of gas encapsulated by a shell. If the incident wave is a sine wave and microbubbles vibrate linearly, the backscattered ultrasound wave will also be sine wave with the same frequency. The positive pressure corresponds to microbubble compression, while negative pressure corresponds to microbubble expansion. However, microbubbles are easy to expand, but not easy to compress. As a result, the backscattered waves will have a negative sine wave shape but modified positive wave shape. Therefore, the backscattered waves will be distorted, similar to but different from sine waves.

For the sine wave, it only has the frequency (i.e., the fundamental frequency) equal to the frequency of the incident wave. For the distorted backscattered wave, it still has the same vibration period as the sine wave, which is the fundamental frequency. On the other hand, the distorted wave contains harmonic frequencies if a Fourier transform is applied to the distorted wave.

Supplementary Discussion 19: Fully integrated wearable ultrasound system

In the current design, the Verasonics system is still necessary to control the ultrasound patch and collect the data. Transcranial volumetric imaging requires a relatively high-power supply to make sure the transmitted ultrasound waves can successfully penetrate through the transcranial windows into the deep brain and be received for further data processing. Additionally, the volumetric ultrafast power Doppler imaging and long-term spectral Doppler monitoring can generate a large dataset (e.g., 1 to 5 GB), which requires a powerful system for fast data transfer and processing. Therefore, current device still faces challenges in terms of miniaturization of a control system and reduction of power consumption before it can be considered a truly wearable ultrasound system.

Recently, important strides have been made in this direction by developing a fully integrated wearable system[40]. This system includes a stretchable ultrasound patch for ultrasound transmission and receiving, a flexible printed circuit board for data acquisition and wireless communication, a lithium-polymer battery for power supply, and a machine learning algorithm for data analysis. The system is capable of monitoring various physiological signals during motion, marking it a significant advancement in wearable ultrasound monitoring. However, one of the primary challenges faced by this fully integrated system is the incapability of volumetric imaging. The current design is optimized for M-mode imaging, which provides one-dimensional, depth-resolved images. While this is effective for monitoring certain physiological signals, it does not provide a comprehensive, 3D views of the tissues under observation. This limitation is primarily due to the complexities involved in implementing beamforming in a wearable ultrasound system. Traditional volumetric beamforming requires substantial computational resources and power, which are challenging to accommodate in a compact device.

Our ongoing efforts are focusing on more advanced beamforming methods. For example, the local micro-beamformer technique can simplify the overall system's computational complexity by conducting initial local beamforming on individual subarrays[140]. This approach breaks down the beamforming process into smaller stages, reducing power consumption and making the technology more suitable for wearable applications. Similarly, multiplexing reduces hardware complexity by reducing the system size, decreasing the number of connections between the transducer and processor, consequently lowering power consumption through reduced bandwidth requirements for data transmission[141,142]. The synthetic aperture method[143] minimizes hardware demands by simulating a larger, virtual array with a smaller physical array, improving imaging resolution and reducing power consumption due to fewer signal processing steps.

There are challenges associated with these techniques. The local micro-beamformer, for instance, can result in suboptimal image quality because of the approximations made during the localized beamforming process. The multiplexing techniques can lead to crosstalk or interference between channels, potentially degrading image quality as signals from different channels overlap or interfere with each other. Additionally, synthetic aperture methods, despite their improvements in

imaging resolution and hardware requirements, require complex algorithms and substantial computational power to form the final image, which tends to be slower than conventional beamforming techniques as they necessitate multiple transmit and receive events. This can result in lower frame rates, which may affect real-time imaging applications.

Therefore, while these advanced methods present promising solutions to the challenges of low power consumption and increased computational power to achieve volumetric imaging by using wearable ultrasound devices, we are working on addressing their drawbacks to optimize and balance these trade-offs, ultimately enabling wearable ultrasound technology to reach its full potential across a wide range of medical applications.

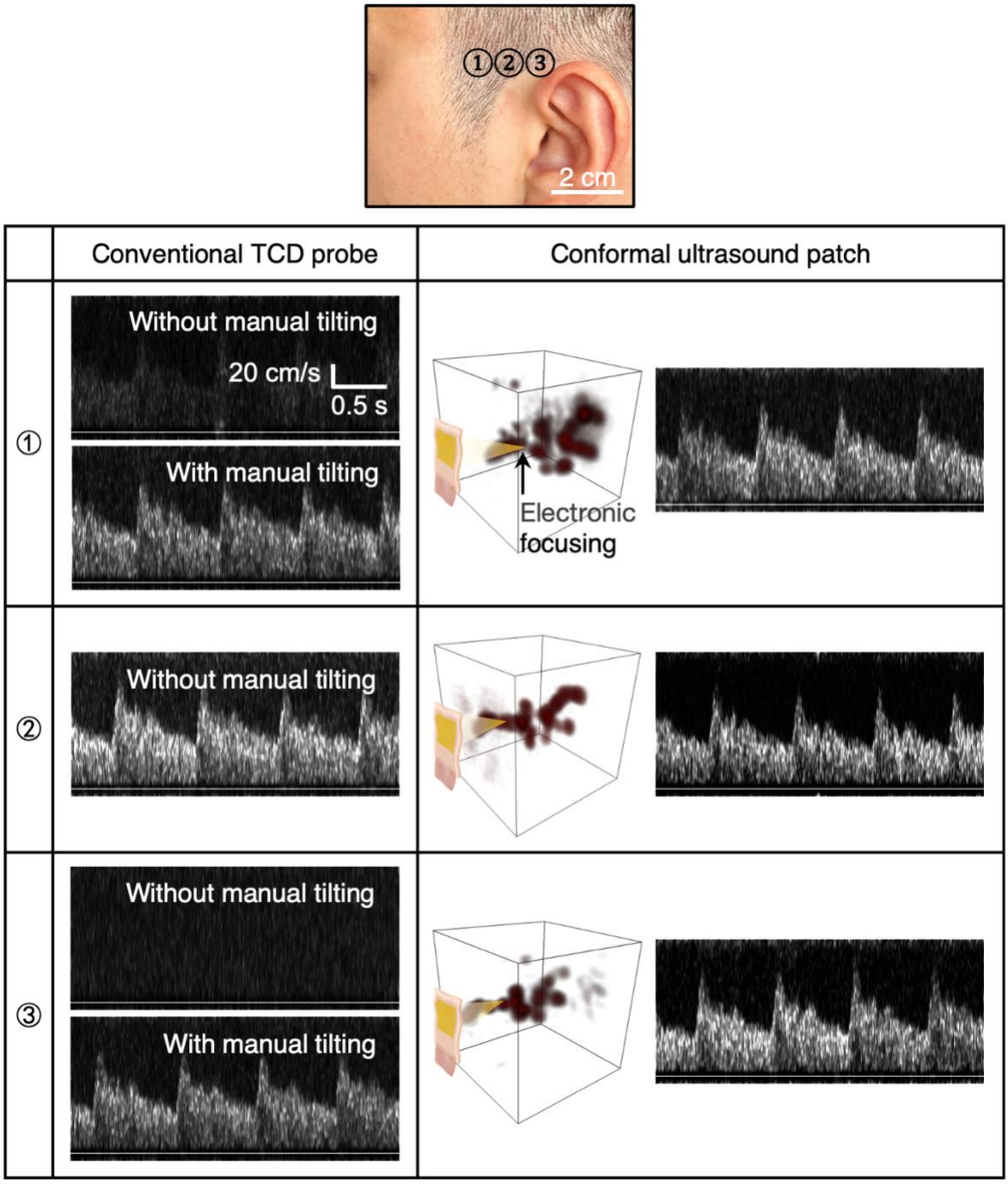

Supplementary Fig. 1 | Blood flow spectra with different device placement positions. Both the conventional TCD probe and the conformal ultrasound patch were tested at three distinct positions for recording blood flow spectra. While at position 2, the conventional TCD probe happened to yield a high-quality spectrum without the need for manual tilting, other positions necessitated manual tilting of the probe to find the optimal angle for quality spectra. This routine adjustment process is not only time consuming but also heavily dependent on the operator's experience and training. Conversely, the ultrasound patch leverages its volumetric imaging capability to electronically focus the ultrasound beams directly onto the target, streamlining the acquisition process. The blood flow spectra share the same scale bars.

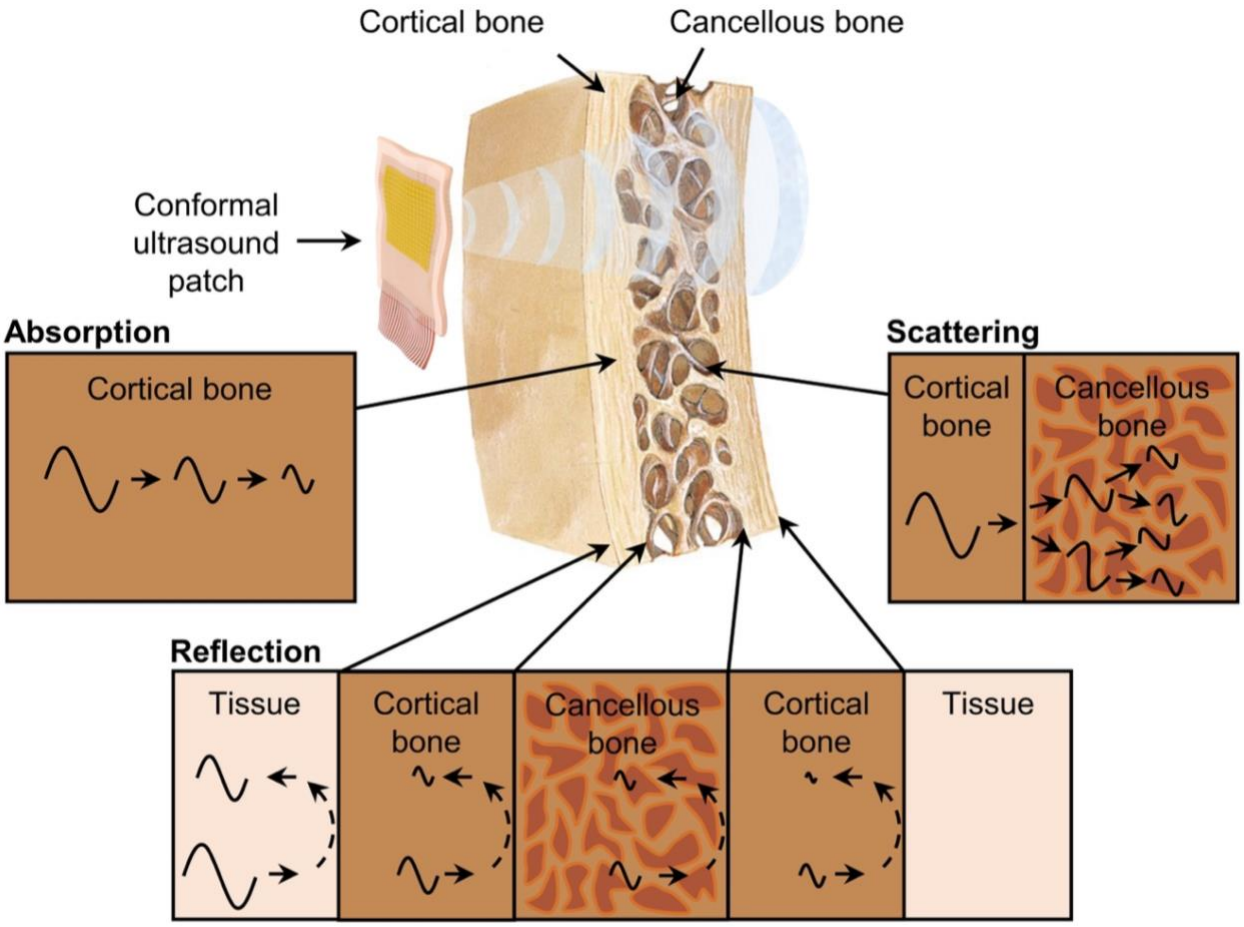

Supplementary Fig. 2 | Acoustic attenuation by the skull. The skull causes three different types of attenuation, including reflection, absorption, and scattering. The scattering mainly happens in the cancellous bone. The reflection mainly happens at the interfaces between media with different acoustic impedances.

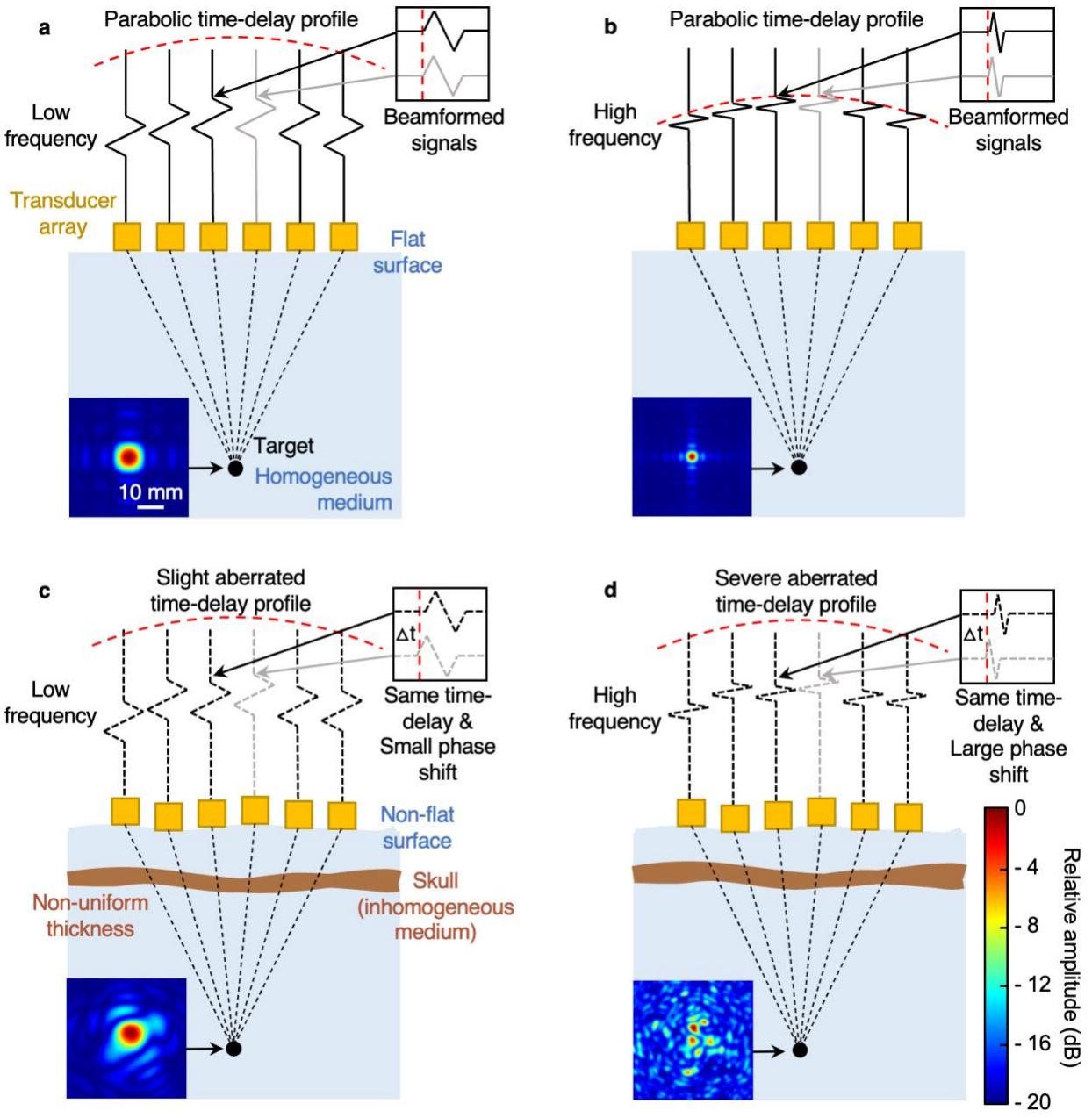

Supplementary Fig. 3 | Phase aberration of the skull with backscattered signals at different ultrasound frequencies. a-b, The transducer array can achieve reliable beamforming with well-defined parabolic time-delay profiles while the target is within a homogeneous medium and the surface is flat at both low and high ultrasound frequencies. Black lines and gray lines of the insets at the upper right corners are the beam formed received signals. The insets at the lower left corners show simulated beamforming results by the transducer array at low and high ultrasound frequencies, respectively. **c-d**, The inhomogeneous composition, non-uniform thickness of the skull, and non-flat surface induce aberration to beamforming, but with a less degree at low frequency than at high frequency. Black dashed lines and gray dashed lines of the insets at the upper right corners are the received signals with the same time-delay (△t) but different phase shifts. The insets at the lower left corners show the simulated beamforming results by the transducer array at low and high ultrasound frequencies, respectively. We adopted an open-source Matlab toolbox

k-Wave to simulate the influence of skull on the sound beams. This toolbox can set the sound speed and density of medium of every voxel in the space. The soft tissue background was also set as homogeneous with a sound speed of 1,540 m/s and a density of 1,000 kg/m^3. A layer of bone with non-uniform thickness was created by setting the sound speed and density as 3,000 m/s and 2,300 kg/m^3, respectively[42]. We could also set the emitted waveform of each element to create a focused beam. All insets share the same scale bars.

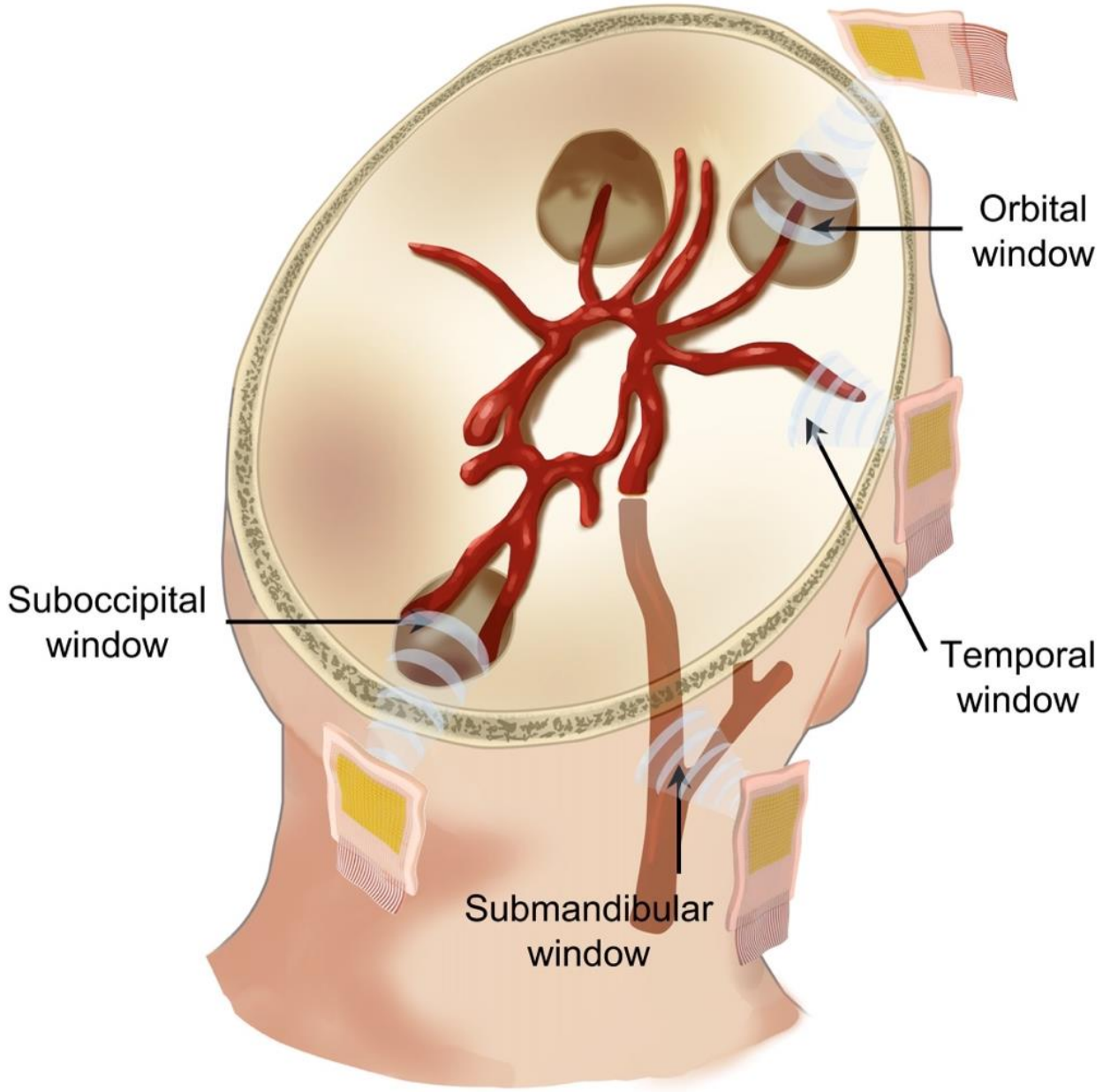

Supplementary Fig. 4 | The common transcranial windows with relatively low acoustic attenuation and phase aberration for TCD sonography. Through the orbital window, the ultrasound beam is directed toward the optic canal and does not pass through the skull. When using the temporal window, the ultrasound beam only needs to transmit through the thin temporal bone. The submandibular window locates at the neck. Through this window, the ultrasound beam can target at the internal carotid artery without transmitting through the skull. The participant can bow the head forward to open up a gap between the cranium and the atlas. The ultrasound beam is directed toward this gap when the patch is attached to the suboccipital window.

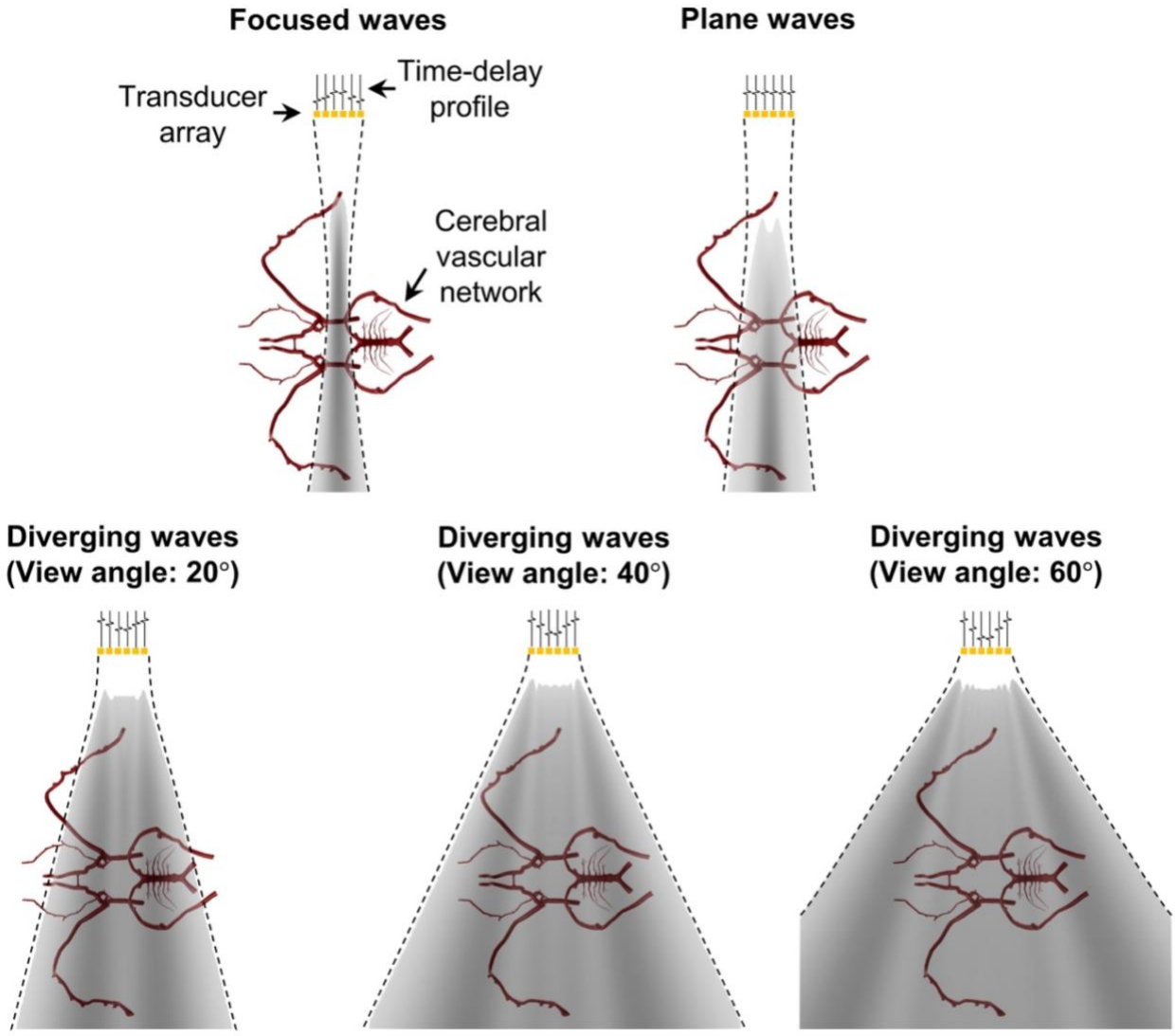

Supplementary Fig. 5 | Schematic ultrasound fields of different beamforming strategies. By using different time-delay profiles, the transducer array can transmit focused, plane, and diverging waves. The focused waves have an ultrasound beam at a local region of the cerebral vascular network. The plane waves have a wider ultrasound field than the focused waves, but their ultrasound field is still rather limited. The diverging waves have ultrasound fields tunable with the view angle. In this work, a view angle of 40° can appropriately insonate the entire cerebral vessels. A view angle of 20° is too narrow whereas a view angle of 60° is redundant, spreading the ultrasound energy to unneeded areas.

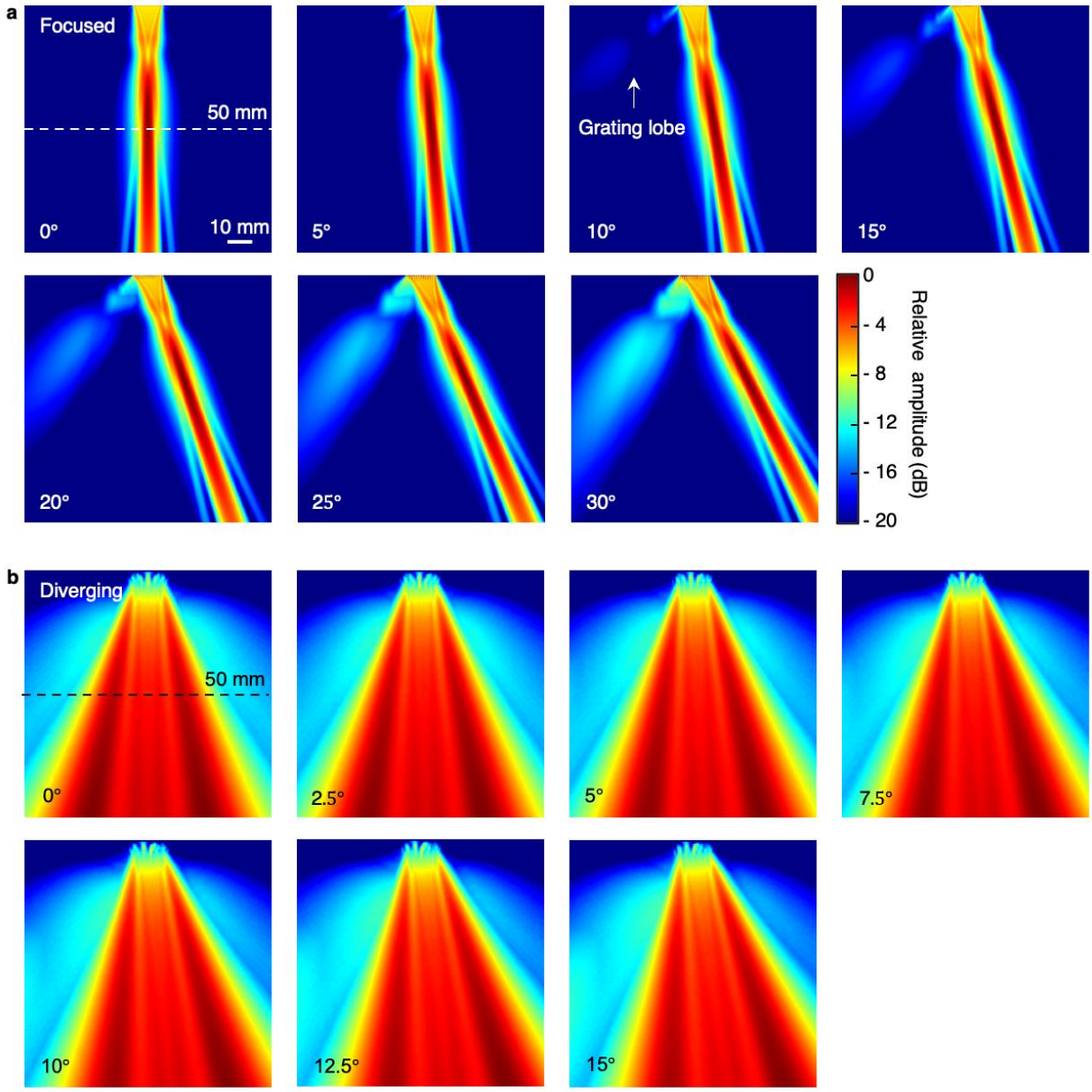

Supplementary Fig. 6 | Simulated ultrasound beam steering. a, Ultrasound waves focus at 50 mm depth with a beam tilting angle of 0°, 5°, 10°, 15°, 20°, 25°, and 30°, respectively. The grating lobe is growing and becomes more obvious when the beam tilting angle is larger**. b**, Diverging ultrasound waves with a beam tilting angle of 0°, 2.5°, 5°, 7.5°, 10°, 12.5°, and 15°, respectively. The simulation was performed using an open-source Matlab toolbox Field II. The medium was set as uniform with a sound speed of 1,540 m/s and a density of 1,000 kg/m^3. The central frequency was 2 MHz, the same as the real probe. We applied the built-in function, "xdc_2d_array", to create the transducer array. The transmitted waveform from each transducer element could be set to be a focused beam or a diverged beam. All simulation results share the same scale bars.

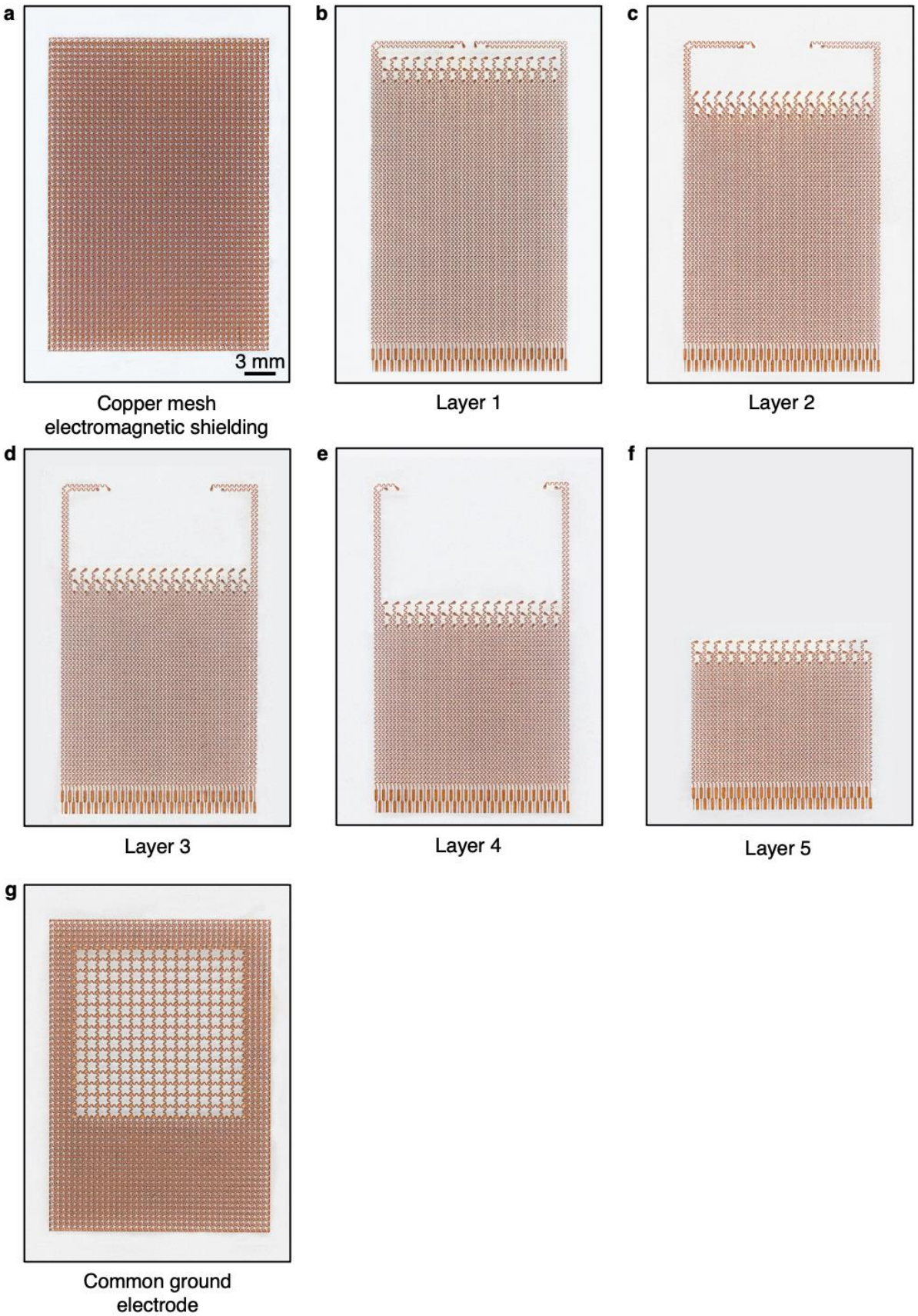
a
3 mm
Copper mesh
electromagnetic shielding
b
Layer 1
c
Layer 2
d
Layer 3
e
Layer 4
f
Layer 5
g
Common ground
electrode

1187

Supplementary Fig. 7 | Design and fabrication of the stretchable electrode. Optical images of **a**, the copper mesh electromagnetic shielding layer, **b-f**, the five-layer stretchable electrode, and **g**, the common ground electrode. This design permits individual activation of each element in the two-dimensional matrix array while keeping the overall device within a small footprint (20 mm × 28 mm). The optical images share the same scale bar.

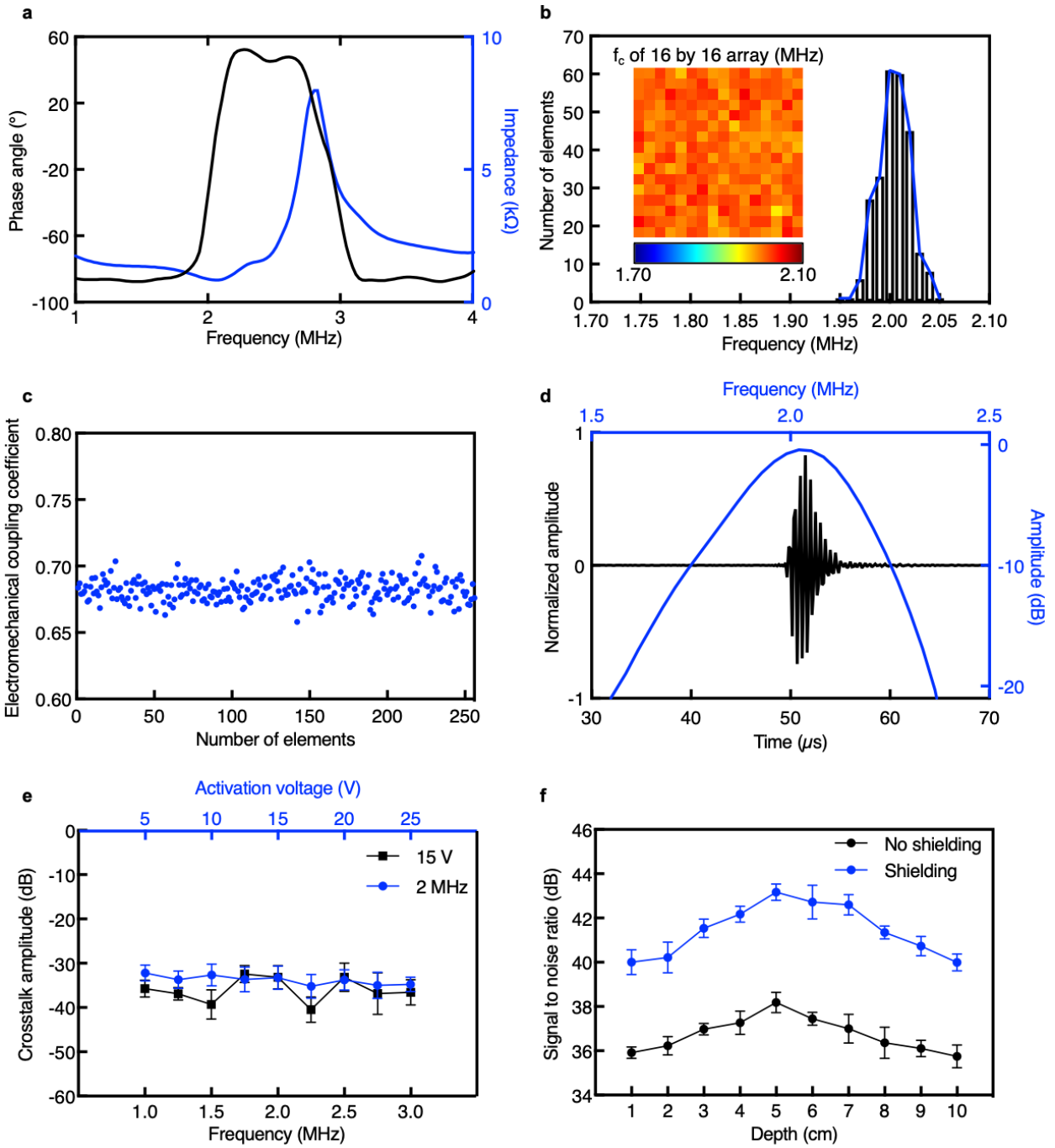

Supplementary Fig. 8 | Characterizations of the conformal ultrasound patch. a, Phase angle and electrical impedance spectra from 1 MHz to 4 MHz. The center frequency is 2.01 MHz with a phase angle of 11.96°. **b**, The center frequency distribution among the 256 elements of the patch. Inset is its distribution map of the 16 by 16 array. **c**, The electromechanical coupling coefficient of the 256 elements. **d**, Pulse-echo response and corresponding frequency spectra of a typical element. The measured -6 dB bandwidth is 17.41%. Doppler signal processing requires extracting Doppler shift in the frequency domain. The small bandwidth provides sharper peaks in the frequency domain. Thus, the frequency difference between transmitted and received signals can be calculated more easily. **e**, Crosstalk between adjacent transducer elements for both frequency sweep and

voltage sweep. **f**, Signal-to-noise ratios with and without the copper mesh electromagnetic shielding layer. Solid circles represent the mean, and error bars are the standard deviation of the mean (n = 12 for **e**; n = 5 for **f**; independent samples).

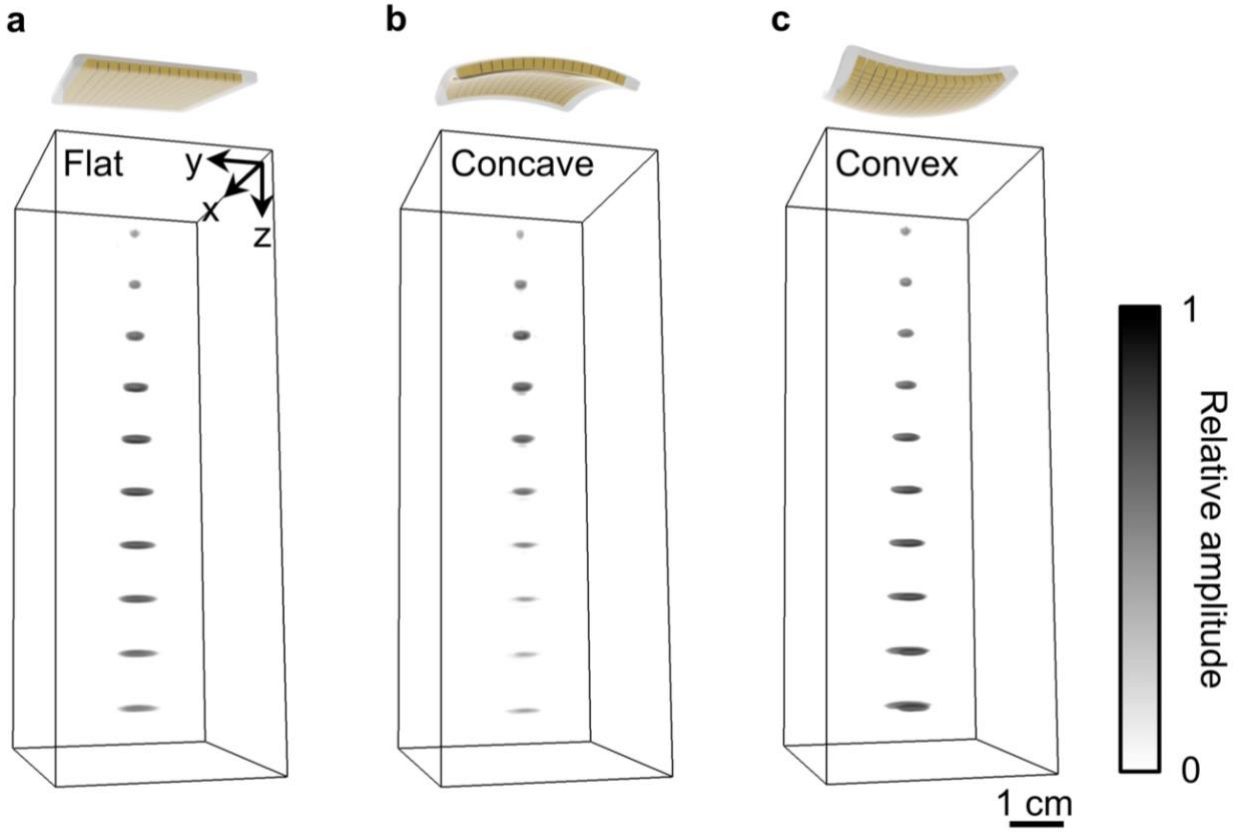

Supplementary Fig. 9 | Simulated 3D images of point phantoms for the patch under different configurations. When the conformal ultrasound patch is attached to the skin, it may cause deformation of the transducer array, which could subsequently result in phase aberration, particularly at high frequencies. However, the ultrasound patch operates at a relatively low frequency of 2 MHz in this study, which has a much higher tolerance for phase aberration. We performed a simulation to illustrate that the skin curvature has a very low influence on the beamforming for low-frequency arrays using the Matlab Field II toolbox. We placed a 2 MHz soft array on **a**, flat, **b**, concave, and **c**, convex surfaces. The radii of curvature for the concave and convex are both 5 cm. A coherent compounding imaging strategy with 5 insonification angles and an interval of 5° is used. The simulation phantom comprises 10 points extending from a depth of 1 cm, with each subsequent point deeper by 1 cm. Simulation results show that for the concave array, the shallow points have higher amplitudes, while the deep points have lower amplitudes, than the flat array. This is because the concave array emits a more focused sound beam compared to the flat array, resulting in higher sound field intensity at a shallower depth. For the convex array, the sound beam is more diverged than the flat array. Therefore, the signal amplitudes are a bit lower than the flat array, and the reconstructed points are a bit larger. Albeit these differences in intensity and resolution, they are still within an acceptable range. The images share the same scale bars.

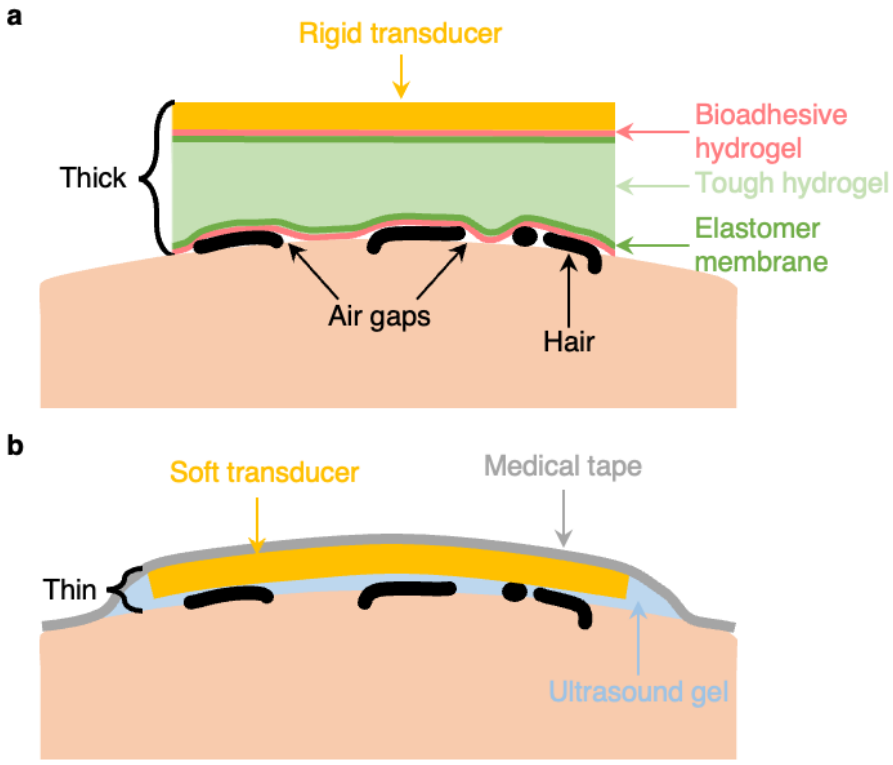

Supplementary Fig. 10 | Schematics show the difference between the rigid probe with bioadhesive hydrogel and the conformal ultrasound patch. a, The rigid BAUS probe[28] uses hydrogel as an acoustic couplant, while the top and bottom surfaces have bioadhesive layers to bond the probe, the couplant, and the skin. Because the elastomer membrane encapsulated hydrogel is solid, there are air gaps between the couplant and the skin, particularly at the temporal window where there is a lot of hair. This will result in compromised bonding and suboptimal acoustic coupling, which is a significant drawback for TCD applications. **b**, In contrast, the conformal ultrasound patch employs liquid ultrasound gel as the acoustic couplant, and we use medical tape (e.g., Tegaderm) to secure the soft probe to the skin. This method ensures stable acoustic coupling. While the temporal window is typically used for TCD detection due to its easy access to numerous blood vessels, a comprehensive assessment requires measuring cerebral blood flow from other windows, such as the orbital and submandibular windows. A hydrogel-based probe may find it difficult to conform to these curved surfaces, limiting its efficacy in TCD imaging. However, the conformal patch, with its superior adaptability, shows great promise in providing a more comprehensive approach to different windows for TCD imaging. Moreover, the BAUS probe necessitates a thick layer of hydrogel as couplant for areas of the skin with a large curvature. The thick form factor could interfere with natural skin movements in wearable applications. The conformal patch, by virtue of being soft and thin, does not present such restrictions. Last but not least, it's crucial to acknowledge that a rigid ultrasound sensor, due to its comparatively simpler circuitry, only offers two-dimensional imaging, which restricts its capability to adequately capture the intricacies of the 3D arterial network in the brain. As different operators may acquire signals from diverse segments of this complex network, the repeatability and reproducibility of results could be compromised. In contrast, the conformal patch facilitates 3D imaging, delivering a more precise and comprehensive visualization of the cerebral vessel network, thereby significantly enhancing the reliability and consistency of the measurements.

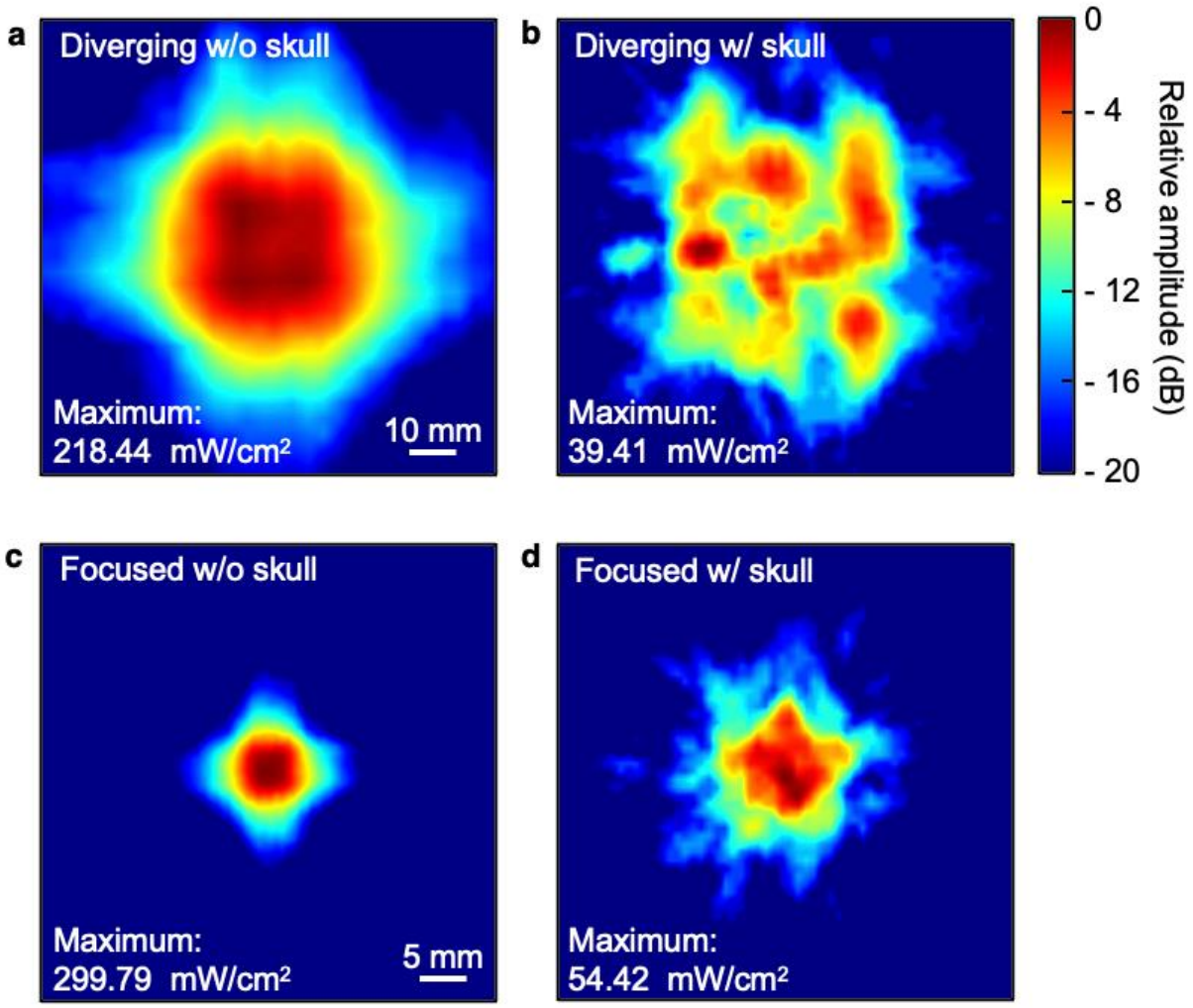

Supplementary Fig. 11 | Ultrasound field mapping. These are the experimentally measured sound fields for different situations. Verasonics system drove the transducer array to emit a focused beam at a depth of 50 mm. The transmitted acoustic waves were received by a hydrophone (HNP-0400, ONDA), digitized by an oscilloscope (PicoScope 5000, Pico Technology), and then visualized by software (Soniq version 5.3.1.0, ONDA). A 3D scanning system (AIMSIII, ONDA) mapped the spatial distribution of the acoustic beam. **a-b**, The ultrasound intensity distribution of diverging waves at 50 mm depth with and without the skull, respectively. The mapping results share the same scale bars. **c-d**, The ultrasound intensity distribution of focused waves at 50 mm depth with and without the skull, respectively. The mapping results share the same scale bars.

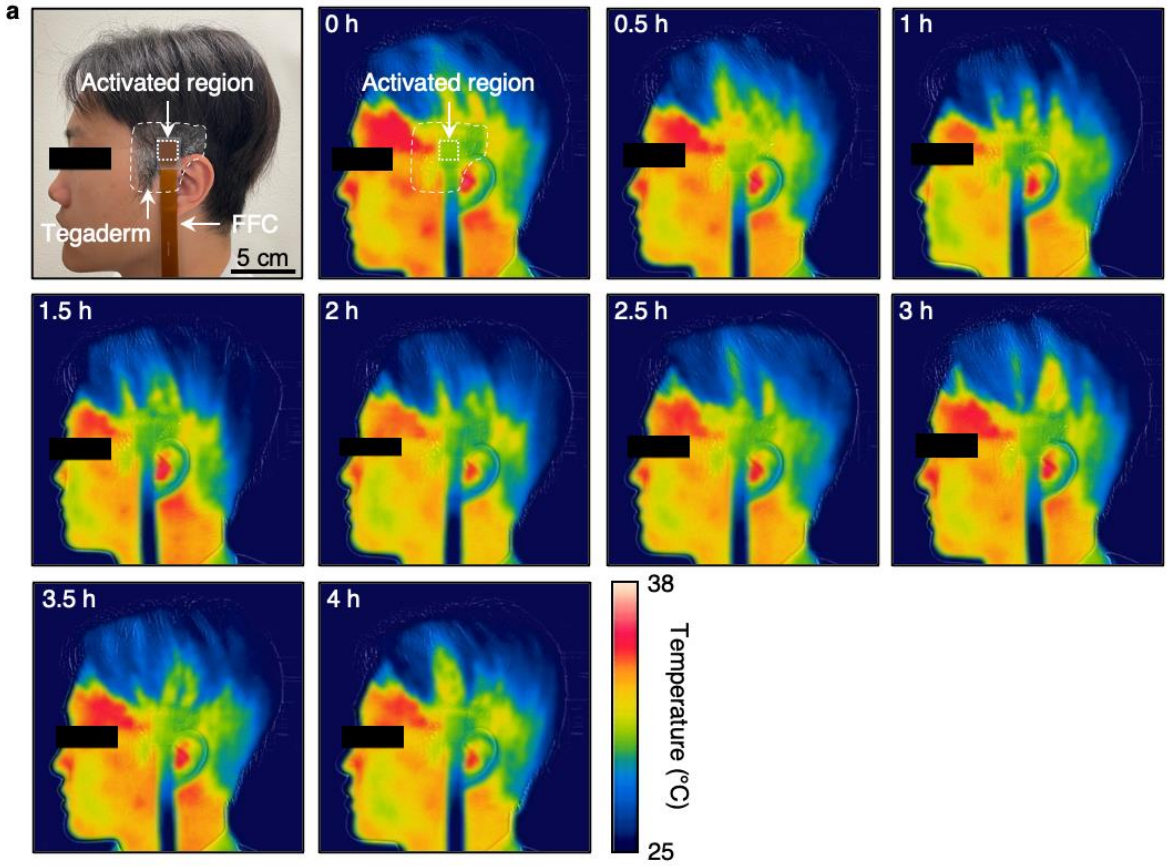

Supplementary Fig. 12 | Thermal characterization of the conformal ultrasound patch. a, Optical and thermal images during four hours of continuous activation of the conformal ultrasound patch on the temporal window. The thermal emissivity of the thermal imaging camera was set to be 0.95 to accurately measure the temperature of organic materials and the human skin. The Tegaderm boundaries are labeled by white dashed lines. All images share the same scale bars. All thermal images share the same temperature scale bar. **b**, The highest temperature of the conformal ultrasound patch during the four hours of activation. The temperature increase was <1 °C. Solid squares represent the mean, and error bars are the standard deviation of the mean (n = 3; independent samples). FFC, flat flexible cable.

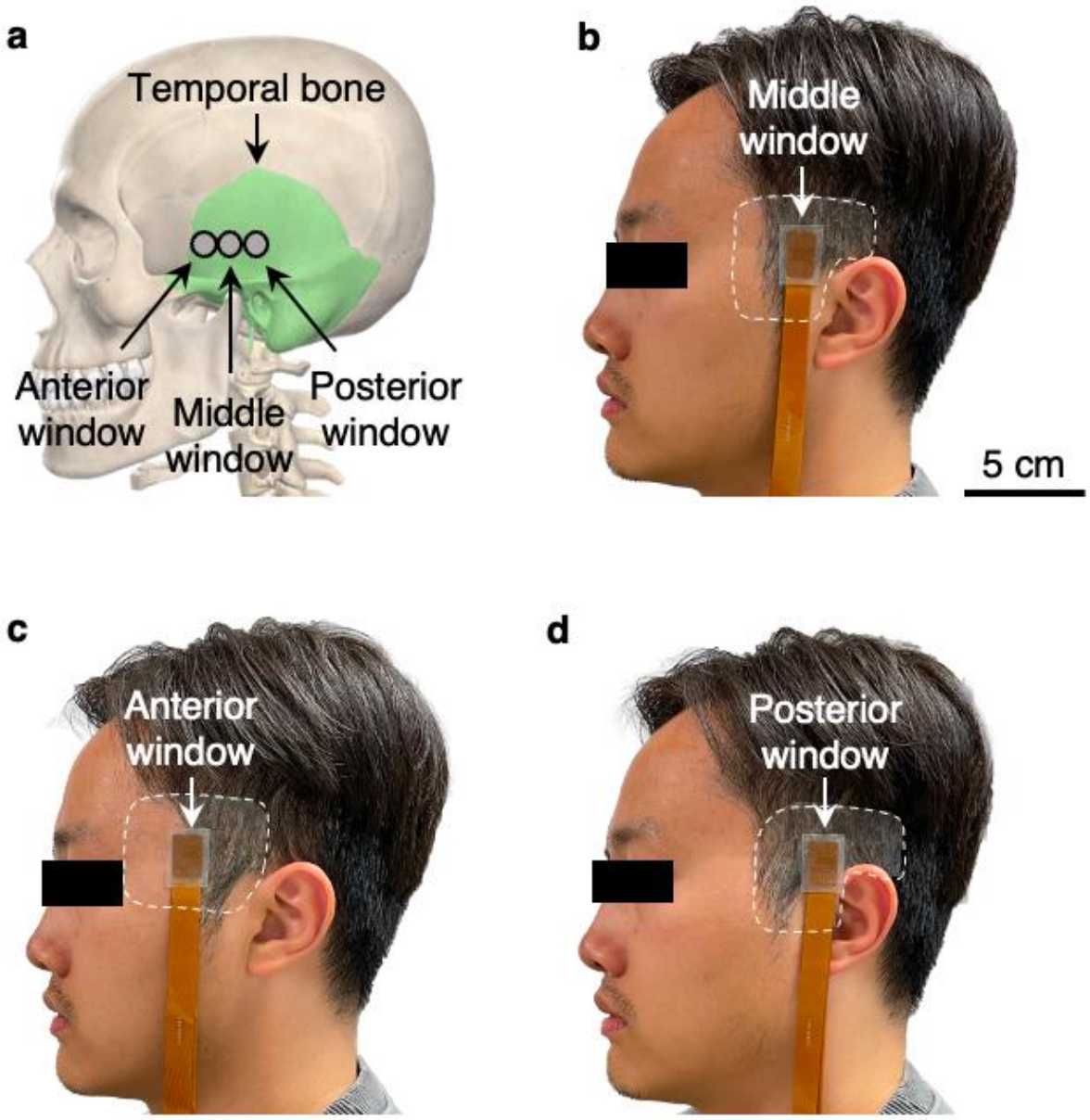

Supplementary Fig. 13 | Temporal windows. a, Three windows on the temporal bone used for TCD sonography in this work. The middle window is cephalad to the zygomatic arch and immediately anterior and slightly superior to the tragus of the ear conch. This window is usually the most promising examination site. The anterior window is located more frontally. The posterior window is immediately cephalad and slightly dorsal to the middle window. Although all three windows can be utilized, physiological differences among participants should be considered when selecting one of the temporal windows for TCD sonography. **b-d**, Optical images of the device on the middle, anterior, and posterior windows, respectively. Considering the relatively flat surface above the entire temporal bone and large curvature tolerance of low ultrasound frequencies (e.g., 2 MHz in this work), the influence of surface curvature on beamforming is negligible. Therefore, the device can be simply attached to any temporal windows without applying any phase aberration correction. The Tegaderm boundaries are labeled by white dashed lines. The optical images share the same scale bar.

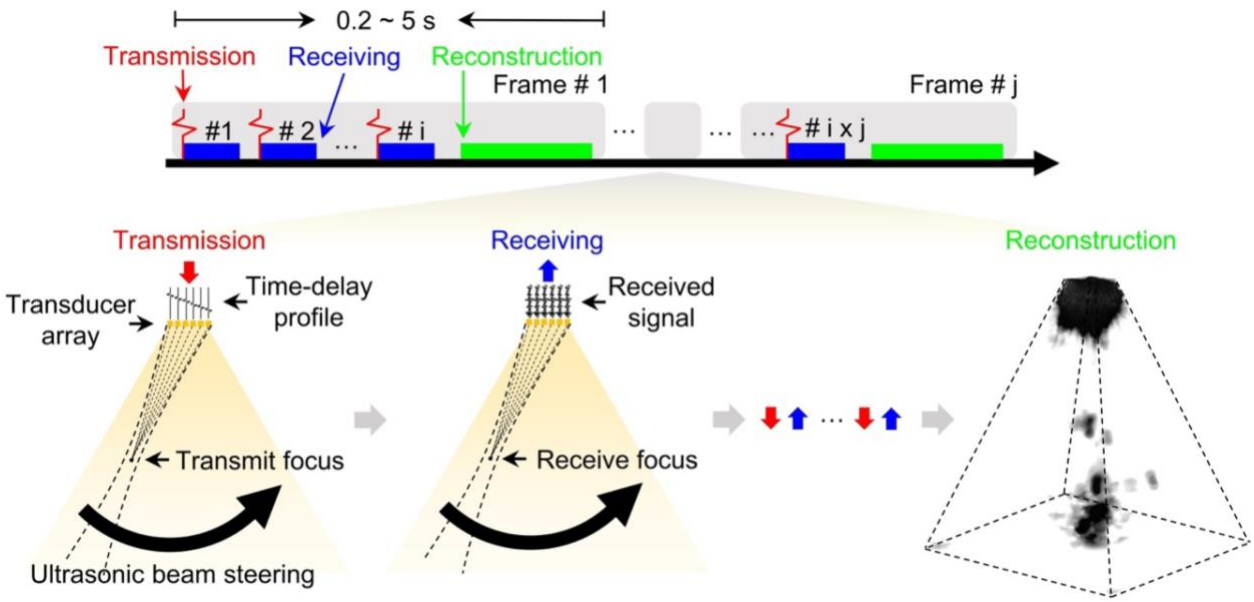

Supplementary Fig. 14 | Process of conventional ultrasound imaging. To show one frame of image, the conventional probe should transmit and receive signals multiple times by using mono-focus ultrasound beams at different positions in the field of view. After the ultrasound beam is steered to scan the entire field of view, all of the data will be used for image reconstruction. The total time to get one frame of volumetric image is 0.2 to 5 s.

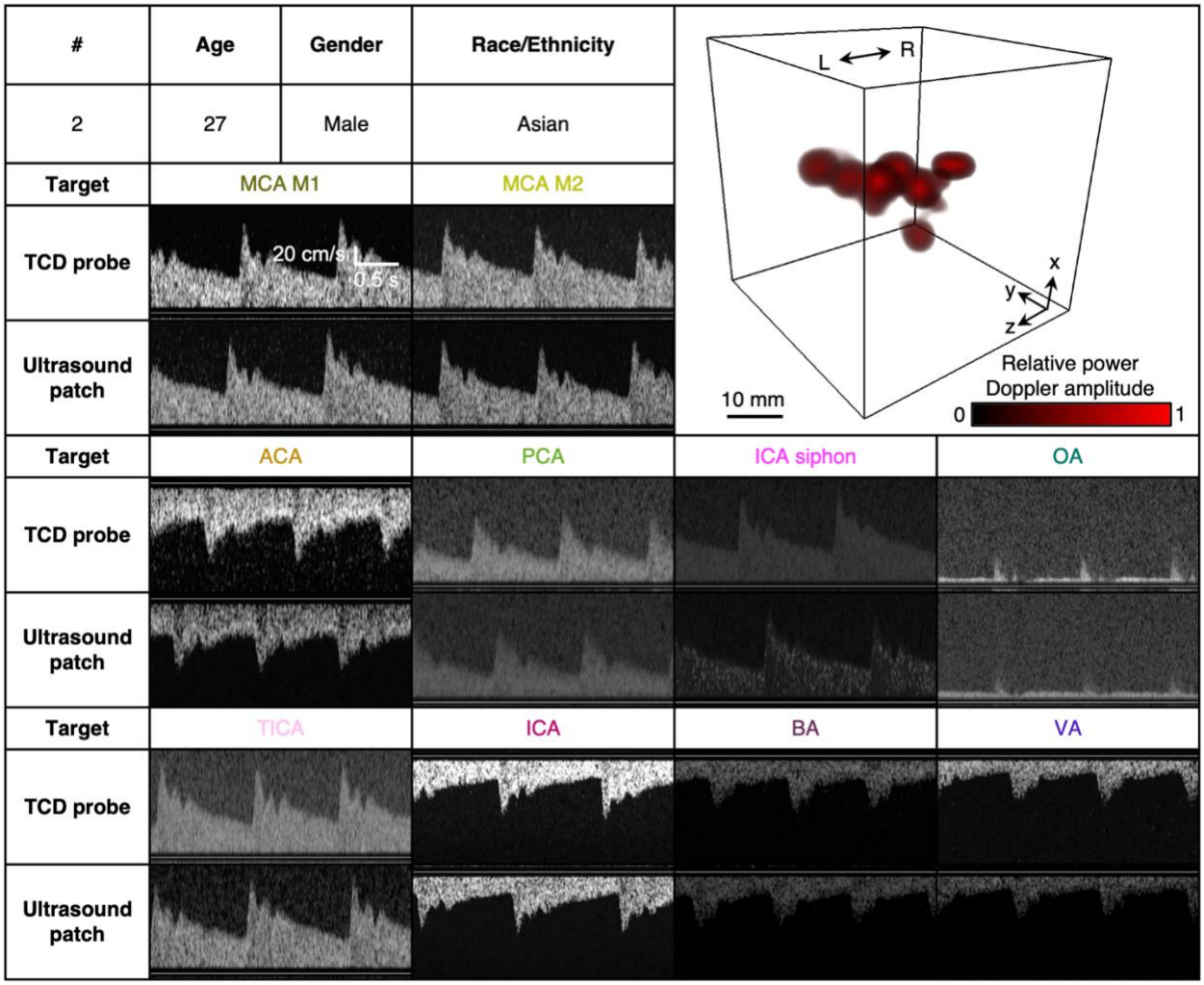

Supplementary Fig. 15 | Volumetric image and blood flow spectra from participant #2. The age, gender, and race/ethnicity that may influence the success rate of TCD sonography were provided. The volumetric image of the cerebral vasculature was collected by the conformal ultrasound patch. The blood flow spectrum of each arterial segment from both the conventional TCD probe and the conformal ultrasound patch was compared accordingly. L, left. R, right. MCA, middle cerebral artery. ACA, anterior cerebral artery. PCA, posterior cerebral artery. ICA, internal carotid artery. OA, ophthalmic artery. TICA, terminal internal carotid artery. BA, basal artery. VA, vertebral artery. All spectra share the same scale bars.

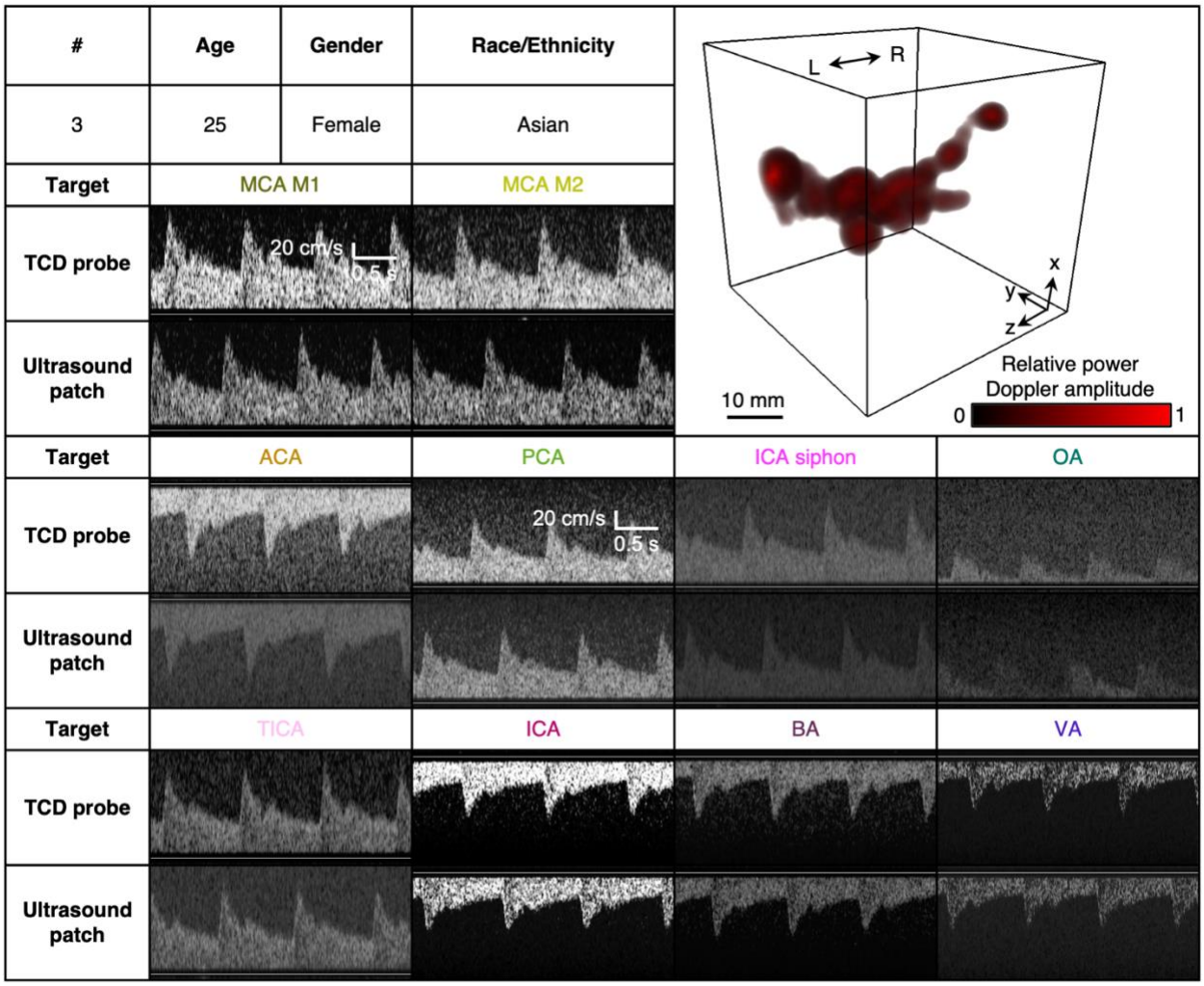

Supplementary Fig. 16 | Volumetric image and blood flow spectra from participant #3. The age, gender, and race/ethnicity that may influence the success rate of TCD sonography were provided. The volumetric image of the cerebral vasculature was collected by the conformal ultrasound patch. The blood flow spectrum of each arterial segment from both the conventional TCD probe and the conformal ultrasound patch was compared accordingly. L, left. R, right. MCA, middle cerebral artery. ACA, anterior cerebral artery. PCA, posterior cerebral artery. ICA, internal carotid artery. OA, ophthalmic artery. TICA, terminal internal carotid artery. BA, basal artery. VA, vertebral artery. The MCA M1, MCA M2, ACA, ICA siphon, and TICA spectra share the same scale bars. The PCA, OA, ICA, BA, and VA spectra share the same scale bars.

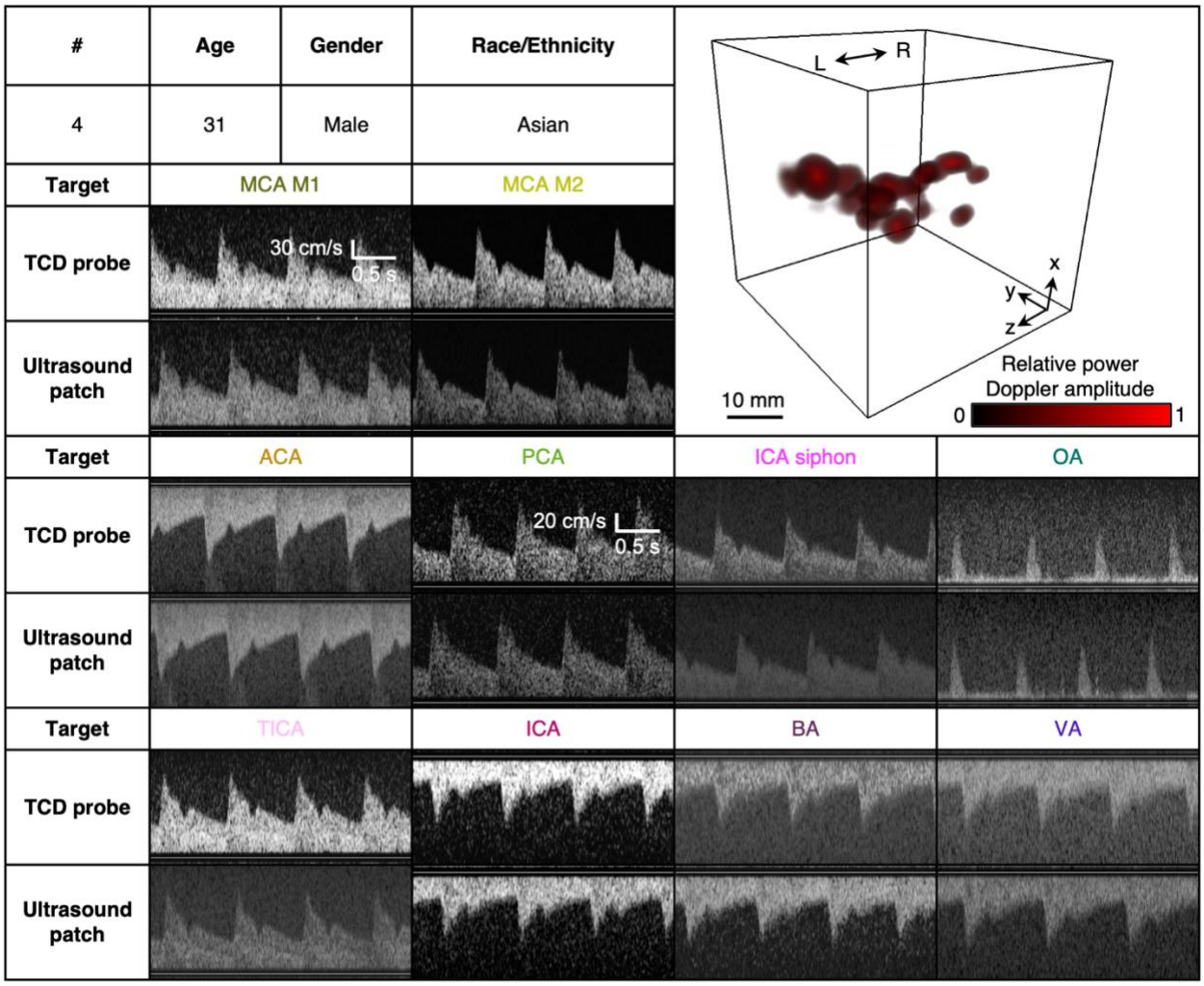

Supplementary Fig. 17 | Volumetric image and blood flow spectra from participant #4. The age, gender, and race/ethnicity that may influence the success rate of TCD sonography were provided. The volumetric image of the cerebral vasculature was collected by the conformal ultrasound patch. The blood flow spectrum of each arterial segment from both the conventional TCD probe and the conformal ultrasound patch was compared accordingly. L, left. R, right. MCA, middle cerebral artery. ACA, anterior cerebral artery. PCA, posterior cerebral artery. ICA, internal carotid artery. OA, ophthalmic artery. TICA, terminal internal carotid artery. BA, basal artery. VA, vertebral artery. The MCA M1, MCA M2, ACA, ICA siphon, and TICA spectra share the same scale bars. The PCA, OA, ICA, BA, and VA spectra share the same scale bars.

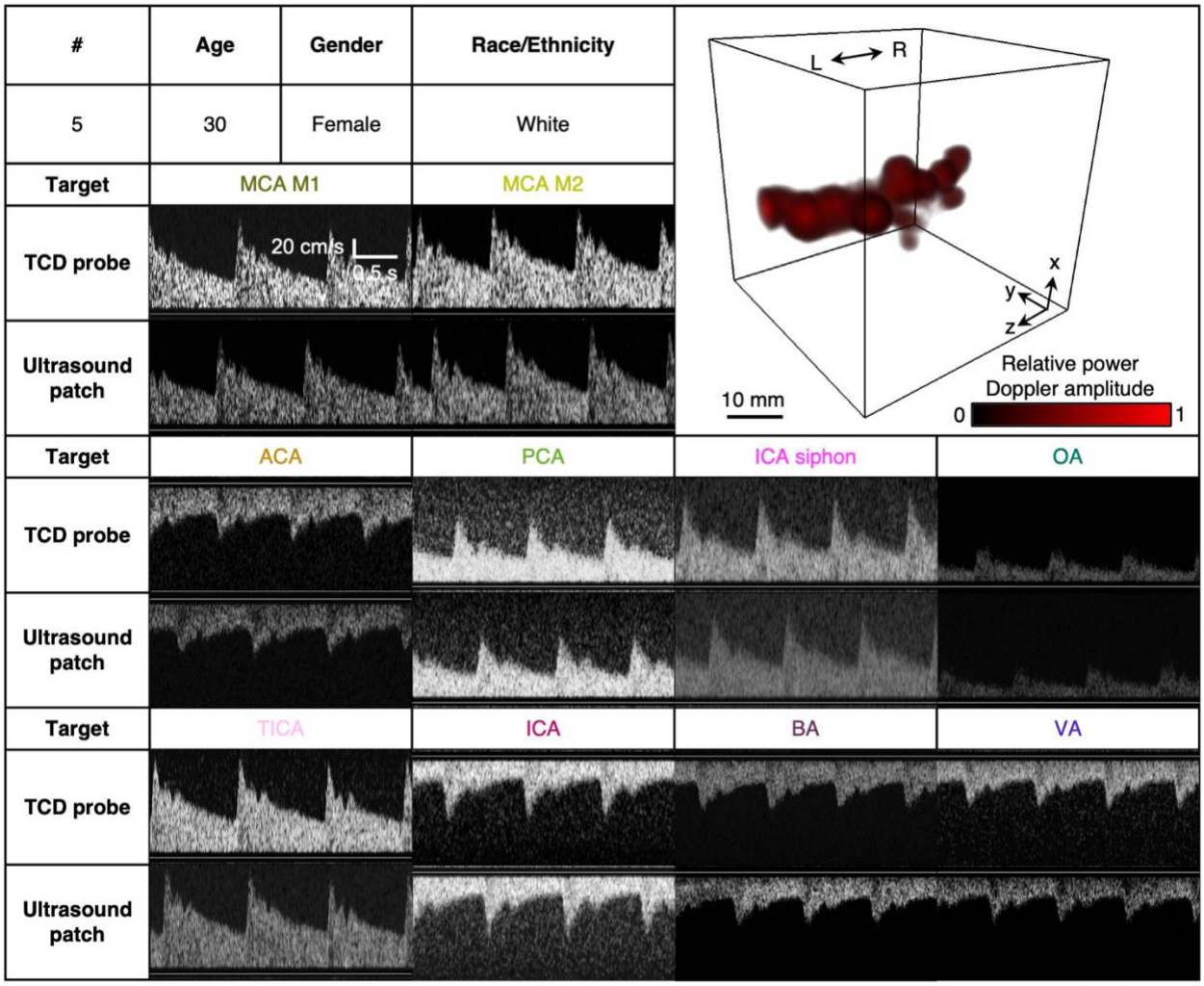

Supplementary Fig. 18 | Volumetric image and blood flow spectra from participant #5. The age, gender, and race/ethnicity that may influence the success rate of TCD sonography were provided. The volumetric image of the cerebral vasculature was collected by the conformal ultrasound patch. The blood flow spectrum of each arterial segment from both the conventional TCD probe and the conformal ultrasound patch was compared accordingly. L, left. R, right. MCA, middle cerebral artery. ACA, anterior cerebral artery. PCA, posterior cerebral artery. ICA, internal carotid artery. OA, ophthalmic artery. TICA, terminal internal carotid artery. BA, basal artery. VA, vertebral artery. All spectra share the same scale bars.

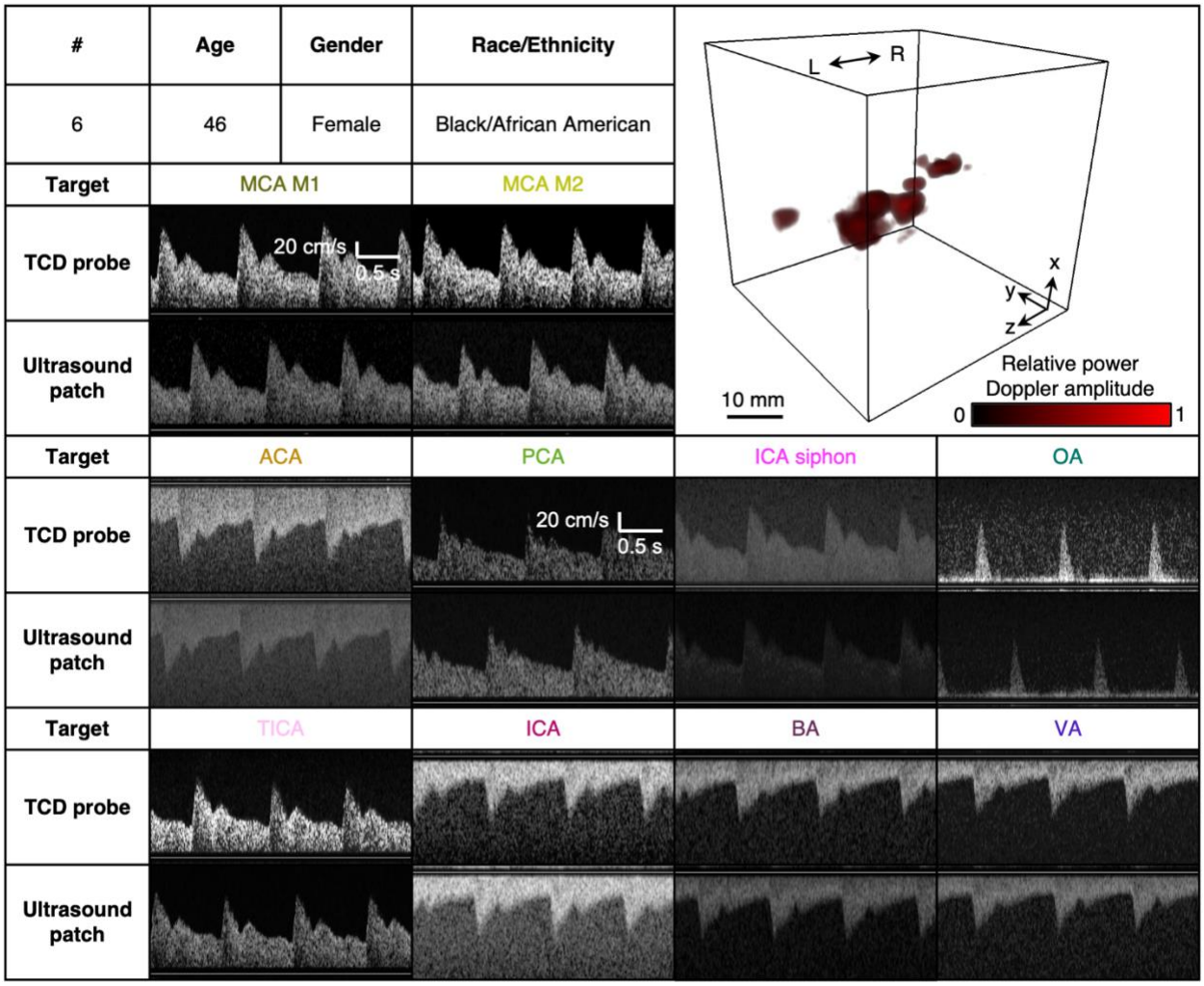

Supplementary Fig. 19 | Volumetric image and blood flow spectra from participant #6. The age, gender, and race/ethnicity that may influence the success rate of TCD sonography were provided. The volumetric image of the cerebral vasculature was collected by the conformal ultrasound patch. The blood flow spectrum of each arterial segment from both the conventional TCD probe and the conformal ultrasound patch was compared accordingly. L, left. R, right. MCA, middle cerebral artery. ACA, anterior cerebral artery. PCA, posterior cerebral artery. ICA, internal carotid artery. OA, ophthalmic artery. TICA, terminal internal carotid artery. BA, basal artery. VA, vertebral artery. The MCA M1, MCA M2, ACA, ICA siphon, and TICA spectra share the same scale bars. The PCA, OA, ICA, BA, and VA spectra share the same scale bars.

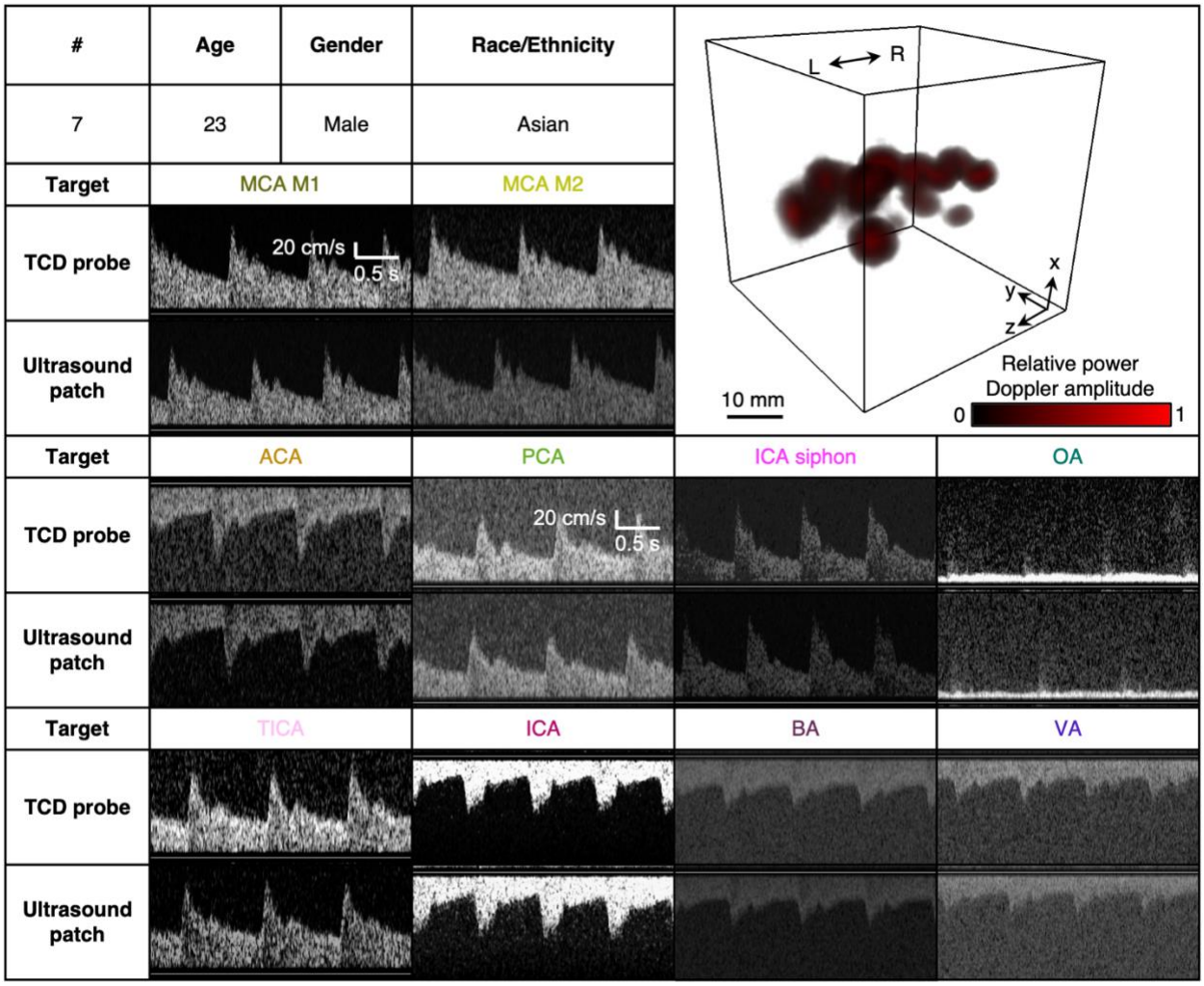

Supplementary Fig. 20 | Volumetric image and blood flow spectra from participant #7. The age, gender, and race/ethnicity that may influence the success rate of TCD sonography were provided. The volumetric image of the cerebral vasculature was collected by the conformal ultrasound patch. The blood flow spectrum of each arterial segment from both the conventional TCD probe and the conformal ultrasound patch was compared accordingly. L, left. R, right. MCA, middle cerebral artery. ACA, anterior cerebral artery. PCA, posterior cerebral artery. ICA, internal carotid artery. OA, ophthalmic artery. TICA, terminal internal carotid artery. BA, basal artery. VA, vertebral artery. The MCA M1, MCA M2, ACA, ICA siphon, and TICA spectra share the same scale bars. The PCA, OA, ICA, BA, and VA spectra share the same scale bars.

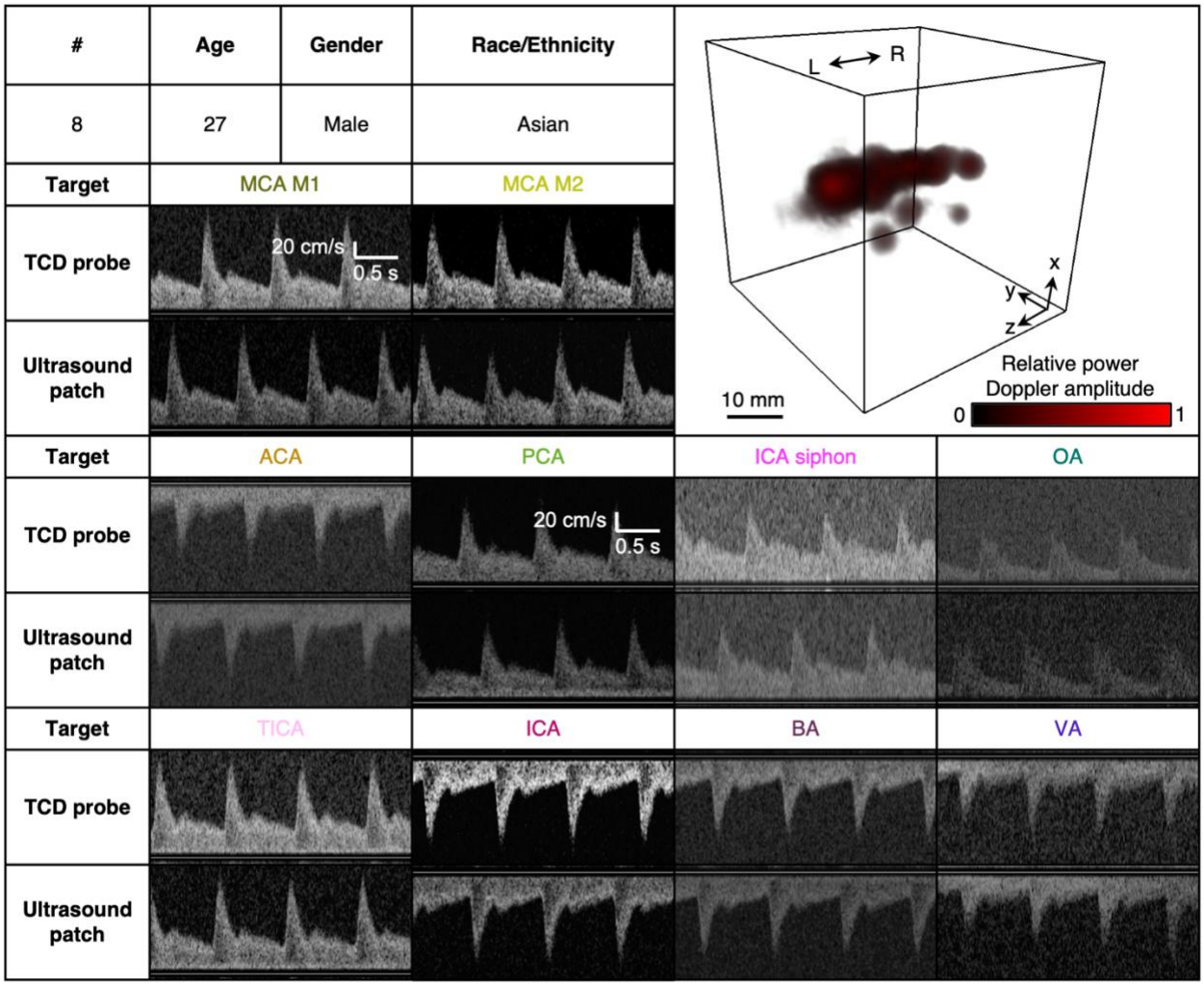

Supplementary Fig. 21 | Volumetric image and blood flow spectra from participant #8. The age, gender, and race/ethnicity that may influence the success rate of TCD sonography were provided. The volumetric image of the cerebral vasculature was collected by the conformal ultrasound patch. The blood flow spectrum of each arterial segment from both the conventional TCD probe and the conformal ultrasound patch was compared accordingly. L, left. R, right. MCA, middle cerebral artery. ACA, anterior cerebral artery. PCA, posterior cerebral artery. ICA, internal carotid artery. OA, ophthalmic artery. TICA, terminal internal carotid artery. BA, basal artery. VA, vertebral artery. The MCA M1, MCA M2, ACA, ICA siphon, and TICA spectra share the same scale bars. The PCA, OA, ICA, BA, and VA spectra share the same scale bars.

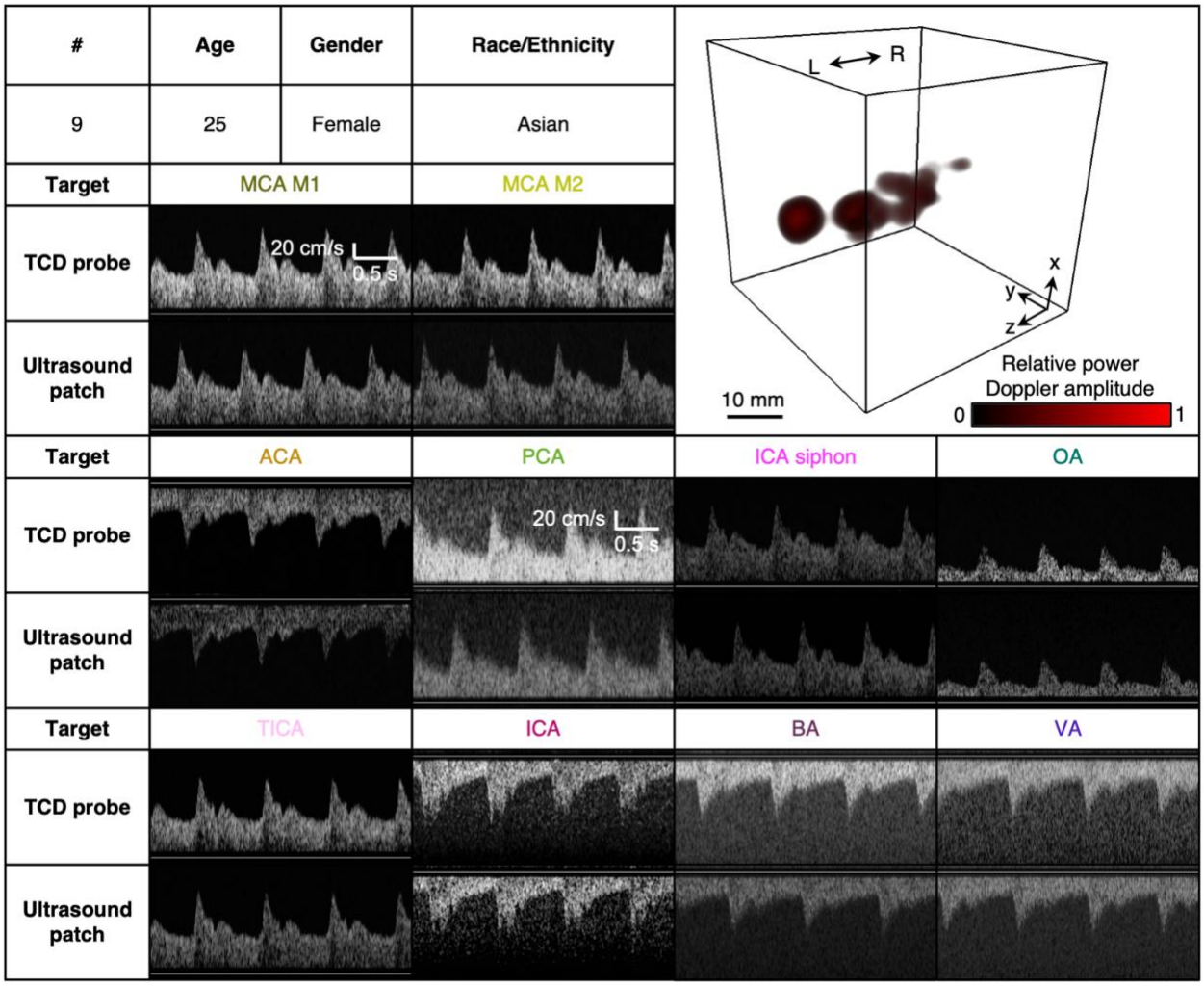

Supplementary Fig. 22 | Volumetric image and blood flow spectra from participant #9. The age, gender, and race/ethnicity that may influence the success rate of TCD sonography were provided. The volumetric image of the cerebral vasculature was collected by the conformal ultrasound patch. The blood flow spectrum of each arterial segment from both the conventional TCD probe and the conformal ultrasound patch was compared accordingly. L, left. R, right. MCA, middle cerebral artery. ACA, anterior cerebral artery. PCA, posterior cerebral artery. ICA, internal carotid artery. OA, ophthalmic artery. TICA, terminal internal carotid artery. BA, basal artery. VA, vertebral artery. The MCA M1, MCA M2, ACA, and ICA siphon spectra share the same scale bars. The PCA, OA, TICA, ICA, BA, and VA spectra share the same scale bars.

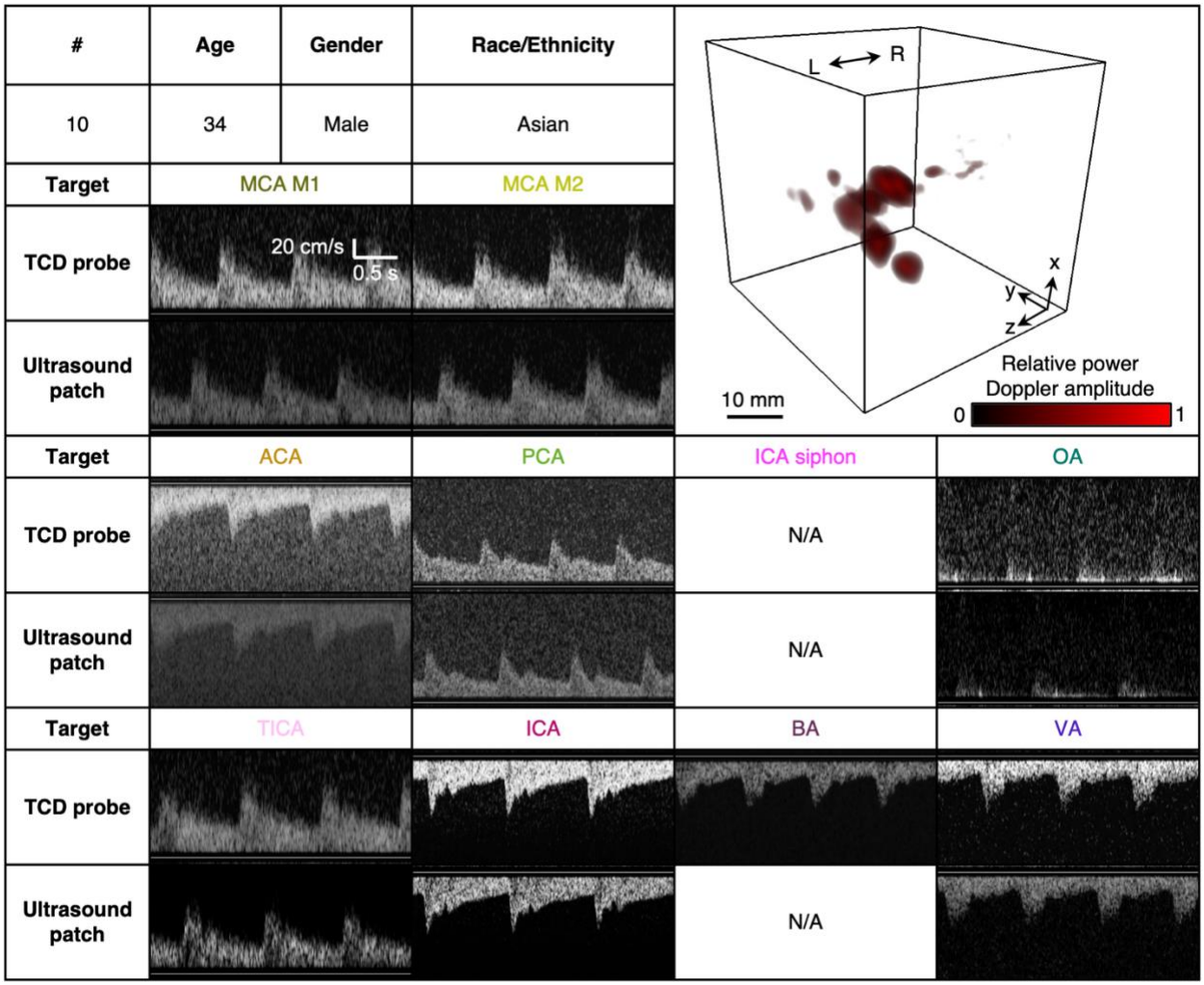

Supplementary Fig. 23 | Volumetric image and blood flow spectra from participant #10. The age, gender, and race/ethnicity that may influence the success rate of TCD sonography were provided. The volumetric image of the cerebral vasculature was collected by the conformal ultrasound patch. The blood flow spectrum of each arterial segment from both the conventional TCD probe and the conformal ultrasound patch was compared accordingly. L, left. R, right. MCA, middle cerebral artery. ACA, anterior cerebral artery. PCA, posterior cerebral artery. ICA, internal carotid artery. OA, ophthalmic artery. TICA, terminal internal carotid artery. BA, basal artery. VA, vertebral artery. All spectra share the same scale bars.

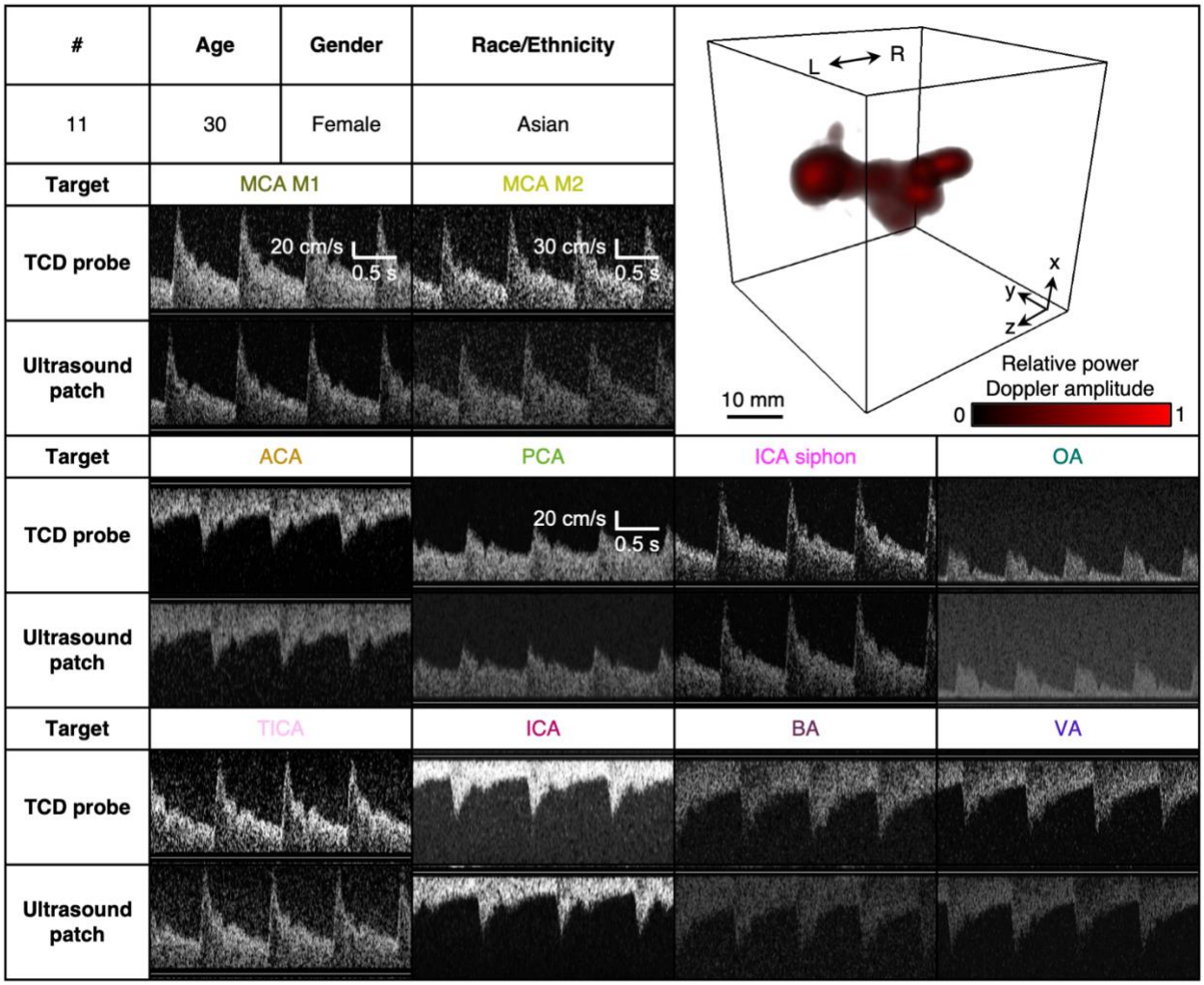

Supplementary Fig. 24 | Volumetric image and blood flow spectra from participant #11. The age, gender, and race/ethnicity that may influence the success rate of TCD sonography were provided. The volumetric image of the cerebral vasculature was collected by the conformal ultrasound patch. The blood flow spectrum of each arterial segment from both the conventional TCD probe and the conformal ultrasound patch was compared accordingly. L, left. R, right. MCA, middle cerebral artery. ACA, anterior cerebral artery. PCA, posterior cerebral artery. ICA, internal carotid artery. OA, ophthalmic artery. TICA, terminal internal carotid artery. BA, basal artery. VA, vertebral artery. The MCA M1 spectra share the same scale bars. The MCA M2, ACA, and TICA spectra share the same scale bars. The PCA, ICA siphon, OA, ICA, BA, and VA spectra share the same scale bars.

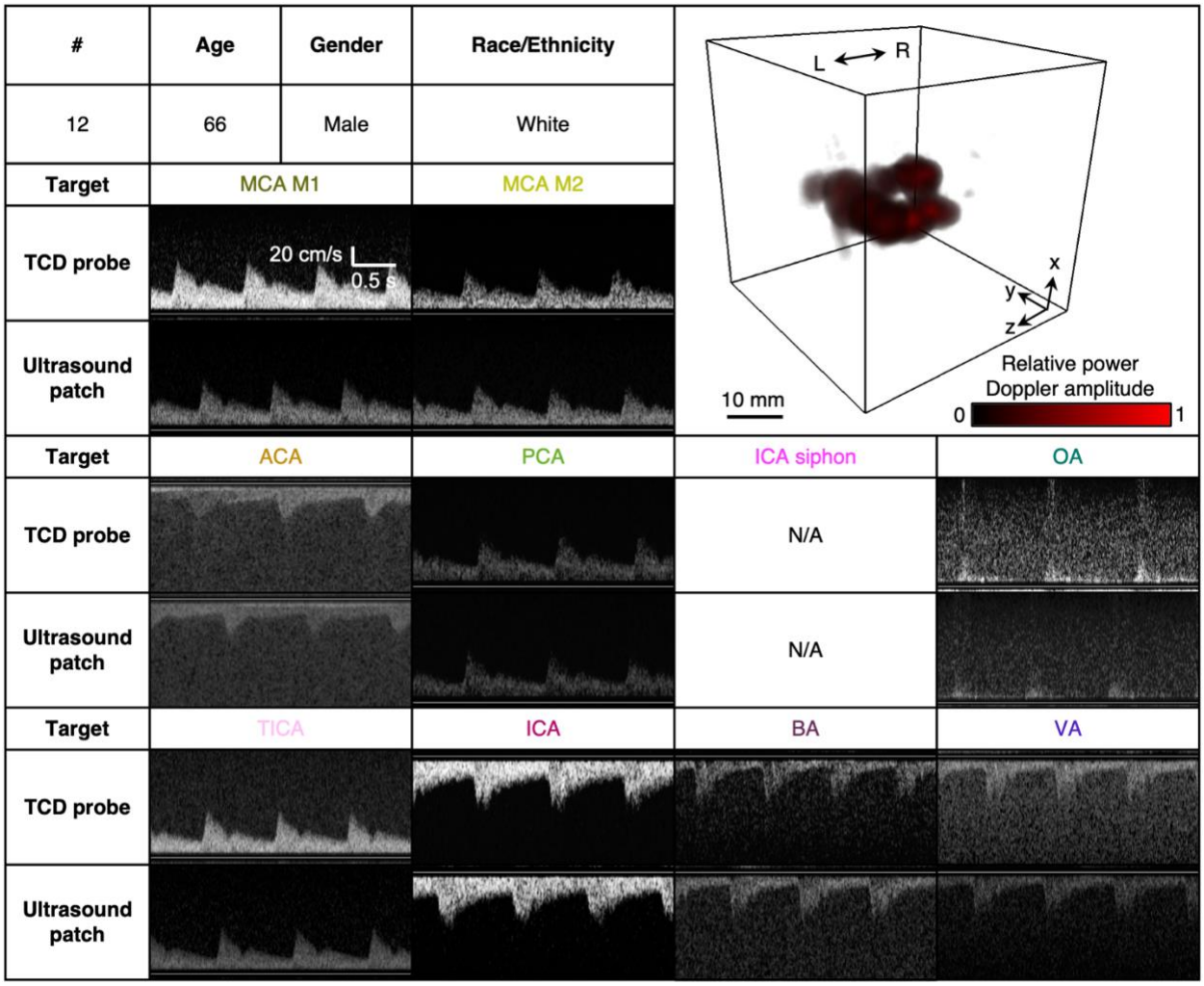

Supplementary Fig. 25 | Volumetric image and blood flow spectra from participant #12. The age, gender, and race/ethnicity that may influence the success rate of TCD sonography were provided. The volumetric image of the cerebral vasculature was collected by the conformal ultrasound patch. The blood flow spectrum of each arterial segment from both the conventional TCD probe and the conformal ultrasound patch was compared accordingly. L, left. R, right. MCA, middle cerebral artery. ACA, anterior cerebral artery. PCA, posterior cerebral artery. ICA, internal carotid artery. OA, ophthalmic artery. TICA, terminal internal carotid artery. BA, basal artery. VA, vertebral artery. All spectra share the same scale bars.

#	Age	Gender	Race/Ethnicity	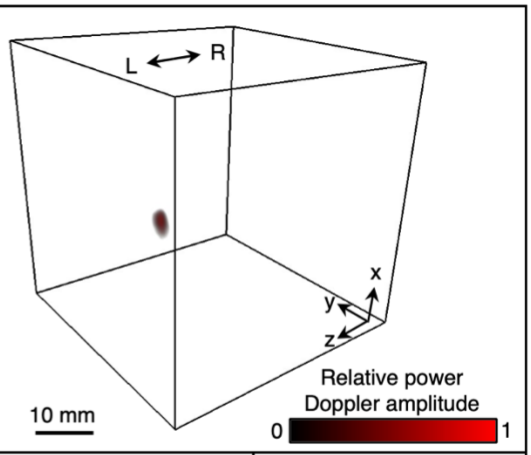
13	72	Female	Black/African American	
Target	MCA M1		MCA M2	
TCD probe	N/A		N/A	
Ultrasound patch	N/A		N/A	
Target	ACA	PCA	ICA siphon	OA
TCD probe	N/A	N/A	N/A	
Ultrasound patch	N/A	N/A	N/A	N/A
Target	TICA	ICA	BA	VA
TCD probe	N/A			
Ultrasound patch	N/A			

Supplementary Fig. 26 | Volumetric image and blood flow spectra from participant #13. The age, gender, and race/ethnicity that may influence the success rate of TCD sonography were provided. The volumetric image of the cerebral vasculature was collected by the conformal ultrasound patch. The blood flow spectrum of each arterial segment from both the conventional TCD probe and the conformal ultrasound patch was compared accordingly. L, left. R, right. MCA, middle cerebral artery. ACA, anterior cerebral artery. PCA, posterior cerebral artery. ICA, internal carotid artery. OA, ophthalmic artery. TICA, terminal internal carotid artery. BA, basal artery. VA, vertebral artery. All spectra share the same scale bars.

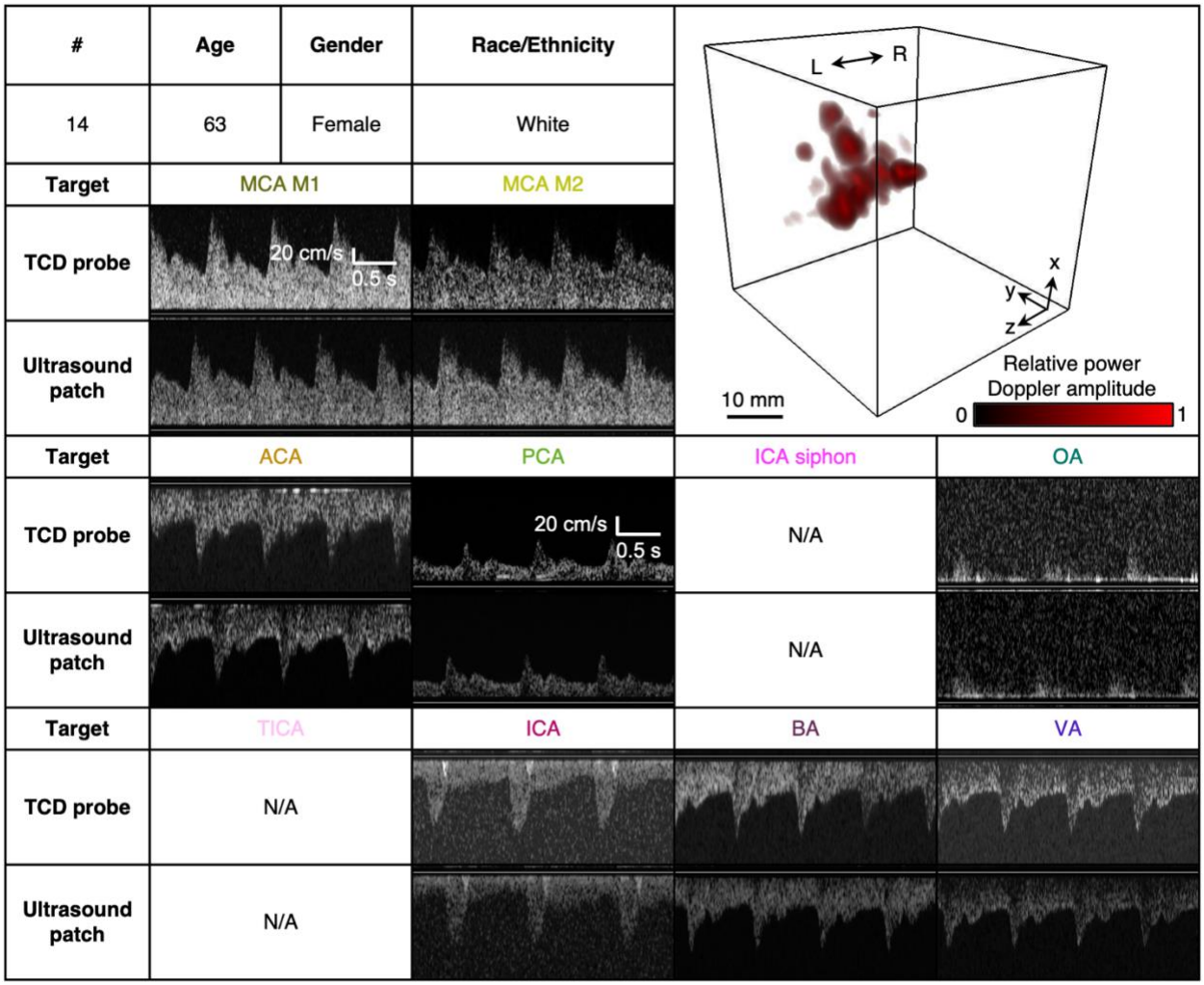

Supplementary Fig. 27 | Volumetric image and blood flow spectra from participant #14. The age, gender, and race/ethnicity that may influence the success rate of TCD sonography were provided. The volumetric image of the cerebral vasculature was collected by the conformal ultrasound patch. The blood flow spectrum of each arterial segment from both the conventional TCD probe and the conformal ultrasound patch was compared accordingly. L, left. R, right. MCA, middle cerebral artery. ACA, anterior cerebral artery. PCA, posterior cerebral artery. ICA, internal carotid artery. OA, ophthalmic artery. TICA, terminal internal carotid artery. BA, basal artery. VA, vertebral artery. The MCA M1, MCA M2, and ACA spectra share the same scale bars. The PCA, OA, ICA, BA, and VA spectra share the same scale bars.

#	Age	Gender	Race/Ethnicity	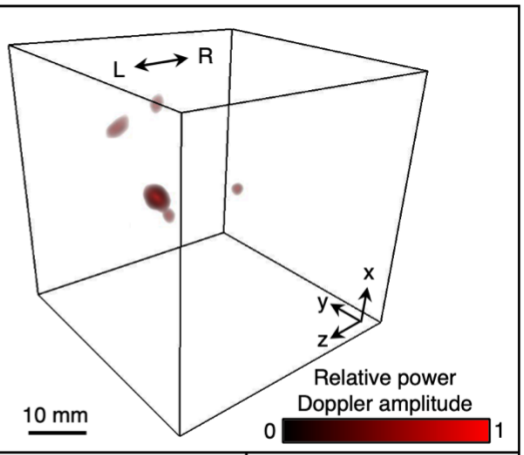
15	49	Male	Black/African American	
Target	MCA M1		MCA M2	
TCD probe	N/A		N/A	
Ultrasound patch	N/A		N/A	
Target	ACA		PCA	ICA siphon / OA
TCD probe	N/A		N/A	N/A / 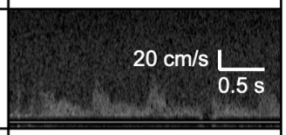
Ultrasound patch	N/A		N/A	N/A / N/A
Target	TICA		ICA	BA / VA
TCD probe	N/A		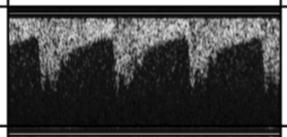	N/A / N/A
Ultrasound patch	N/A		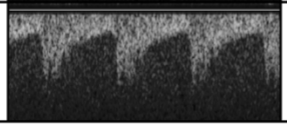	N/A / N/A

Supplementary Fig. 28 | Volumetric image and blood flow spectra from participant #15. The age, gender, and race/ethnicity that may influence the success rate of TCD sonography were provided. The volumetric image of the cerebral vasculature was collected by the conformal ultrasound patch. The blood flow spectrum of each arterial segment from both the conventional TCD probe and the conformal ultrasound patch was compared accordingly. L, left. R, right. MCA, middle cerebral artery. ACA, anterior cerebral artery. PCA, posterior cerebral artery. ICA, internal carotid artery. OA, ophthalmic artery. TICA, terminal internal carotid artery. BA, basal artery. VA, vertebral artery. All spectra share the same scale bars.

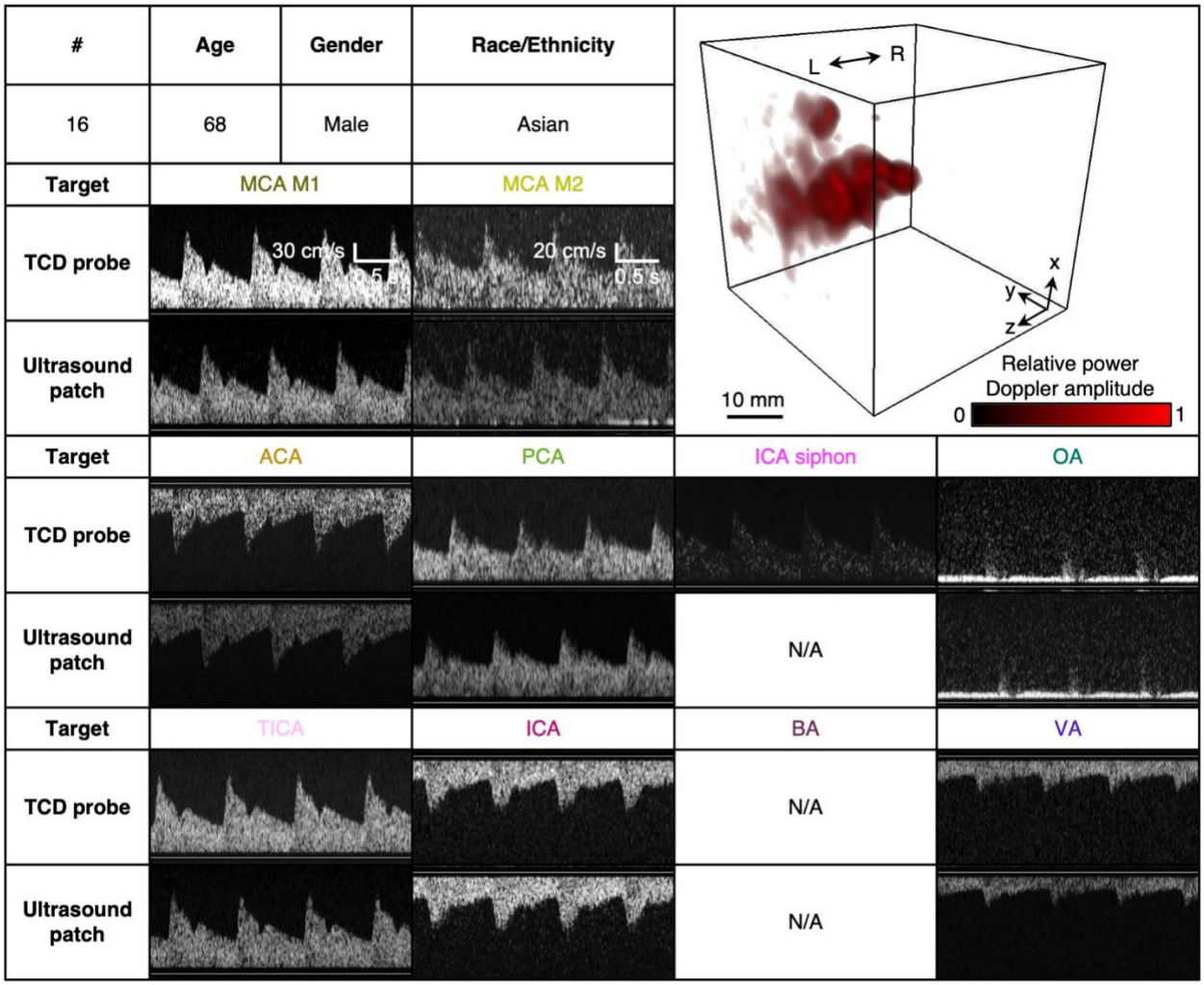

Supplementary Fig. 29 | Volumetric image and blood flow spectra from participant #16. The age, gender, and race/ethnicity that may influence the success rate of TCD sonography were provided. The volumetric image of the cerebral vasculature was collected by the conformal ultrasound patch. The blood flow spectrum of each arterial segment from both the conventional TCD probe and the conformal ultrasound patch was compared accordingly. L, left. R, right. MCA, middle cerebral artery. ACA, anterior cerebral artery. PCA, posterior cerebral artery. ICA, internal carotid artery. OA, ophthalmic artery. TICA, terminal internal carotid artery. BA, basal artery. VA, vertebral artery. The MCA M1, ACA, ICA siphon and TICA spectra share the same scale bars. The MCA M2, PCA, OA, ICA, and VA spectra share the same scale bars.

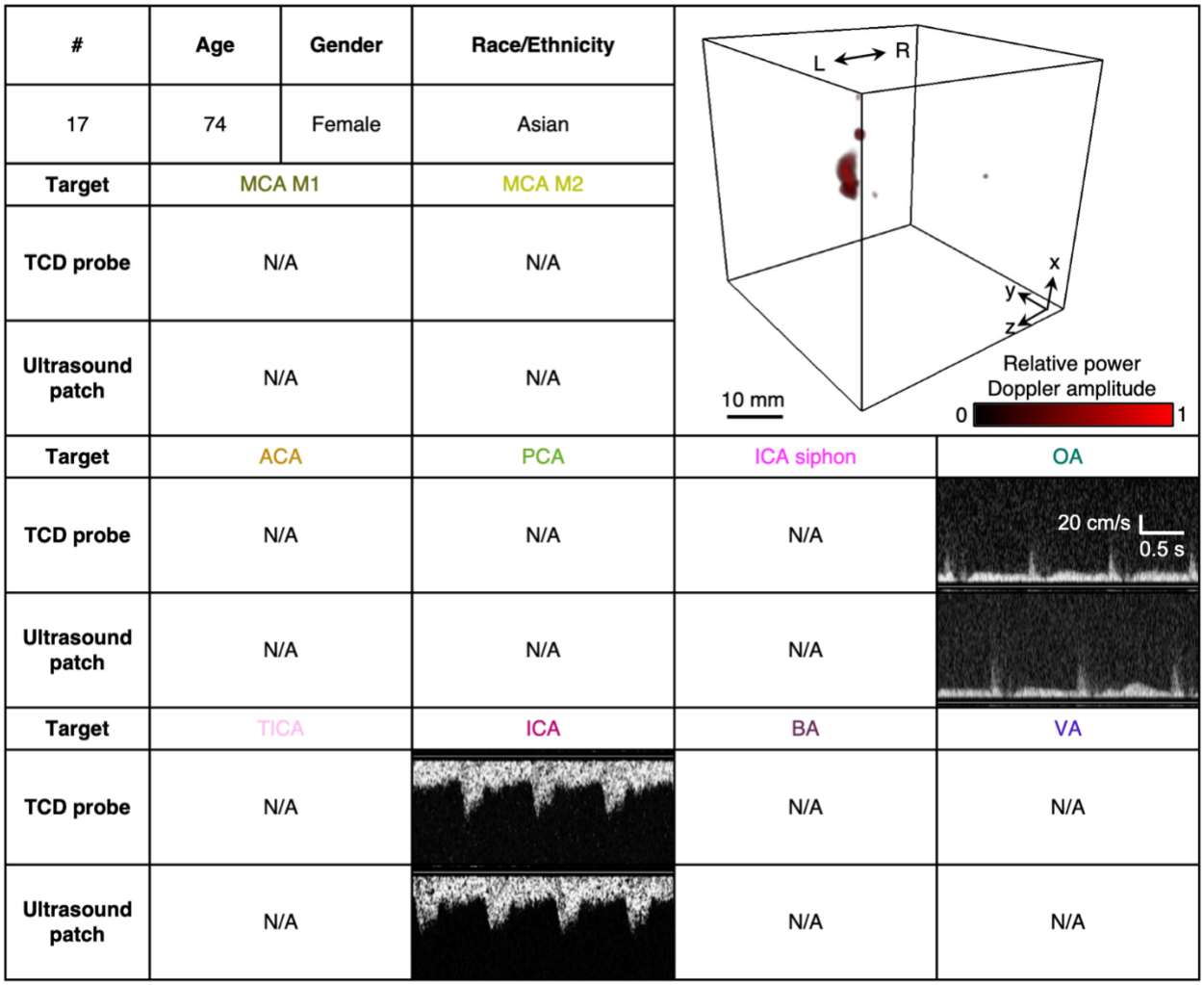

Supplementary Fig. 30 | Volumetric image and blood flow spectra from participant #17. The age, gender, and race/ethnicity that may influence the success rate of TCD sonography were provided. The volumetric image of the cerebral vasculature was collected by the conformal ultrasound patch. The blood flow spectrum of each arterial segment from both the conventional TCD probe and the conformal ultrasound patch was compared accordingly. L, left. R, right. MCA, middle cerebral artery. ACA, anterior cerebral artery. PCA, posterior cerebral artery. ICA, internal carotid artery. OA, ophthalmic artery. TICA, terminal internal carotid artery. BA, basal artery. VA, vertebral artery. All spectra share the same scale bars.

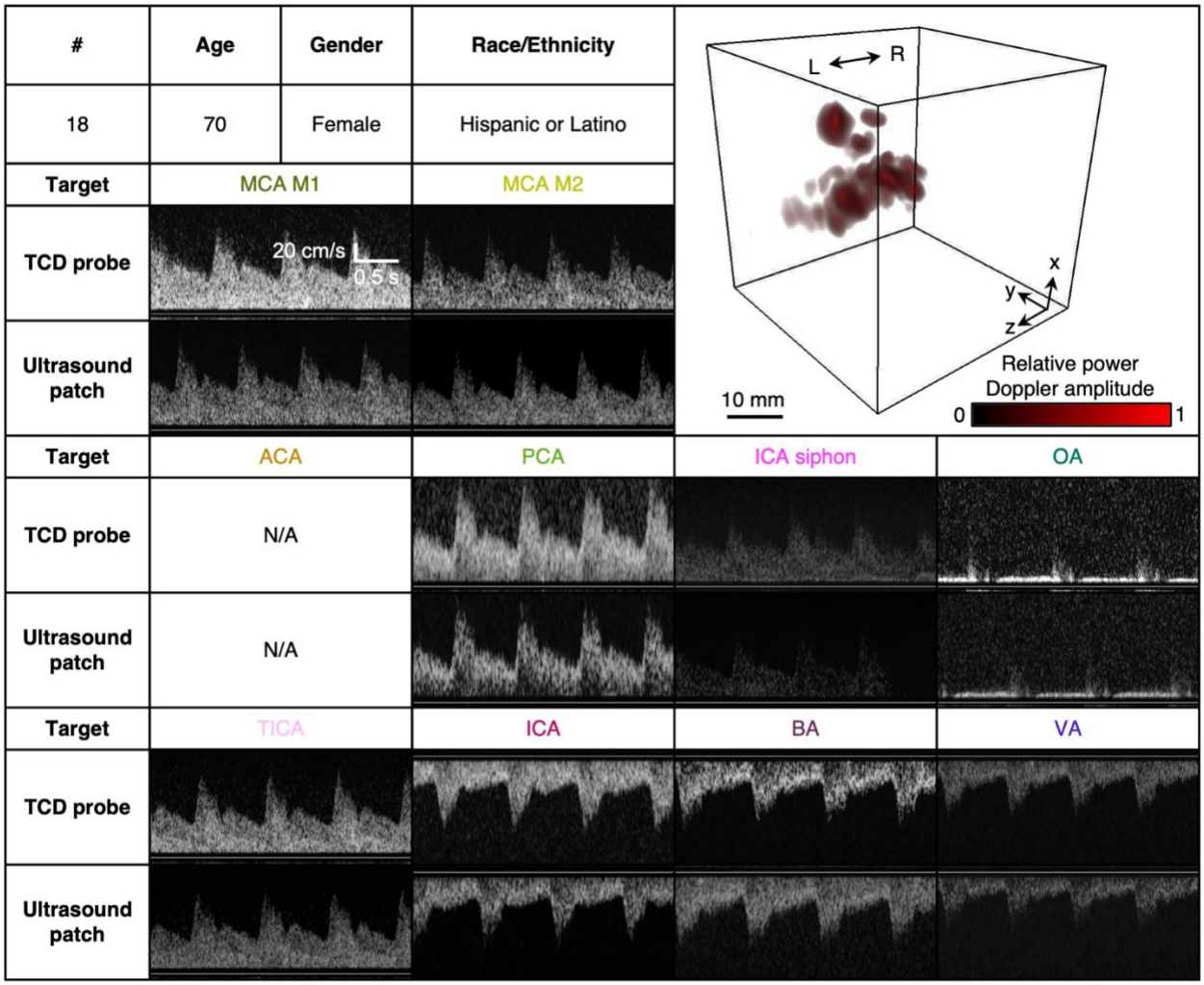

Supplementary Fig. 31 | Volumetric image and blood flow spectra from participant #18. The age, gender, and race/ethnicity that may influence the success rate of TCD sonography were provided. The volumetric image of the cerebral vasculature was collected by the conformal ultrasound patch. The blood flow spectrum of each arterial segment from both the conventional TCD probe and the conformal ultrasound patch was compared accordingly. L, left. R, right. MCA, middle cerebral artery. ACA, anterior cerebral artery. PCA, posterior cerebral artery. ICA, internal carotid artery. OA, ophthalmic artery. TICA, terminal internal carotid artery. BA, basal artery. VA, vertebral artery. All spectra share the same scale bars.

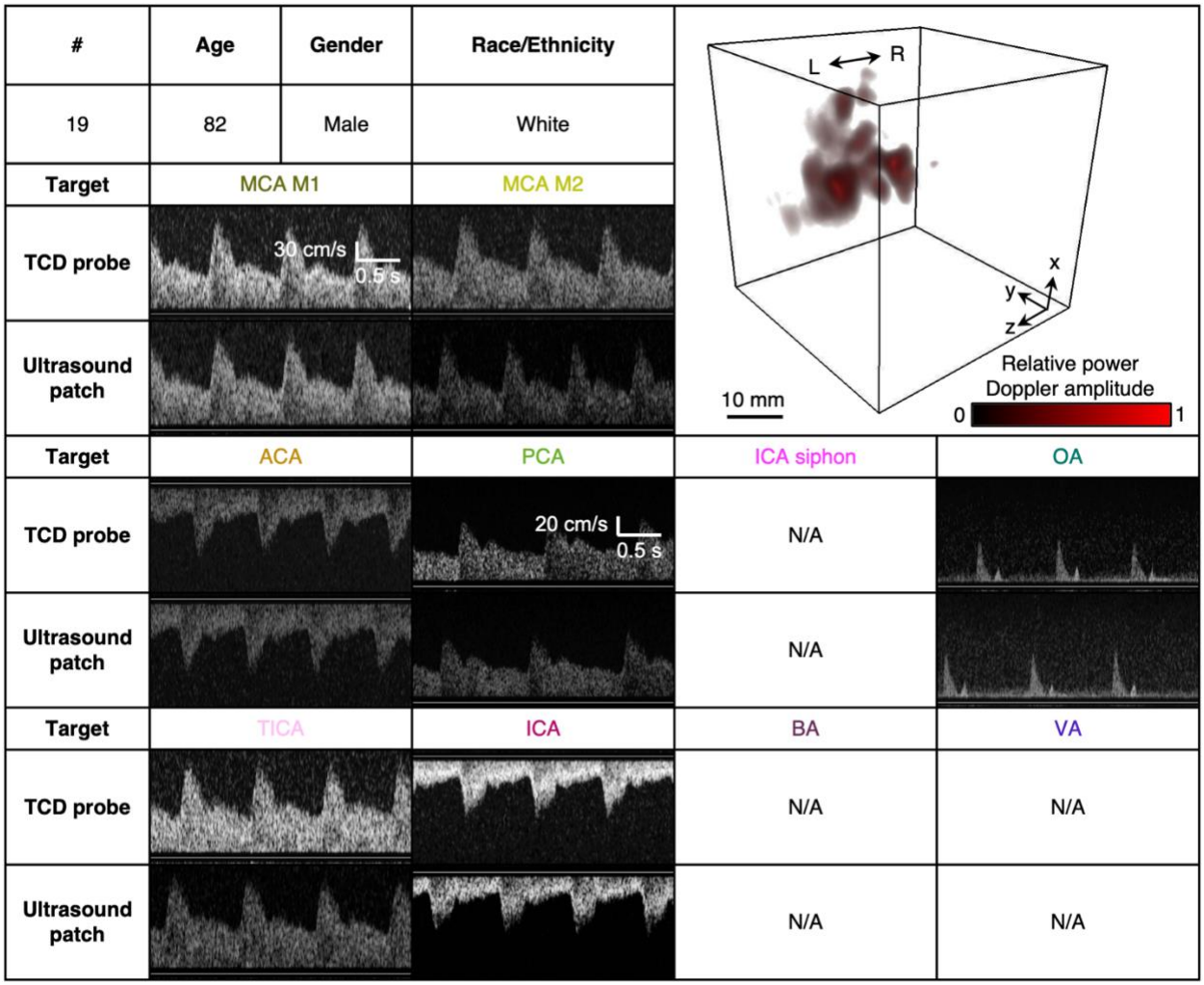

Supplementary Fig. 32 | Volumetric image and blood flow spectra from participant #19. The age, gender, and race/ethnicity that may influence the success rate of TCD sonography were provided. The volumetric image of the cerebral vasculature was collected by the conformal ultrasound patch. The blood flow spectrum of each arterial segment from both the conventional TCD probe and the conformal ultrasound patch was compared accordingly. L, left. R, right. MCA, middle cerebral artery. ACA, anterior cerebral artery. PCA, posterior cerebral artery. ICA, internal carotid artery. OA, ophthalmic artery. TICA, terminal internal carotid artery. BA, basal artery. VA, vertebral artery. The MCA M1, MCAM2, ACA, and TICA spectra share the same scale bars. The PCA, OA, and ICA spectra share the same scale bars.

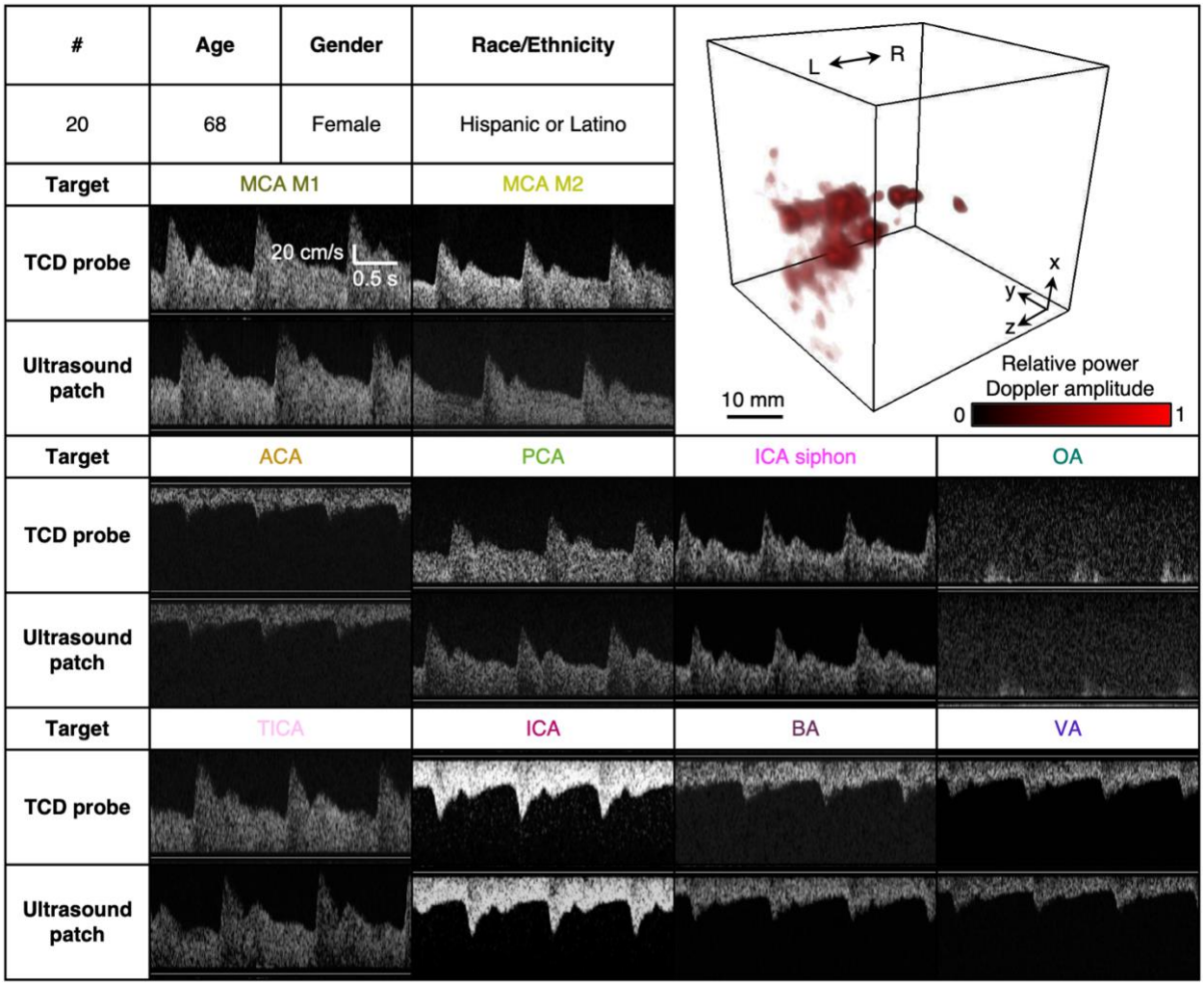

Supplementary Fig. 33 | Volumetric image and blood flow spectra from participant #20. The age, gender, and race/ethnicity that may influence the success rate of TCD sonography were provided. The volumetric image of the cerebral vasculature was collected by the conformal ultrasound patch. The blood flow spectrum of each arterial segment from both the conventional TCD probe and the conformal ultrasound patch was compared accordingly. L, left. R, right. MCA, middle cerebral artery. ACA, anterior cerebral artery. PCA, posterior cerebral artery. ICA, internal carotid artery. OA, ophthalmic artery. TICA, terminal internal carotid artery. BA, basal artery. VA, vertebral artery. All spectra share the same scale bars.

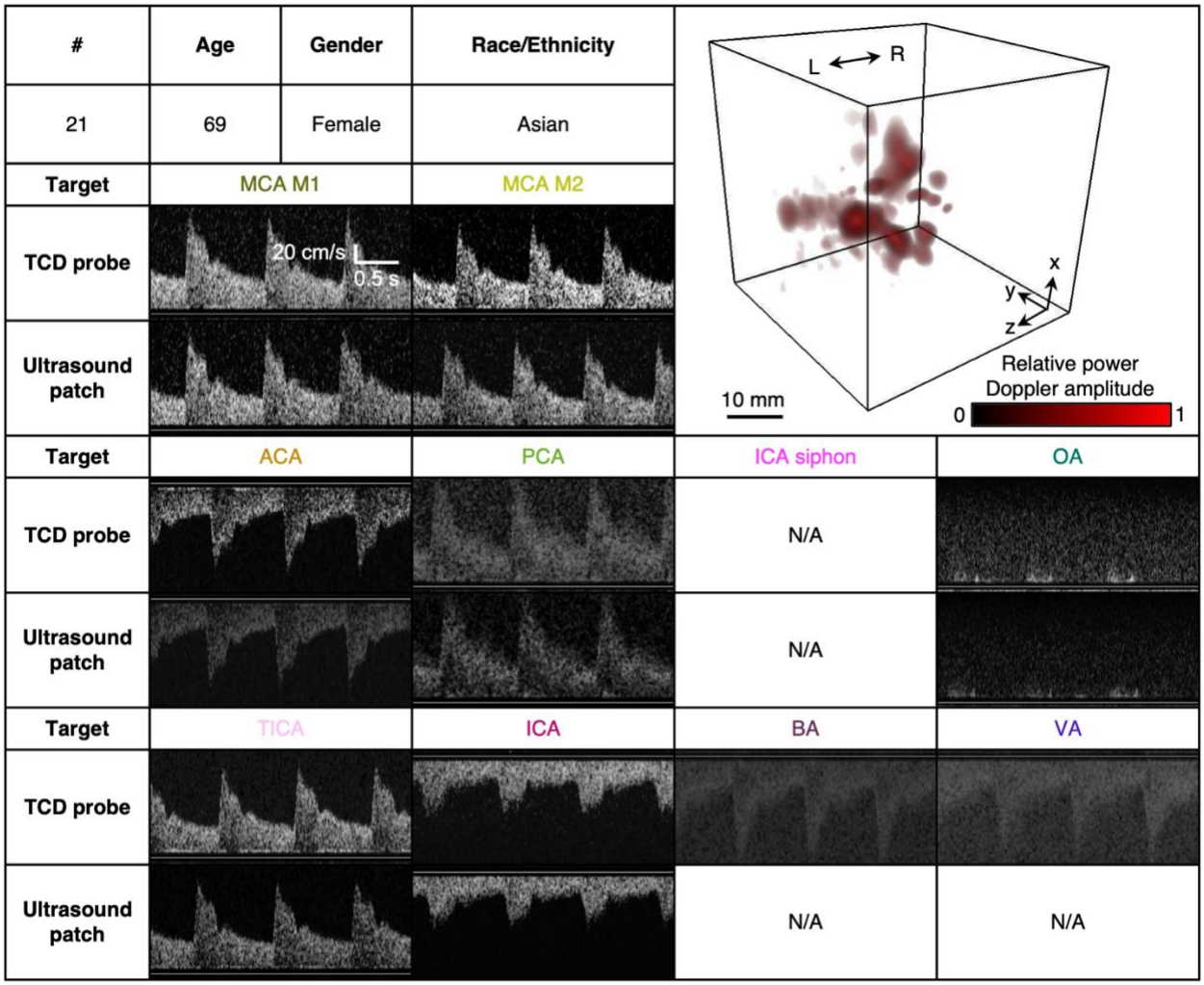

Supplementary Fig. 34 | Volumetric image and blood flow spectra from participant #21. The age, gender, and race/ethnicity that may influence the success rate of TCD sonography were provided. The volumetric image of the cerebral vasculature was collected by the conformal ultrasound patch. The blood flow spectrum of each arterial segment from both the conventional TCD probe and the conformal ultrasound patch was compared accordingly. L, left. R, right. MCA, middle cerebral artery. ACA, anterior cerebral artery. PCA, posterior cerebral artery. ICA, internal carotid artery. OA, ophthalmic artery. TICA, terminal internal carotid artery. BA, basal artery. VA, vertebral artery. All spectra share the same scale bars.

#	Age	Gender	Race/Ethnicity	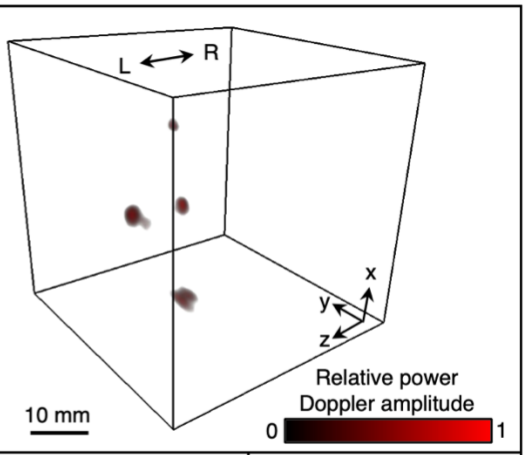	
22	55	Female	White		
Target	MCA M1		MCA M2		
TCD probe	N/A		N/A		
Ultrasound patch	N/A		N/A		
Target	ACA		PCA	ICA siphon	OA
TCD probe	N/A		N/A	N/A	N/A
Ultrasound patch	N/A		N/A	N/A	N/A
Target	TICA		ICA	BA	VA
TCD probe	N/A		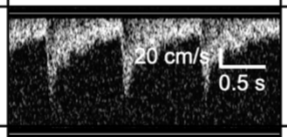	N/A	N/A
Ultrasound patch	N/A		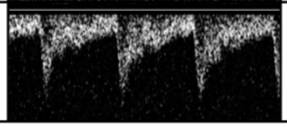	N/A	N/A

Supplementary Fig. 35 | Volumetric image and blood flow spectra from participant #22. The age, gender, and race/ethnicity that may influence the success rate of TCD sonography were provided. The volumetric image of the cerebral vasculature was collected by the conformal ultrasound patch. The blood flow spectrum of each arterial segment from both the conventional TCD probe and the conformal ultrasound patch was compared accordingly. L, left. R, right. MCA, middle cerebral artery. ACA, anterior cerebral artery. PCA, posterior cerebral artery. ICA, internal carotid artery. OA, ophthalmic artery. TICA, terminal internal carotid artery. BA, basal artery. VA, vertebral artery. All spectra share the same scale bars.

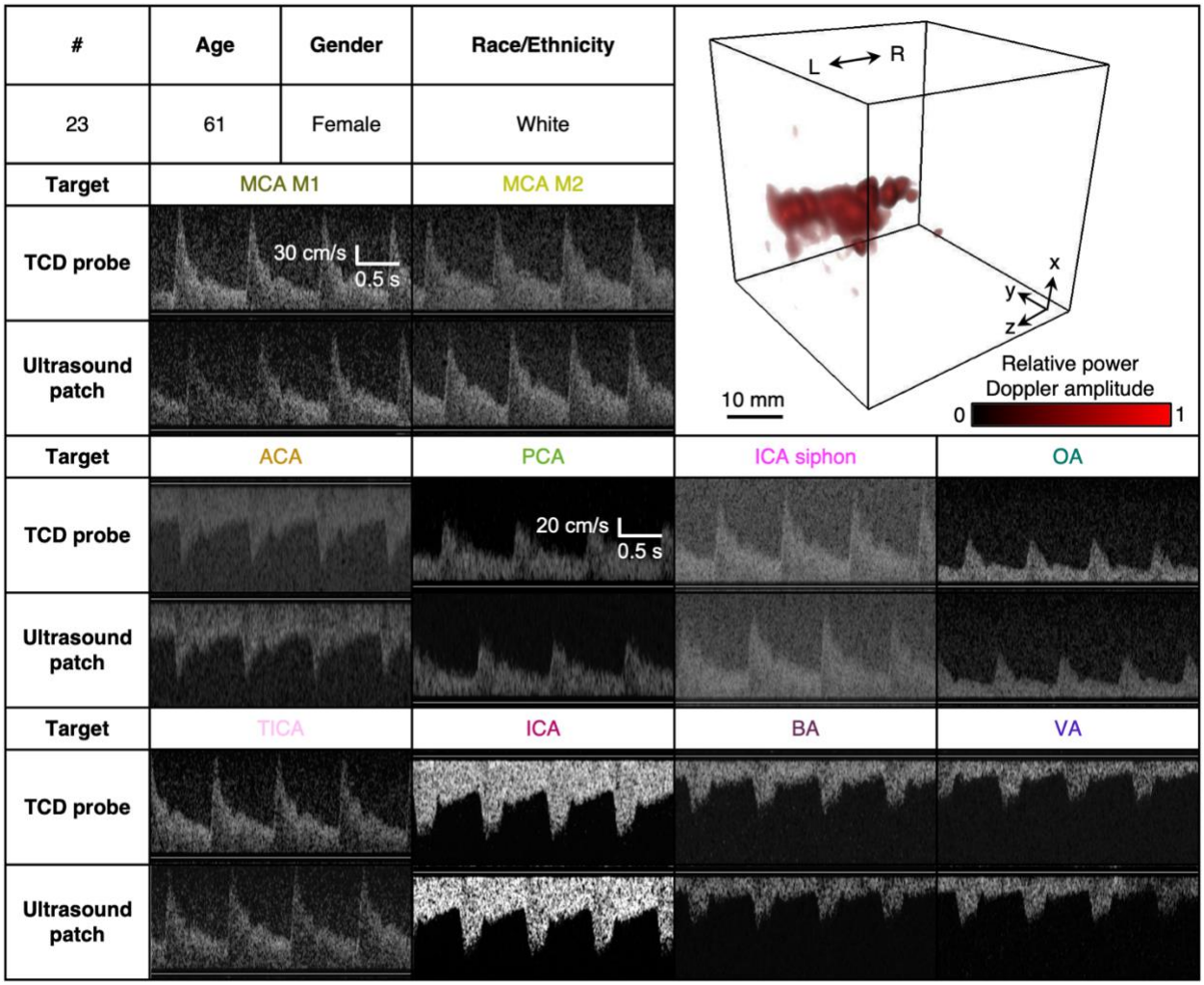

Supplementary Fig. 36 | Volumetric image and blood flow spectra from participant #23. The age, gender, and race/ethnicity that may influence the success rate of TCD sonography were provided. The volumetric image of the cerebral vasculature was collected by the conformal ultrasound patch. The blood flow spectrum of each arterial segment from both the conventional TCD probe and the conformal ultrasound patch was compared accordingly. L, left. R, right. MCA, middle cerebral artery. ACA, anterior cerebral artery. PCA, posterior cerebral artery. ICA, internal carotid artery. OA, ophthalmic artery. TICA, terminal internal carotid artery. BA, basal artery. VA, vertebral artery. The MCA M1, MCA M2, ACA, ICA siphon and TICA spectra share the same scale bars. The PCA, OA, ICA, BA, and VA spectra share the same scale bars.

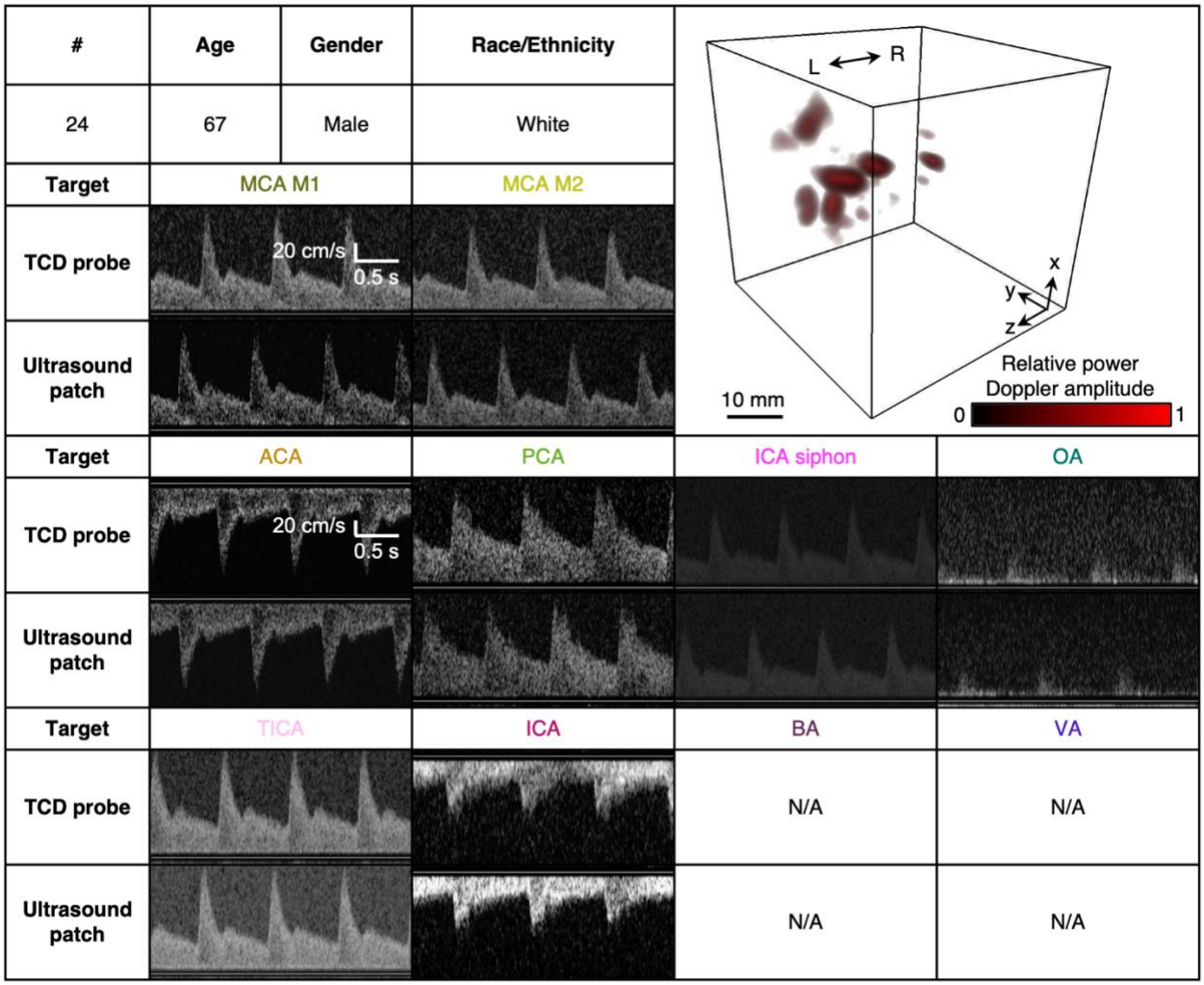

Supplementary Fig. 37 | Volumetric image and blood flow spectra from participant #24. The age, gender, and race/ethnicity that may influence the success rate of TCD sonography were provided. The volumetric image of the cerebral vasculature was collected by the conformal ultrasound patch. The blood flow spectrum of each arterial segment from both the conventional TCD probe and the conformal ultrasound patch was compared accordingly. L, left. R, right. MCA, middle cerebral artery. ACA, anterior cerebral artery. PCA, posterior cerebral artery. ICA, internal carotid artery. OA, ophthalmic artery. TICA, terminal internal carotid artery. BA, basal artery. VA, vertebral artery. The MCA M1, MCA M2, PCA, ICA siphon, OA, TICA, and ICA spectra share the same scale bars. The ACA spectra share the same scale bars.

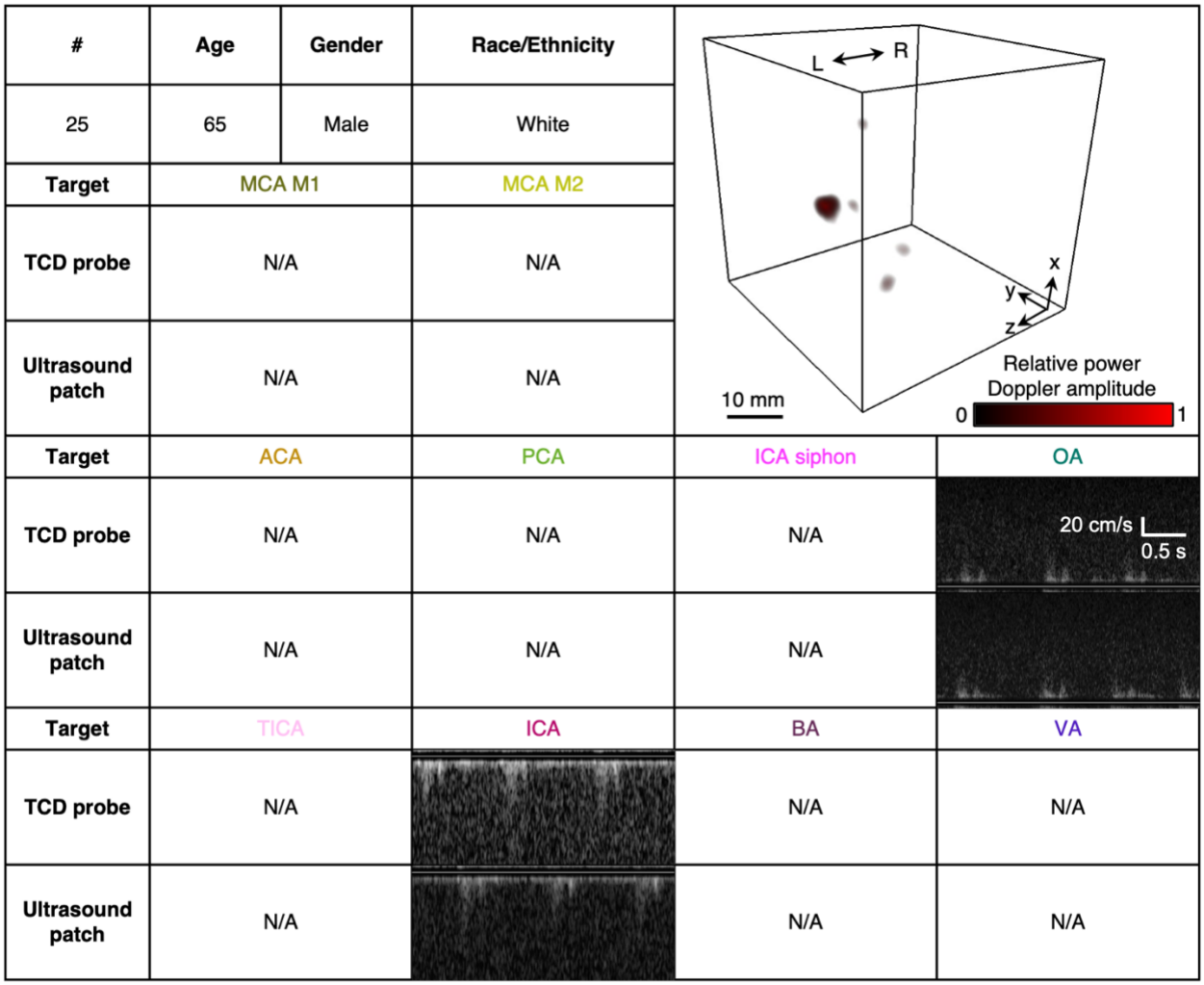

Supplementary Fig. 38 | Volumetric image and blood flow spectra from participant #25. The age, gender, and race/ethnicity that may influence the success rate of TCD sonography were provided. The volumetric image of the cerebral vasculature was collected by the conformal ultrasound patch. The blood flow spectrum of each arterial segment from both the conventional TCD probe and the conformal ultrasound patch was compared accordingly. L, left. R, right. MCA, middle cerebral artery. ACA, anterior cerebral artery. PCA, posterior cerebral artery. ICA, internal carotid artery. OA, ophthalmic artery. TICA, terminal internal carotid artery. BA, basal artery. VA, vertebral artery. All spectra share the same scale bars.

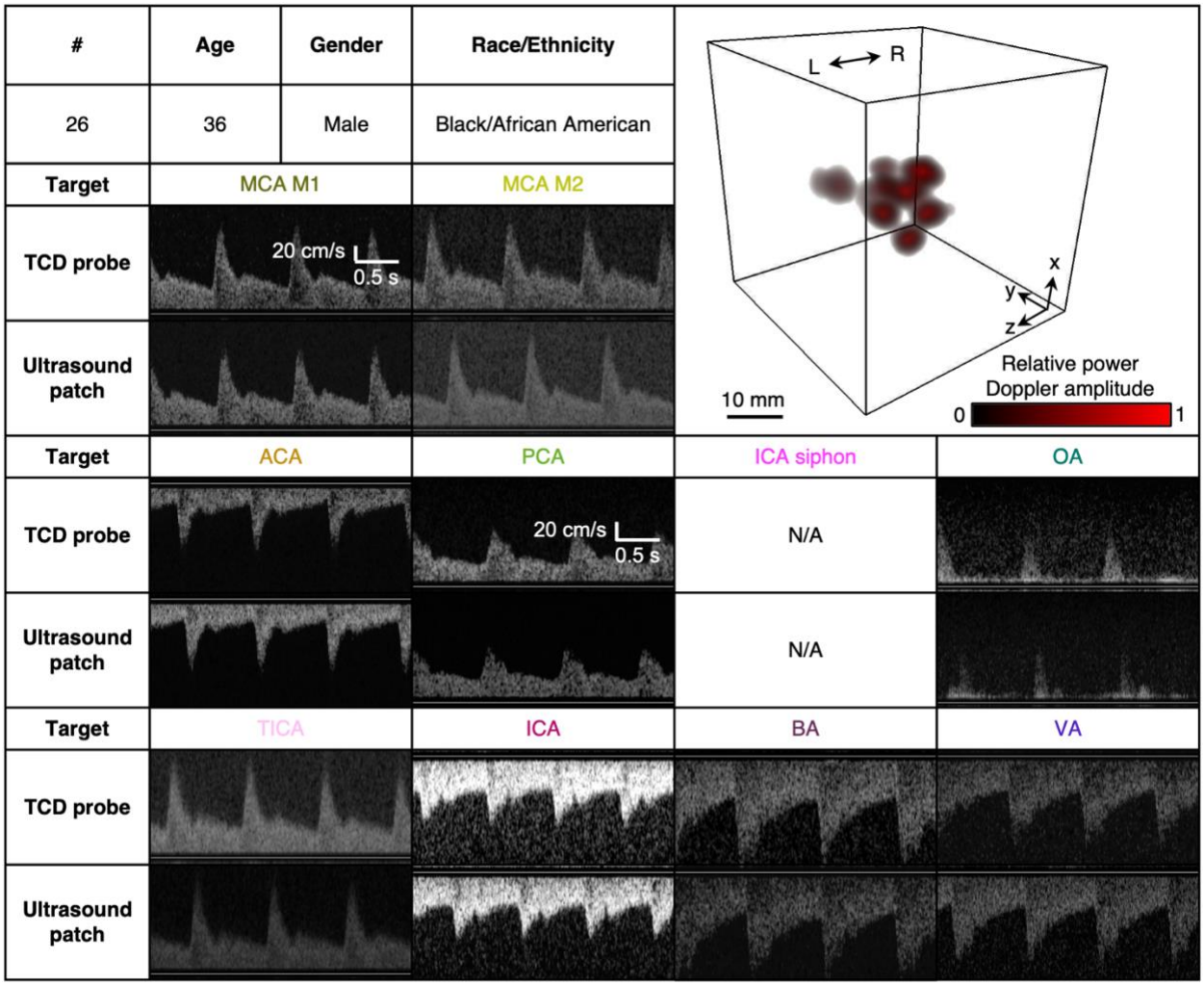

Supplementary Fig. 39 | Volumetric image and blood flow spectra from participant #26. The age, gender, and race/ethnicity that may influence the success rate of TCD sonography were provided. The volumetric image of the cerebral vasculature was collected by the conformal ultrasound patch. The blood flow spectrum of each arterial segment from both the conventional TCD probe and the conformal ultrasound patch was compared accordingly. L, left. R, right. MCA, middle cerebral artery. ACA, anterior cerebral artery. PCA, posterior cerebral artery. ICA, internal carotid artery. OA, ophthalmic artery. TICA, terminal internal carotid artery. BA, basal artery. VA, vertebral artery. The MCA M1, MCA M2, ACA, and TICA spectra share the same scale bars. The PCA, OA, ICA, BA, and VA spectra share the same scale bars.

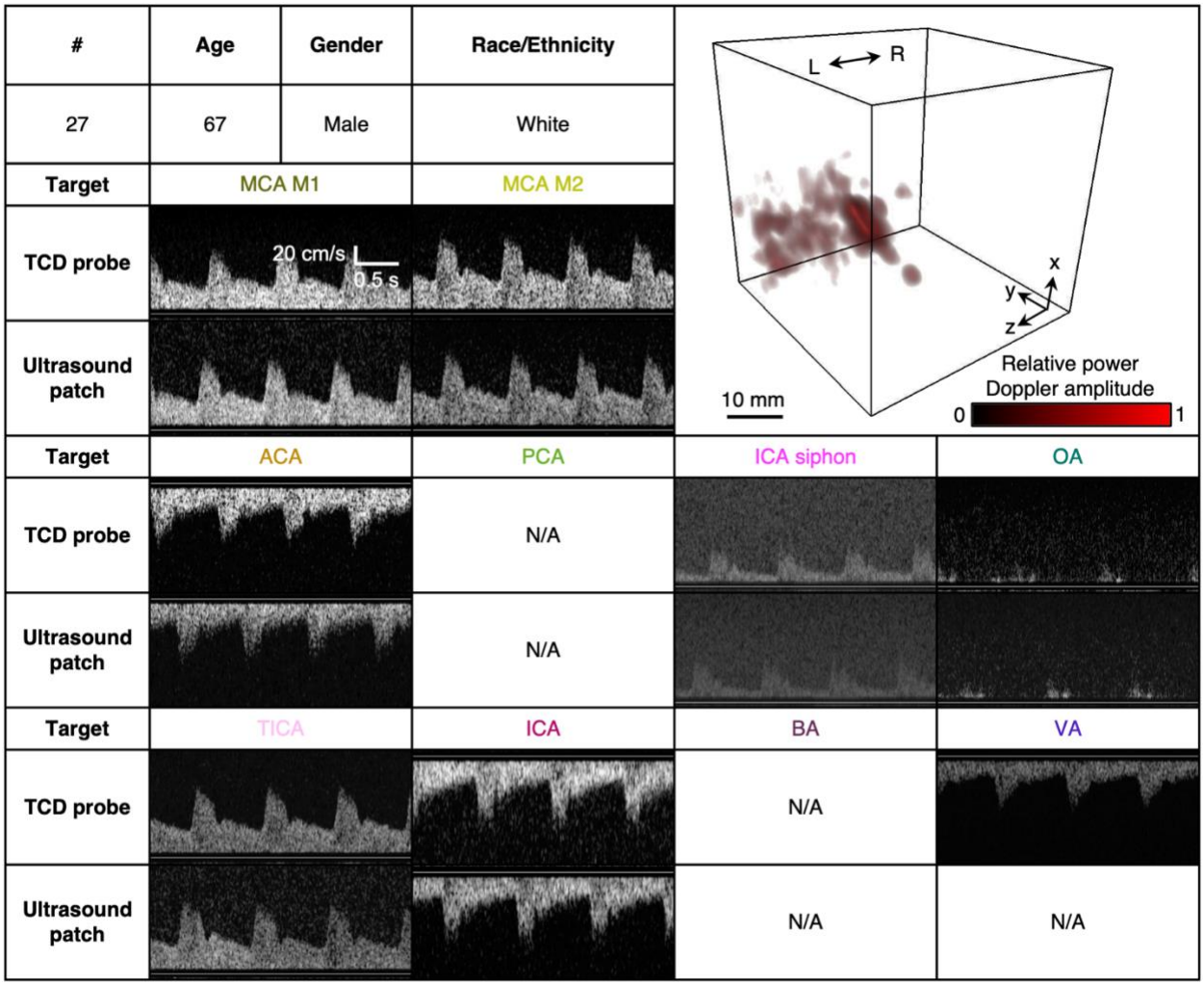

Supplementary Fig. 40 | Volumetric image and blood flow spectra from participant #27. The age, gender, and race/ethnicity that may influence the success rate of TCD sonography were provided. The volumetric image of the cerebral vasculature was collected by the conformal ultrasound patch. The blood flow spectrum of each arterial segment from both the conventional TCD probe and the conformal ultrasound patch was compared accordingly. L, left. R, right. MCA, middle cerebral artery. ACA, anterior cerebral artery. PCA, posterior cerebral artery. ICA, internal carotid artery. OA, ophthalmic artery. TICA, terminal internal carotid artery. BA, basal artery. VA, vertebral artery. All spectra share the same scale bars.

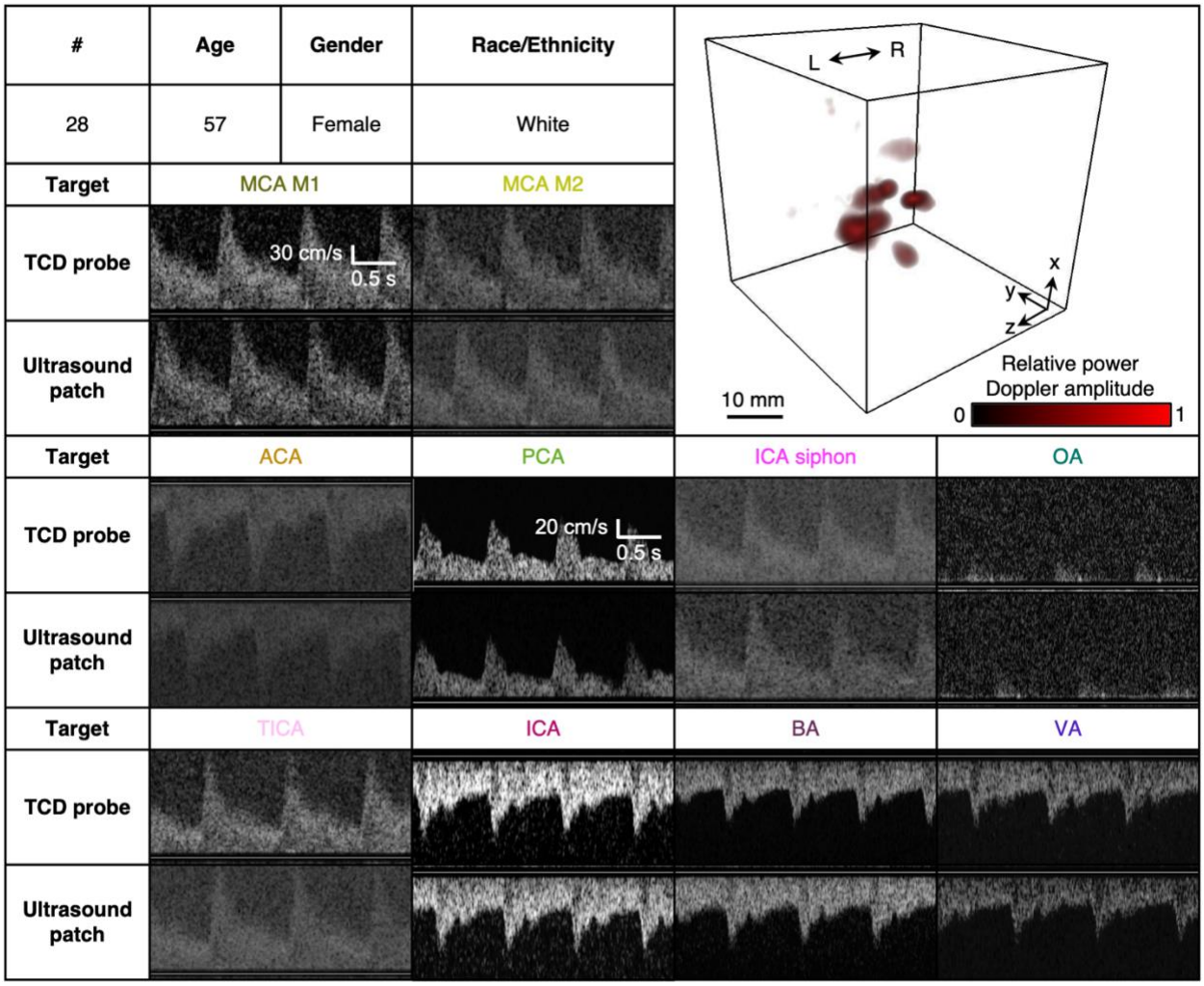

Supplementary Fig. 41 | Volumetric image and blood flow spectra from participant #28. The age, gender, and race/ethnicity that may influence the success rate of TCD sonography were provided. The volumetric image of the cerebral vasculature was collected by the conformal ultrasound patch. The blood flow spectrum of each arterial segment from both the conventional TCD probe and the conformal ultrasound patch was compared accordingly. L, left. R, right. MCA, middle cerebral artery. ACA, anterior cerebral artery. PCA, posterior cerebral artery. ICA, internal carotid artery. OA, ophthalmic artery. TICA, terminal internal carotid artery. BA, basal artery. VA, vertebral artery. The MCA M1, MCA M2, ACA, ICA siphon and TICA spectra share the same scale bars. The PCA, OA, ICA, BA,and VA spectra share the same scale bars.

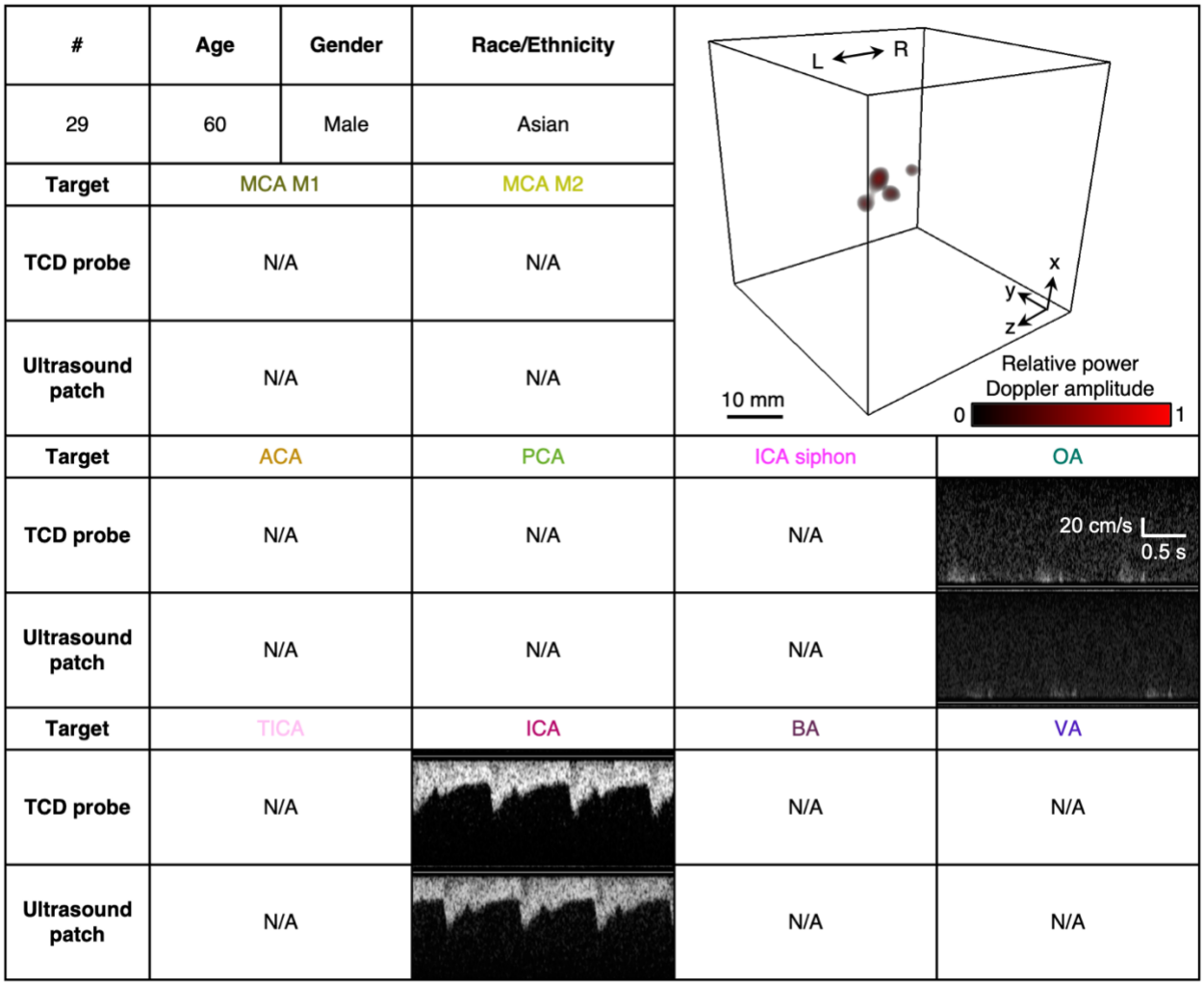

Supplementary Fig. 42 | Volumetric image and blood flow spectra from participant #29. The age, gender, and race/ethnicity that may influence the success rate of TCD sonography were provided. The volumetric image of the cerebral vasculature was collected by the conformal ultrasound patch. The blood flow spectrum of each arterial segment from both the conventional TCD probe and the conformal ultrasound patch was compared accordingly. L, left. R, right. MCA, middle cerebral artery. ACA, anterior cerebral artery. PCA, posterior cerebral artery. ICA, internal carotid artery. OA, ophthalmic artery. TICA, terminal internal carotid artery. BA, basal artery. VA, vertebral artery. All spectra share the same scale bars.

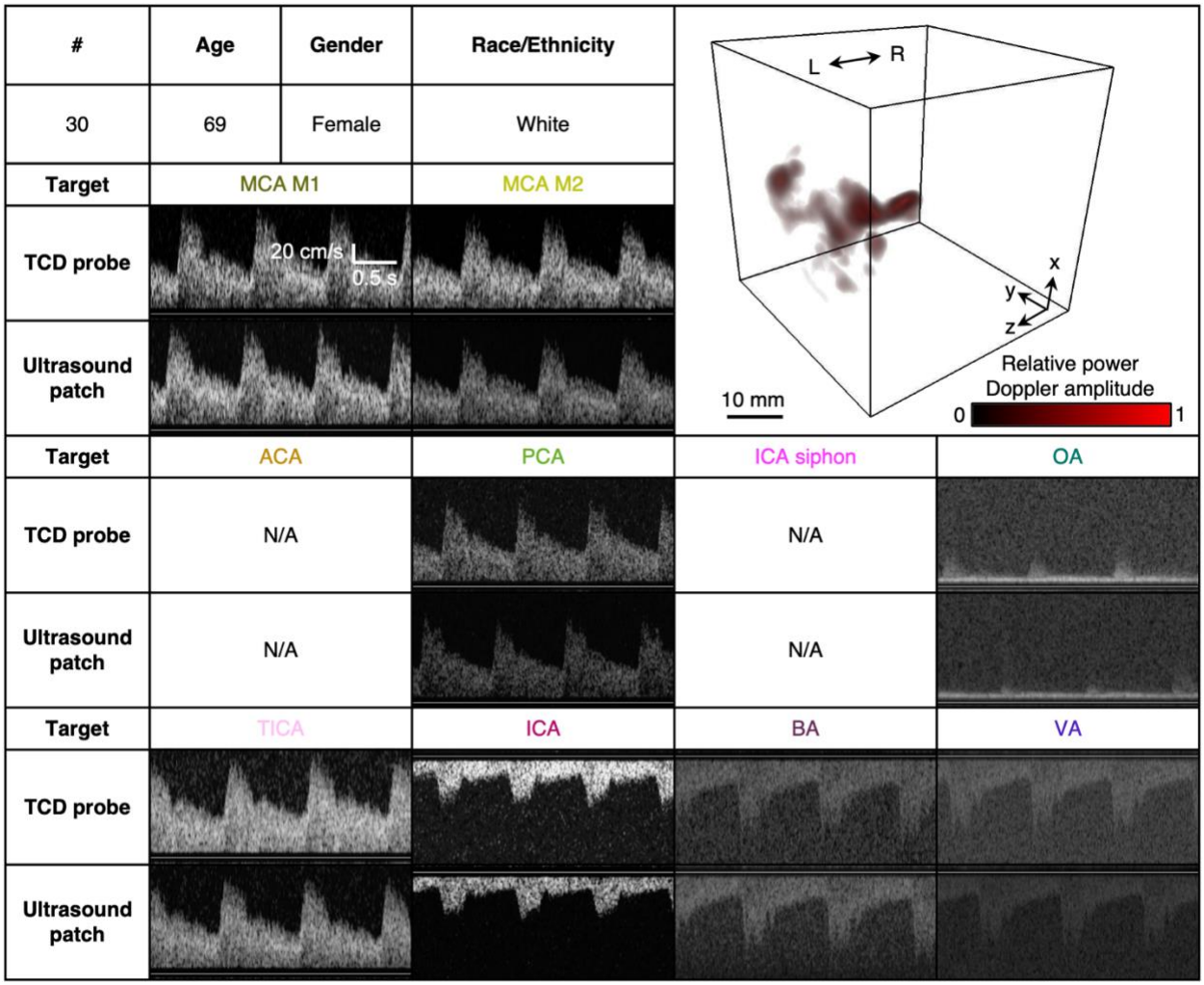

Supplementary Fig. 43 | Volumetric image and blood flow spectra from participant #30. The age, gender, and race/ethnicity that may influence the success rate of TCD sonography were provided. The volumetric image of the cerebral vasculature was collected by the conformal ultrasound patch. The blood flow spectrum of each arterial segment from both the conventional TCD probe and the conformal ultrasound patch was compared accordingly. L, left. R, right. MCA, middle cerebral artery. ACA, anterior cerebral artery. PCA, posterior cerebral artery. ICA, internal carotid artery. OA, ophthalmic artery. TICA, terminal internal carotid artery. BA, basal artery. VA, vertebral artery. All spectra share the same scale bars.

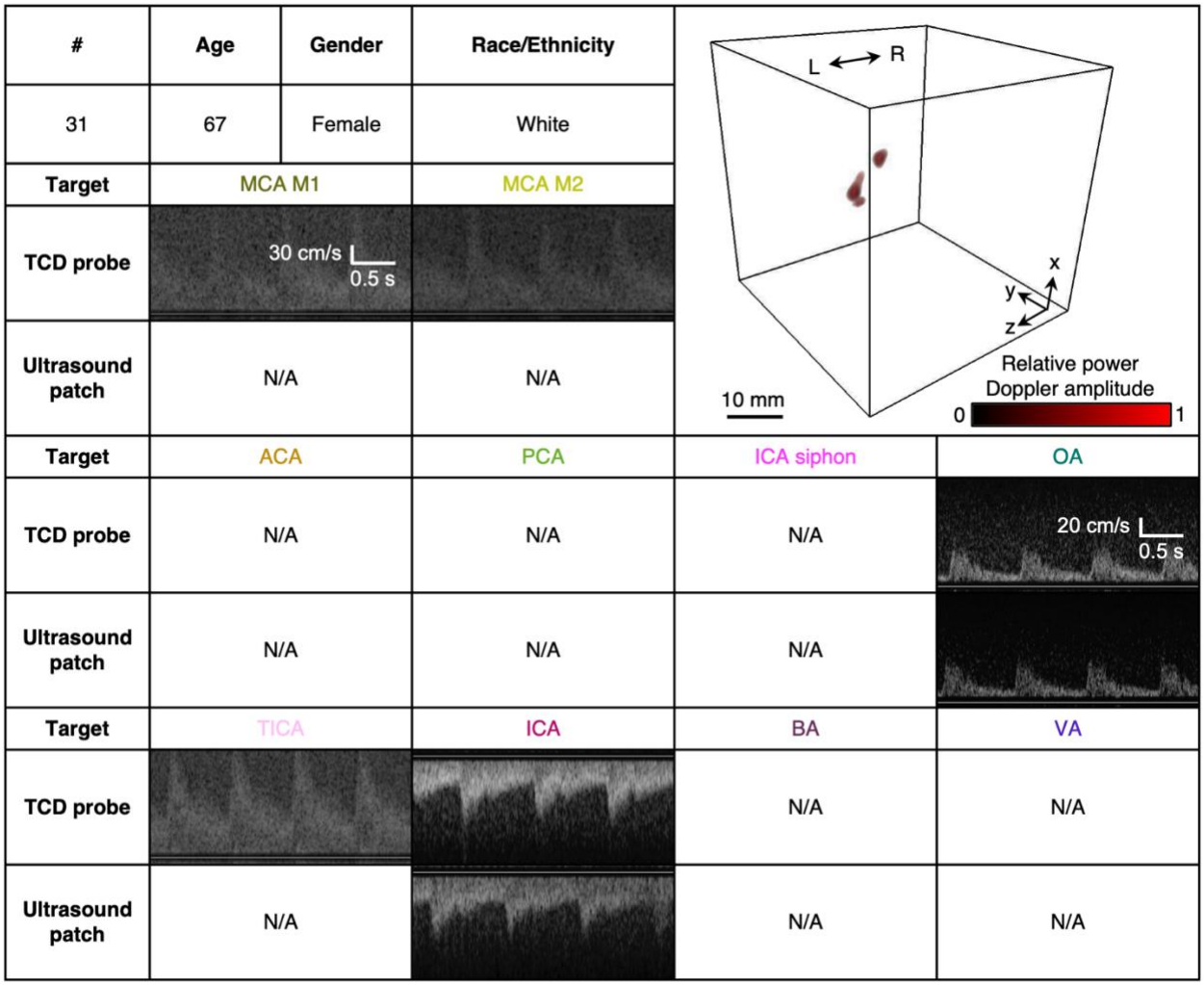

Supplementary Fig. 44 | Volumetric image and blood flow spectra from participant #31. The age, gender, and race/ethnicity that may influence the success rate of TCD sonography were provided. The volumetric image of the cerebral vasculature was collected by the conformal ultrasound patch. The blood flow spectrum of each arterial segment from both the conventional TCD probe and the conformal ultrasound patch was compared accordingly. L, left. R, right. MCA, middle cerebral artery. ACA, anterior cerebral artery. PCA, posterior cerebral artery. ICA, internal carotid artery. OA, ophthalmic artery. TICA, terminal internal carotid artery. BA, basal artery. VA, vertebral artery. The MCA M1, MCA M2, and TICA spectra share the same scale bars. The OA and ICA spectra share the same scale bars.

#	Age	Gender	Race/Ethnicity	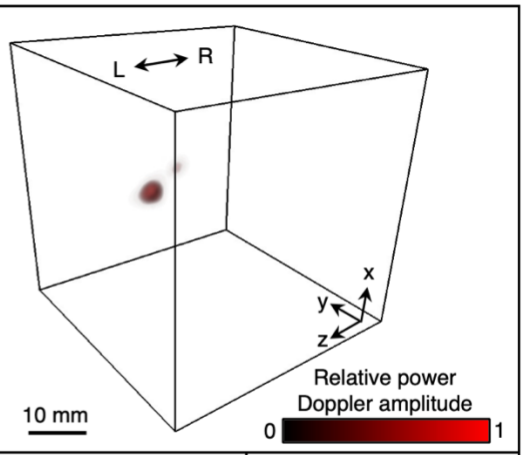
32	70	Male	Hispanic or Latino	
Target	MCA M1		MCA M2	
TCD probe	N/A		N/A	
Ultrasound patch	N/A		N/A	
Target	ACA		PCA	ICA siphon / OA
TCD probe	N/A		N/A	N/A / N/A
Ultrasound patch	N/A		N/A	N/A / N/A
Target	TICA		ICA	BA / VA
TCD probe	N/A		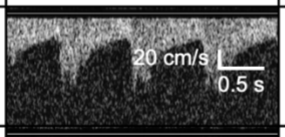	N/A / N/A
Ultrasound patch	N/A		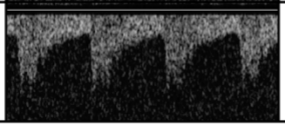	N/A / N/A

Supplementary Fig. 45 | Volumetric image and blood flow spectra from participant #32. The age, gender, and race/ethnicity that may influence the success rate of TCD sonography were provided. The volumetric image of the cerebral vasculature was collected by the conformal ultrasound patch. The blood flow spectrum of each arterial segment from both the conventional TCD probe and the conformal ultrasound patch was compared accordingly. L, left. R, right. MCA, middle cerebral artery. ACA, anterior cerebral artery. PCA, posterior cerebral artery. ICA, internal carotid artery. OA, ophthalmic artery. TICA, terminal internal carotid artery. BA, basal artery. VA, vertebral artery. All spectra share the same scale bars.

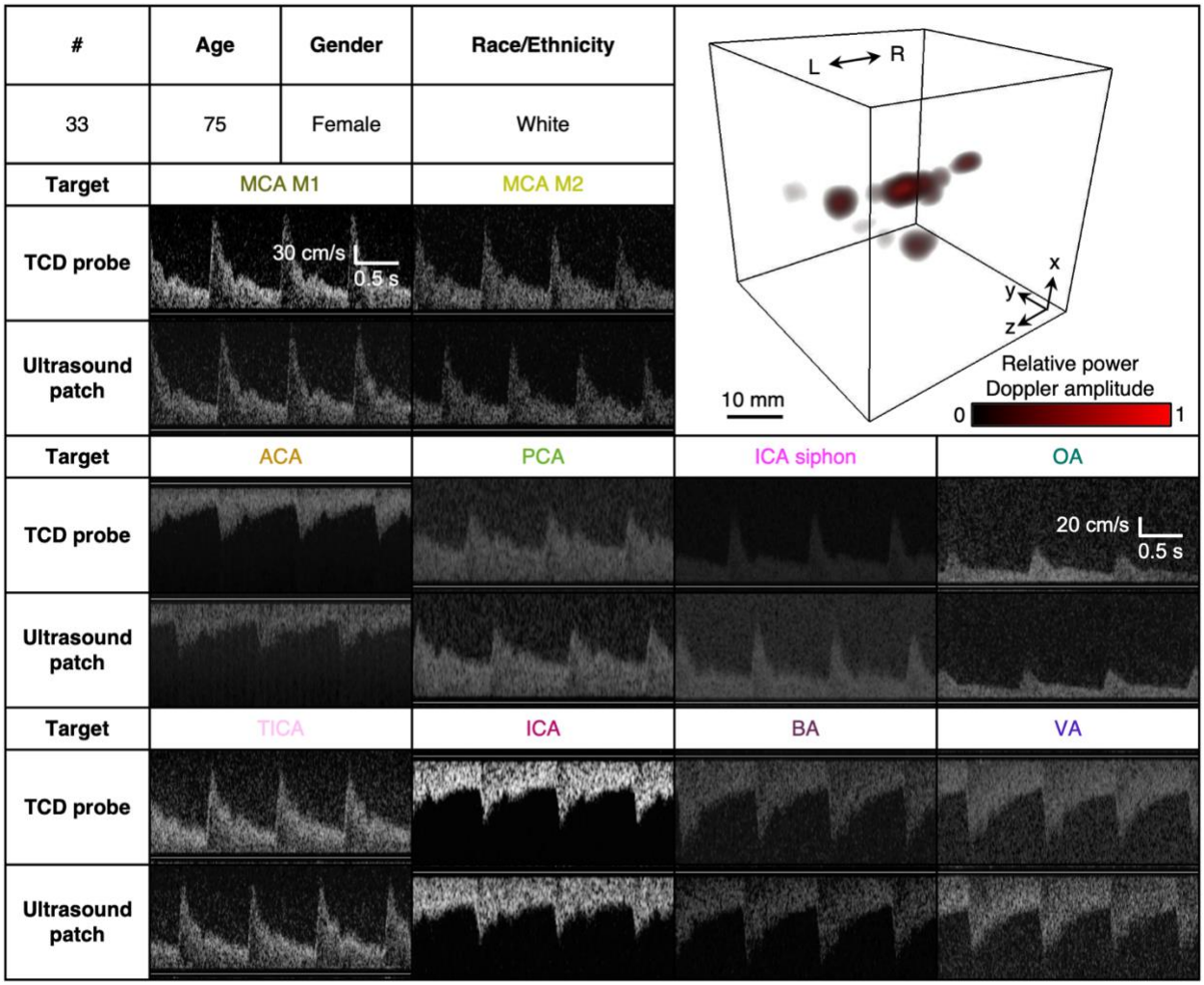

Supplementary Fig. 46 | Volumetric image and blood flow spectra from participant #33. The age, gender, and race/ethnicity that may influence the success rate of TCD sonography were provided. The volumetric image of the cerebral vasculature was collected by the conformal ultrasound patch. The blood flow spectrum of each arterial segment from both the conventional TCD probe and the conformal ultrasound patch was compared accordingly. L, left. R, right. MCA, middle cerebral artery. ACA, anterior cerebral artery. PCA, posterior cerebral artery. ICA, internal carotid artery. OA, ophthalmic artery. TICA, terminal internal carotid artery. BA, basal artery. VA, vertebral artery. The MCA M1, MCA M2, ACA, PCA, ICA siphon, TICA, and ICA spectra share the same scale bars. The OA, BA, and VA spectra share the same scale bars.

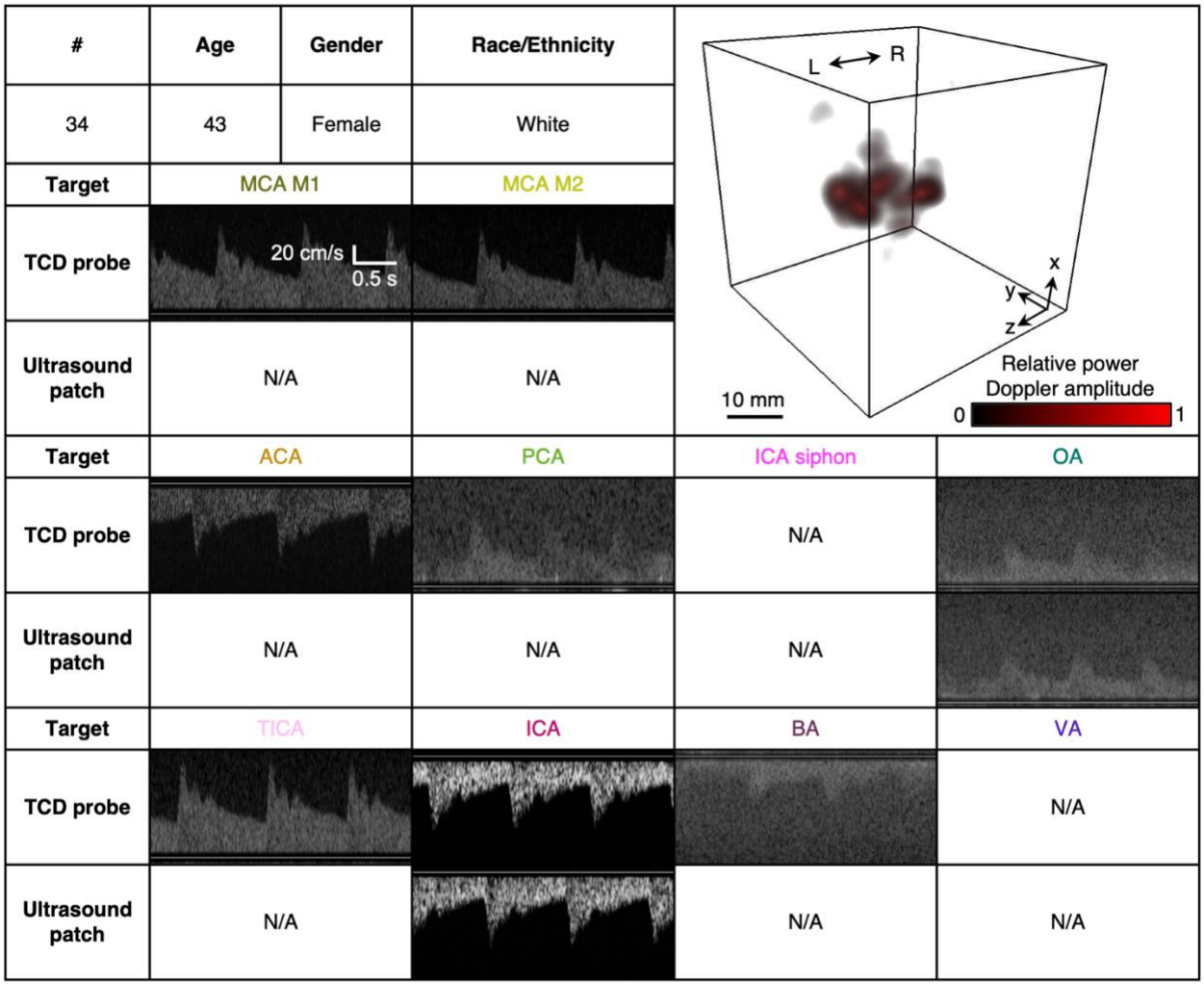

Supplementary Fig. 47 | Volumetric image and blood flow spectra from participant #34. The age, gender, and race/ethnicity that may influence the success rate of TCD sonography were provided. The volumetric image of the cerebral vasculature was collected by the conformal ultrasound patch. The blood flow spectrum of each arterial segment from both the conventional TCD probe and the conformal ultrasound patch was compared accordingly. L, left. R, right. MCA, middle cerebral artery. ACA, anterior cerebral artery. PCA, posterior cerebral artery. ICA, internal carotid artery. OA, ophthalmic artery. TICA, terminal internal carotid artery. BA, basal artery. VA, vertebral artery. All spectra share the same scale bars.

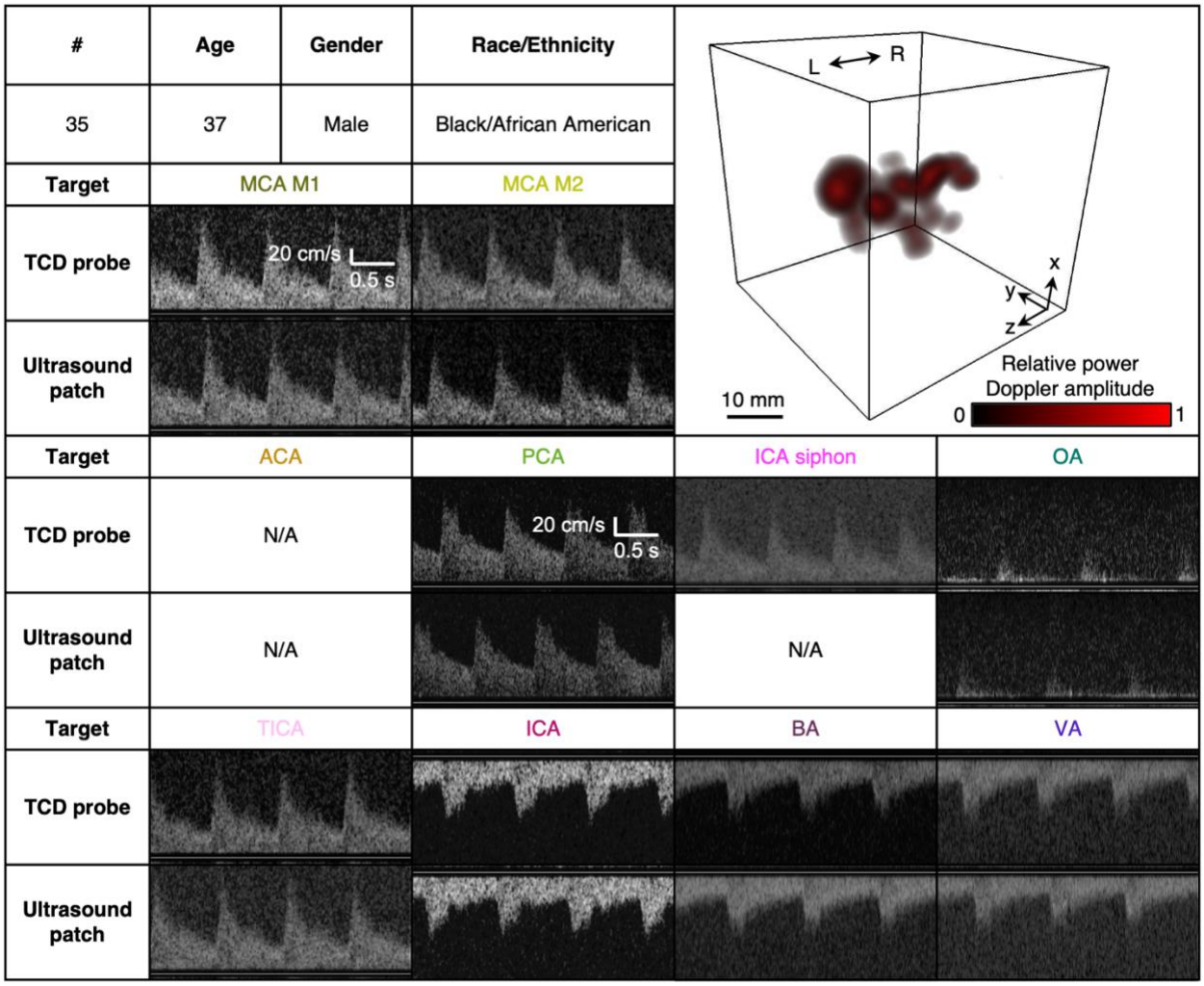

Supplementary Fig. 48 | Volumetric image and blood flow spectra from participant #35. The age, gender, and race/ethnicity that may influence the success rate of TCD sonography were provided. The volumetric image of the cerebral vasculature was collected by the conformal ultrasound patch. The blood flow spectrum of each arterial segment from both the conventional TCD probe and the conformal ultrasound patch was compared accordingly. L, left. R, right. MCA, middle cerebral artery. ACA, anterior cerebral artery. PCA, posterior cerebral artery. ICA, internal carotid artery. OA, ophthalmic artery. TICA, terminal internal carotid artery. BA, basal artery. VA, vertebral artery. The MCA M1, MCA M2, and ICA siphon spectra share the same scale bars. The PCA, OA, TICA, ICA, BA, and VA spectra share the same scale bars.

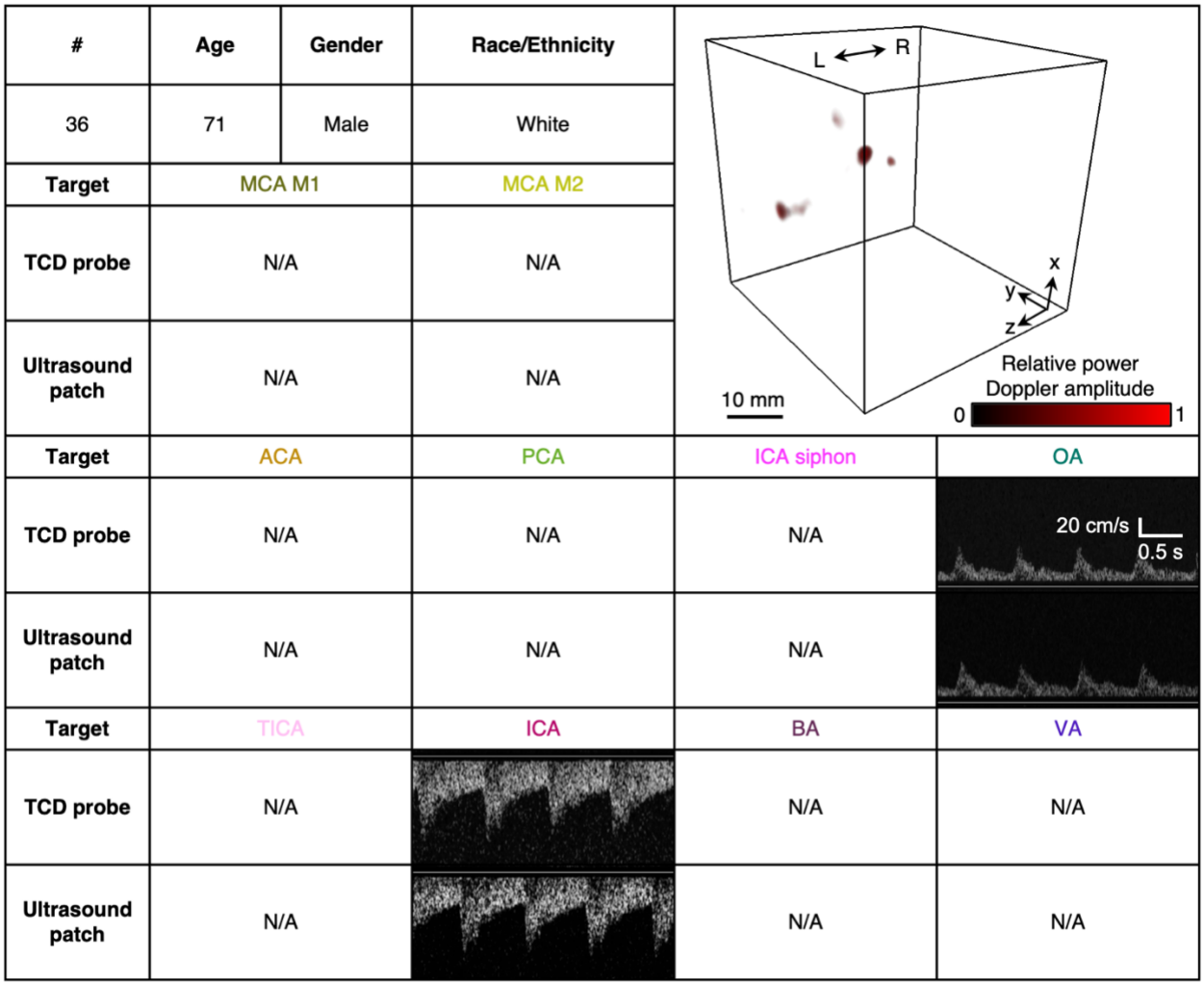

Supplementary Fig. 49 | Volumetric image and blood flow spectra from participant #36. The age, gender, and race/ethnicity that may influence the success rate of TCD sonography were provided. The volumetric image of the cerebral vasculature was collected by the conformal ultrasound patch. The blood flow spectrum of each arterial segment from both the conventional TCD probe and the conformal ultrasound patch was compared accordingly. L, left. R, right. MCA, middle cerebral artery. ACA, anterior cerebral artery. PCA, posterior cerebral artery. ICA, internal carotid artery. OA, ophthalmic artery. TICA, terminal internal carotid artery. BA, basal artery. VA, vertebral artery. All spectra share the same scale bars.

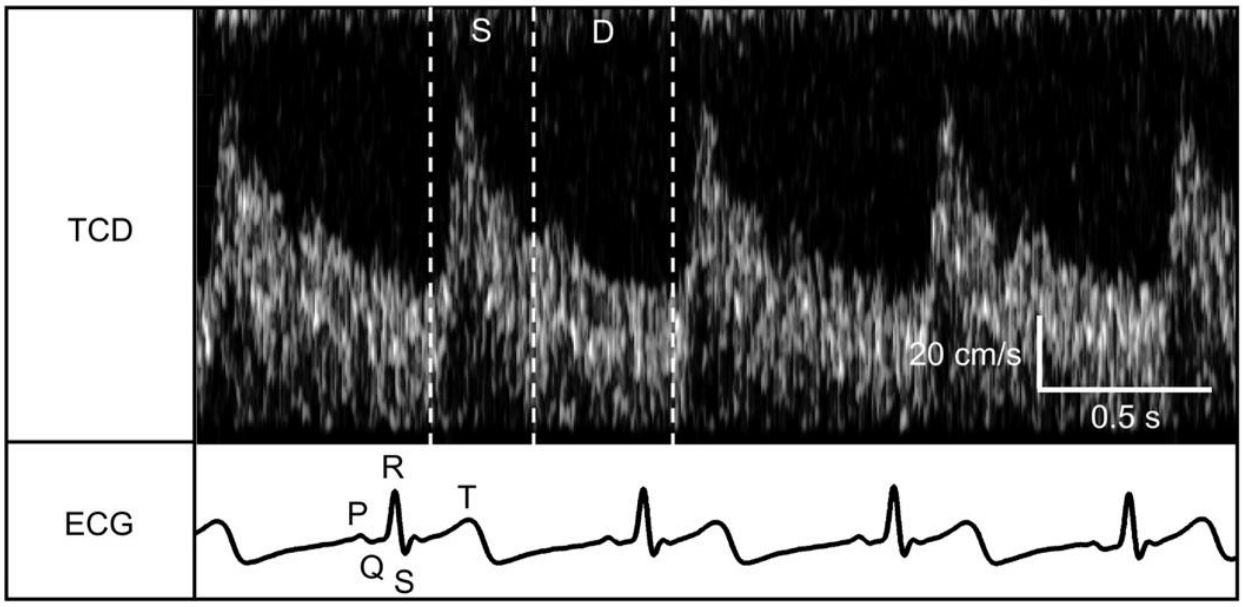

Supplementary Fig. 50 | Analysis of the spectrum in different cardiac phases. The cerebral blood flow spectrum by the conformal ultrasound patch and the electrocardiogram by two electrodes are recorded simultaneously. Different phases in these two waveforms can be correlated. S, systole. D, diastole. ECG, electrocardiogram.

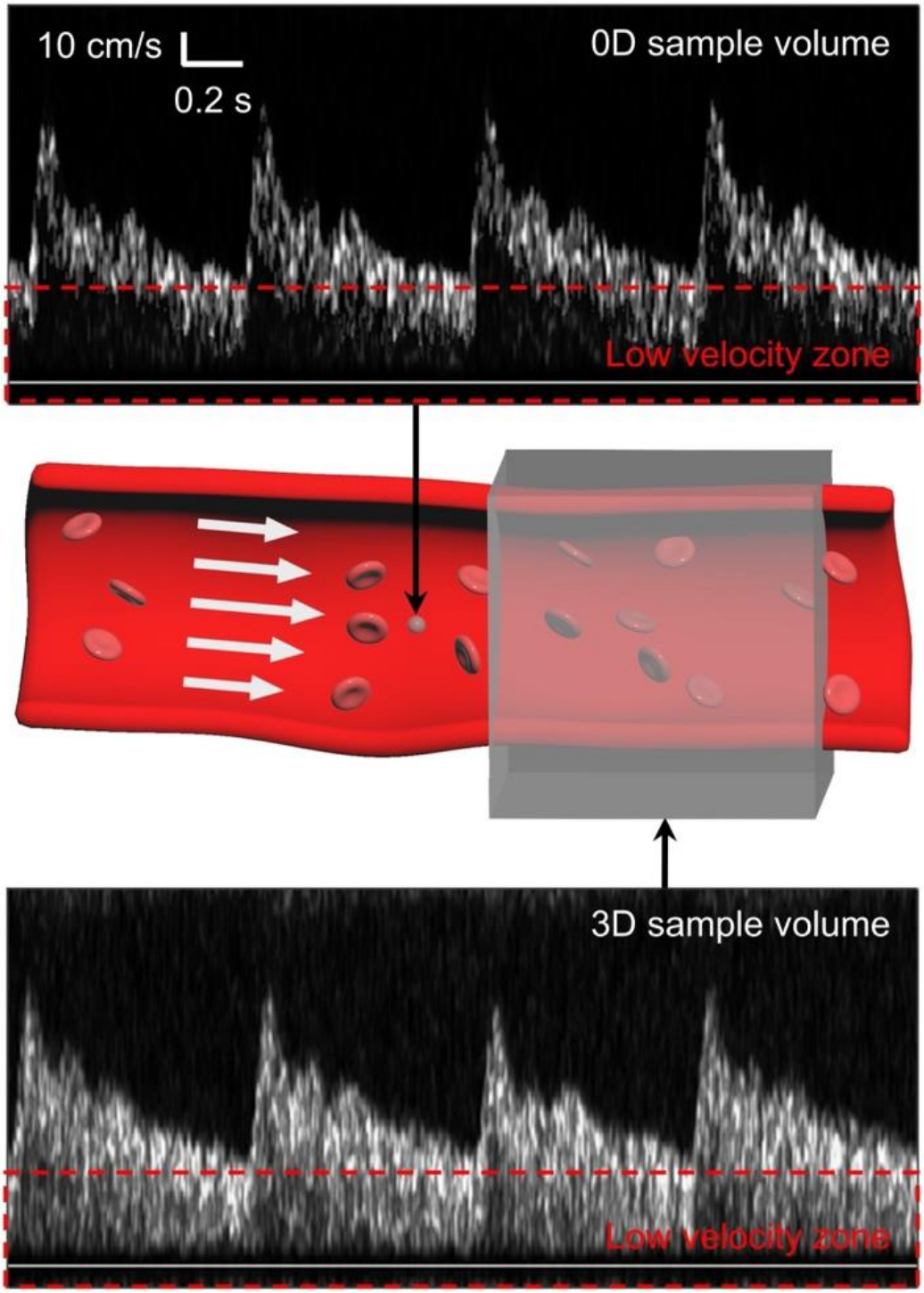

Supplementary Fig. 51 | Sample volume optimization. The comparison of blood flow spectra from different sample volumes. The 0D sample volume (single pixel, around 0.77×0.77×0.77 mm^3) only contains partial blood flow distributions, while the 3D sample volume (216 pixels, around 4.62×4.62×4.62 mm^3) contains the entire blood flow distributions of the target blood vessel segment. For patients with cerebral arterial diseases such as stenosis, the turbulence flow pattern may happen in the zone of low frequency shift (i.e., low blood flow velocity), which can be seen only if an appropriate 3D sample volume is selected. The spectra share the same scale bars.

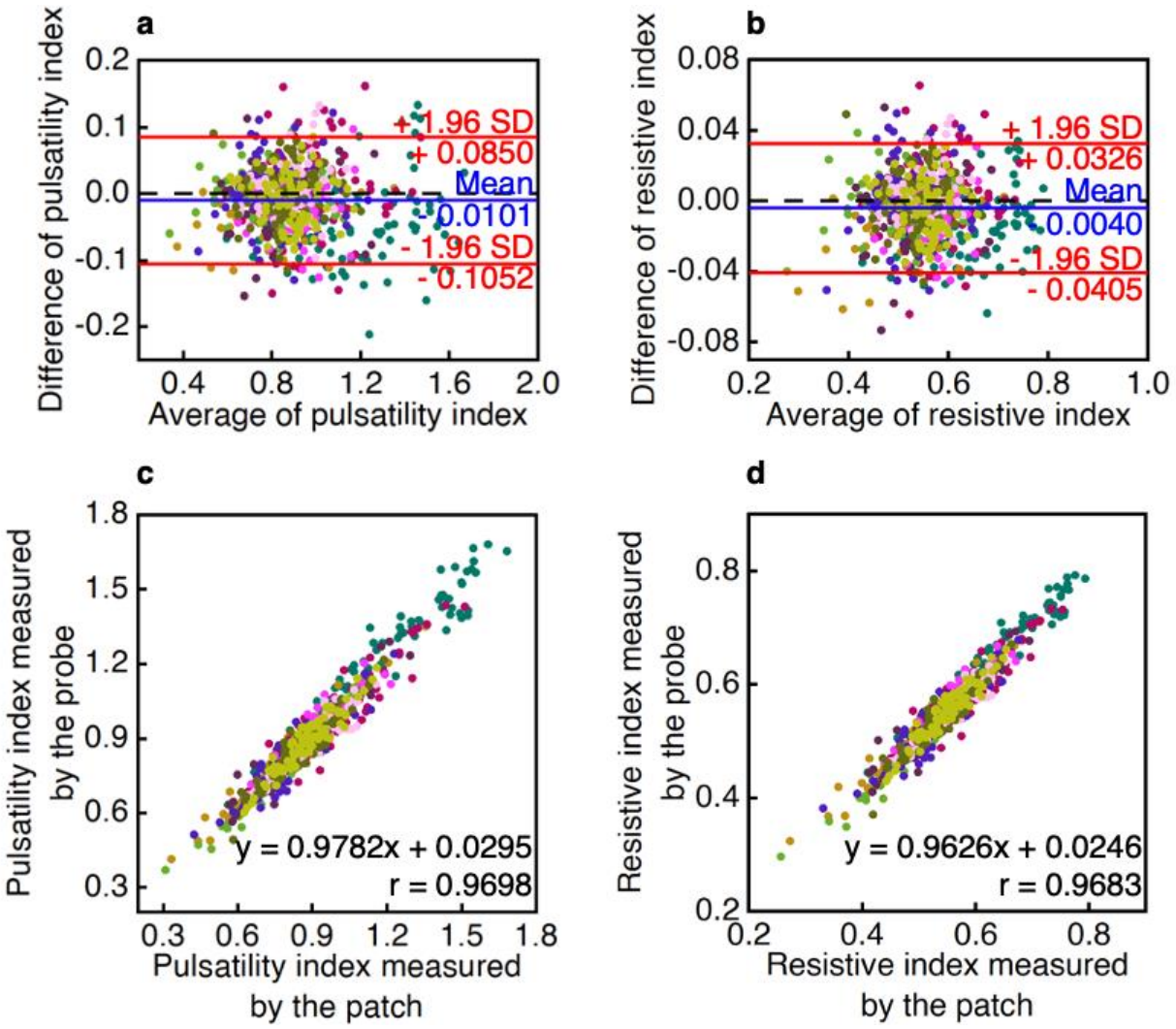

Supplementary Fig. 52 | Statistical analysis of the pulsatility index and resistive index. Bland-Altman plots of **a**, pulsatility index, and **b**, resistive index measured by a conventional TCD probe and the conformal ultrasound patch on all 36 participants. Solid blue lines are the mean differences of the measurements between the two modalities. Solid red lines are 95% limits of agreement (i.e., 1.96 standard deviations above and below the mean differences). Black dashed lines are the zero difference of the measurements between the two modalities. The small mean difference and standard deviation of the difference suggest a strong agreement between these two sensing modalities. Scatter plots of **c**, the pulsatility index, and **d**, the resistive index measured by a conventional TCD probe and the conformal ultrasound patch. The linear regression equations and Pearson correlation coefficient r is labelled in each plot. Both of the Pearson correlation coefficients are larger than 0.9, indicating a strong correlation between the pulsatility index and resistive index measurements from the two modalities. Each plot has 762 data points that are color-coded for different arterial segments (i.e., cider for ACA, dark cyan for OA, xanthic for MCA M2, juniper for MCA M1, boysenberry for BA, blueberry for VA, hibiscus for ICA, kelly green for PCA, magenta for ICA siphon, and carnation pink for TICA). SD, standard deviation. r, the Pearson correlation coefficient.

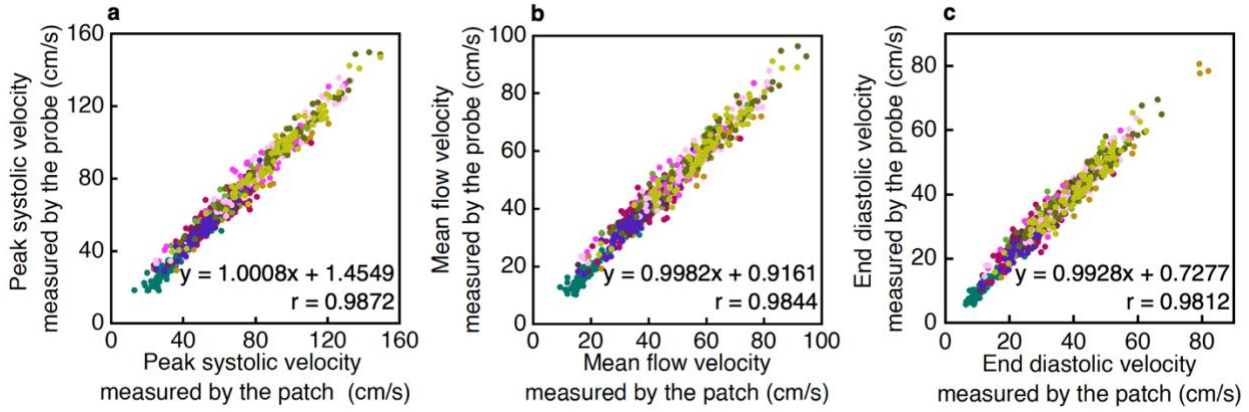

Supplementary Fig. 53 | Correlation analysis of blood flow velocity measurements. Scatter plots show a comparison between a conventional TCD probe and the conformal ultrasound patch in measuring **a**, peak systolic velocity, **b**, mean flow velocity, and **c**, end diastolic velocity on all 36 participants. The linear regression equations and Pearson correlation coefficient r for each set of data are displayed within each respective plot. The high Pearson correlation coefficients indicate a strong correlation between blood flow measurements made by the conventional TCD probe and the conformal ultrasound patch. Each plot has 762 data points that are color-coded for different arterial segments (i.e., cider for ACA, dark cyan for OA, xanthic for MCA M2, juniper for MCA M1, boysenberry for BA, blueberry for VA, hibiscus for ICA, kelly green for PCA, magenta for ICA siphon, and carnation pink for TICA). r, the Pearson correlation coefficient.

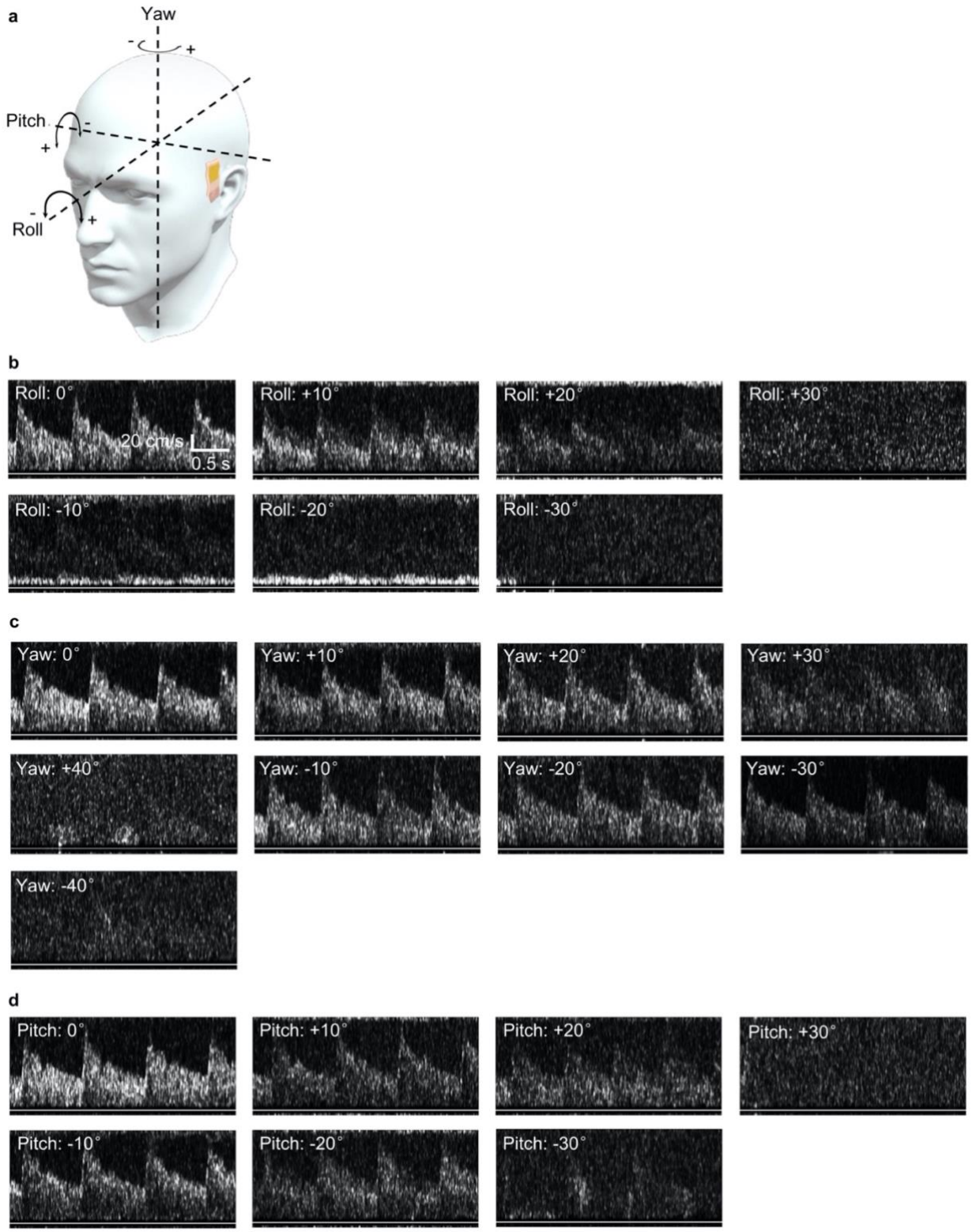

Supplementary Fig. 54 | Motion tolerance of the conformal ultrasound patch. a, Schematic illustration of head rotations in three degrees of freedom, including rolling, yawing, and pitching. **b-d**, MCA spectra recorded under different degrees of rolling, yawing, and pitching. The rotation may result in relative movements between the patch and the scalp because of the ultrasound gel at

the interface. The relative movements lead to gradual signal loss when the rotation angle increases. The conformal ultrasound patch can tolerate a larger degree of yawing than rolling and pitching. The spectra share the same scale bars.

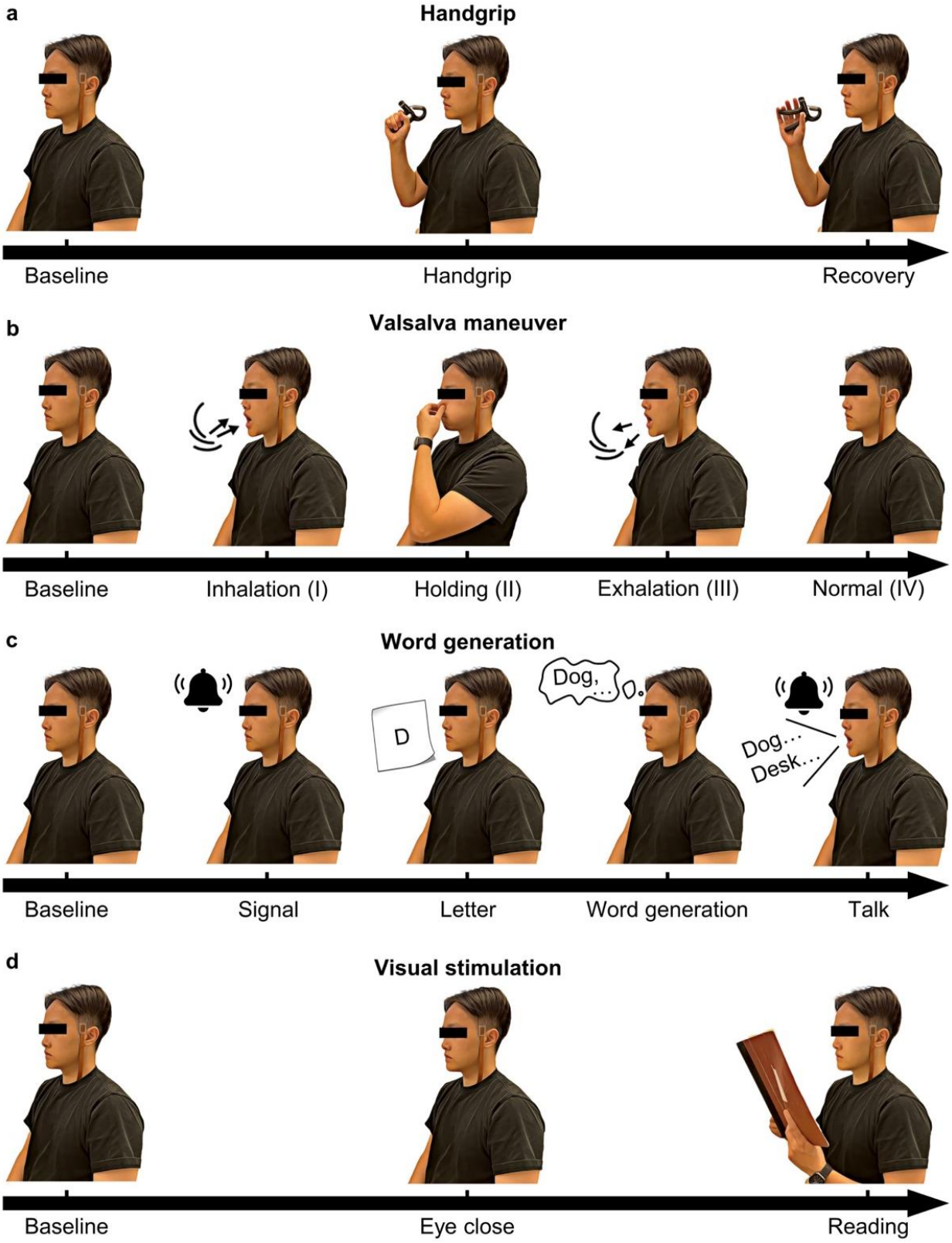

Supplementary Fig. 55 | Activities for altering cerebral flow. a, For handgrip, the participant performed baseline recording, handgrip exercise, and recovery. The recorded left MCA is contralateral to the gripping right hand. **b**, For Valsalva maneuver, the participant performed

baseline recording, deep inhalation, breath holding, exhalation, and normal breathing. The left MCA is recorded during the entire activity. **c**, For word generation, after baseline recording, the participant was cued by tone stimulation, given a letter, asked to make up as many words as possible using the given letter, and asked to orally report them after a second auditory signal. The left MCA is recorded during the entire activity. **d**, For visual stimulation, the participant performed baseline recording, eye closing, and reading a news magazine. The left PCA is recorded during the entire activity.

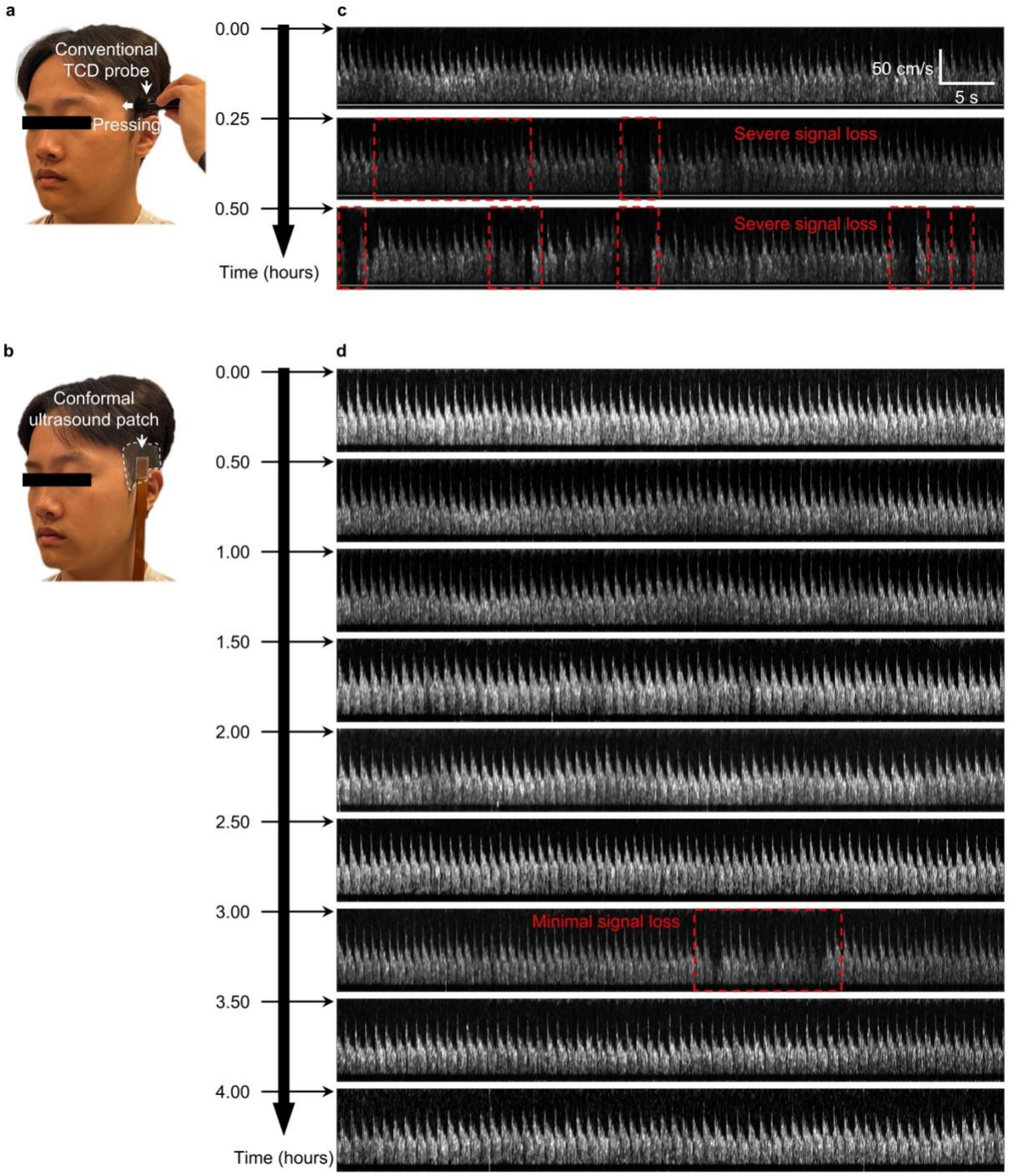

Supplementary Fig. 56 | Long-term MCA spectra recording. a-b, Operational setups of a conventional TCD probe and the conformal ultrasound patch. The conventional TCD probe needs to be manually held. Pressing is required on the probe-skin interface, whereas the ultrasound patch can conform to the skin with Tegaderm. The Tegaderm boundary is labeled in a white dashed line. **c**, 30 min continuous monitoring of the MCA spectra by the conventional TCD probe. 1 min spectra are shown every 15 min. There are periods with severe signal loss during relative movement between the head and the probe. The spectra share the same scale bars. **d**, 4 hours

continuous monitoring of the MCA spectra by the conformal ultrasound patch. 1 min spectrum is shown every 30 min. The ultrasound patch can conform to the transcranial windows with minimal displacement between the device and target arteries. As a result, the patch can tolerate considerably more motion than its conventional counterpart. The spectra share the same scale bars.

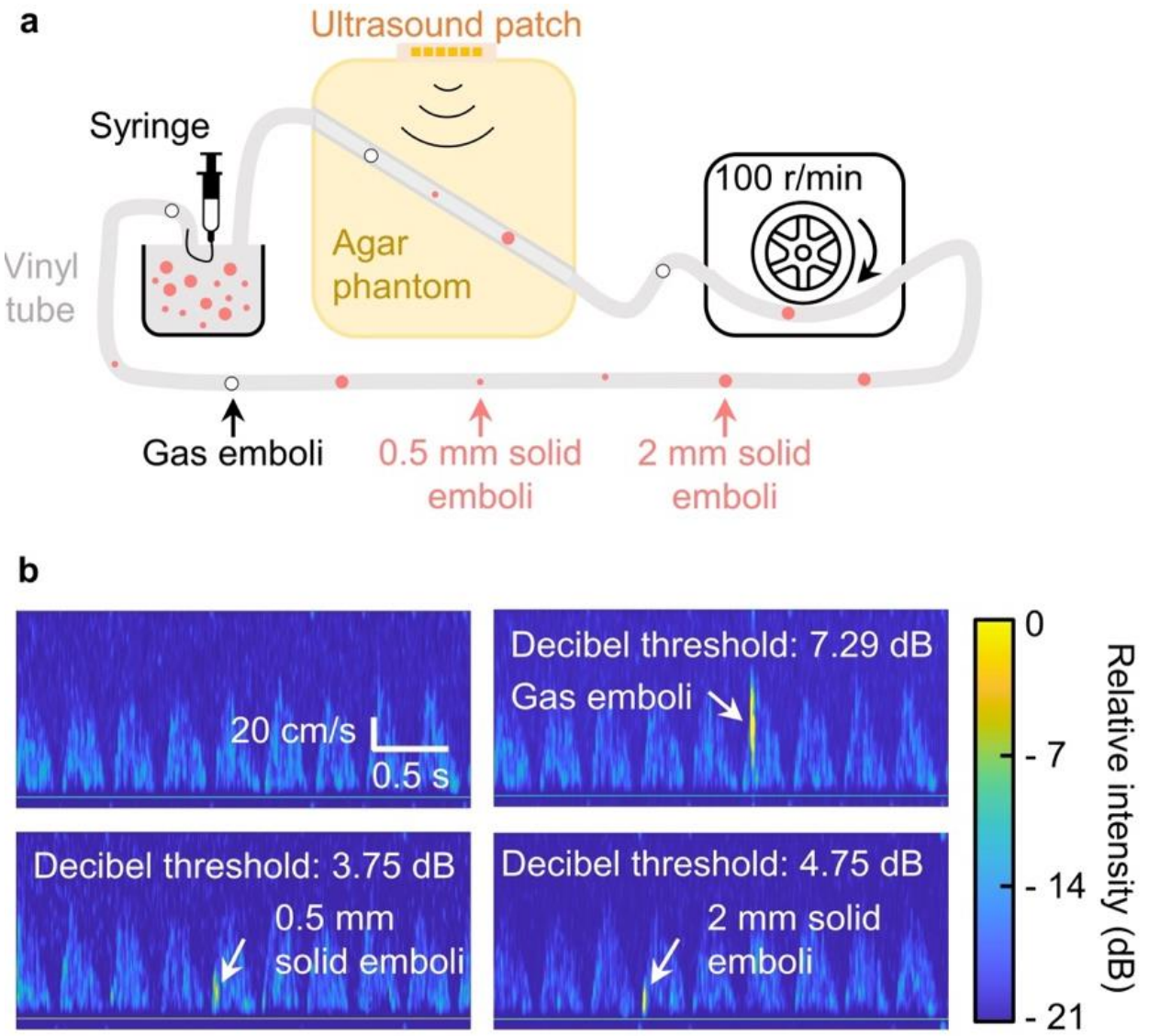

Supplementary Fig. 57 | Conformal ultrasound patch for emboli detection on phantom. a, Schematic experimental setup. Three different types of emboli are used, including gas emboli, 0.5 mm solid emboli, and 2 mm solid emboli. **b**, Flow spectra of baseline, with gas emboli, with 0.5 mm solid emboli, and with 2 mm solid emboli, respectively. The spectra share the same scale bars.

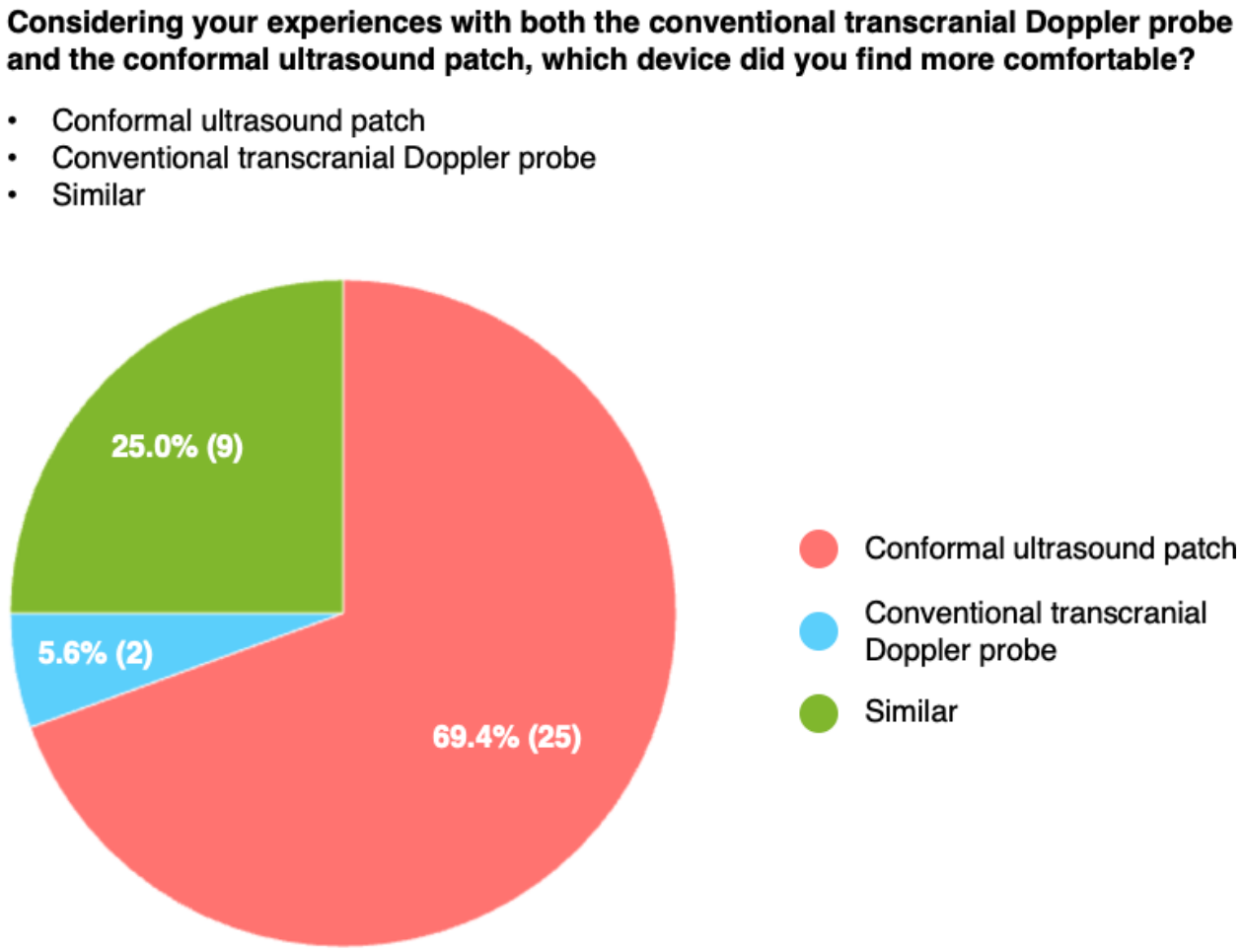

Supplementary Fig. 58 | Survey of users' experience. Comparison of comfort levels between the conformal ultrasound patch and the conventional TCD probe based on participant feedback. Out of the 36 participants, 69.4% (25) found the conformal patch more comfortable, 25% (9) found both devices equally comfortable. Notably, the 5.6% (2 participants) who preferred the TCD probe felt discomfort from tape removal associated with the ultrasound patch. The duration of measurement by the conventional TCD probe was about 15 minutes for the majority of participants. An extended duration of measurement with the conventional TCD probe may increase the preference for the conformal ultrasound patch, as the latter potentially offers greater comfort over longer periods of utilization.

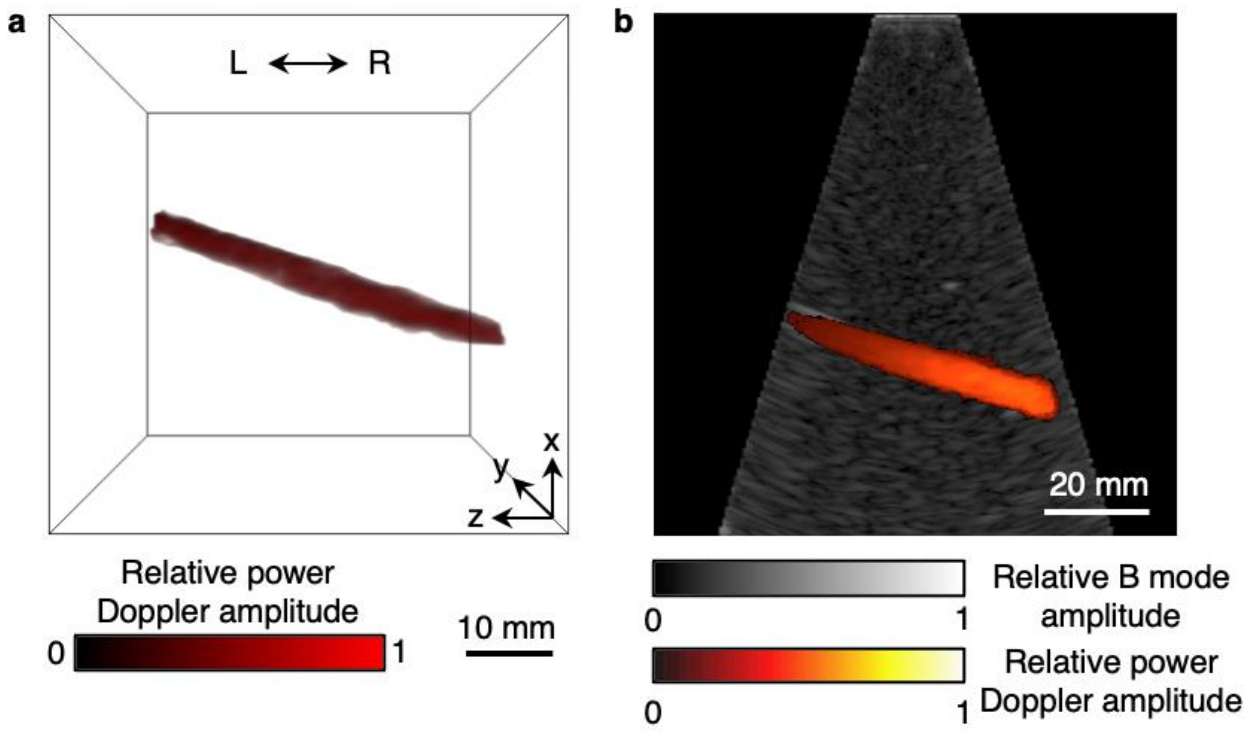

Supplementary Fig. 59 | Characterization of flow in an arterial phantom. We pumped Doppler fluid (769DF, CIRS) through a Doppler flow phantom (ATS 523A, CIRS) with 4 mm in diameter at an approximate depth of 60-80 mm. The figure shows volumetric flow imaging results from the ultrasound patch alongside the ground truth obtained by a commercial ultrasound probe (e.g., a P4_2v phased array probe) using duplex mode (B mode and power Doppler mode) imaging. **a**, A volumetric image of the flow in the phantom captured by the ultrasound patch. **b**, The ground truth collected by the commercial ultrasound probe. These results demonstrate that the vessel structure measurement from the ultrasound patch is consistent with that from conventional imaging devices, validating its accuracy in capturing blood flow dynamics. L, left. R, right.

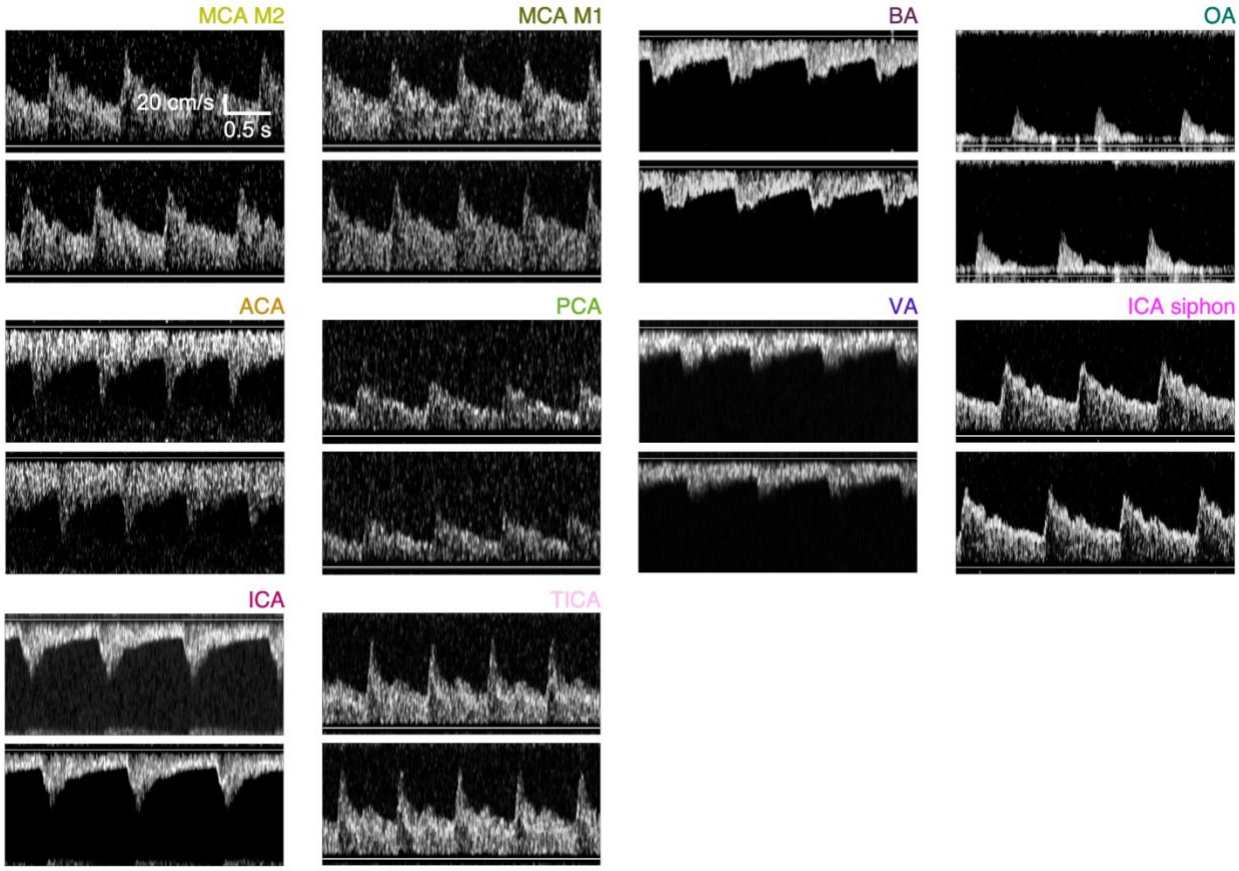

Supplementary Fig. 60 | The comparison of blood flow spectra measurements. The measurements were taken by a clinically qualified ultrasonographer (i.e., A. Lam) with more than 30 years of experience in TCD (upper spectra) and S. Zhou (lower spectra) on all different target arterial sections by using a conventional TCD probe. All side-by-side comparison datasets illustrate similar waveforms and spectral properties, reinforcing the reliability and the accuracy of the measurements made by S. Zhou. The spectra share the same scale bars.

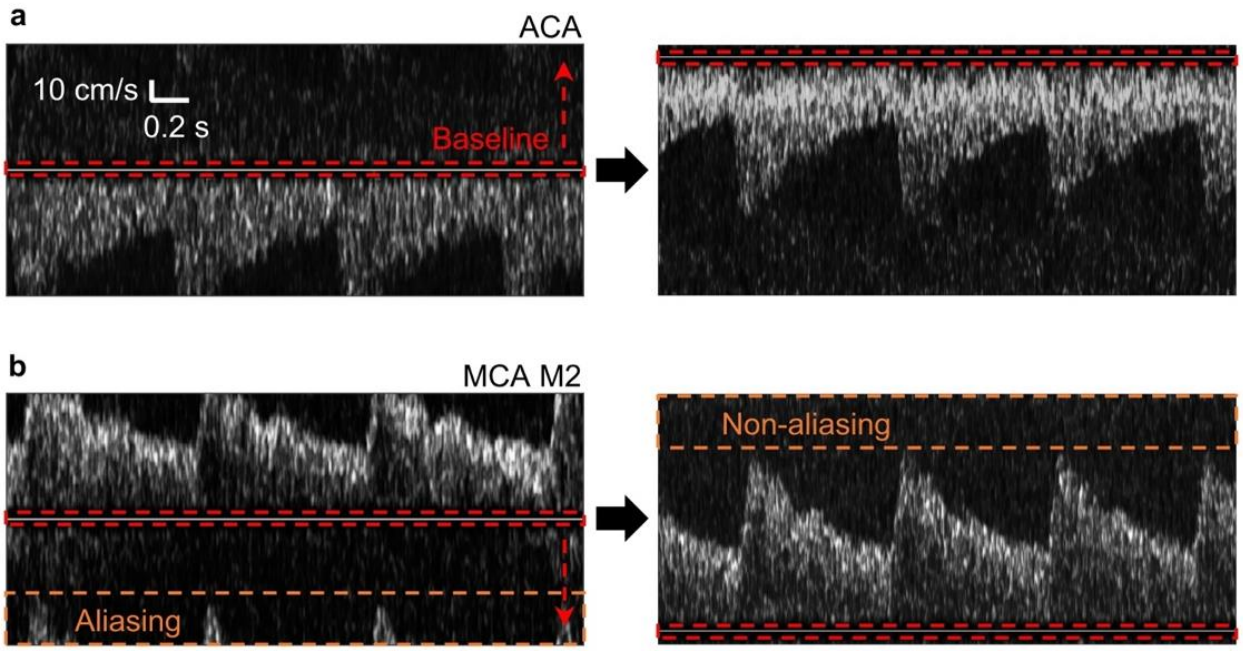

Supplementary Fig. 61 | Baseline shifting and aliasing prevention. Once a signal is sampled below the Nyquist rate, the under sampled signals result in an inability to record direction and velocity accurately, which is known as the aliasing effect. For ACA and MCA M2 spectra monitoring, the baselines labelled by the red dashed boxes can be shifted **a**, up and **b**, down to prevent the aliasing effect labelled by the orange dashed boxes. The spectra share the same scale bars.

Ischemic cerebrovascular diseases	Peri-procedural / operative procedures	Neurological / Neurosurgical intensive care	Others
Microembolus detection	Cerebral thrombolysis in acute stroke	Vasospasm after subarachnoid hemorrhage	Pharmacologic vasomotor testing
Sickle cell disease	Carotid endarterectomy	Raised intracranial pressure	Cerebral autoregulation
Right to left cardiac shunts	Carotid angioplasty and stenting	Head injury	Functional TCD for brain activity mapping
Intra and extra-cranial arterial steno-occlusive disease	Coronary artery bypass surgery	Cerebral circulatory arrest and brain death	Preeclampsia
Arteriovenous malformations and fistulas	Heart surgery	Intracerebral aneurysm and parenchymal hematoma detection	Liver failure/Hepatic encephalopathy
Internal carotid artery stenosis	Coronary angioplasty		
Acute brain infarction			

Supplementary Table 1 | Applications of TCD sonography. The existing applications of TCD sonography includes diagnosing ischemic cerebrovascular diseases, monitoring in peri-procedural/operative procedures, neurological/neurosurgical intensive care, and many others. The conformal ultrasound patch demonstrated in this work holds implications for all of these applications.

Windows	Targets	Depth (mm)	Velocities (cm/s)	Directions
Temporal	ACA	60-75	50 ± 11	Away
	MCA M2	30-65	55 ± 12	Toward
	MCA M1	30-65	55 ± 12	Toward
	PCA	60-70	40 ± 10	Bidirectional
	TICA	55-65	39 ± 9	Toward
Orbital	OA	45-55	20 ± 5	Toward
	ICA Siphon	60-80	45 ± 15	Bidirectional
Submandibular	ICA	30-60	37 ± 9	Away
Suboccipital	BA	80-100	41 ± 10	Away
	VA	60-80	38 ± 10	Away

Supplementary Table 2 | TCD sonography protocols used in this work. The protocols are summarized according to the transcranial window for each cerebral vessel, depth range of the target vessel, corresponding mean flow velocity, and flow directions in these cerebral artery segments relative to the device.

Supplementary Video 1 | 25 s of MCA blood flow spectrum recording with audio. The audio play can be used for training new sonographers and diagnosing diseases (e.g., bruits and murmurs in stenosis[48,144], and chirps and beeps in embolism[145]).

References

1 Foreman, B. & Claassen, J. Quantitative EEG for the detection of brain ischemia. *Crit. Care* **16**, 216 (2012).

2 Fantini, S., Sassaroli, A., Tgavalekos, K. T. & Kornbluth, J. Cerebral blood flow and autoregulation: current measurement techniques and prospects for noninvasive optical methods. *Neurophotonics* **3**, 031411 (2016).

3 Ke, X.-Y. *et al.* Advances in electrical impedance tomography-based brain imaging. *Mil. Med. Res.* **9**, 1-22 (2022).

4 Muehllehner, G. & Karp, J. S. Positron emission tomography. *Phys. Med. Biol.* **51**, R117 (2006).

5 Høedt-Rasmussen, K., Sveinsdottir, E. & Lassen, N. A. Regional Cerebral low in Man Determined by Intral-artrial Injection of Radioactive Inert Gas. *Circ. Res.* **18**, 237-247 (1966).

6 Yandrapalli, S. & Puckett, Y. *SPECT Imaging*. (StatPearls Publishing, 2020).

7 Pindzola, R. R. & Yonas, H. The xenon-enhanced computed tomography cerebral blood flow method. *Neurosurgery* **43**, 1488-1491 (1998).

8 Hoeffner, E. G. *et al.* Cerebral perfusion CT: technique and clinical applications. *Radiology* **231**, 632-644 (2004).

9 Shaban, S. *et al.* Digital subtraction angiography in cerebrovascular disease: current practice and perspectives on diagnosis, acute treatment and prognosis. *Acta Neurol. Belg.* **122**, 763-780 (2022).

10 Scalzo, F. & Liebeskind, D. S. Perfusion Angiography in Acute Ischemic Stroke. *Comput. Math Methods Med.* **2016**, 2478324 (2016).

11 Boxerman, J. L. *et al.* Consensus recommendations for a dynamic susceptibility contrast MRI protocol for use in high-grade gliomas. *Neuro-oncology* **22**, 1262-1275 (2020).

12 Petcharunpaisan, S., Ramalho, J. & Castillo, M. Arterial spin labeling in neuroimaging. *World J. Radiol.* **2**, 384-398 (2010).

13 Kety, S. S. & Schmidt, C. F. The determination of cerebral blood flow in man by the use of nitrous oxide in low concentrations. *Am. J. Physiol.* **143**, 53-66 (1945).

14 Wilson, E. M. & Halsey Jr, J. H. Bilateral jugular venous blood flow by thermal dilution. *Stroke* **1**, 348-355 (1970).

15 Carter, L. P. Thermal diffusion flowmetry. *Neurosurg. Clin. N. Am.* **7**, 749-754 (1996).

16 Tidswell, T., Gibson, A., Bayford, R. H. & Holder, D. S. Three-dimensional electrical impedance tomography of human brain activity. *NeuroImage* **13**, 283-294 (2001).

17 Bagshaw, A. P. *et al.* Electrical impedance tomography of human brain function using reconstruction algorithms based on the finite element method. *NeuroImage* **20**, 752-764 (2003).

18 Seubert, C. N., Cibula, J. E. & Mahla, M. E. in *Textbook of Neurointensive Care* Chapter 7, 109-126 (Springer, 2013).

19 Le Roux, P. in *Textbook of Neurointensive Care* Chapter 8, 127-145 (Springer, 2013).

20 Samaei, S. *et al.* Time-domain diffuse correlation spectroscopy (TD-DCS) for noninvasive, depth-dependent blood flow quantification in human tissue in vivo. *Sci. Rep.* **11**, 1-10 (2021).

21 Moerman, A. & Wouters, P. Near-infrared spectroscopy (NIRS) monitoring in contemporary anesthesia and critical care. *Acta Anaesthesiol. Belg.* **61**, 185-194 (2010).

22 Pham, T., Tgavalekos, K., Sassaroli, A., Blaney, G. & Fantini, S. Quantitative

measurements of cerebral blood flow with near-infrared spectroscopy. *Biomed. Opt. Express* **10**, 2117-2134 (2019).
23 Sanderson, M. & Yeung, H. Guidelines for the use of ultrasonic non-invasive metering techniques. *Flow Meas.* **13**, 125-142 (2002).
24 Willie, C. K. *et al.* Utility of transcranial Doppler ultrasound for the integrative assessment of cerebrovascular function. *J. Neurosci. Methods* **196**, 221-237 (2011).
25 Pietrangelo, S. J., Lee, H.-S. & Sodini, C. G. in *Intracranial Pressure & Neuromonitoring XVI* 111-114 (Springer, 2018).
26 Lindsey, B. D. *et al.* The ultrasound brain helmet: new transducers and volume registration for in vivo simultaneous multi-transducer 3-D transcranial imaging. *IEEE Trans. Ultrason. Ferroelectr. Freq. Control* **58**, 1189-1202 (2011).
27 Purkayastha, S. & Sorond, F. Transcranial Doppler ultrasound: technique and application. *Semin. Neurol.* **32**, 411-420 (2012).
28 Clarke, B. Normal bone anatomy and physiology. *Clin. J. Am. Soc. Nephrol.* **3**, S131-139 (2008).
29 Hoskins, P. R., Martin, K. & Thrush, A. *Diagnostic ultrasound: physics and equipment*. (CRC Press, 2019).
30 Laugier, P. & Haïat, G. *Bone quantitative ultrasound*. Vol. 576 (Springer, 2011).
31 Wear, K. A. Mechanisms of Interaction of Ultrasound With Cancellous Bone: A Review. *IEEE Trans. Ultrason. Ferroelectr. Freq. Control* **67**, 454-482 (2020).
32 Deverson, S., Evans, D. H. & Bouch, D. C. The effects of temporal bone on transcranial Doppler ultrasound beam shape. *Ultrasound Med. Biol.* **26**, 239-244 (2000).
33 Food and Drug Administration. Marketing clearance of diagnostic ultrasound systems and transducers: Guidance for industry and Food and Drug Administration staff. *Food Drug Admin., Silver Spring, MD, USA, Tech. Rep. FDA-2017-D-5372* (2023).
34 Li, P.-C. & O'Donnell, M. Phase aberration correction on two-dimensional conformal arrays. *IEEE Trans. Ultrason. Ferroelectr. Freq. Control* **42**, 73-82 (1995).
35 Flax, S. & O'Donnell, M. Phase-aberration correction using signals from point reflectors and diffuse scatterers: Basic principles. *IEEE Trans. Ultrason. Ferroelectr. Freq. Control* **35**, 758-767 (1988).
36 Kyriakou, A. *et al.* A review of numerical and experimental compensation techniques for skull-induced phase aberrations in transcranial focused ultrasound. *Int. J. Hyperthermia.* **30**, 36-46 (2014).
37 Yin, X. & Hynynen, K. A numerical study of transcranial focused ultrasound beam propagation at low frequency. *Phys. Med. Biol.* **50**, 1821-1836 (2005).
38 Lin, M., Hu, H., Zhou, S. & Xu, S. Soft wearable devices for deep-tissue sensing. *Nat. Rev. Mater.* **7**, 850-869 (2022).
39 Wang, C. *et al.* Monitoring of the central blood pressure waveform via a conformal ultrasonic device. *Nat. Biomed. Eng.* **2**, 687-695 (2018).
40 Lin, M. *et al.* A fully integrated wearable ultrasound system to monitor deep tissues in moving subjects. *Nat. Biotechnol.* (2023).
41 Wang, C. *et al.* Continuous monitoring of deep-tissue haemodynamics with stretchable ultrasonic phased arrays. *Nat. Biomed. Eng.* **5**, 749-758 (2021).
42 Wang, C. *et al.* Bioadhesive ultrasound for long-term continuous imaging of diverse organs. *Science* **377**, 517-523 (2022).
43 Hu, H. *et al.* A wearable cardiac ultrasound imager. *Nature* **613**, 667-675 (2023).

44 Zhang, L. *et al.* A conformable phased-array ultrasound patch for bladder volume monitoring. *Nat. Electron.* **7**, 77-90 (2023).
45 Gao, X. *et al.* A photoacoustic patch for three-dimensional imaging of hemoglobin and core temperature. *Nat. Commun.* **13**, 7757 (2022).
46 Hu, H. *et al.* Stretchable ultrasonic arrays for the three-dimensional mapping of the modulus of deep tissue. *Nature Biomed. Eng.* (2023).
47 Konan, L. M., Reddy, V. & Mesfin, F. B. *Neuroanatomy, Cerebral Blood Supply*. (StatPearls Publishing, 2018).
48 Aaslid, R. *Transcranial doppler sonography*. (Springer Science & Business Media, 2012).
49 Silverman, A. & Petersen, N. *Physiology, cerebral autoregulation*. (StatPearls Publishing, 2022).
50 Jones, J. D., Castanho, P., Bazira, P. & Sanders, K. Anatomical variations of the circle of Willis and their prevalence, with a focus on the posterior communicating artery: A literature review and meta-analysis. *Clin. Anat.* **34**, 978-990 (2021).
51 Hindenes, L. B. *et al.* Variations in the Circle of Willis in a large population sample using 3D TOF angiography: The Tromso Study. *PLoS One* **15**, e0241373 (2020).
52 Yeniceri, I. O., Cullu, N., Deveer, M. & Yeniceri, E. N. Circle of Willis variations and artery diameter measurements in the Turkish population. *Folia Morphol. (Warsz)* **76**, 420-425 (2017).
53 Chen, J. *et al.* Anterior Communicating Artery Aneurysms: Anatomical Considerations and Microsurgical Strategies. *Front. Neurol.* **11**, 1020 (2020).
54 Kılıç, T. & Akakın, A. Anatomy of cerebral veins and sinuses. *Handbook on cerebral venous thrombosis* **23**, 4-15 (2008).
55 Hufnagle, J. J. & Tadi, P. in *StatPearls [Internet]* (StatPearls Publishing, 2021).
56 Uddin, M. A., Haq, T. U. & Rafique, M. Z. Cerebral venous system anatomy. *J. Pak. Med. Assoc.* **56**, 516 (2006).
57 Valdueza, J. M., Schmierer, K., Mehraein, S. & Einhaüpl, K. M. Assessment of normal flow velocity in basal cerebral veins: a transcranial Doppler ultrasound study. *Stroke* **27**, 1221-1225 (1996).
58 https://verasonics.com/volume-imaging/.
59 Harris, G. R. *et al.* Hydrophone Measurements for Biomedical Ultrasound Applications: A Review. *IEEE Trans Ultrason. Ferroelectr. Freq. Control* **70**, 85-100 (2022).
60 Wear, K. A. Hydrophone Spatial Averaging Correction for Acoustic Exposure Measurements From Arrays-Part I: Theory and Impact on Diagnostic Safety Indexes. *IEEE Trans. Ultrason. Ferroelectr. Freq. Control* **68**, 358-375 (2021).
61 International Electrotechnical Commission. IEC 62127-2 "Ultrasonics – Hydrophones – Part 2: Calibration for ultrasonic fields up to 40 MHz". *International Electrotechnical Commission, Geneva, Switzerland*, Ed. 2.1 (2013).
62 International Electrotechnical Commission. IEC 62359:2010/AMD1:2017 "Ultrasonics – Field Characterization – Test methods for the determination of thermal and mechanical indices related to medical diagnostic ultrasonic fields". *International Electrotechnical Commission, Geneva, Switzerland*, Ed. 2.1 (2017).
63 International Electrotechnical Commission. IEC 62127-1:2022 "Ultrasonics – Hydrophones – Part 1: Measurement and characterization of medical ultrasonic fields". *International Electrotechnical Commission, Geneva, Switzerland*, Ed. 2.0 (2022).
64 Duck, F. A. Medical and non-medical protection standards for ultrasound and infrasound.

Prog. Biophys. Mol. Biol. **93**, 176-191 (2007).
65 International Electrotechnical Commission. IEC 60601-2-37 "Medical Electrical Equipment – Part 2 – 37: Particular Requirements for the Basic Safety and Essential Performance of Ultrasonic Medical Diagnostic and Monitoring Equipment". *International Electrotechnical Commission, Geneva, Switzerland*, Ed. 2.1 (2015).
66 https://www.aium.org/resources/official-statements/view/recommended-maximum-scanning-times-for-displayed-thermal-index-(ti)-values.
67 Bigelow, T. A. *et al.* The thermal index: its strengths, weaknesses, and proposed improvements. *J. Med. Ultrasound* **30**, 714-734 (2011).
68 Montaldo, G., Tanter, M., Bercoff, J., Benech, N. & Fink, M. Coherent plane-wave compounding for very high frame rate ultrasonography and transient elastography. *IEEE Trans. Ultrason. Ferroelectr. Freq. Control* **56**, 489-506 (2009).
69 Montaldo, G. *et al.* in *2010 IEEE International Symposium on Biomedical Imaging: From Nano to Macro.* 324-327 (IEEE).
70 Bercoff, J. *et al.* Ultrafast compound Doppler imaging: Providing full blood flow characterization. *IEEE Trans. Ultrason. Ferroelectr. Freq. Control* **58**, 134-147 (2011).
71 Demene, C. *et al.* Spatiotemporal Clutter Filtering of Ultrafast Ultrasound Data Highly Increases Doppler and fUltrasound Sensitivity. *IEEE Trans. Med. Imaging* **34**, 2271-2285 (2015).
72 Baranger, J. *et al.* Adaptive Spatiotemporal SVD Clutter Filtering for Ultrafast Doppler Imaging Using Similarity of Spatial Singular Vectors. *IEEE Trans. Med. Imaging* **37**, 1574-1586 (2018).
73 https://viasonix.com/products/transcranial-doppler/.
74 Mathieu, J. & Scott, J. *An introduction to turbulent flow*. (Cambridge University Press, 2000).
75 Quarteroni, A. *Modeling the heart and the circulatory system*. Vol. 14 (Springer, 2015).
76 Puppo, C. in *Neurosonology in Critical Care* 215-232 (Springer, 2022).
77 Marinoni, M., Ginanneschi, A., Forleo, P. & Amaducci, L. Technical limits in transcranial Doppler recording: Inadquate acoustic windows. *Ultrasound Med. Biol.* **23**, 1275-1277 (1997).
78 Bakker, S. L. *et al.* Cerebral haemodynamics in the elderly: the rotterdam study. *Neuroepidemiology* **23**, 178-184 (2004).
79 Lee, C. H., Jeon, S. H., Wang, S. J., Shin, B. S. & Kang, H. G. Factors associated with temporal window failure in transcranial Doppler sonography. *Neurol. Sci.* **41**, 3293-3299 (2020).
80 Brunser, A. M. *et al.* Transcranial Doppler in a Hispanic-Mestizo population with neurological diseases: a study of sonographic window and its determinants. *Brain Behav.* **2**, 231-236 (2012).
81 Kwon, J. H., Kim, J. S., Kang, D. W., Bae, K. S. & Kwon, S. U. The thickness and texture of temporal bone in brain CT predict acoustic window failure of transcranial Doppler. *J. Neuroimaging* **16**, 347-352 (2006).
82 Nader, J. A., Andrade, M. L., Espinosa, V., Zambrano, M. & Del Brutto, O. H. Technical difficulties due to poor acoustic insonation during transcranial Doppler recordings in Amerindians and individuals of European origin. A comparative study. *Eur. Neurol.* **73**, 230-232 (2015).
83 Yagita, Y. *et al.* Effect of transcranial Doppler intensity on successful recording in

Japanese patients. *Ultrasound Med. Biol.* **22**, 701-705 (1996).
84 Wijnhoud, A. D., Franckena, M., van der Lugt, A., Koudstaal, P. J. & Dippel, E. D. Inadequate acoustical temporal bone window in patients with a transient ischemic attack or minor stroke: role of skull thickness and bone density. *Ultrasound Med. Biol.* **34**, 923-929 (2008).
85 Lin, Y.-P., Fu, M.-H. & Tan, T.-Y. Factors Associated with No or Insufficient Temporal Bone Window Using Transcranial Color-coded Sonography. *J. Med. Ultrasound* **23**, 129-132 (2015).
86 Chan, M. Y. *et al.* Success Rate of Transcranial Doppler Scanning of Cerebral Arteries at Different Transtemporal Windows in Healthy Elderly Individuals. *Ultrasound Med. Biol.* **49**, 588-598 (2023).
87 Wong, K. S. *et al.* Use of transcranial Doppler ultrasound to predict outcome in patients with intracranial large-artery occlusive disease. *Stroke* **31**, 2641-2647 (2000).
88 Krejza, J. *et al.* Suitability of temporal bone acoustic window: conventional TCD versus transcranial color-coded duplex sonography. *J. Neuroimaging* **17**, 311-314 (2007).
89 Rabut, C. *et al.* 4D functional ultrasound imaging of whole-brain activity in rodents. *Nat. Methods* **16**, 994-997 (2019).
90 Heiles, B. *et al.* Ultrafast 3D Ultrasound Localization Microscopy Using a 32 x 32 Matrix Array. *IEEE Trans. Med. Imaging* **38**, 2005-2015 (2019).
91 de Riva, N. *et al.* Transcranial Doppler pulsatility index: what it is and what it isn't. *Neurocrit. Care* **17**, 58-66 (2012).
92 Czosnyka, M., Richards, H. K., Whitehouse, H. E. & Pickard, J. D. Relationship between transcranial Doppler-determined pulsatility index and cerebrovascular resistance: an experimental study. *J. Neurosurg.* **84**, 79-84 (1996).
93 Naqvi, J., Yap, K. H., Ahmad, G. & Ghosh, J. Transcranial Doppler ultrasound: a review of the physical principles and major applications in critical care. *Int. J. Vasc. Med.* **2013**, 629378 (2013).
94 Hall, C. N. *et al.* Capillary pericytes regulate cerebral blood flow in health and disease. *Nature* **508**, 55-60 (2014).
95 Davis, M. J. Perspective: physiological role(s) of the vascular myogenic response. *Microcirculation* **19**, 99-114 (2012).
96 Paulson, O., Strandgaard, S. & Edvinsson, L. Cerebral autoregulation. *Cerebrovasc. Brain Metab. Rev.* **2**, 161-192 (1990).
97 Mehta, J. & Li, D. Identification and autoregulation of receptor for OX-LDL in cultured human coronary artery endothelial cells. *Biochem. Biophys. Res. Commun.* **248**, 511-514 (1998).
98 Golding, E. M., Robertson, C. S. & Bryan, R. M. The consequences of traumatic brain injury on cerebral blood flow and autoregulation: a review. *Clin. Exp. Hypertens.* **21**, 299-332 (1999).
99 Lee, Y. F., Gerashchenko, D., Timofeev, I., Bacskai, B. J. & Kastanenka, K. V. Slow Wave Sleep Is a Promising Intervention Target for Alzheimer's Disease. *Front. Neurosci.* **14**, 705 (2020).
100 Newell, D. W., Aaslid, R., Stooss, R. & Reulen, H. J. The relationship of blood flow velocity fluctuations to intracranial pressure B waves. *J. Neurosurg.* **76**, 415-421 (1992).
101 Newell, D. W., Nedergaard, M. & Aaslid, R. Physiological Mechanisms and Significance of Intracranial B Waves. *Front. Neurol.* **13**, 872701 (2022).

102 Grubb, S. & Lauritzen, M. Deep sleep drives brain fluid oscillations. *Science* **366**, 572-573 (2019).
103 Fultz, N. E. *et al.* Coupled electrophysiological, hemodynamic, and cerebrospinal fluid oscillations in human sleep. *Science* **366**, 628-631 (2019).
104 Alexandrov, A. V. *et al.* Practice standards for transcranial Doppler ultrasound: part I--test performance. *J. Neuroimaging* **17**, 11-18 (2007).
105 Alexandrov, A. V. *et al.* Practice standards for transcranial Doppler (TCD) ultrasound. Part II. Clinical indications and expected outcomes. *J. Neuroimaging* **22**, 215-224 (2012).
106 Rigamonti, A., Ackery, A. & Baker, A. J. Transcranial Doppler monitoring in subarachnoid hemorrhage: a critical tool in critical care. *Can. J. Anaesth.* **55**, 112-123 (2008).
107 Mastantuono, J. M., Combescure, C., Elia, N., Tramer, M. R. & Lysakowski, C. Transcranial Doppler in the Diagnosis of Cerebral Vasospasm: An Updated Meta-Analysis. *Crit. Care Med.* **46**, 1665-1672 (2018).
108 Svedung Wettervik, T., Howells, T., Lewen, A., Ronne-Engstrom, E. & Enblad, P. Temporal Dynamics of ICP, CPP, PRx, and CPPopt in High-Grade Aneurysmal Subarachnoid Hemorrhage and the Relation to Clinical Outcome. *J. Neurocrit. Care* **34**, 390-402 (2021).
109 Spencer, M. P., Thomas, G. I., Nicholls, S. C. & Sauvage, L. R. Detection of middle cerebral artery emboli during carotid endarterectomy using transcranial Doppler ultrasonography. *Stroke* **21**, 415-423 (1990).
110 Ringelstein, E. B. *et al.* Consensus on microembolus detection by TCD. *Stroke* **29**, 725-729 (1998).
111 Smits, H. *et al.* Pulmonary embolism after thrombolysis of hemodialysis grafts. *J. Am. Soc. Nephrol.* **8**, 1458-1461 (1997).
112 Sheriff, F. *et al.* Microemboli After Successful Thrombectomy Do Not Affect Outcome but Predict New Embolic Events. *Stroke* **51**, 154-161 (2020).
113 Gossetti, B. *et al.* Embolism to the brain during carotid stenting and surgery. *Acta Chir. Belg.* **107**, 151-154 (2007).
114 Chiba, T. *et al.* Superb Microvascular Imaging Ultrasound for Cervical Carotid Artery Stenosis for Prediction of the Development of Microembolic Signals on Transcranial Doppler during Carotid Exposure in Endarterectomy. *Cerebrovasc. Dis. Extra* **11**, 61-68 (2021).
115 Spence, J. D. Cardioembolic stroke: everything has changed. *Stroke Vasc. Neurol.* **3**, 76-83 (2018).
116 Christoph, M. *et al.* Simple periprocedural precautions to reduce Doppler microembolic signals during AF ablation. *J. Interv. Card. Electrophysiol.* **64**, 359-365 (2022).
117 Palmon, S. C., Moore, L. E., Lundberg, J. & Toung, T. Venous air embolism: a review. *J. Clin. Anesth.* **9**, 251-257 (1997).
118 Bellner, J. *et al.* Transcranial Doppler sonography pulsatility index (PI) reflects intracranial pressure (ICP). *Surg. Neurol.* **62**, 45-51; discussion 51 (2004).
119 Kashif, F. M., Verghese, G. C., Novak, V., Czosnyka, M. & Heldt, T. Model-based noninvasive estimation of intracranial pressure from cerebral blood flow velocity and arterial pressure. *Sci. Transl. Med.* **4**, 129ra144 (2012).
120 Markus, H., Droste, D. & Brown, M. Ultrasonic detection of cerebral emboli in carotid stenosis. *The Lancet* **341**, 1606 (1993).
121 Romano, J. G. *et al.* Detection of microemboli by transcranial Doppler ultrasonography in

aneurysmal subarachnoid hemorrhage. *Neurosurgery* **50**, 1026-1031 (2002).
122 Goertler, M. *et al.* Rapid decline of cerebral microemboli of arterial origin after intravenous acetylsalicylic acid. *Stroke* **30**, 66-69 (1999).
123 Cottin, V., Delafosse, B. & Viale, J.-P. Gas embolism during laparoscopy. *Surg. Endosc.* **10**, 166-169 (1996).
124 Groenman, F. A., Peters, L. W., Rademaker, B. M. & Bakkum, E. A. Embolism of air and gas in hysteroscopic procedures: pathophysiology and implication for daily practice. *J. Minim. Invasive Gynecol.* **15**, 241-247 (2008).
125 Young, M. L., Smith, D. S., Murtagh, F., Vasquez, A. & Levitt, J. Comparison of surgical and anesthetic complications in neurosurgical patients experiencing venous air embolism in the sitting position. *Neurosurgery* **18**, 157-161 (1986).
126 Florescu, S. C., Anastase, D.-M., Munteanu, A.-M., Stoica, I. C. & Antonescu, D. Venous thromboembolism following major orthopedic surgery. *Maedica* **8**, 189-194 (2013).
127 Pearson, D., Carter, R., Hammo, M. & Waterhouse, P. in *Towards safer cardiac surgery* 325-354 (Springer, 1981).
128 Markus, H. *et al.* Microscopic air embolism during cerebral angiography and strategies for its avoidance. *The Lancet* **341**, 784-787 (1993).
129 Errico, C. *et al.* Ultrafast ultrasound localization microscopy for deep super-resolution vascular imaging. *Nature* **527**, 499-502 (2015).
130 Kirsch, J. D., Mathur, M., Johnson, M. H., Gowthaman, G. & Scoutt, L. M. Advances in transcranial Doppler US: imaging ahead. *Radiographics* **33**, E1-E14 (2013).
131 Demene, C. *et al.* 4D microvascular imaging based on ultrafast Doppler tomography. *NeuroImage* **127**, 472-483 (2016).
132 Tiecks, F. P. *et al.* Effects of the Valsalva maneuver on cerebral circulation in healthy adults: a transcranial Doppler study. *Stroke* **26**, 1386-1392 (1995).
133 Ogoh, S. *et al.* Dynamic cerebral autoregulation during and after handgrip exercise in humans. *J. Appl. Physiol.* **108**, 1701-1705 (2010).
134 Gutierrez-Sigut, E., Payne, H. & MacSweeney, M. Investigating language lateralization during phonological and semantic fluency tasks using functional transcranial Doppler sonography. *Laterality* **20**, 49-68 (2015).
135 Mace, E. *et al.* Functional ultrasound imaging of the brain. *Nat. Methods* **8**, 662-664 (2011).
136 Demene, C. *et al.* Transcranial ultrafast ultrasound localization microscopy of brain vasculature in patients. *Nat. Biomed. Eng.* **5**, 219-228 (2021).
137 Edelman, B. J. & Macé, E. Functional ultrasound brain imaging: Bridging networks, neurons, and behavior. *Curr. Opin. Biomed. Eng.* **18**, 100286 (2021).
138 Anvari, A., Forsberg, F. & Samir, A. E. A Primer on the Physical Principles of Tissue Harmonic Imaging. *Radiographics* **35**, 1955-1964 (2015).
139 Yusefi, H. & Helfield, B. Ultrasound Contrast Imaging: Fundamentals and Emerging Technology. *Front. Phys.* **10**, 100 (2022).
140 Daeichin, V. *et al.* Acoustic characterization of a miniature matrix transducer for pediatric 3D transesophageal echocardiography. *Ultrasound Med. Biol.* **44**, 2143-2154 (2018).
141 Liu, Q., Chen, C., Chang, Z.-y., Prins, C. & Pertijs, M. A. in *2015 IEEE International Ultrasonics Symposium (IUS)*. 1-4 (IEEE).
142 Chavignon, A. *et al.* 3D Transcranial Ultrasound Localization Microscopy in the Rat Brain With a Multiplexed Matrix Probe. *IEEE Trans. Biomed. Eng.* **69**, 2132-2142 (2022).
143 Jensen, J. A., Nikolov, S. I., Gammelmark, K. L. & Pedersen, M. H. Synthetic aperture

ultrasound imaging. *Ultrasonics* **44**, e5-15 (2006).
144 Aaslid, R. & Nornes, H. Musical murmurs in human cerebral arteries after subarachnoid hemorrhage. *J. Neurosurg.* **60**, 32-36 (1984).
145 Miller, R. D. *et al. Miller's anesthesia e-book*. (Elsevier Health Sciences, 2014).